Keele
University

Diels Alder-mediated release of gemcitabine from nanoparticles: developing improved methods for pancreatic cancer drug delivery

By

Adeolu Oluwasanmi

A thesis submitted in partial fulfilment of the requirements of Keele University for the degree of Doctor of Philosophy at the School of Pharmacy

June 2017

Abstract

Pancreatic cancer or pancreatic ductal adenocarcinoma (PDAC), is the deadliest type of cancerous malignancy with a survival rate of only 3.7 % after 5 years. The first line current treatment is a drug called gemcitabine, which has been shown to display effectiveness in only 23.8 % of patients. Hybrid nanoparticles (HNPs) comprised of an iron oxide core and outer gold coat have shown great potential for anti-cancer therapies. The magnetic iron oxide cores and the surface plasmon resonance (SPR) properties of the gold surface provide the HNPs with the capabilities of diagnostic imaging and drug delivery, making them true theranostic agents.

A novel thiolated thermally labile drug (TTLD) analogue of gemcitabine was successfully synthesized and attached to the surface of HNPs forming a novel drug formulation called TTLD+HNP. This TTLD compound is comprised of a gemcitabine molecule with a Diels Alder cycloadduct. Gem-Mal, a maleimide derivative of gemcitabine is released during retro Diels Alder (rDA). The mode of release involves heat-activation of the rDA reaction facilitated by the SPR of the gold shell. TTLD was characterised with mass spectrometry, nuclear magnetic spectroscopy and IR spectroscopy.

Preliminary studies determined that the TTLD compound doesn't undergo rDA at 20 °C and a subsequent 4 week study displayed no rDA occurring at 20 °C. Afterwards *in vitro* experiments including the MTT and trypan blue assay determined that Gem-Mal is 4.6 times less cytotoxic than gemcitabine but is taken up by cells 11 fold faster when attached to the HNPs. Upon heat-activation at 44 °C, the TTLD+HNP formulations cytotoxicity increased by 56 % outperforming gemcitabine by 26 %, confirming its temperature driven activity. The TTLD+HNP drug formulation is the first of its kind and has displayed superior anti-cancer activity to the current first line drug gemcitabine after heat mediated controlled release.

Keywords: Theranostics, Thermoresponsive drug delivery, Diels Alder, Pancreatic cancer

Contents

List of Tables

List of Figures

xviii

Acknowledgements

I would not have succeeded in completing my PhD, nor have such a rich and rewarding experience throughout if it was not for the boundless support and guidance provided by my supervisors, Dr Clare Hoskins and Dr Anthony Curtis. They have made my studies at Keele University a truly wonderful time and inspired within me, a drive to pursue a lifelong career in academic research.

I would also like to thank my parents and brother for believing in me and displaying loving patience, especially when I decided to go to university a third time! Knowing you're cheering me on from back home helped me through the highs as well as the lows. Thank you greatly Keele University! I have worked and live here on this beautiful campus and I will be sad to leave.

A great thank you to the nanopharmaceutics group. It has been enjoyable working with you all in the labs. Your advice, warmth and friendship will stay with me forever. I especially want to thank May for strongly insisting that I eat the food she offers for my own good and for generally looking out for me, Ali and Mohanad for all the great laughs in the labs as well as those oddly deep conversations we'd drift into and Wejdan who helped me greatly with my cell work.

Phil and Dennis, thanks for bearing with me for all the questions I'd frequently ask and I'd also like to thank Mark and Neil who helped me with setting up some of my experiments. Last but certainly not least, many thanks to you Karen for your assistance and training in TEM imaging.

I now look to the future with excitement knowing I gave it my all to get to where I am now.

Adeolu

CHAPTER 1: INTRODUCTION

1.0. Cancer

Cancer is one of the biggest causes of death for humans worldwide. It occurs due to irregular cell growth and uncontrolled cellular division (Yang *et al*. 2013; Bouyssou *et al*. 2014; Su *et al*. 2014). Cell growth and division is common in nearly every type of tissue, which is why cancer comes in many forms and can be found anywhere in the human body. Neoplasia is new tissue caused by the abnormal growth of cells, which exceed the growth rate of the cells around it forming a condensed mass of tissue in that region (de Wilde *et al*. 2012). Neoplasia can be caused by mutations in oncogenes, which are genes that have the potential to cause cancers as they control cell growth and division via the oncoproteins they produce (de Wilde *et al*. 2012; Aird & Zhang 2015). Other causes of cancer are attributed to cells losing the ability to undergo apoptosis, which is programmed cell death (Felt *et al*. 2015). Neoplasia of the pancreas (Pancreatic Intraepithelial Neoplasia or PanIN) can progress into malignant cancerous tissue called pancreatic ductal adenocarcinoma (PDAC) (Yuqing Zhang *et al*. 2013a). The smallpox vaccine was the first of its kind and responsible for the subsequent eradication of this disease worldwide (Foster *et al*. 2011; Tarantola & Foster 2011). Other diseases such as polio and measles have seen significant reductions in the last few decades with fewer cases occurring annually (Doshi *et al*. 2015; Mwenge *et al*. 2016). These advances are partly due to the fact that the agent responsible for each disease is known. The genetic and physical structure have been elucidated and treatments can be designed to halt the ability of the disease to infect or augment the body in fighting the disease. Unlike infectious diseases, cancer is best described as our own bodies working against us. There is no singular cause for cancer and it affects every person differently because every persons body is unique and therefore, every cancer is unique. At the present time, we have specific vaccines designed to combat specific diseases that are effective in the majority of people. However it's highly unlikely that we will have a single treatment that is effective on all cancer types in almost all patients, although research into cancer vaccines is already underway (Corocleanu 2008). The causes of cancer are many and include; exposure to carcinogens, infections, ionising radiation, lifestyle choices and genetic predisposition.

About 5-10 % of cancers are caused by genetic defects (Nagy *et al*. 2004). This leaves about 90-95 % of all cancers being attributed to lifestyle and environmental factors. 25-30 % of

cancer related deaths are due to tobacco use and 30-35 % is linked to diet and exercise(Anand et al. 2008). Infections are linked to 15-20 % of cancer related deaths(Anand et al. 2008). The human papilloma virus for example, is an infectious agent that has been linked to over 5 % of all cancer cases worldwide and is responsible for 99.7 % of all cervical cancer cases (Ault 2006). Viruses infect human cells by inserting their genetic code into our DNA. Its code can then be used by the human cell to produce more copies of itself and produce proteins (Anand *et al*. 2008). Some of these genes are oncogenes such as the E6 and E7, which prevents apoptosis (Ault 2006). Carcinogen is a term used to describe something that causes cancer. These are often chemical compounds, but can also include ionising radiation such as gamma rays and radioactive atoms (Barlow & Schlatter 2010). Asbestos is responsible for over 100,000 deaths annually, which is over half of all occupational cancer deaths, due to exposure from airborne fibres (Turci *et al*. 2016). Ionizing radiation such as UV exposure can damage the DNA of healthy cells causing mutations (Megha *et al*. 2015). These often cause the cell to trigger apoptosis. In some cases the cell might lose the ability to signal cellular apoptosis due to DNA damage, which can lead to the formation of cancerous cells.

1.0.1. Types of cancers

Neoplasm is a term used to describe the abnormal growth of localised cells. These cells can form a mass called a tumour. The two main types of tumour tissues are benign and malignant. Benign tumours lack the ability to metastasize and are therefore not classed as malignant cancers (Hanahan & Weinberg 2000). Examples of benign tumours include; moles, lipomas and adenomas (Horibe *et al*. 2016; Schofield 2009; Namiki *et al*. 2016). Moles are abnormal skin growths that can be subdermal (beneath the skin) or on the surface. Surface moles are darker due to having a higher concentration of the skin pigment melanin (Schofield 2009). Lipomas are benign tumours formed from fat tissues and are more commonly found in middle aged and the elderly (Bagherzade & Etemad 2016). Adenomas are benign tumours of glandular tissue and/or the epithelial cells that line glandular organs (Peters *et al*. 2016; Jayaram *et al*. 2015; L. Yang *et al*. 2016). These can grow from many of the body's glandular tissue, such as the prostate, adrenal, pituitary and pancreas. Benign tumours are often harmless to the organism and are sometimes left alone without any ill effects. However, some benign tumours, depending on their type and

location may be harmful (Hruban & Fukushima 2008; Eyesan *et al*. 2011; Galea 2016). This can be due to their presence causing the compression of neighbouring tissues and blocking blood vessels. This can cause poor blood flow in certain areas of the body that can lead to nerve, organ damage and necrosis. Others benign tumours, such as some adenomas may secret hormones leading to an elevated level of them within the body (Jukes *et al*. 2016). Due to the random chance occurrence of neoplastic growths, they have the potential to occur at any age group. The average number of moles is between 1 and 3, for a child of European descent under the age of 10. A 20 year old young adult of European descent has roughly 21. This number climbs to around 22 for men and 33 for women in their thirties (Mackie *et al*. 1985). Malignant neoplasm of the skin is one of a plethora of possible cancer types that can occur.

Malignant or cancerous cells possess the ability to migrate away from their parent location and form satellite tumours in another location or organ in the body. This process is called metastasis and it's what distinguishes them from benign tumours (Chambers *et al*. 2002). These secondary tumours will be comprised of the same cell types as their original tumour. For example, metastasised pancreatic cancer cells in the liver will be made up of pancreatic cancer cells, not liver cancer cells. In order for a tissue to be described as cancerous it must satisfy the "hallmarks of cancer". There were initially 6 hallmarks which were; avoidance of programmed apoptosis, promoting the formation of new blood vessels, heightened rate of cell division, continuous growth, unlimited number of cell divisions and the ability to spread to new sites (metastasize) (Hanahan & Weinberg 2000). A further 4 hallmarks were added which are; genome instability, abnormal metabolic pathways, tumour promoting inflammation and the avoidance of immune mediated destruction (Hanahan & Weinberg 2011). Cancer occurs due to an accumulation of mutations in the DNA over multiple cell divisions as shown in Figure 1. Some of these mutations such as a mutation of the k-ras gene might cause continuous cell division leading to the formation of tumours (Reckamp *et al*. 2016; Almoguera *et al*. 1988). Another mutation might affect the p53 gene for example, which is important for tumour suppression (Li *et al*. 1998). Genes that causes this are called oncogenes. Normally these genes help cells grow and divide. If these genes become mutated they may become overexpressed or permanently switched on leading to rapid and continuous cell division.

Figure 1: Diagram depicting how a series of mutations leads to the formation of malignant carcinomas.

Tumour suppressor genes slow down cell division and detect DNA damage. They can also trigger cellular apoptosis especially when mutated genes are present. If these genes are inhibited or mutated then the cell can grow without resistance (Li *et al*. 1998). The development of cancer can be described as a miniature example of evolution. Each mutation might confer an advantage to the survival of each daughter cell allowing it to outlive neighbouring normal cells.

1.0.2. Pancreatic cancer

Pancreatic cancer is caused by the formation of neoplasia within the intraepithelial regions of the pancreas (Roshani *et al*. 2014; de Wilde *et al*. 2012; Zhi *et al*. 2014). The pancreas is located within the abdomen surrounded by several other organs, major blood vessels and tissue types. This allows pancreatic cancer to spread quickly to neighbouring areas (Zhi *et al*. 2014). They can spread when a single cancer cell enters the bloodstream. They are quickly swept away and usually settle when they reach a capillary (Z'graggen *et al*. 2001). Afterwards they pass through the wall of the blood vessel and attach to other tissues, organs or bone forming secondary cancers. The process of cancer cells emigrating to new sites is highly unlikely because it is very stressful for the cells which nearly always perish before completing the journey. However it only takes one out of the multitude of cancer

cells to survive. Pancreatic cancer cells have the advantage of being situated near many blood vessels, multiple organ and tissue targets as well as the lymphatic system (Paiella et al. 2016). The lymphatic system consists of lymphatic vessels that transport a fluid called lymph around the body. Lymph nodes are clusters of lymph tissue that are found along these lymphatic vessels. Pancreatic cancer cells can penetrate the lymphatic system and collect at lymph nodes forming tumours as well as travel along the lymphatic system spreading to other organs via this route (Xiao et al. 2014). This makes transport though the lymphatic system, an ideal method of invasion of for cancerous cells. Therefore even with successful treatment pancreatic cancer still has the possibility of reoccurring from satellite sites (Z'graggen *et al*. 2001; Prasad & Katiyar 2013). Surgery is the only method capable of curing pancreatic cancer and is often accompanied by post-operative chemotherapy to reduce the chances of recurrence (Bockhorn *et al*. 2014). Even after early detection, subsequent surgery and post-operation chemotherapy the survival rate only increases to 21 % (Yuqing Zhang *et al*. 2013c; Bockhorn *et al*. 2014). A contributing reason for this is because pancreatic cancer rarely causes noticeable symptoms primarily attributed to cancer until it is fairly advanced and has spread to surrounding tissues (Ling *et al*. 2013). Once this has occurred, surgery is no longer an option and patient quality of life becomes the top priority. Most patients rarely survive beyond one year after a pancreatic cancer diagnosis, therefore a balance has to be struck between the patients quality of life and the extension of their life (Kristensen *et al*. 2016).

1.0.3. Cancer statistics

Pancreatic cancer has an absolute 5 year survival rate of 3.7 % (Vincent et al. 2011). This means that after the disease is first diagnosed the patient has less than 5 % chance of surviving after 5 years (Yuqing Zhang *et al*. 2013b; Liu *et al*. 2012a; Tran *et al*. 2013a). This particularly deadly type of cancer has the worst prognosis of all cancer types (Yuqing Zhang *et al*. 2013c; Al Shemaili *et al*. 2014; Malvezzi *et al*. 2013). Pancreatic cancer is the 5th most common cause of cancer death in the UK (Maraveyas *et al*. 2012) and 4th most common in the US (Zhang *et al*. 2011; Pinho *et al*. 2014). It occurs in only 2.6 % of all cancer cases as of 2011, but is responsible for 5.2 % of cancer deaths in the UK which is a significantly disproportionate survival statistic owing to its poor prognosis. The 5 year survival rate of pancreatic cancer has only increased from 2 % to 3.7 % on average since 1975. These

statistics show the deadliness and great importance in improving the survival rates of those who are diagnosed with pancreatic cancer. In contrast to pancreatic cancer's prognosis is testicular cancer which has a 5 year survival rate of 97.2 % according to Cancer Research UK in all stages. After 10 years the survival rate is still very high at 96 %. Therefore the 97.2 % survival rate is deemed the "cure" rate according to Cancer Research UK (Brock *et al*. 1993). The statement "cured of cancer" is rarely used by medical professionals due to the possibility of reoccurrence with a more aggressive form of the cancer. The term "remission" is used instead. To say that a cancer like testicular cancer is "cured" must signify that it has an extremely good prognosis. Unlike the poor prognosis history of pancreatic cancer, other forms of cancer like breast and prostate, have an improved prognosis over the last four decades. Survival rates as high as 90 % in all age brackets, after 5 years have been witnessed with elderly age being a significant factor in survival (Thakur *et al*. 2014; Fontein *et al*. 2013; Tyson & Castle 2014). Survival rates for some common cancers types have improved over the last 4 decades. Breast cancer for example has shown an improvement in survival rates from 52 % to 85.1 % since 1975 which is attributed to early detection. This is because medical professionals often selectively screen for these cancers during routine medical examinations and also because of advances in breast cancer research (Thakur *et al*. 2014).

1.1. Current treatments for pancreatic cancer:

1.1.1. Surgical resection (Whipple's Procedure)

Surgical resection remains the only curative method of ensuring the complete removal of pancreatic cancer tumours in order to establish a remission state in a patient. However this option is rarely available to the majority of people diagnosed with pancreatic cancer as it's often diagnosed too late when metastasis has occurred (Casadei *et al*. 2015). A well-known trait of pancreatic cancer is that it often lacks significant symptoms in early stages. The name of the surgical procedure for treating pancreatic cancer is called the Whipples procedure (Sa *et al*. 2010; Kang *et al*. 2016). This procedure is named after Allen Oldfather Whipple who established the resection (Sa *et al*. 2010). The anatomy of the pancreas and surrounding organs is shown in Figure 2 where the pancreas sits within the duodenal curve and along the duodenum and base of the stomach (Sa *et al*. 2010).
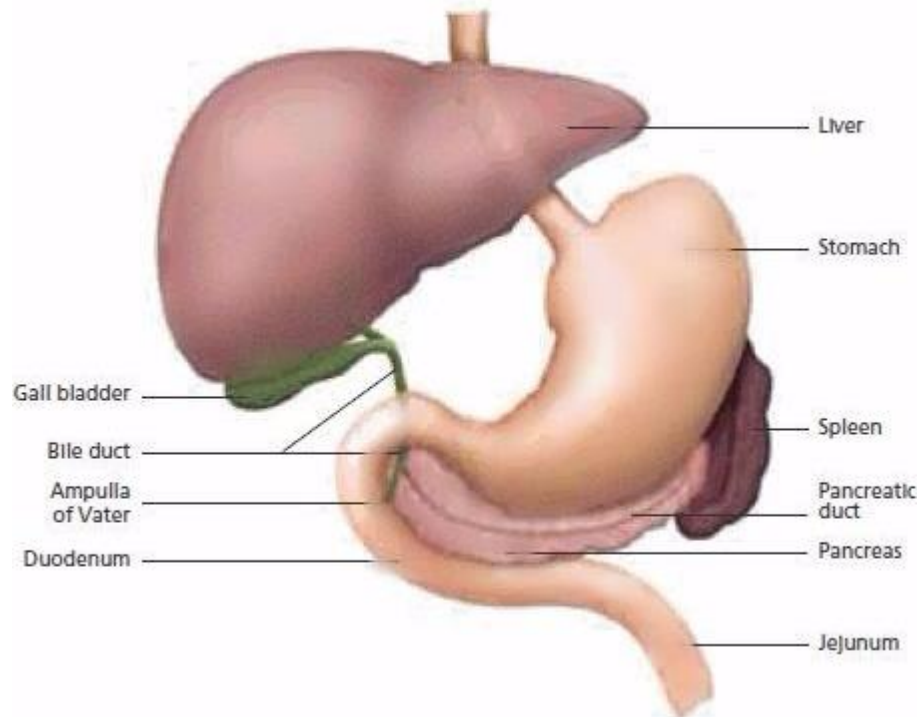
Figure 2: The preoperative anatomy of the pancreas and surrounding organs (Sa *et al*. 2010).

These areas are common regions for secondary tumour sites when pancreatic cancer has metastasised (Paiella et al. 2016). Therefore to ensure complete removal of pancreatic tumours, large areas of these organs have to be removed. The Whipples procedure illustrated in Figure 3 involves the removal of the pancreatic head, duodenum, common bile duct, gall bladder, and the bottom half of the stomach (Sa et al. 2010).
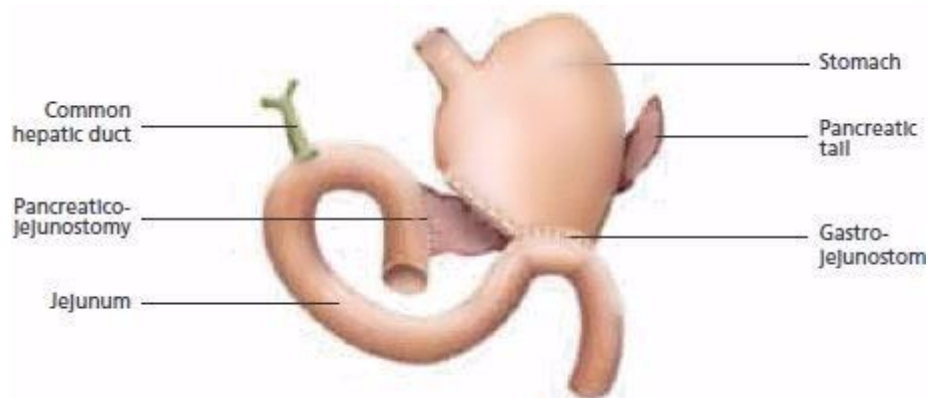
Figure 3: Post Whipple's surgery anatomy (Sa et al. 2010).

The survival rate of the Whipple procedure has improved from 70 % to 98 % over the last century. One study noted that patients have an 18 % chance of being readmitted to hospital within 30 days of discharge, which was due to post-operative complications and failure to

thrive (Kagedan *et al*. 2015). Some post-operative complications include infections at the surgical site, internal bleeding, delayed gastric emptying and in rare cases thrombosis of the superior mesenteric vein (Huťan *et al*. 2014). The latter is a vein that carries blood from the small intestine, stomach and pancreas. Thrombosis can cause intestinal necrosis, which can lead to patient death (Huťan *et al*. 2014). The quality of life diminishes noticeably in patients following a Whipple's procedure. Common issues include pancreatic/abdominal pain, nausea and vomiting, (Shah *et al*. 2013). A combination of these complications, coupled with the diminished post operation quality of life, factors in the eligibility of the Whipples procedure on a patient by patient basis.

1.1.2. Chemotherapy

Chemotherapy is the term used to describe the treatment of cancers such as pancreatic cancer with cytotoxic anti-neoplastic drugs (Batmani & Khaloozadeh 2013). Examples of drugs that are used to treat pancreatic cancer include: fluorouracil (5-Fu), cisplatin, capecitabine and gemcitabine. Cytotoxic drugs inhibit tumour growth by interacting with the processes involved in the synthesis of new proteins vital for cell proliferation. They also inhibit cell growth by also inhibiting DNA replication or causing enough stress to the cells leading to apoptosis (Batmani & Khaloozadeh 2013).

1.1.2.1. 5-Fluorouracil
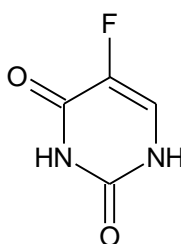
Figure 4: The structure of 5-fluorouracil a structural analogue to pyrimidine.

5-Fu is a thymidylate synthase inhibitor. This enzyme is responsible for the synthesis of thymidine which is a nucleoside required for DNA replication. After 5-Fu is administered, it is quickly metabolised to 5-fluorodeoxyuridine monophosphate (FduMP) which binds to thymidine synthase blocking its ability to methylate uracil. This makes 5-fluorouracil a prodrug. Uracil forms base pairs with adenine during DNA transcription. It is methylated to form thymine, which is required for DNA replication. Without the action of thymidylate

synthase, the cell become starved of thymidine after multiple divisions (Mohamed & Safwat 2016). 5-Fu can also be triphosphorylated and become incorporated into RNA in the place of uracil blocking DNA transcription which ultimately stops the growth of cancerous cells.

1.1.2.2. Gemcitabine
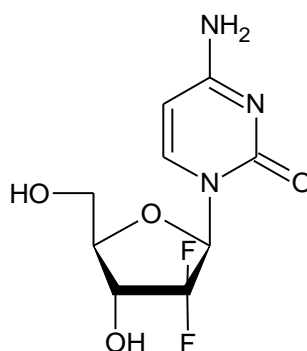
Figure 5: The structure of gemcitabine a structural analogue to cytidine.

In most cases of pancreatic cancer, where the patient is within their stage 4 metastatic phase, gemcitabine is the first line treatment because it demonstrates improved clinical benefits and reduced side effects when compared to 5-fluorouracil. (Brown et al. 2014; Heinemann 2001). Even with the increased survival rate with gemcitabine, the prognosis for pancreatic cancer is still abysmal and urgent improvements and novel strategies in pancreatic cancer chemotherapeutics are needed.

Gemcitabine is a pro drug, which is a drug that is administered in an inactive form shown in Figure 5 and phosphorylated into its clinically active form gemcitabine triphosphate within cells after cellular uptake (Baraniak *et al*. 2014; Yuan Zhang *et al*. 2013). This active form inhibits DNA elongation by replacing the nucleoside cytidine leading to cell death (Pliarchopoulou & Pectasides 2009). On an unrelated note, this activity has also been exploited for antiviral treatments. Gemcitabine has been shown to inhibit the proliferation of enterovirus, coxsackievirus and HIV by preventing the replication of the virus's genetic code. Its active form replaces cytidine in the viral code producing highly mutated non-viable strains (Yun et al. 2009; Kang et al. 2015).

When gemcitabine is introduced into the body it can travel along several routes before reaching the target via an IV injection due to the circulatory system. It is usually injected

into the arm of the patient as a drip over roughly 30 minutes to several hours (Pliarchopoulou & Pectasides 2009). This is to prevent localised toxicity around the site of administration. It may degrade or be unable to pass through certain membranes due to its location after administration. It may also be metabolised in the liver in significant amounts before reaching certain organs. This is called first pass metabolism (Qiong Gao *et al*. 2014; Lee *et al*. 2013). Drugs, especially cytotoxic drugs, are dose limited which lowers the effective amount of active pharmaceutical ingredient working at the intended site of treatment. Not all cancers behave the same, and the same type of cancer may vary in difficulty from a patient to patient basis. One treatment may be highly effective in one patient and unsuccessful in another even at the same stage of progression (Santhosh & Ulrih 2013a). For example, gemcitabine has been described as having a response rate of 23.8 % which means that 76.2 % of patients taking gemcitabine see no viable response to the drug (Hoskins *et al*. 2010; Burris *et al*. 1997) (Hoskins *et al*., 2010, Moore, 1995), while Kim *et al* states that the response rate is as low as 5.4 % (Kim & Gallick 2008).

A clinical study was carried out comparing the typical 2.2 g m^{-2} 30 minute single dose infusion of gemcitabine (Arm A) with a fixed dose rate (FDR) 1500 mg m^{-2} administered at a rate of 10 mg m^{-2} min, over 150 min (Arm B). Arm B showed the greatest response rate where the overall response rate was 11.6 % compared to Arm A which had a lower response rate of 7.3 % (Hochster 2003). Multiple research groups state different response rates for gemcitabine, some stating that it is as high as 23.8 % or as low as 5.4 % from established sources while others have observed intermediate values of 7.3 % and 11.6 % depending on their experimental method. However the conclusion remains the same regardless of the variation in gemcitabine response rates. Gemcitabine may be the most favourable drug for combating pancreatic cancer, but its response rate is too low and advances in the treatment of pancreatic cancer with chemotherapeutics are urgently required.

Gemcitabine is cytotoxic and indiscriminately targets both cancerous and non-cancerous cells leading to the side effects associated with chemotherapy such as hair loss, nausea, bone marrow suppression, diarrhoea, liver problems, fever and fatigue (Zhang et al. 2011; W. Song et al. 2014). It has a low efficacy meaning that most of the drug is metabolised and excreted before being able to carry out its intended pharmaceutical activity. Even with significant cytotoxic effects, its dosage must be as high as possible to ensure that enough

pharmaceutical activity at the site of action occurs, due to its poor biocompatibility. Its small molecular weight contributes to its rapid renal clearance. Combating this clinically involves providing frequent high doses of the drug which can cause hepatic and renal toxicity (Sadjadi & Annamaraju 2012). If these side effects are too significant then treatment has to be discontinued even if there is a tumour response to the drug (Vandana & Sahoo 2010). Improvements with the application of gemcitabine and other cytotoxic anti-cancer agents are achievable if methods of improving the activity and/or improving biocompatibility were implemented (Wagstaff *et al*. 2012; Vandana & Sahoo 2010).

Localised administration via an intratumor injection route has been shown to possess advantages over the conventional intravenous methods (Shirley et al. 2013). For example, pancreatic adenocarcinomas are typically hypovascular, which means they have relatively less surrounding blood vessels which are the main routes for intravenously administered gemcitabine (Shirley et al. 2013). They also possess a dense stroma, which is a growth of connective tissue that reduces the diffusion and therefore accumulation of gemcitabine within tumours (Whatcott et al. 2012). Intratumour injections directly into the tumour would bypass these problems faced by the intravenous route of administration. A major disadvantage of the intratumour administration route, is that it will be ineffective for secondary cancer tumours that are too small to be detected yet. This is especially true for most patients diagnosed with pancreatic cancer because this occurs in the late stages of the disease.

1.1.2.3. Cisplatin
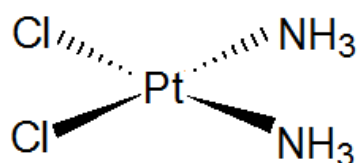
Figure 6: The structure of cisplatin.

Cisplatin is widely regarded as the first platinum containing anti-cancer drug. Other anti-cancer drugs belonging to this group include carboplatin and oxaliplatin (Dasari & Bernard Tchounwou 2014). Cisplatin is a metallic coordination compound with two chlorine and two amine ligands in a cis conformation. It is used in the treatment of various cancers including ovarian, lung and neck cancers. It is also often employed in combination with

other chemotherapeutic drugs for the treatment of other cancers such as breast, prostate and pancreatic cancer (Dasari & Bernard Tchounwou 2014). The uptake of cisplatin into cells is carried out by the copper membrane transporter (CTR1). Once inside a cell, the chloride atoms are replaced by water molecules forming a very strong nucleophile which is a compound that donates electrons to form covalent bonds. In this form, it can bind to the N7 purine shown in Figure 7.
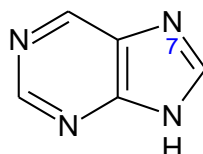
Figure 7: Chemical structure of purine.

This dative covalent binding forms DNA adducts which cause DNA damage and block cell division which leads to apoptotic cell death (Dasari & Bernard Tchounwou 2014). The DNA adducts cause the DNA strand to bend 34˚, which triggers cell repair mechanisms (Katarzyna & Basiak n.d.; Rosenberg n.d.). Due to cisplatin's presence, cell repair is not successful and cellular apoptosis occurs.
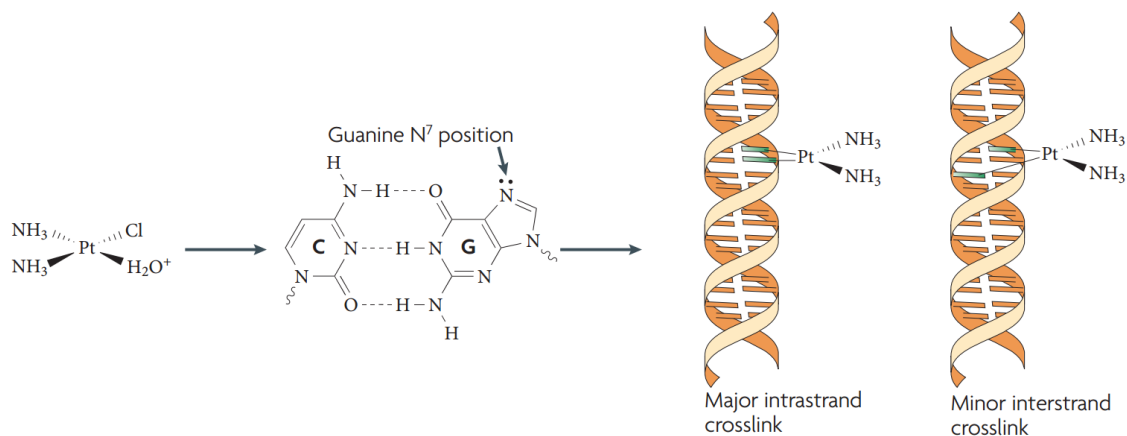
Figure 8: Binding of cisplatin to DNA.

1.1.2.4 Multidrug resistance of cancer

Multidrug resistance is the resistance acquired by cancerous cells to multiple chemotherapeutic drugs, even those that have not been exposed to the cancerous cells previously (Wu *et al*. 2014). Once this occurs, the cancerous cells are less sensitive to the cytotoxic drugs. Increasing the dose may improve the effectiveness because the cells gain resistance, not immunity to the drug. However drugs like gemcitabine and 5-FU are cytotoxic and therefore dose limiting (Wu *et al*. 2014). Multidrug resistance is the most common reason for failed chemotherapy treatment and can arise before treatment where it is described as primary or intrinsic resistance (Hagmann *et al*. 2010). This is due to some cancer cells possessing functional characteristics such as an enhanced DNA repair system, which prevent DNA damage caused by drugs like cisplatin, ultimately prevent apoptosis (Dasari & Bernard Tchounwou 2014). Alternatively, acquired resistance occurs after exposure to chemotherapeutics (Wu *et al*. 2014). A commonly observed effect of gemcitabine is a marked response to the drug initially, followed by a rapid increase in resistance. This confirms that some of the cancerous cells within tumours already possess intrinsic resistance to cytotoxic agents like gemcitabine before the first dose is even administered, which inevitably leads to poor patient outcomes (Kim & Gallick 2008). Cells that were not killed by the chemotherapy can also mutate conferring an acquired resistance to future generations. Multidrug resistance can arise because of multiple reasons. These include, an immune response to the drug/drug transporter, DNA repair and changes in the drug target caused by mutations (Ling *et al*. 2005). Over expression of proteins responsible for producing efflux pumps like p-glycoprotein is also a major contributor to multi drug resistance. Because cancer drugs are cytotoxic, macrophages may become increasingly sensitive to their presence and increase the rate of drug metabolism (Markman *et al*. 2013). The liver is responsible for much of the detoxification within the body and may improve the rate of drug metabolism after repeated doses (Tsume *et al*. 2014). Mutations in the DNA within cancer cells can make them more resistant to cytotoxic drugs or even make them harder to attack due to the high specificity of certain drugs (Patel *et al*. 2013; Di Gangi *et al*. 2014). Pancreatic cancer cells can acquire resistance to gemcitabine by disrupting its conversion, to its active triphosphate form by the down regulation of deoxycytidine kinases (Fryer et al. 2011). The copper transporter 1 (CTR1) is

important for the uptake of platinum compounds. Research has shown that cisplatin degrades CTR1 which further inhibits its uptake. Cancer cells that already exhibit under expression of CTR1, display resistance to cisplatin (Shen et al. 2012). Thymidylate synthase is the main target of 5-Fu and their subsequent binding inhibits thymidylate synthase preventing the production of thymine. The overexpression of thymidylate synthase allows the cancer cell to continue producing thymidylate synthase, even though some are inhibited. This provides the cancer cell resistance to 5-Fu. This leads to higher 5-Fu dose requirements, which may not be possible due to its cytotoxic nature (Wang et al. 2014).

1.2. The use of nanotechnology in drug delivery systems

Nanotechnology is a term used to describe the engineering of materials and structures on the nanoscale (Y. Gao *et al*. 2014; Parhi *et al*. 2012). These can include organic nanoparticles like liposomes and dendrimers as well as metallic/core shell nanoparticles like silver nanoparticles and gold coated nanoparticles. Synthetically, a nanoscale material or structure is produced by self-assembly methods where components under the right conditions would arrange themselves to form structures. Examples of these include micelles, vesicles, carbon nanotubes and metallic nanoparticles which are used for drug delivery systems (Shu *et al*. 2014; Islam & Miyazaki 2010; Salameh *et al*. 2014). Each type of nanoparticle drug delivery system as shown in Figure 9 has its own advantages and disadvantages for the transportation of various cargoes such as chemotherapeutic drugs, proteins and RNA.
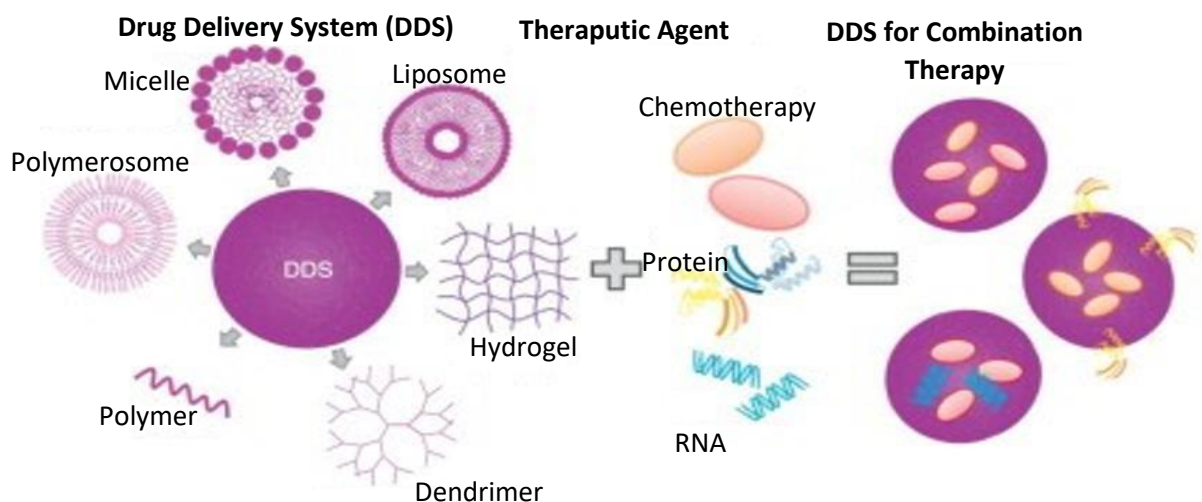
Figure 9: Diagram showing drug delivery systems for multiple types of cargo including cytotoxic agents, proteins and genetic materials like RNA (Eldar-Boock *et al*. 2013).

Nano sized drug delivery vehicles and systems can be used to overcome the common problems associated with drug discovery such as poor bioavailability, water solubility and rapid clearance, which typically prevent promising drug candidates from becoming clinically viable. Lipid based carrier systems such as micelles and liposomes, can encapsulate hydrophobic drugs to aid in drug solubility and bioavailability. This is achieved by creating a hydrophobic cavity to transport the drug cargo, that is bordered by a hydrophilic shell, that increases the overall solubility of the drug carrier system (Gupta et al. 2013). Hydrogels which are cross linked polymer chains arranged in a grid or net formation (Okay n.d.). These can store water and any drugs currently dissolved during gel formation, physically trapping the drug molecules in between the chains. Hydrogels can swell during pH or temperature changes facilitating the release of their cargo through the larger gaps within the gel network (Vashist & Ahmad 2013; Okay n.d.).

1.2.1. Micelles

Micelles are the end results of the aggregation of amphiphilic molecules in a liquid colloid. Amphiphiles are molecules that possess a hydrophobic (water hating) and hydrophilic (water loving) regions. Examples of amphiphiles include surfactants, detergents and wetting agents. Within an aqueous solution, these amphiphiles will first arrange themselves at the surface of an aqueous solution. The hydrophilic regions shown in Figure 10 will extend into the aqueous solution while the hydrophobic regions will be positioned above the solution. This reduces the surface tension which can assist in the mixing of oils and aqueous solutions. Once the surface has been saturated with an amphiphilic compound it will then begin to form micelles. This occurs when the amphiphiles arrange themselves to form spherical conformations where the hydrophilic region interacts with the aqueous solution forming the outside edge of the sphere and the hydrophobic regions aggregate together.
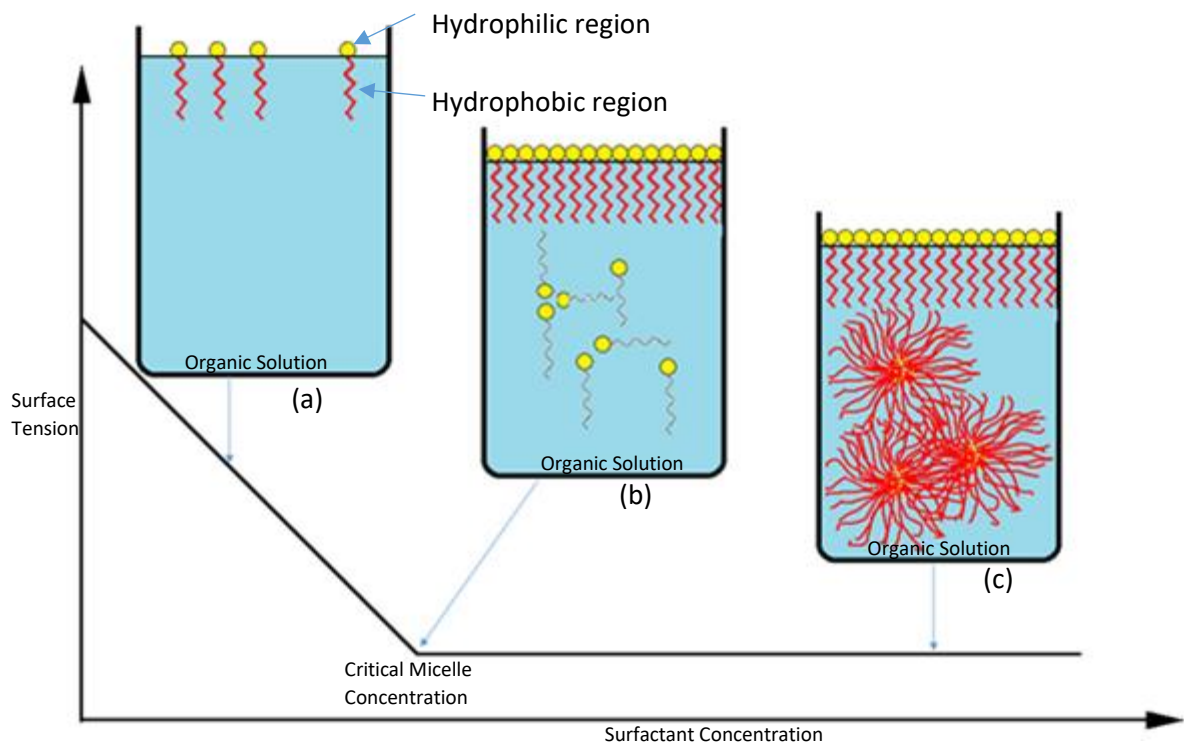
Figure 10: Model depicting the reduction of surface tension as the surfactant concentration increases to the point micelles form, beyond the CMC.

The further introduction of amphiphilic compounds will lead to the formation of more micelles. The concentration, when this occurs is called the critical micelle concentration. The formation of micelles depends on another attribute specific to each amphiphile species, which is the critical micelle temperature. This is the minimum temperature where micelles will form. If the critical micelle concentration is reached, the introduction of more amphiphilic compounds will lead to the formation of crystalline structures. If enough energy in the form of heat is supplied the entropic forces overcome those keeping the crystalline structure leading to the formation of micelles. Therefore the critical micelle concentration and the critical micelle temperature must be both reached to form micelles with the critical micelle temperature being the most important criteria. The critical micelle concentration and temperature can be determined experimentally (Chakraborty et al. 2011). The characteristics of surfactant containing solutions displays a sudden fall in concentration related properties when the critical micelle concentration and temperature is reached. These characteristics can include the change in surface tension, due to surface saturation of surfactants and the change in the absorption of water insoluble dyes, which decreases as emerging micelles encapsulate them (Chakraborty et al. 2011). One of the biggest detriments a novel drug can have is poor aqueous solubility. Drugs must have

aqueous solubility if they are going to pass through the various biological barriers that can exist such as the lining of the stomach and small intestine. If a hydrophobic species such as a hydrophobic drug is introduced into an aqueous solution above the critical micelle concentration and temperature, these micelles may spontaneously form around these drugs encapsulating them. This provides micelles with the ability to act as drug carriers. Micelles are often called detergents because of their ability to promote the mixing of oily and aqueous solutions which often do not mix.

The treatment of pancreatic cancer with micelle based nano drug delivery vehicles has been established in literature (Kesharwani et al. 2015). Curcumin is a naturally occurring dye that has been reported to possess anti-proliferative and apoptotic effects on pancreatic cancer cells, as well as increasing the chemo sensitivity of these cells (Kesharwani *et al.* 2015). However, like many promising anti-cancer agents, the poor aqueous solubility and rapid clearance makes it unsuitable for clinical use. Styrene-maleic acid is an amphiphilic compound that was utilised as a micelle to encapsulate and transport curcumin. The results of this study noted a 162-fold improvement in its systemic half-life (Kesharwani et al. 2015). Curcumin has yet to successfully complete a clinical trial due to its poor bioavailability, solubility rapid clearance (Nelson et al. 2017). Research into styrene-maleic acid micelles is as drug carriers for curcumin to neutralise these unfavourable characteristics is ongoing, but has not reached the clinical trial stage (Alsaab et al. 2017).

1.2.2. Liposomes

Before the term "nanoparticle" was coined by Norio Taniguchi in 1974, they were referred to as "ultrafine particles". This term was mainly used to describe liposomes and micelles. Liposomes are largely composed of phospholipids and are prepared by the solvent evaporation of lipid solutions to form thin lipid films. Hydration and subsequent agitation (sonication) of the stacked lipid layers cause them to break and reform as liposomes. Cholesterol can be added prior to agitation to confer membrane stability to the liposomes (Yu *et al.* 2001).

Like biologically occurring vesicles, liposomes are used to surround and capture substances such as active pharmaceutical ingredients and compounds in aqueous solutions. Their greatest advantage is that their structure is very similar to cell membranes (Wang *et al.*

2013). At their biological target their lipid bilayer could fuse with cancerous cell membranes releasing their contents in the process into the cell cytoplasm. Their cargo is often DNA, hydrophilic drugs and charged substances that dissolved into the aqueous solution within the liposome structure. Substances that did not readily pass through the lipid membrane surrounding cells now had a means to, through the use of liposomes. Figure 11 depicts the increasing complexity of liposomes as drug delivery systems. Initially (A) the traditional structure is a simple lipid bilayer with an entrapped hydrophilic drug like gemcitabine (a) within the cavity, or an incorporated lipophilic drug (b) within the membrane (Yang *et al*. 2011). Currently (E) liposomes can be surface protected with polymers (i) in which some are functionalised with antigens for targeted delivery (j) or peptides (p). Within the cavity the liposomes can carry their hydrophilic drugs as traditionally intended but also magnetic nanoparticles for targeted delivery (r) and colloidal silver or gold nanoparticles for microscopic analysis(s) (Yang *et al*. 2011).
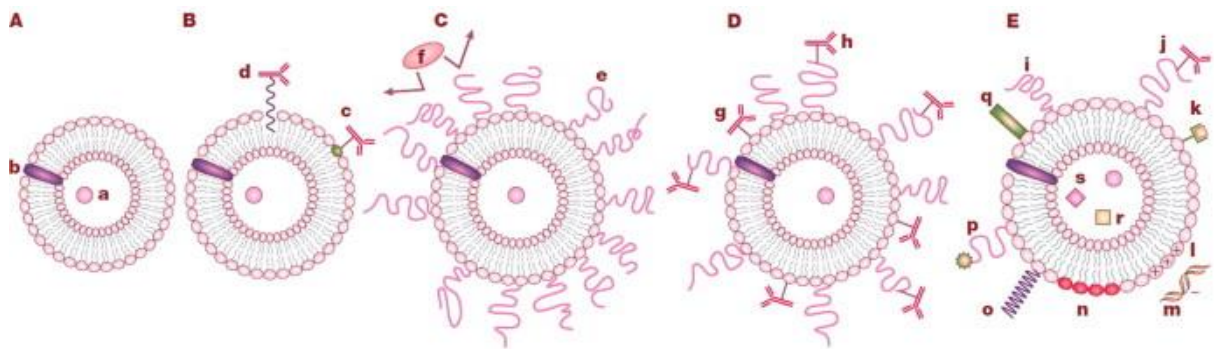
Figure 11: The evolution of liposomes in nanomedicine (Yang *et al*., 2011).

GemLip, a novel liposomal formulation of gemcitabine has been found to possess improved pharmacodynamics and pharmacokinetics than conventional gemcitabine (Yang *et al*. 2011). Theories for the improved efficacy include the passive tumour targeting and sustained release of gemcitabine. Passive tumour targeting is achievable with nanoparticles of a sufficiently small size because the capillaries supplying tumours are more porous and nanoparticles will remain in the bloodstream until they arrive and are able to pass through these pores into tumours (Martin *et al*. 2010; Yang *et al*. 2011). Sustained release of gemcitabine has also been linked to improved response rates in another clinical study (Hochster 2003). The difference between these two studies is that (Hochster 2003)utilised fixed dose rates to administer gemcitabine, while (Yang *et al*. 2011) reproduced this effect with the use of liposomes. The use of GemLip stalled the progression

of pancreatic cancer tumour growth from 2.7 months to 4.6 months and improved median survival times from 7.2 months with gemcitabine monotherapy to 9.4 months with the use of gemcitabine. Fixed dosing by (Hochster 2003) meant the patient had to receive the treatment over 150 min instead of the typical 30 min. The median survival time of fixed dose rate patients was improved to 8 months from the 5 months they observed. This is a significant improvement on the life extension of gemcitabine, but it still falls short of the life extension potential of GemLip. These liposomes can also be infused with magnetic nanoparticles to image their movement through the body and magnetically target them towards tumour sites (Yang *et al*. 2011). N,N'- bis(salicylidene)ethylenediamine iron (Fe(Salen)) possesses both anti-cancer and magnetic properties (Eguchi et al. 2015). Magnetic guidance of (Fe(Salen)) within micelles was shown to improve its cytotoxicity, compared to non-magnetically guided trials by concentrating them around tumours, improving their uptake by 10-fold (Eguchi et al. 2015).

The disadvantage of utilizing liposomes is that they can be expensive to produce, have poor drug loading, limited shelf life and can only slowly release their cargo (Gupta *et al*. 2008). They tend to aggregate at lower concentrations than other compartmental drug delivery systems like amphiphilic block copolymers (Hoskins, Paul Kong Thoo-Lin & Cheng 2012a). Because their synthesis is based on the agitation of lipid layers, the structure and size of individual liposomes can vary leading to poor yields of suitable liposomes (Yu et al. 2001). Slow release of drugs like gemcitabine has been shown to improve the effect of treatment, but mainly because it helps reduce the proportion of gemcitabine that is metabolised by the liver allowing it to build up in tumour cells (Kiew et al. 2010). Methods of rapidly exposing tumour cells to gemcitabine while bypassing metabolism in the liver and removal by the kidneys will prove superior to slow release methods (Affram et al. 2015).

1.2.3. Amphiphilic polymers

Amphiphiles are molecules that contain both hydrophilic and lipophilic regions. Phospholipids are an example of amphiphiles containing a hydrophilic phosphate head and a lipophilic lipid tail. When arranged into specific structures such as liposomes, they allow the compartmental storage of hydrophilic and charged substances (Yang *et al*. 2013). Block copolymers are polymers derived from more than one type of polymeric monomer subunit. These can range from simple repeating ABABAB block polymer chains shown in Figure 12

to branched systems where polymer chains are branched with different polymeric monomers subunit (Hoskins, Paul Kong Thoo-Lin & Cheng 2012a; Yan *et al*. 2012)
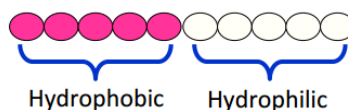
Figure 12: Simplified structure example of an amphiphilic block copolymer (Hoskins, Paul Kong Thoo-Lin & Cheng 2012b).

If the block copolymer contains both hydrophilic and lipophilic subunits then it can be described as an amphiphilic block copolymer (Hoskins, Paul Kong Thoo-Lin & Cheng 2012b). Like liposomes, these can arrange themselves into structures such as polymeric micelles useful for drug encapsulation and nanodelivery systems as described by (Xiong *et al*. 2012) in Figure 13.
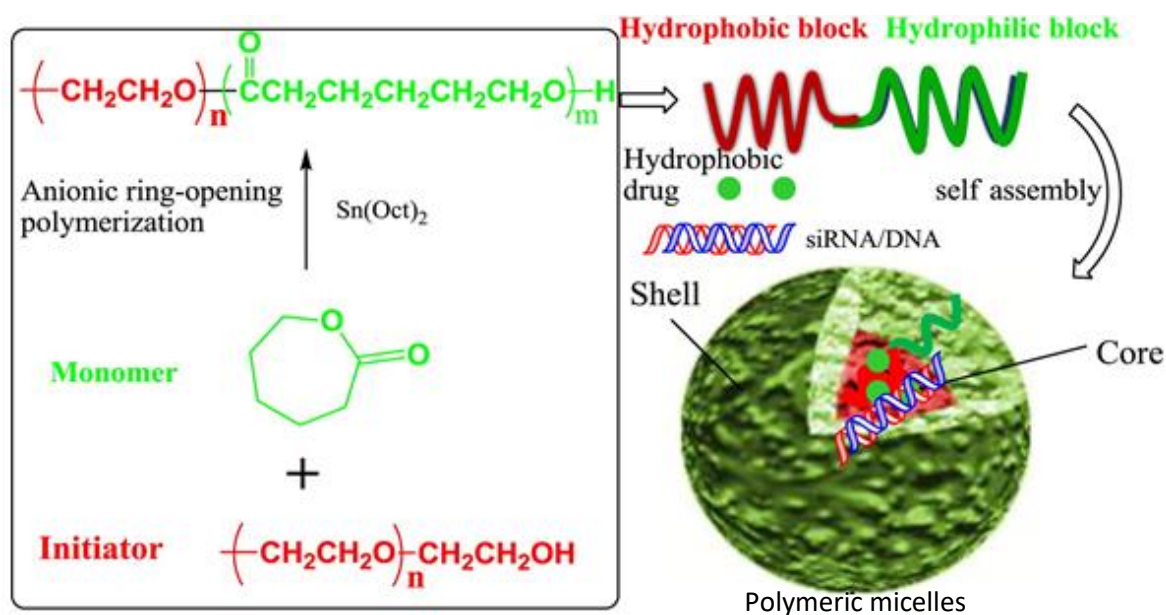
Figure 13: Schematic representation of the self-assembly of amphiphilic block co-polymers to polymeric micelles (Xiong *et al*. 2012).

An advantage of utilizing amphiphilic block copolymers is that their properties can be modified by changing the length of block copolymer chains, type of monomer subunits used and the addition of functional groups at specific regions within the block copolymer structure that can affect hydrophobicity, stability at certain pHs and for conjugation to substances such as metallic nanoparticles (Vukovic *et al*. 2013; Ma'Radzi *et al*. 2014; Sugihara *et al*. 2010). Future chapters within this thesis will discuss how gold coated iron oxide nanoparticles, can be functionalised with Diels Alder cycloadducts linkers via a thiol-

Au dative covalent bond. These Diels Alder linkers could potentially be attached to amphiphilic block copolymers as side chains. Unlike liposomes, the properties of each block copolymer are identical from structure to structure as they are built in a stepwise manner (Sugihara *et al*. 2010). This has been known to confer improved biocompatibility, low immunogenicity and improve the lifespan of these structures as they are quite stable when compared to liposomes (Xiong *et al*. 2012). Specific targeting of cancerous cells by functionalization of amphiphilic polymer structures, could aid in the improved uptake of cytotoxic agents like gemcitabine into cells (Xiong *et al*. 2012). Another type of amphiphilic polymer is graft or "comb shaped" polymers as shown in Figure 14. These are polymers comprised of a hydrophilic polymer backbone attached hydrophobic side polymer chains. The polymer backbone of a block copolymer can be made up of two or more types of polymers.
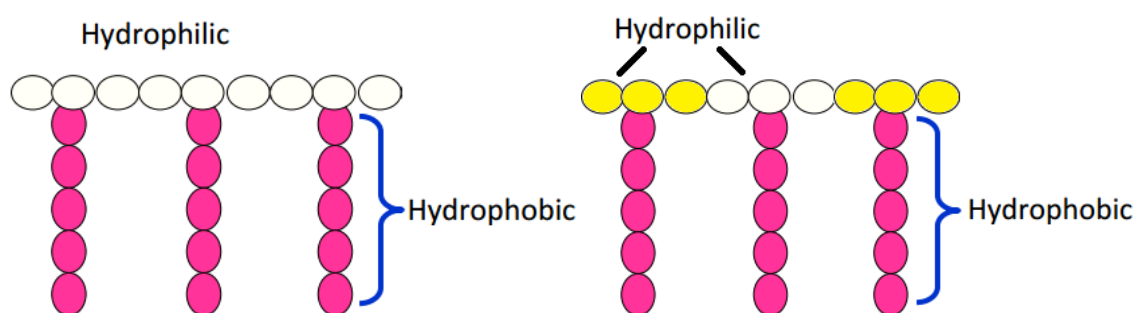
Figure 14: Simplified structure example of an amphiphilic comb shaped polymer with a homopolymer backbone (left) and a block copolymer backbone (right) (Hoskins, Paul Kong Thoo-Lin & Cheng 2012a).

Comb shaped polymers can self-assemble into micelle-like structures encapsulating hydrophobic drugs within the core (M. Barnett 2013). Like liposomes, these micelle-like polymers can carry multiple types of cargo including magnetic IONP's for magnetically guided therapies and diagnostic imaging. Poly(allyamine) (PAA) polymer backbones were chosen by (M. Barnett 2013) because of their established potential as universal drug solubilisers evaluated by (Hoskins, Paul Kong Thoo Lin, Tetley, et al. 2012b) These were grafted with 5-(4-chlorophenyl)-1,3,4-oxadiazole-2-thiol (Ox5) to produce the comb like polymer structure in Figure 15. Addition of the magnetic nanoparticles in the form of Au-IONP's was achievable due to gold's affinity to covalently bond with thiol groups. Au-IONP's were described as hybrid nanoparticles (HNP's) and their addition to the PAA-Ox5 led to the production of PAA-Ox5-HNP's in Figure 15 (Hoskins, Paul Kong Thoo Lin, Tetley, et al. 2012b).
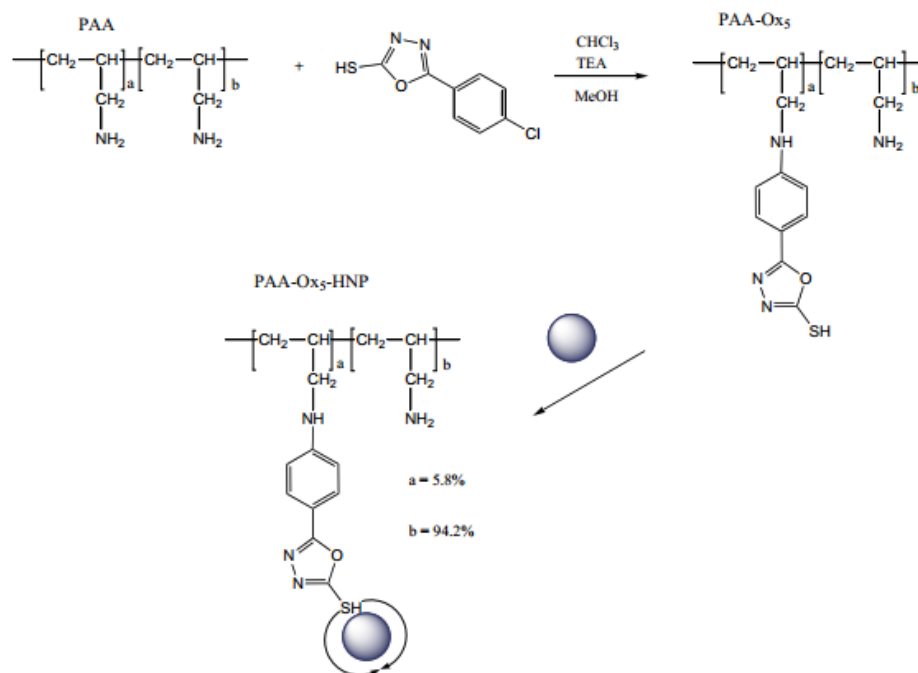
Figure 15: Synthesis route of PAA-Ox5-HNP's from a PAA backbone (Hoskins *et al.*, 2012).

In vitro drug release comparisons of the PAA nano-aggregates with model drugs including Propofol, Griseofulvin, BNIPDaoct, 6-TG was carried out by (M. Barnett 2013). All of the drug formulations displayed a spike in drug release in Figure 16 within the first 4 hours with some formulations having 100 % of the drug being released within 72 hours including both forms of Propofol.
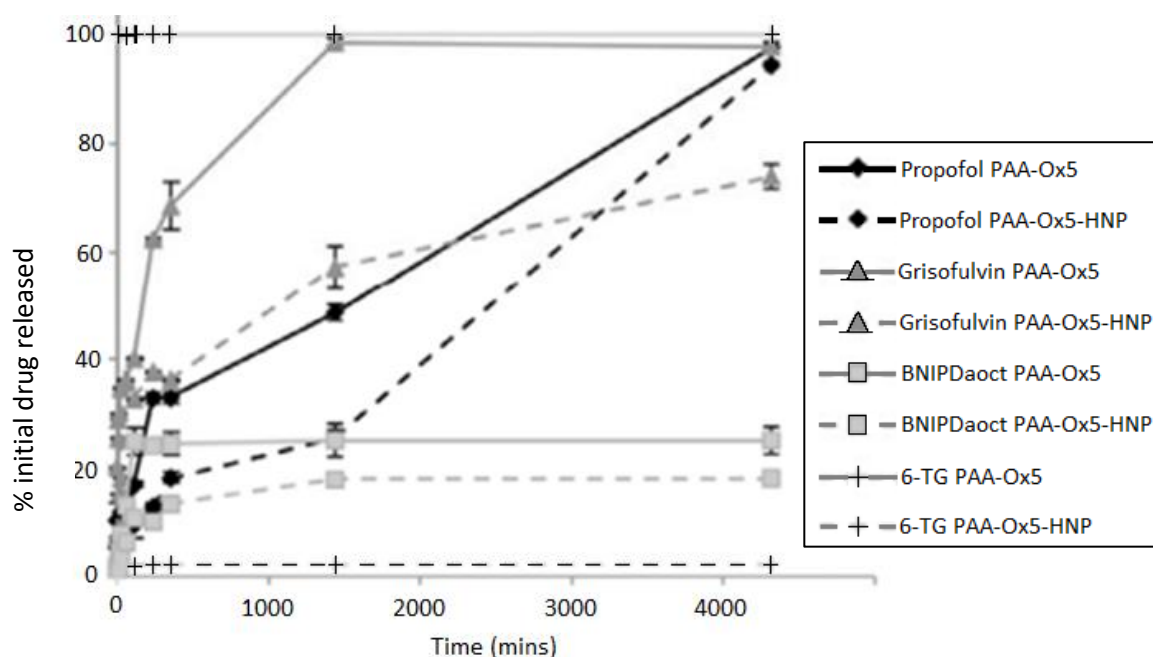
Figure 16: Drug release from optimal formulations over 72 h. Study carried out in PBS under sink conditions at 37 °C with constant stirring (n=3, ±SD) (M. Barnett 2013).

The formulations containing the HNP's displayed slower release rates than with PAA-Ox5. Prolonged release of cytotoxic drugs like gemcitabine has been linked with enhanced patient life extension (Yang *et al*. 2011; Hochster 2003). BNIPDaoct has a 25 % release over 72 hours held by hydrophobic-hydrophobic interactions with PAA-Ox5, most of this occurring within the first few hours of the experiment. The use of HNP's with PAA-Ox5 decreased the release rate to 18 %. After the initial burst release of BNIPDaoct, these comb like polymers displayed a prolonged ability to contain their payload.

BNIPDaoct cytotoxicity tests on BxPC-3 pancreatic adenocarcinoma cells with the PAA nano-aggregates revealed a 10-fold and 13-fold decrease in IC_{50} values compared with the free drug forms (C. Barnett et al. 2013). This highly significant increase in cytotoxicity on pancreatic adenocarcinoma cells displays the potential of PAA-Ox5 and PAA-Ox5-HNP encapsulated BNIPDaoct (M. Barnett 2013). Reduction of the dose required to elicit the same therapeutic response as a method of improving life extension was stated as a significant criteria in improving current treatments of pancreatic cancer (Vandana & Sahoo 2010; Wagstaff *et al*. 2012). These PAA nano-aggregates as described by (M. Barnett 2013) only allowed the partial release of BNIPDaoct due to their hydrophobicity. Therefore they energetically favour the hydrophobic core. Because gemcitabine is also a hydrophobic drug, it may display the same drug retention properties within the PAA nano-aggregates (M. Barnett 2013). 6-TG, also known as thioguanine is a cytotoxic drug for the treatment of leukaemia (Karim *et al*. 2013). 6-TG was completely released from the PAA-Ox5 nano aggregates within minutes of testing, due to its solubility in aqueous environments. This makes it unsuitable with PAA-Ox5, because total release of the drug would occur as soon as the formulation was injected into the aqueous environment of the circulatory system. The 6-TG PAA-Ox5-HNP formulation had the opposite behaviour and only showed a 2 % release due to its covalent bonding to the HNPs preventing its release. These results suggest that PAA formulations are effective when the drugs are bound with hydrophobic-hydrophobic interactions (M. Barnett 2013) but not with hydrophilic drugs freely dissolved within the aqueous compartment.

An alternative to encapsulating drugs like gemcitabine with comb shaped polymers like PAA (M. Barnett 2013) was tested and evaluated by (Vandana & Sahoo 2010) in Figure 17, where they opted to attach polyethylene glycol (PEG) directly to gemcitabine.

24

Gemcitabines small molecular weight, means that it has a short plasma circulation time of 150 min (peaking at 60 min) after administration and is rapidly cleared by the kidneys after its conversion to the inactive 2', 2'-difluorodeoxyuridine (Vandana & Sahoo 2010). To combat this, gemcitabine is given in frequent high doses, contributing to the toxicity and associated side effects. PEG is a water soluble amphiphilic polymer known for its high biocompatibility (Vandana & Sahoo 2010). It can be synthesised into a myriad of molecular weights for different purposes. PEGylated gemcitabine is synthesised by reacting polyethylene glycol-N-hydroxysuccinimide (PEG-NHS) with gemcitabine hydrochloride in dimethyl sulfoxide (DMSO) in the presence of triethylamine in a molar concentration of 1:2:20 respectively under a nitrogen atmosphere (Vandana & Sahoo 2010).
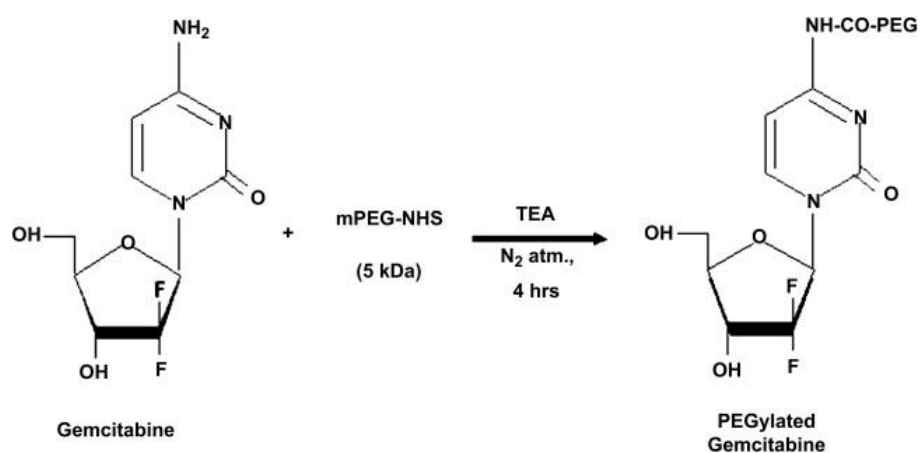
Figure 17: Schematic illustration of the reaction involved in the synthesis of the PEGylated gemcitabine (Vandana & Sahoo 2010).

The PEGylation of gemcitabine increased size and reduces its uptake rate into cells leading to slower renal clearance (Vandana & Sahoo 2010). Therefore less PEGylated gemcitabine is absorbed by healthy cells. Tumours have leaky blood vessels that allow PEGylated gemcitabine to penetrate tumours and be loaded into cancerous cells over time. The leaky blood vessels that feed tumours are generated by angiogenesis signalling by cancerous cells which promote the rapid growth of new but defective blood vessels (Nagy et al. 2009). Ultimately this reduces the systemic toxicity while increasing the circulation time of gemcitabine in this form. *In vivo* experiments in mice showed that PEGylated gemcitabine remained in circulation after 24 hours after administration into the tail vein. From Figure 18 we can see that after 30 min of administration, the retention of PEGylated gemcitabine within the blood plasma was 1.7 times that of the native dosage form. After 60 min, this

difference was now 21-fold between the levels of PEGylated and native gemcitabine. After 24 hours (Vandana & Sahoo 2010) reported no native gemcitabine while PEGylated gemcitabine was still detectable.
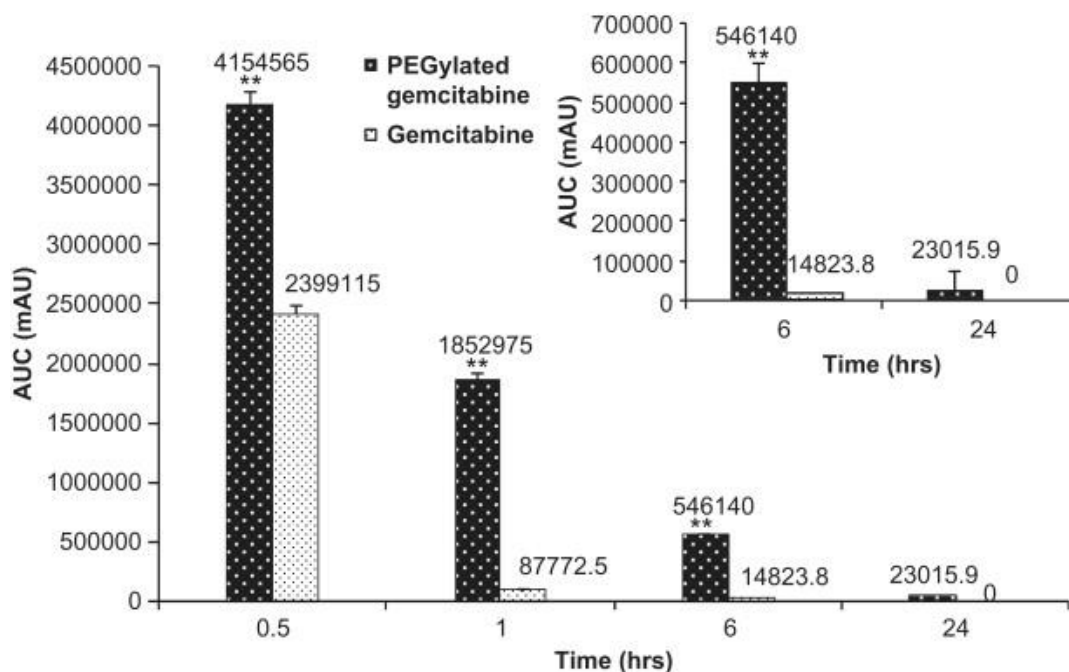
Figure 18: Comparison of PEGylated and native gemcitabine concentrations in the blood plasma of mice after administration (Vandana & Sahoo 2010).

PEGylated gemcitabines potential as a drug delivery system for pancreatic cancer treatment is established by (Vandana & Sahoo 2010). Increasing the retention time of gemcitabine within the circulatory system by attachment to PEG, improves the total uptake of gemcitabine which has the potential of improving the life extension properties of gemcitabine as discussed by (Yang *et al*. 2011; Hochster 2003). This attribute of improved retention time is shared with PAA (M. Barnett 2013). PAA-Ox5-HNPs also improve the cytotoxicity of their formulations as well compared to PAA-Ox5 (M. Barnett 2013). PEG has also been used as a polymer coat on nanoparticles with attached antibodies and should have the potential to attach drugs like gemcitabine to nanoparticles via PEG linkers (Sinha *et al*. 2014). However the PAA nano-aggregates display limitation to only drugs bound by hydrophobic-hydrophobic interactions. Propofol, another hydrophobic drug required 72 hours to completely release from its PAA formulation which is significantly longer than current blood plasma retention times (Hochster 2003) and with PEGylated formulations (Vandana & Sahoo 2010). Polymers, display significant potential in improving the efficacy

of existing cytotoxic drugs for the treatment of pancreatic cancer. This applies to both micelle like graft polymers for hydrophobic drug formulations (M. Barnett 2013) and PEGylated drugs like gemcitabine (Vandana & Sahoo 2010). The addition of HNPs, and the potential attachment of HNP's to PEGylated drug formulations boosts this efficacy further. However drugs encapsulated in graft polymers formulations are superior to PEGylated drug formulations in that they are able to improve circulatory retention, especially with hydrophobic drugs for longer than the 24 hour period PEGylated drugs can (Vandana & Sahoo 2010; Hochster 2003).

1.2.4. Iron oxide nanoparticles

Nanoparticles have gathered increased scientific interest due to their high surface to volume ratio and unique properties that can differ from bulk forms (Li *et al*. 2012; Salameh *et al*. 2014). Nanoparticles typically range from 1 to 1000 nm in diameter and have shown great promise in biomedical applications in the form of nanomedicines, diagnostic imaging tools and drug delivery systems (Li *et al*. 2012; Salameh *et al*. 2014; Markman *et al*. 2013). Figure 19 displays graphically how interest in nano-science, medicine and technology increased over the last 18 years. While these were known under different names such as ultra-fine particles, the interest in nano related research only saw a significant increase at the turn of the century, where it flourished and rapidly expanded from 64 references to over 7000 in 12 years (Anada *et al*. 2009; Markman *et al*. 2013).
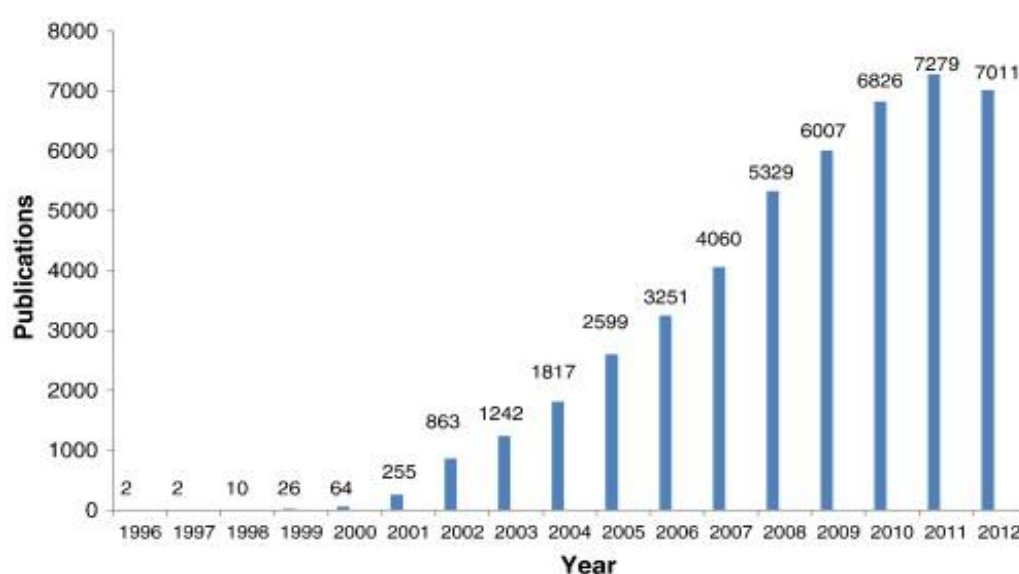
Figure 19: The number of references under the research topics of "nanomedicine," "nanoscience," and "nanotechnology" from 1996 to 2012. (Markman *et al*. 2013).

27

Iron oxide nanoparticles (IONP's) have applications in many medical related fields such as cancer treatment, cancer detection, drug transportation, cell labelling and magnetic cell sorting (Saritas *et al*. 2013). They come in multiple shapes such as spherical, hexagonal, cubic and also in the form of nanorods as shown in Figure 20s TEM images (de Montferrand *et al*. 2013).
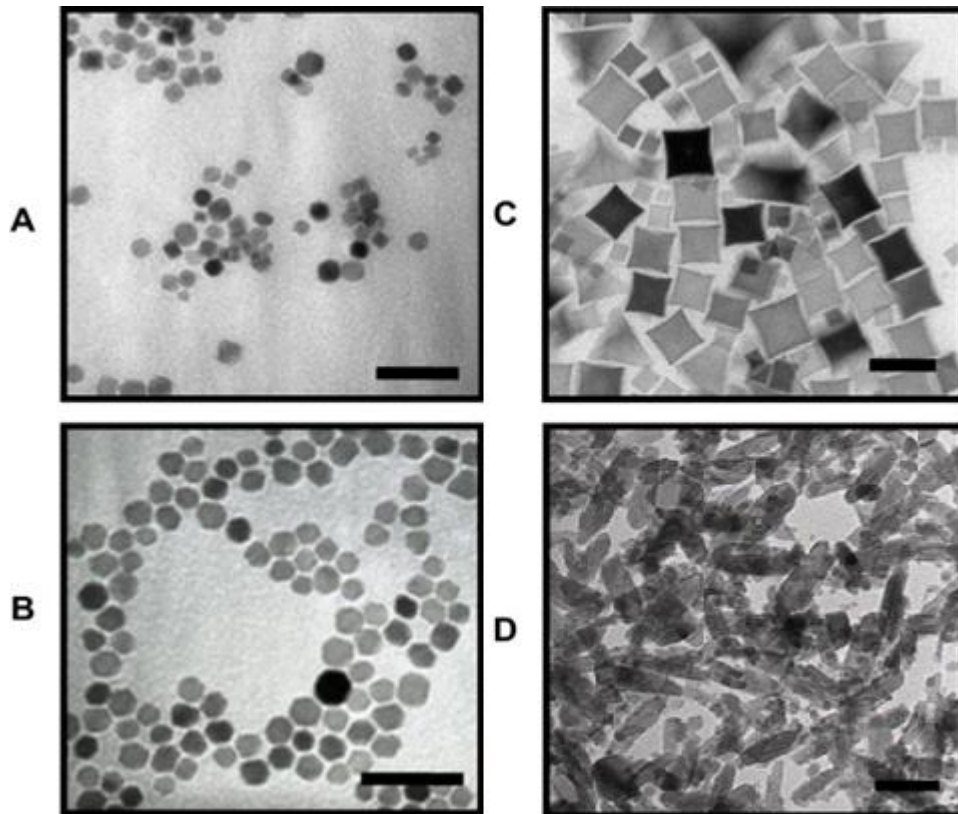
Figure 20: TEM images for (A) spherical, (B) hexagonal, (C) cubic and (D) rod-shaped ferrite nanoparticles. Scale bar 50 nm (de Montferrand *et al*. 2013).

IONPs of different shapes can be synthesised by using a precursor called iron (III) acetylacetonate at a high temperature in the presence of 1, 2-hexadecanediol and the surfactants oleic acid and oleylamine. Altering the amount of each component of this mixture led to the different IONP shapes (de Montferrand *et al*. 2013).

IONPs smaller than 20 nm are superparamagnetic which means that they gain magnetism under a magnetic field. Unlike ferromagnetic materials, they do not retain their magnetism after the magnetic field is removed (Xie *et al*. 2010; Rosen *et al*. 2012). Superparamagnetism only occurs with nanoparticles because their size is small enough to occupy a single magnetic domain, which are small regions within a magnetic substance

where all the atoms are magnetically aligned in the same direction. Paramagnetic material of sufficient size contains several magnetic domains. The atoms within each domain align themselves in the same direction (uniform magnetism). Adjacent domains align in different directions which reduce the overall magnetostatic energy of the bulk paramagnetic material causing permanent magnetism. IONPs can be produced at a small enough size, that the entire nanoparticle occupies a single domain (Santhosh & Ulrih 2013a). By being superparamagnetic the IONPs and attached drugs can be magnetically guided to their target, but the real advantage is that they lose their magnetism upon the removal of a magnetic field, causing the IONPs to disperse. This prevents aggregation and reduces the rate that macrophages identify and subsequently engulf them, rendering them useless (Santhosh & Ulrih 2013a).

Guiding the drug directly to its target increases the amount of active pharmaceutical ingredients at work. This leads to either more effective treatment and/or a lower dose requirement, which can help avoid or reduce some side effects associated with larger doses. Multidrug resistance is a constant problem when treating cancer with cytotoxic drugs. These cells become resistant but not immune to cytotoxic agents. Increasing the amount of cytotoxic agents such as gemcitabine with the use of magnetic IONPs at the intended target, improves the efficacy of the drug per dose administration.

Magnetic IONPs will generate heat when subjected to strong magnetic fields. Magnetic crystal suspensions of IONPs store the energy of alternating magnetic fields and release this energy as heat causing hyperthermic stress in cancer cells (Laurent *et al*. 2011). To prevent systemic hyperthermia, liposomal IONPs were injected directly into tumours of hamsters by (Matsuoka *et al*. 2004). Application of an external alternating magnetic field increased the temperature of the tumours to 42˚C. They reported complete tumour regression in 100 % of the treated hamsters with the average tumour size of 1/1000 of control hamsters after 12 days of treatment as shown in Figure 21.
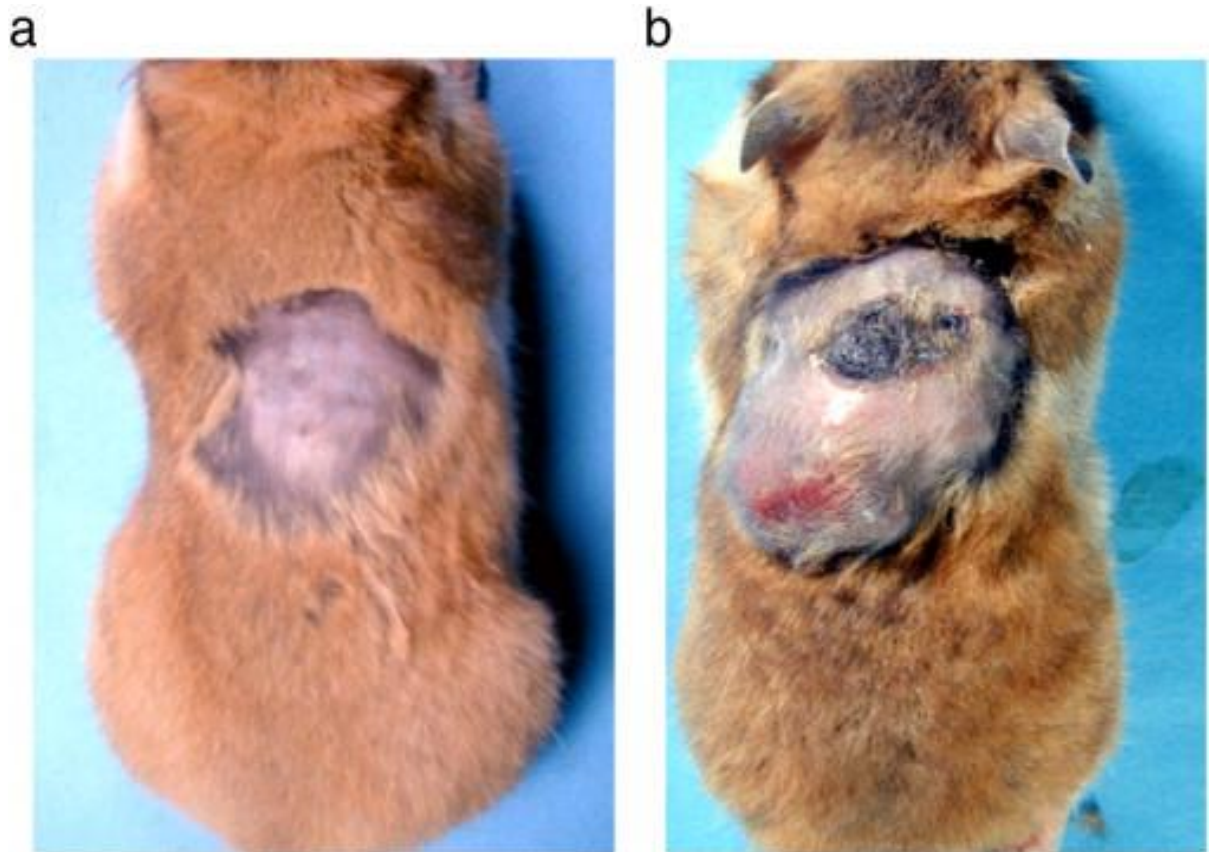
Figure 21: Typical photographs of hamsters on day 20 after injection with 0.4 mL of the cationic magnetoliposomes (net magnetite weight 3 mg). (A) Treatment group. (B) Control animals without alternating magnetic field treatment (Matsuoka *et al*., 2004, Laurent *et al*., 2011).

Magnetic particle imaging (MPI) involves the imaging of superparamagnetic iron oxide nanoparticles by using the generated magnetic fields as tracers (Khandhar *et al*. 2013; Saritas *et al*. 2013). It is a new technique, still in the development stages but is showing great promise as a potentially useful biomedical imaging technique (Borgert *et al*. 2012; Saritas *et al*. 2013). The mouse in Figure 22 was injected with Resovist a superparamagnetic contrast agent. The volume-rendered MPI image (a) and the photo of the mouse injected with 100 μL undiluted Resovist via tail vein and sacrificed 30 sec post-injection (b). The heart and liver can be clearly seen as the Resovist flows along the circulation system and becomes filtered within the liver (Saritas *et al*. 2013).
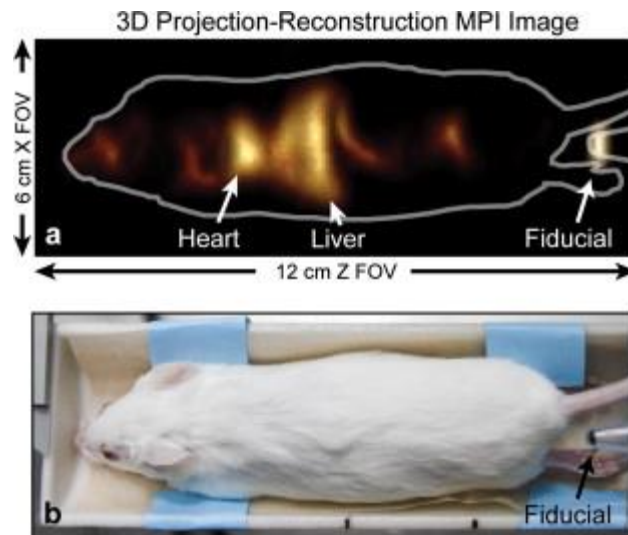
Figure 22: 3D projection reconstruction MPI image showing the Resovist tracer flowing to the heart and filtering in the liver of a mouse (Saritas *et al*. 2013).

In Figure 23, a helical phantom was constructed to test the effectiveness of MPI. Medical phantoms are apparatus constructed to be scanned or imaged to test the capabilities of a particular imaging technique or imaging equipment. Image (c) in Figure 23 shows a bare helical phantom and the subsequent MPI image (a). Tissue is used to surround the phantom (d) and the resultant MPI image is shown in (b).
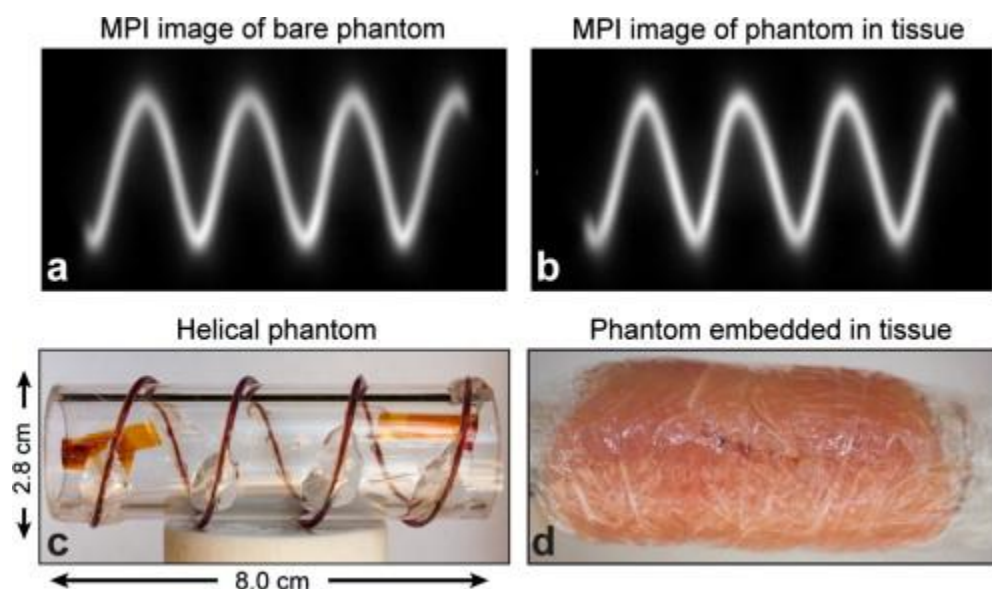
Figure 23: Imaging of helical phantoms to elucidate the effectiveness of Resovist as a tracer in the presence (d) and absence (c) of animal tissue (Saritas et al. 2013).

A 3D MPI experiment shown in Figure 23 demonstrated no depth attenuation or tissue contrast. (a–b) Projection Reconstruction 3D MPI images show no attenuation with depth

for the phantom embedded in tissue, nor any tissue contrast. Helical phantom (c) was filled with SPIOs and (d) the same phantom was embedded in animal tissue (wild turkey)(Saritas *et al.* 2013). Note that the MPI images appear identical regardless of whether the phantoms were surrounded by animal tissue. Certain tissues have a tendency of contrasting biomedical images. These include bones such as the ribcage when the abdomen for example is imaged (Saritas *et al.* 2013). However the clinical use of iron oxide nanoparticles has come under scrutiny following the discontinuation of several iron oxide contrasting agents including Feridex, Combidex, Clariscan and Ferropharm. Resovist is still available in some countries as of 2015 (Wang 2015). Feridex was reportedly discontinued due to poor sales, while Resovist has seen reduced use in many countries due to more efficient MRI options available to consumers (Wang 2015).

1.2.5. Gold nanoparticles

Gold nanoparticles have shown promise as useful components in targeted drug delivery. This includes iron oxide nanoparticles which are coated in a layer of gold (C. M. Barnett et al. 2013; Vigderman & Zubarev 2013). Like IONP's, gold nanoparticles also come in a variety of shapes including, spheres, rods and tetrapods displayed in Figure's 24 and 25.
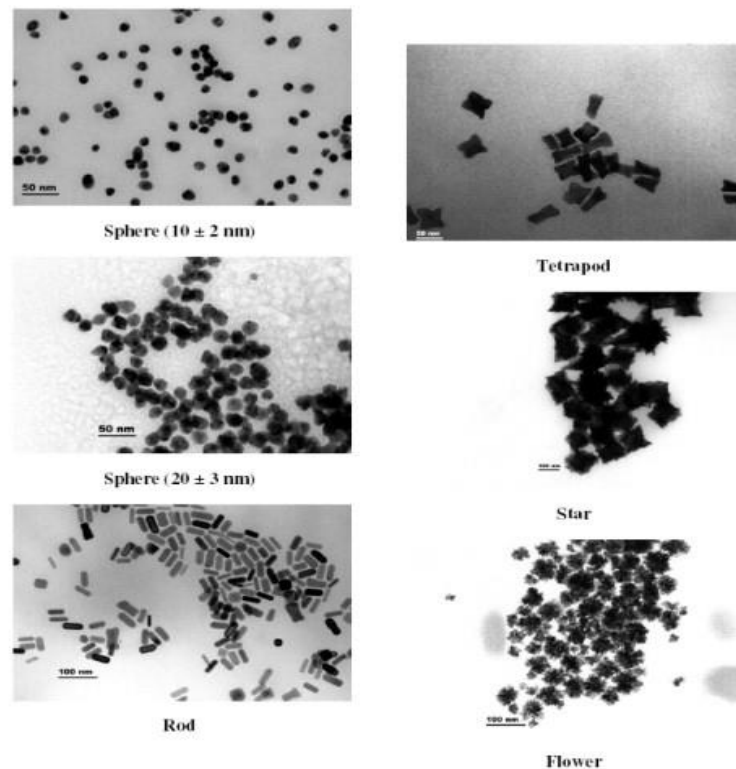
Figure 24: Typical TEM photographs of different GNPs (Das *et al.* 2014).

32
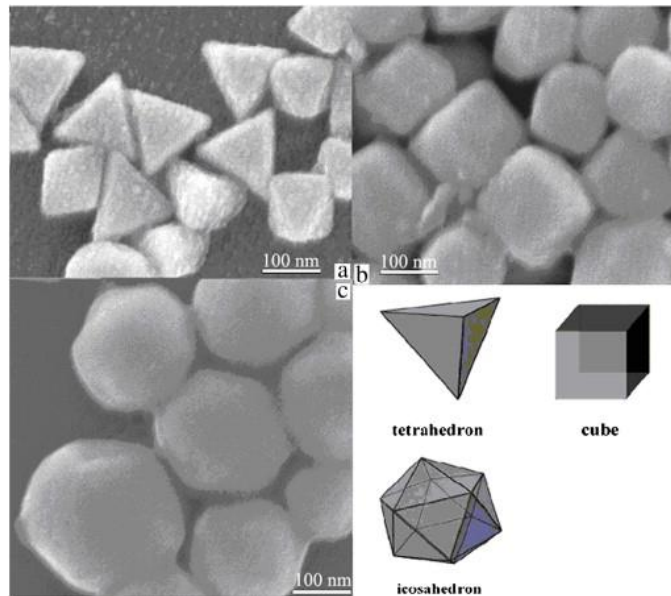
Figure 25: SEM images of three gold particles (a. tetrahedral, b. cubes and c. icosahedral) (Dong *et al*. 2011).

Gold as an element is generally regarded as non-toxic (Teixeira et al. 2016). It is a noble metal that has filled electronic d-bands. This makes gold resistant to oxidation, corrosion, and acidic conditions that can be found within the body. Gold can be strongly bonded covalently to thiol groups, an organic functional group that can be found on drug compounds or attached via the use of linkers (Wang *et al*. 2013). One example of such a linker is polyethylene glycol (PEG). Thiolated PEG can be attached to a gold nanoparticle at one end and a drug compound at another. Therefore one gold nanoparticle can be used to carry multiple drug compounds via a PEG linker as illustrated in Figure 26 by (Wang *et al*. 2013). This allows for higher doses of certain drugs which have significant side effects such as gemcitabine to be used (Wagstaff *et al*. 2012).
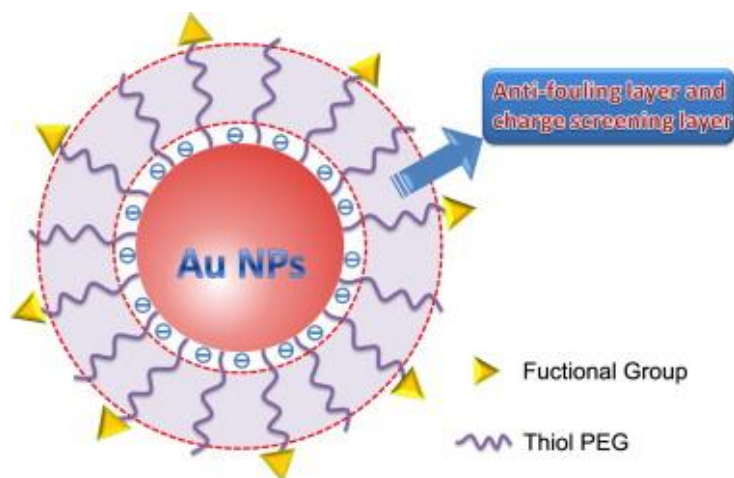
Figure 26: Structure of thiol-PEG-modified AuNPs (PEGylated AuNPs) (Wang *et al*., 2013a).

The use of gold nanoparticles as cancer cell imaging was researched by (Lima *et al*. 2014). An illustration of their process is shown in Figure 27. They produced these gold nanoparticles using established methods (Gasparotto *et al*. 2012) and conjugated two antibodies called anti-β-catenin and anti-E-cadherin, which specifically bind to colorectal carcinoma cells (Lima *et al*. 2014).
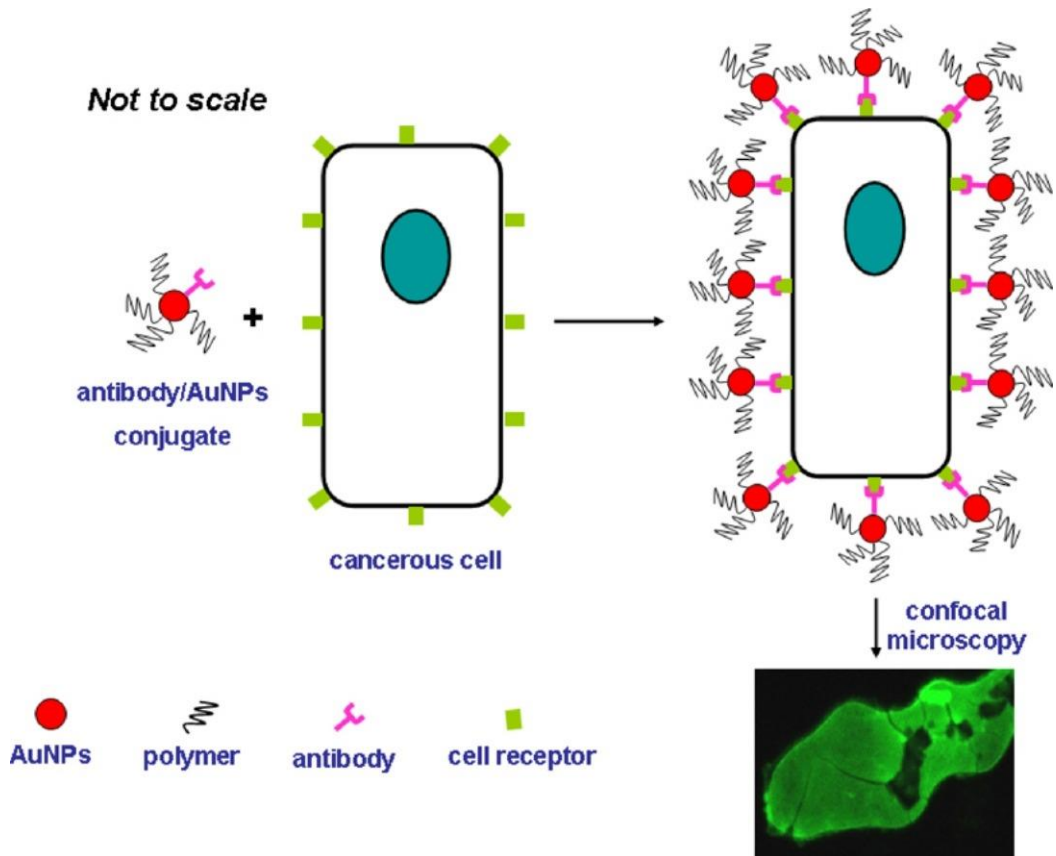
Figure 27: The schematic for the binding of conjugated gold nanoparticles to colorectal carcinoma cells (Lima *et al*. 2014).

Figures 28 and 29 show the difference in fluorescence in the healthy and cancerous cells. The cancerous cells have a higher expression of both β-catenin (A1-3 on both Figure 28 and 29) and E-cadherin (B1-3 on both Figure 28 and 29). Therefore the conjugated anti-β-catenin and anti-E-cadherin on the nanoparticles attach more readily to the cancer cells. This shows that the use of conjugated nanoparticles is a powerful tool for the diagnostic imaging of cancer cells (Lima *et al*. 2014).

Non-Cancerous Cells
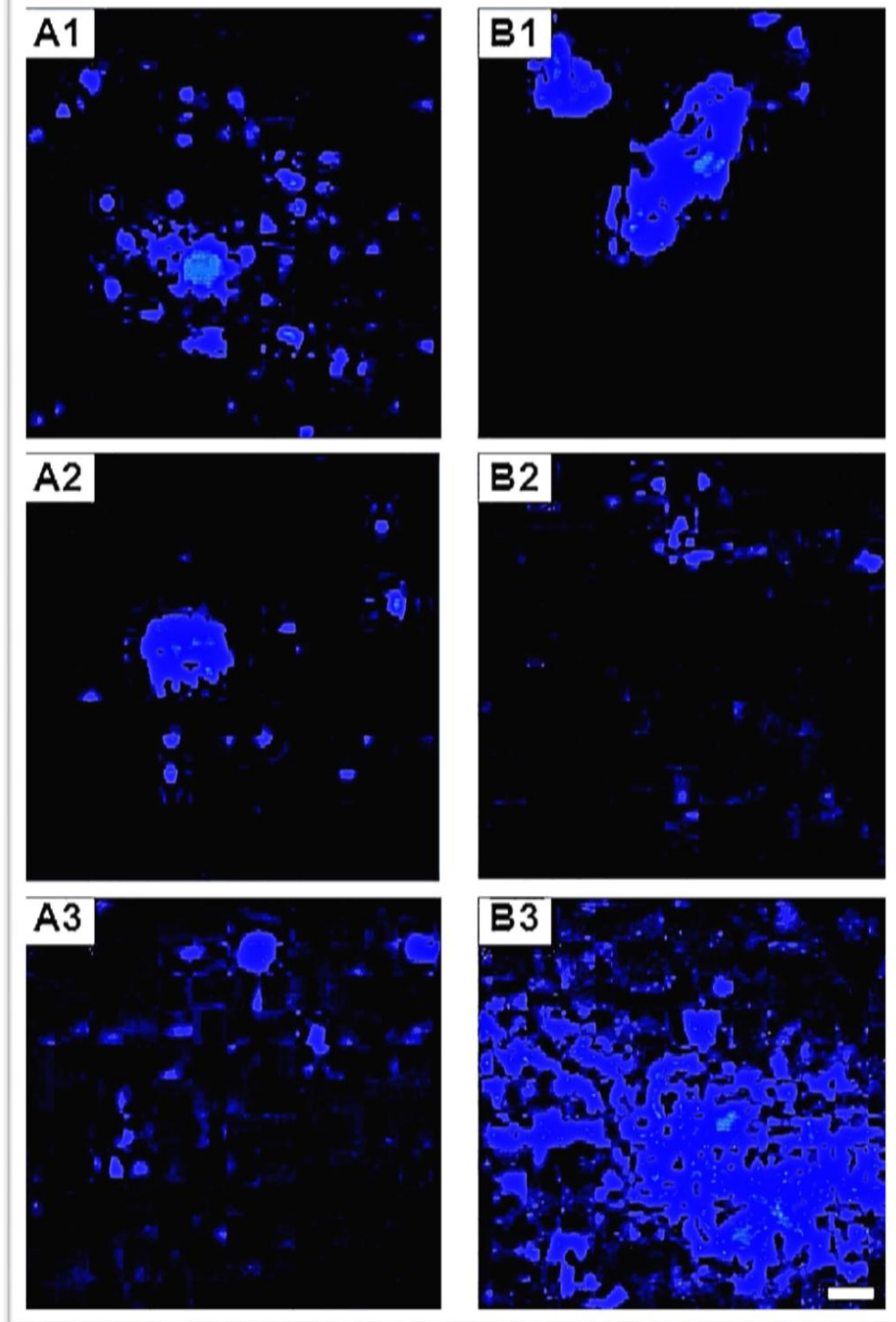
Figure 28: Confocal images of healthy cells acquired at an excitation laser of 520 nm. Left column: images acquired with the conjugate of β-catenin. The conjugates had β-catenin/AuNPs ratios of (A1) 6.1×10^{-3}, (A2) 4.1×10^{-3} and (A3) 3.0×10^{-3}. Right column: images acquired with the conjugate of E-cadherin. The conjugates had E-cadherin/AuNPs ratios of (B1) 6.1×10^{-3}, (B2) 4.1×10^{-3} and (B3) 3.0×10^{-3}. Magnification: 10×. Scale bar = 100 μm (Lima *et al*. 2014).

Cancerous Cells
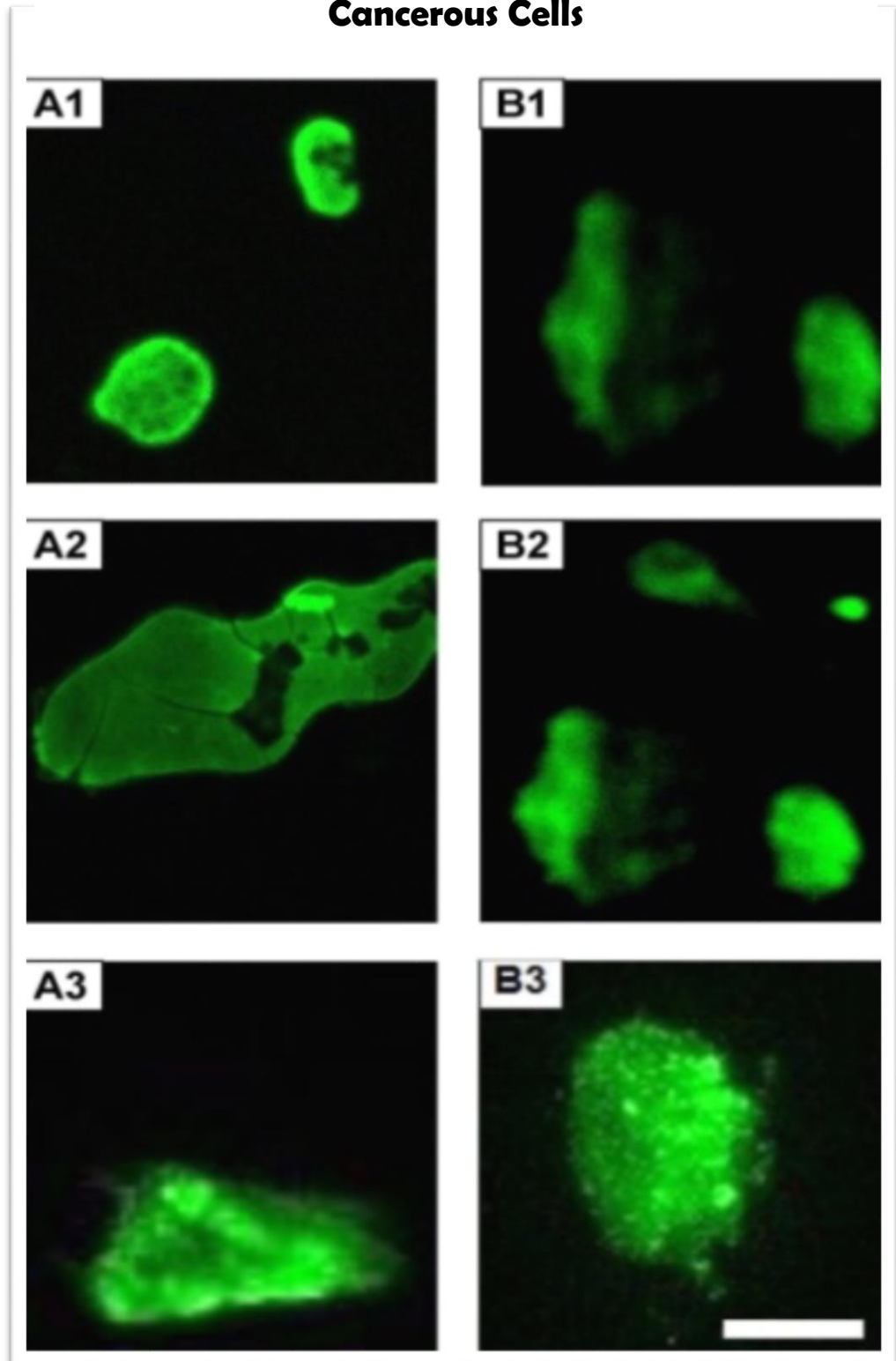
Figure 29: Confocal images of cancerous cells. Left column: images acquired with the conjugate of β-catenin. The conjugates had β-catenin/AuNPs ratios of (A1) 6.1×10^{-3}, (A2) 4.1×10^{-3} and (A3) 3.0×10^{-3}. Right column: images acquired with the conjugate of E-cadherin. The conjugates had E-cadherin/AuNPs ratios of (B1) 6.1×10^{-3}, (B2) 4.1×10^{-3} and (B3) 3.0×10^{-3}. Magnification: 40×. Scale bar = 100 μm (Lima *et al.* 2014).

Gold is not magnetic and therefore lacks the potential magnetic guidance of IONP's. However its biocompatibility, ability to carry drug formulations, ease of synthesis and surface plasmon resonance properties make it a powerful tool in the treatment of pancreatic cancer. One characteristic of gold is its ability to absorb near infra-red (NIR) radiation and generate heat due surface plasmon resonance (SPR). SPR is the term used to describe the oscillation of free electrons when light is shone on a metal surface. These resonating free electrons produce an electromagnetic wave (light) that travels away from the bulk phase of the solid (Zhang *et al*. 2007; Verma *et al*. 2012). Generating heat using NIR radiation *via* SPR is ideal considering the high transparency of tissue at that wavelength. A laser emitting NIR radiation can be used to target a specific area where gold nanoparticles are situated, such as within a cluster of neoplasia in the pancreas. Heat generated from the photo thermal effect will raise the temperature of the cancer cells killing them. Because the lasers area of effect is small, this would also prevent damage being caused to nearby healthy tissues (Vigderman & Zubarev 2013).

1.2.6. Silver nanoparticles

Like gold nanoparticles, silver nanoparticles also display surface plasmon resonance (Liang *et al*. 2012). Silver nanoparticles are more visible than gold, to optical sensors (Miao *et al*. 2014). Silver nanoparticles have antimicrobial properties and their cytotoxic effects are already an established fact (Mukherjee *et al*. 2012; Meyer *et al*. 2010). They are currently used in wound dressings, contraceptive devices and as surgical instruments coatings (Mukherjee *et al*. 2012). Silver nanoparticles are synthesised from silver nitrate reduced with sodium citrate. While heating, sodium borohydride is added to the stirring mixture before the heat is switched off and the mixture is allowed to continue stirring for several hours (Hayden *et al*. 2013). The shapes of silver nanoparticles is important for their desired use as described by (Chen *et al*. 2011) in Figure 30.

Shapes	Preparation methods	Potential applications
Nanosphere	Chemical reduction Laser ablation	Bactericide, SERS-based sensing
Nanowire	Wet chemical synthesis Soft solution method	Opto-electronics
Nanobelt	Chemical reduction Laser ablation	Photonics, electronics
Nanoplate	Chemical reduction Photochemical method	Catalysis, opto-electronics, biological sensing
Nanocube	Chemical reduction	Photonics, catalysis, SERS-based sensing

Figure 30: A summary of different shapes of Ag NPs and their potential applications (Chen *et al*. 2011).

The metal nanoparticles iron oxide, gold and silver have their own properties that make them suitable as drug delivery, imaging and therapeutic agents for the treatment of cancers such as pancreatic cancer. Iron oxide is magnetic and can be guided to its target with the use of external magnetic field (Santhosh & Ulrih 2013a). They can also be used as excellent contrasting agents to study the movement of IONP formulations within the body or image specific areas such as tumours when guided by magnetic fields. Silver nanoparticles are also highly visible to optical sensors. They can also be used to generate heat by SPR causing hyperthermia in cells (Liang *et al*. 2012). However they are not magnetic and therefore cannot be guided to specific regions and held there with magnetic fields. Gold nanoparticles also lack the magnetic properties of IONPs but share in silver's SPR properties. More importantly, gold is very biocompatible; an advantage it has over IONPs and silver nanoparticles. Combining the properties of these metals into nanoparticles, such as silver-gold and iron oxide-gold, which will be discussed in the next section.

1.2.7. Silver-gold nanohybrids

Hybrid nanoparticles are nanoparticles comprised of nanocomponents within a nanoassembly. One example of hybrid nanoparticles is silver-gold core-shell nanoparticles. Hybrid nanoparticles are utilised to fulfil multiple roles such as drug delivery, imaging, or conferring useful properties such as reduced toxicity. Research into the detection of carcinoembryoic antigen (CEA) using silver-gold core shell hybrid nanoparticles was carried out by (Miao *et al*. 2014). Increased levels of CEA can signal the presence of various types of cancer including pancreatic cancer. Typical amounts range from 3-5 ng mL^{-1} in a healthy individual and rapid detection methods such as dynamic light scattering have been utilised by (Miao *et al*. 2014) to detect CEA. An antigen called anti-CEA selectively binds to CEA. Attachment of core shell nanoparticles like iron-silver nanoparticles to anti-CEA, will allow the imaging of areas showing heightened levels of CEA (Miao *et al*. 2014) due to CEA binding to anti-CEA. Silver nanoparticles are not considered biocompatible but are known for having a 100x molar extinction coefficients compared to gold nanoparticles making the overall core shell nanoparticles more sensitive to optical sensors. The surface gold layer on these core shell nanoparticles provides biocompatibility, something that silver nanoparticles lack. Silver-gold core shell nanoparticles make up for the deficiencies of individual gold and silver nanoparticles (Miao *et al*. 2014). The average size of the core shell

nanoparticles shown in Figure 31 is 63.3 nm determined with dynamic light scattering (Miao et al. 2014). Addition of 1 ng mL^{-1} and 10ng mL^{-1} of CEA increased their sizes to 138.7 and 201.6 nm respectively due to the attachment of anti-CEA in the core shell nanoparticles, to the CEA in the PBS buffer (Miao *et al.* 2014).
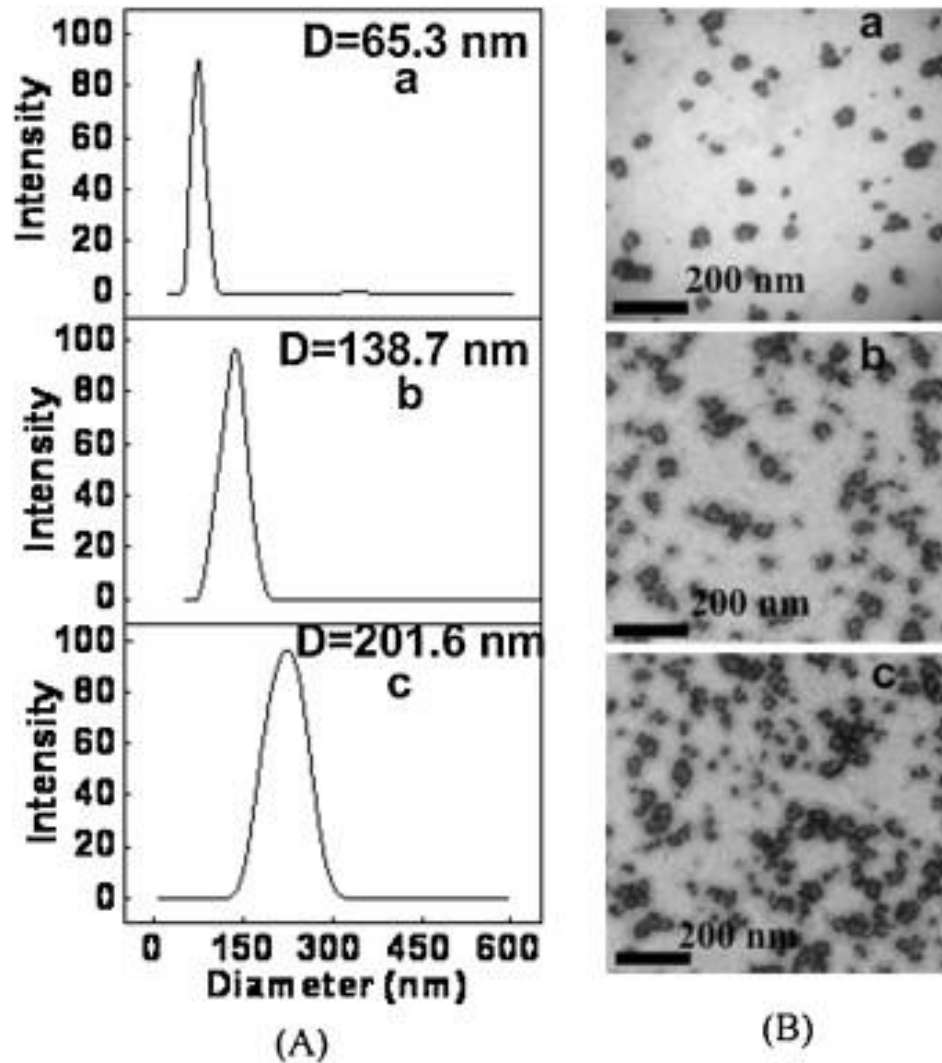
Figure 31: The size distribution (A) and TEM images (B) of 4.0 μg/mL of Ag@Au/anti-CEA probes in the presence of 0 ng/mL (a), 1.0 ng/mL (b) and 10.0 ng/mL (c) of CEA. Experiments were conducted in 10 mM of PBS buffer (pH 7.4) (Miao *et al.* 2014).

1.2.8. Iron oxide gold nanohybrids

The gold coating around the iron oxide core such as the one shown in Figure 32 provides the structure with non-immunogenic properties. Gold is highly unreactive and nontoxic, an attribute that it confers to the nanohybrid structure (Wagstaff *et al*. 2012). The gold coating does not diminish the magnetic properties of the iron oxide core, retaining the potential for magnetic guidance to the target site of action. The magnetic iron oxides can be used as a tracer during magnetic particle imaging. Au-IONPs have been described as having cytotoxic effects as well (Guo *et al*. 2013). Therefore Au-IONPs both have a therapeutic and diagnostic role in the treatment of cancers and can be described as theranostic agents.

Figure 32: Diagram of a gold coated iron oxide nanoparticle (Wagstaff *et al*. 2012).

The physical stability of HNPs was evaluated by (C. M. Barnett et al. 2013) by suspending them in solutions of pH 7.2 and 4.5 to mimic blood and lysosomal physiological conditions after drug administration.

Blood is comprised of many components including plasma, cells, proteins, mineral ions and platelets. These components interact with one another, undergo metabolism and move through the circulatory system. Depending on their location within the body, their composition and characteristics can change significantly. Blood in the pulmonary arteries is oxygen poor and blood vessels around the small intestine are rich in digested nutrients. The sheer level of complexity in blood makes it difficult to accurately measure the relationship between known variables due to the potential of unknown mechanisms affecting results. This is why cell media, a relatively simple solution is used for in vitro experiments.

The solutions were stirred over a 14 day period within a dialysis membrane and analysed frequently for Fe and Au using inductively coupled plasma-optical emission spectroscopy (ICP-OES). Figure 33 displays the relationship between the attachment of PEG on HNP's and

the rate of release over a 2 week period at two biological pHs (7.2 for blood and 4.6 for lysosomes).
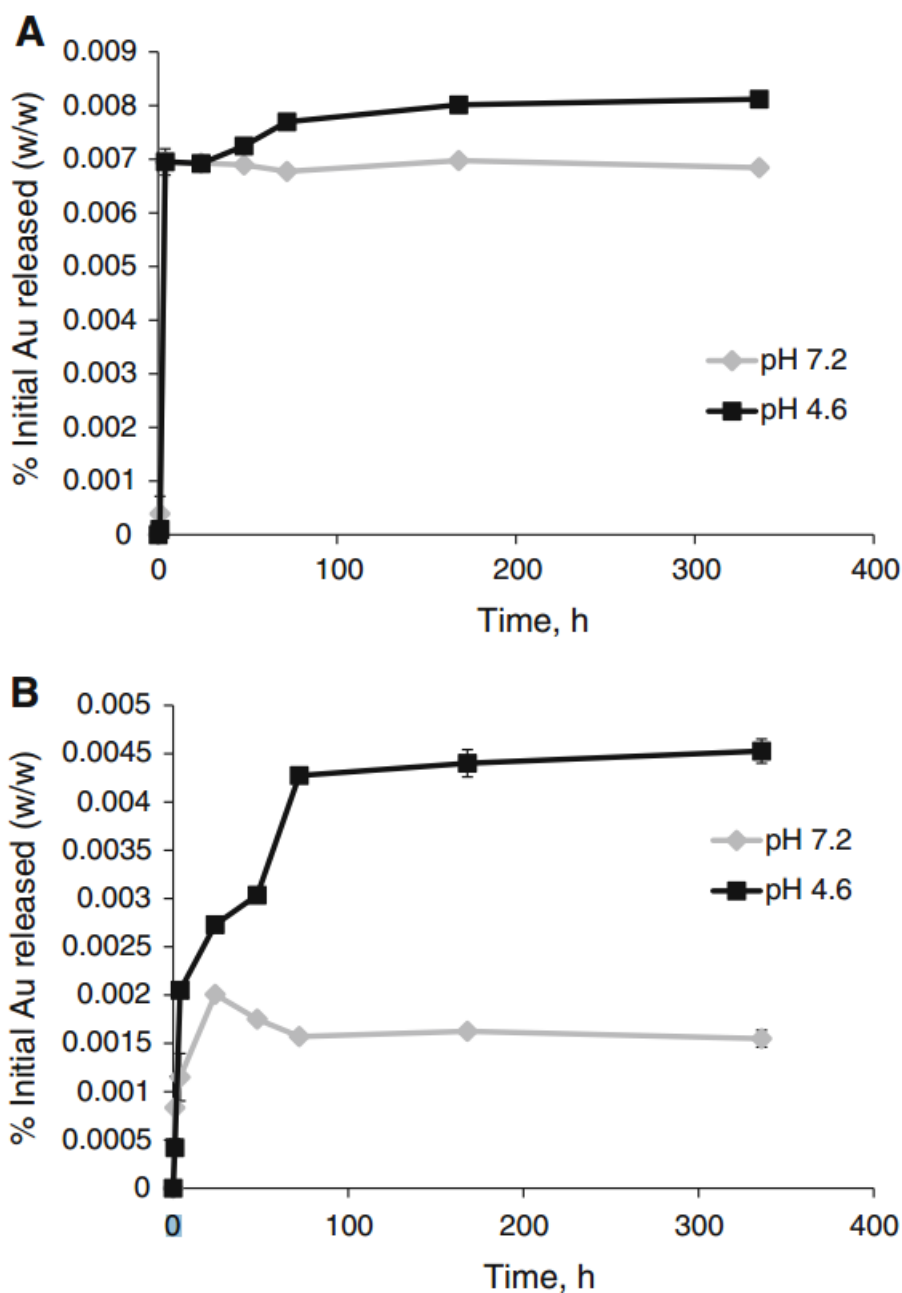
Figure 33: Stability of HNPs in solution under in biological conditions at pH 7.2 and 4.6. (A) HNP and (B) HNP-PEG. Study carried out under in *sink* conditions over 2 week period and percentage initial Au determined (n = 3 ± SD) (C. M. Barnett et al. 2013).

A rapid increase in the rate of release of gold occurs within a few hours. Non-PEG HNPs rapid increase in the rate of gold release promptly stabilizes at 0.007 %. This is maintained at a pH of 4.6 (lysosome) and gradually rises to 0.008 % at a pH of 7.2 (blood). Barring the initial rapid release of gold, the HNPs display a high amount of stability at these two pHs.

When PEG is attached to the HNPs, less gold is released across the dialysis membrane than without PEG. A sharp increase in gold release within the first few hours occurs with the addition of PEG, but like the non-PEG HNPs this quickly stabilizes. In the case of PEG HNPs this stabilization occurs after lower amounts of gold has been released. The HNPs display higher stability at a pH of 7.2 (blood) of around 0.0016 compared to the amount of gold released at pH 4.6 (lysosome), which is still gradually releasing gold, although at a much lower rate beyond 0.002 % release and at an even lower rate after 0.0043 %. With PEG, the HNPs are therefore 2.7 times more stable over 2 weeks at a pH of 7.2 compared to 4.6 (Barnett *et al*., 2013). Overall the HNPs remain stable in terms of the amount of gold being released over a 2 week period. Different conditions and the presence of PEG affect the onset stabilization with PEG providing improved stability by reducing the amount of gold release (C. M. Barnett et al. 2013). Au-IONPs were also stored in solution for 6 months at room temperature in order to determine their physical stability over an extended period of time. The data acquired from this experiment is shown in Figure 34.

Physical property	0 months[a]	6 months
Size using photon correlation spectroscopy, nm	250 (22)	255 (62)
Polydipersity index	0.112 (0.010)	0.312 (0.021)
Zeta potential, mV	+2.4 (0.00)	+2.4 (0.01)
Size from transmission electron microscopy, nm	70 (0.5)	70 (0.4)
Magnetic coercivity from SQUID measurement, kAm^{-1}	10.35 (5)	6.2 (0.2)
T2 relaxivity from MRI measurement, $mM^{-1} s^{-1}$	175.3 (1)	161.7 (7.3)
ΔT from laser irradiation of 10 µg mL^{-1} suspended in 2 % agar, °C	7.0 (0.5)	7.5 (0.8)

Figure 34: Results for the physical stability study of Au-IONP's stored in solution at room temperature for 6 months (C. M. Barnett et al. 2013).

After 6 months the nanoparticles retained their size of 70 nm and showed no loss of gold coating due to no differences in the zeta potential. Therefore Au-IONPs display excellent

chemical stability and shelf life. TEM images confirmed that the Au-IONPs also retained their particle morphology as well (C. M. Barnett et al. 2013).

The method for synthesizing Au-IONPs was described by (C. M. Barnett et al. 2013). First, iron oxide nanoparticles were produced by an established co-precipitation method. The IONP's are coated with a polymer called poly (ethylenimine) (PEI) with a molecular weight of roughly 750000g mol^{-1}. This allows the gold seeds to attach to the iron oxide cores easier. Gold seeds were produced by reducing $HAuCl_4$ solution with $NaBH_4$. Purification during the Au-IONP synthesis involved magnetic separation and multiple decanting steps aided by the magnetic properties of the IONPs and subsequent Au-IONPs as shown in Figure 35.
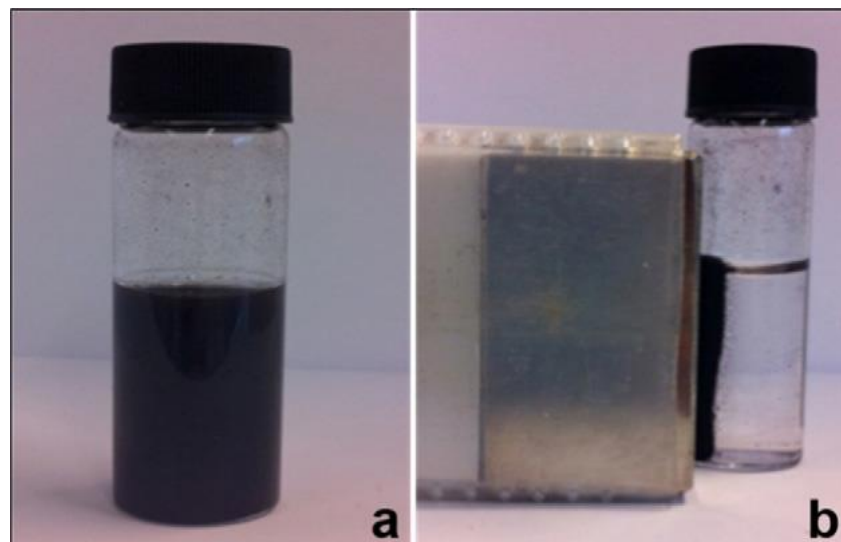
Figure 35: Photographic images of (a) gold-coated iron nanoparticles (Au@FeNPs) demonstrating the purple colour associated with the presence of metallic gold and (b) the magnetic separation of the Au@FeNPs which leaves in solution any pure gold nanoparticles which form during the coating of the FeNPs (Wagstaff *et al*. 2012).

30 nm Au-IONPs were synthesised by established methods and tested on pancreatic cancer cell cultures at different concentrations (Guo *et al*. 2013). Determination of the effect of the laser light (808 nm) on the pancreatic cancer cells after 5 min of exposure revealed no reduction in cell proliferation and a temperature increase of 12.89°C from 20°C (Guo *et al*. 2013) in Figure 36 (A). A wavelength of 808 nm was chosen due to iron oxide having a very low absorption at this range. Therefore all absorbed light from the laser, would be attributed to the gold layer (Guo et al. 2013). The laser provided a surface power density of 7.9W cm^{-2}. The effect of changing the surface power density on the rate and extent of

cell culture heating is displayed graphically in Figure 36 and with microscopic imaging in Figure 37.
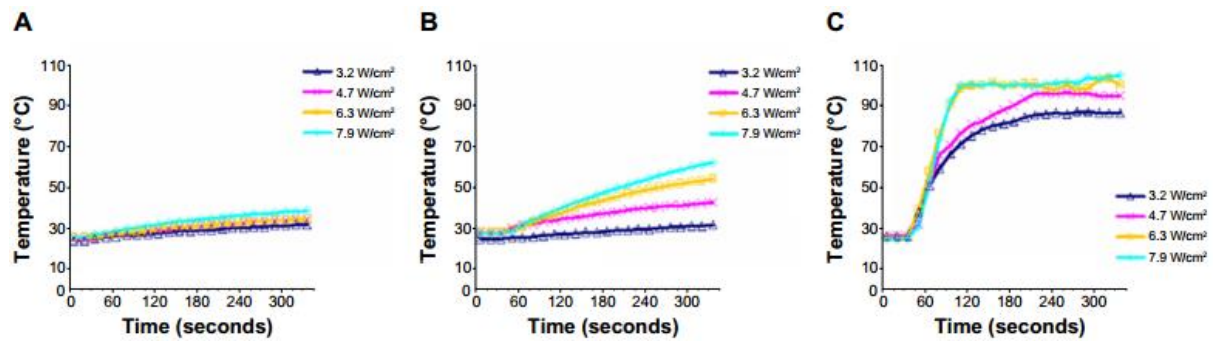
Figure 36: Photothermal response of 0 (A), 25 (B), and 50 (C) µg/mL nanoparticle samples at 3.2, 4.7, 6.3, and 7.9 W cm-2 (Guo et al. 2013).
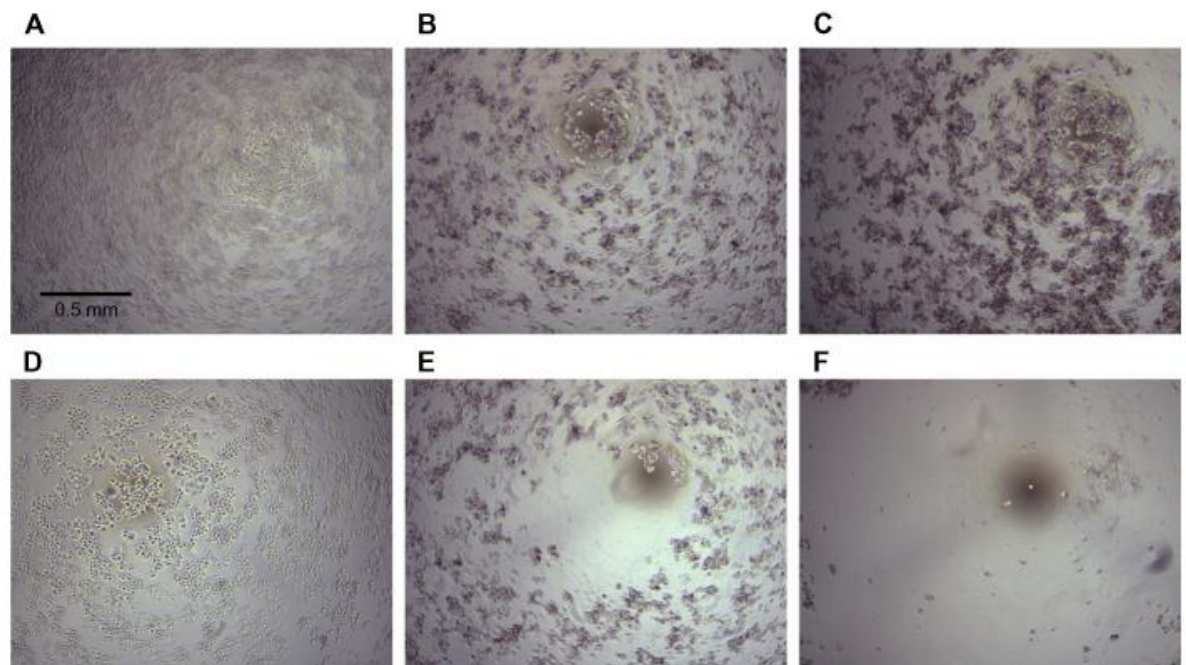
Figure 37: PaNc-1 cells exposed to 0, 25, and 50 µg mL-1 dose of nanoparticles, respectively, without laser irradiation (A–C) and with laser irradiation at 7.9 W cm-2 power density (D–F) (Guo *et al*. 2013)

Addition of 25 µg mL^{-1}(B) and 50 µg mL^{-1}(C) Au-IONP's without photothermal ablation reduced cell proliferation to 71.3 % and 47 % respectively. Photothermal ablation at the same concentrations reduced cell proliferation to 21.9 % (E) and 2.3 % (F) revealing that the cytotoxic properties of Au-IONP's coupled with heat generation has a significant increase in the reduction of pancreatic cancer cell proliferation. The heat generated by the 7.9W laser was not the main contributor to the temperature rise of the irradiated cells. This heat generation was due to the surface plasmon resonance properties of gold (Guo *et al*. 2013).

45

1.3. The Diels Alder reaction

The Diels Alder reaction is a [4+2] cycloaddition reaction between a diene and a substituted dienophile, which forms a substituted cyclohexene. It was first described in 1928 by Otto Diels and Kurt Alder (Diels & Alder 1929). Ethene, the dienophile shown in Figure 38, is analogous to maleimide, while 1.3-butadiene is analogous to furan. After Diels Alder has taken place, the resulting cycloadduct retains the secondary amine, and carbonyl groups of the maleimide as well as the ether oxygen of the furan. This is because they were not involved in the 4+2 cycloaddition.
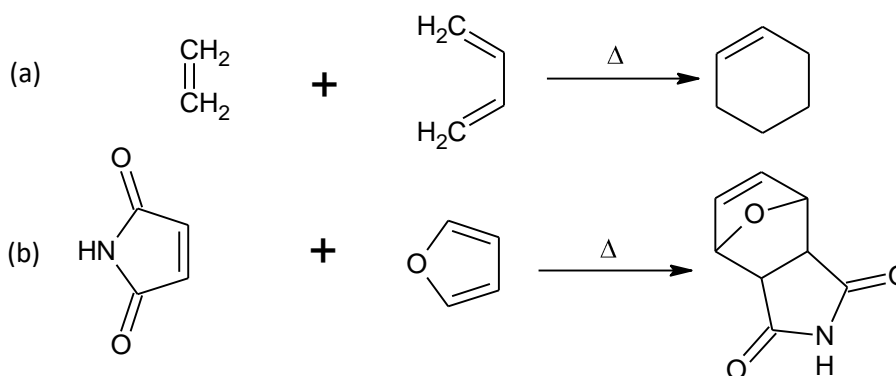
Figure 38: The simplest cycloaddition between ethene and 1,3-butadiene to produce cyclohexene (a). Analogous Diels Alder reaction between maleimide and furan (b).

Drug formulations in clinical use must be tested to ensure every conceivable reaction that could possibly take place is recorded and evaluated. In regards to drug formulation for chemotherapy, the Diels Alder reaction conservation of atoms is an advantageous property. This is because the only compounds of interest are the cycloadduct, diene and dienophile when ascertaining their individual effect upon introduction into the body. A cycloaddition like the example in Figure 39 is pericyclic reaction. These reactions have a transition state where all of the bond breaking and formation occurs simultaneously in a cyclic fashion (Sauer & Sustmann 1980).
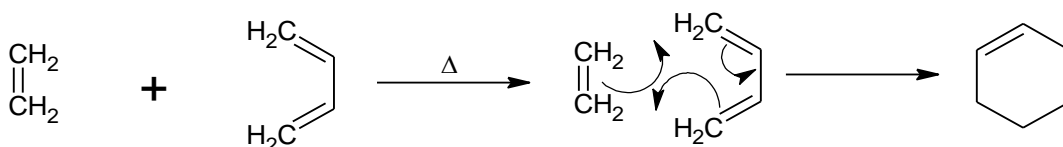
Figure 39: Diagram depicting the pericyclic transition state of a Diels Alder reaction between ethene and 1,3-butadiene to produce cyclohexene.

The diene has 4 π electrons (2 π bonds) and the dienophile has 2 π electrons (1 π bond) involved in this pericyclic reaction. Three π bonds break as a new π bond and 2 σ sigma bonds form. Figure 40 above shows the π orbitals of the diene and dienophile. The dienophiles single π bond has two possible conformations while the diene has four. The LUMO within the dienophile matches the arrangement of the HOMO of the diene. The energy gap is also similar enough to allow electrons from the HOMO of the electron rich diene to transfer to the LUMO of the electron poor dienophile.
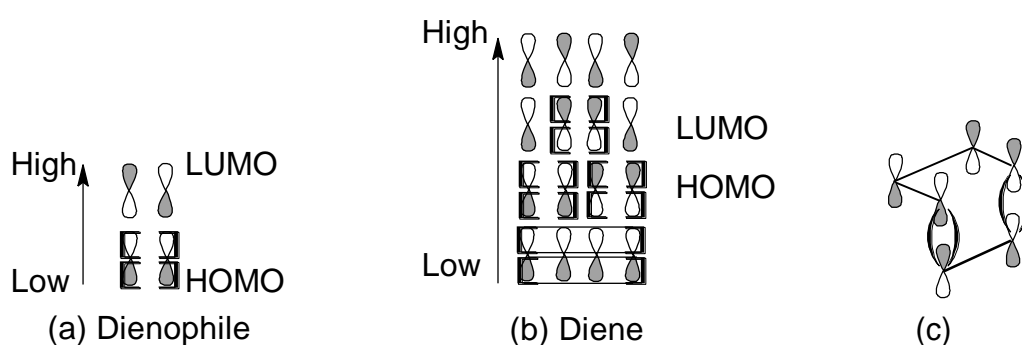
Figure 40: π orbital interaction around a single π bond (a), two π bonds (b) and the interaction of LUMO (a) and HOMO (b).

The orbitals have to be orientated specifically, in order for the bond forming electron transfers to occur, during the concerted transition state. This requires the diene to be in an s-cis (-C=C-) conformation. It is possible for the diene to be electron poor if it has an electron withdrawing group such as ($-CH_2=CH_2-CH=O$) carbonyl group. A dienophile in this condition can still undergo Diels Alder with an electron rich dienophile. This is called inverse Diels Alder (Knall *et al*. 2014). Three π bonds are still broken to form a new π bond and two σ bonds. The Diels Alder reaction between furan and maleimide can produce both endo and exo products. This is due to maleimide being able to arrange itself in two possible orientations and still have its π orbitals line up with furans. The endo isomer is formed from the endo transition state where the substituents of the dienophile are facing towards the π bond of the diene. In the exo isomer the substituents are facing away from the diene π bond.

The potential outcome of any chemical reaction is based on two aspects. The first is the thermodynamic energy of the product and this governs the stability of the product(s) in a reaction. In terms of ΔG which is Gibbs free energy, if the reaction releases energy, it can

be described as exothermic and spontaneous. This is shown in the Gibbs free energy equation:[$\Delta G = \Delta H - T\Delta S$] where the free energy of a system (G) is equal to its enthalpy (H) at normal pressure minus the product of the temperature (T) and entropy (S) of the system. If ΔG is negative the reaction is spontaneous and Diels Alder will occur. This is the case with Diels Alder where the product has a lower energy than the starting material. Figure 41 goes on to illustrate that the thermodynamic product is more energetically stable than the reactants.
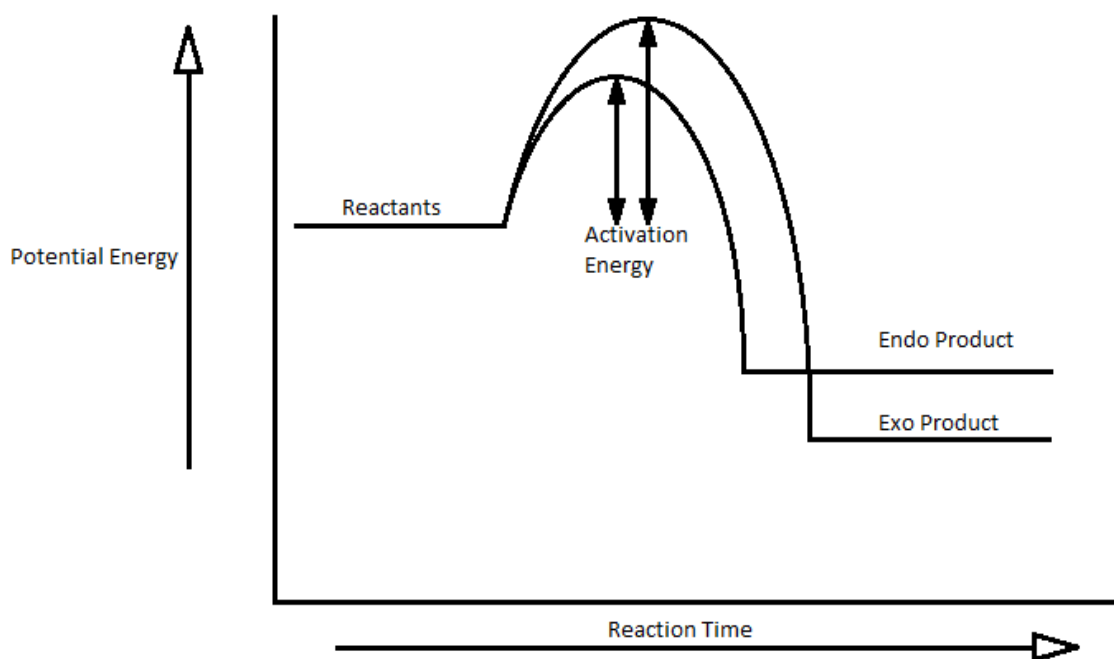
Figure 41: Reaction energy diagram of a Diels Alder reaction. Note that the endo product has more potential energy and forms faster.

The thermodynamically more stable product will be the exo isomer due to having less steric congestion. The second factor influencing the outcome of a chemical reaction is the kinetic aspect. The kinetics of a reaction describe the rate in which products are formed. Overall, the Diels Alder reaction between furan and maleimide produces a mixture of endo and exo isomers. The endo transition state in Figure 42, is produced faster because of non-bond forming interactions between the electron withdrawing carbonyls π orbitals of the maleimide and the middle two π orbitals of the diene. This lowers the activation energy leading to a faster reaction as shown in Figure 41.
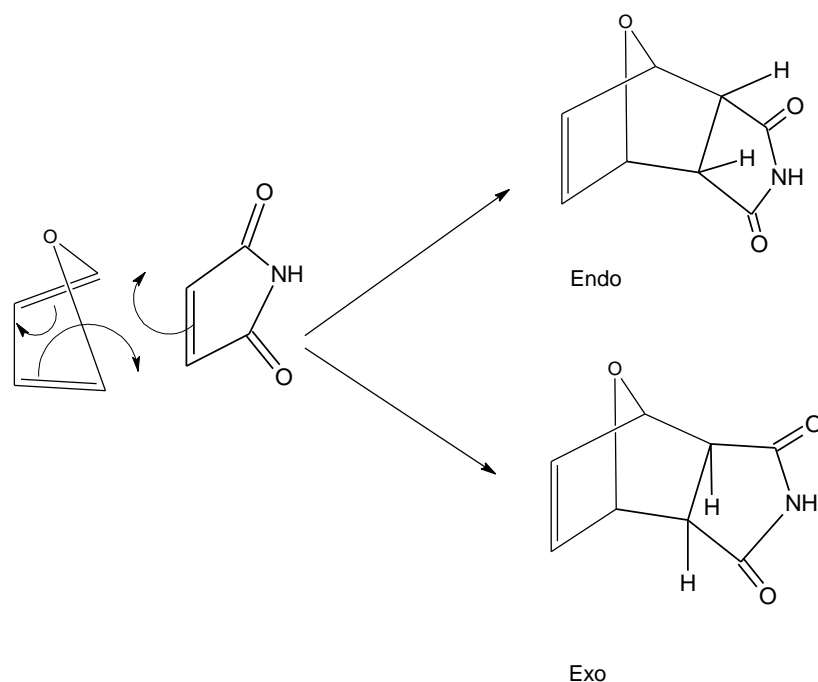
Figure 42: Diagram showing the endo and exo isomer products produced by a Diels Alder reaction between furan and maleimide.

The Diels Alder reaction requires an activation energy threshold to be reached before it can proceed (Boutelle & Northrop 2011a). In some cases, especially in the presence of electron withdrawing group, the activation energy may be low enough for the [4+2] cycloaddition to occur spontaneously. Therefore some Diels Alder reactions can proceed at room temperature (Scheltjens *et al*. 2013). In terms of the cycloaddition between furan and maleimide, both the exo and endo isomers form because conditions satisfy both outcomes. The endo isomer is the major product however because it forms faster (Boutelle & Northrop 2011a).

Under elevated temperatures a cycloadduct formed from a Diels Alder reaction will reverse forming the diene and dienophile (Kuramoto *et al*. 1994). This can be explained with the Gibbs free energy equation: $[\Delta G = \Delta H - T\Delta S]$ where elevated temperatures can surpass the enthalpy component causing the free energy (ΔG) to be positive. This allows the reverse reaction to occur spontaneously (Boutelle & Northrop 2011a). As stated previously, the endo isomer has a higher enthalpy than the exo isomer. If enough energy is supplied to the system the endo isomer having reached a positive ΔG will be able to undergo retro Diels Alder (Boutelle & Northrop 2011a). The rate of this reversal is temperature dependant and the equilibrium ratio between starting materials and cycloadduct increases at higher

temperatures. The exo isomer as the more thermodynamic product is more stable, possessing a lower enthalpy. In order to undergo retro Diels Alder it will require more energy than the endo isomer. As a result there is a temperature range unique to each cycloadduct where only the endo isomer will undergo retro Diels Alder. Therefore the starting materials are regenerated and some will undergo Diels Alder again via the exo transition state. Over time the exo isomer accumulates and becomes the major product (Boutelle & Northrop 2011a).

The Diels Alder cycloadduct is the key attribute that a suitable thermally labile linker possesses that meets the requirements. However said thermally labile linker also has a pharmaceutical agent (gemcitabine) and thiol group in order to attach to the gold surfaces of hybrid nanoparticles. Because a suitable thermally labile linker structurally rests in between the pharmaceutical component and the thiol group it must have the ability to covalently bond to both. The thiol group in particular can pose a problem for the formation of a Diels Alder adduct between a substituted furan and maleimide, as it specifically undergoes a Michael addition with maleimides producing a highly stable thioether (Onbulak *et al*. 2012). This reaction will remove the π bonds of maleimide rendering a Diels Alder reaction impossible, as shown in Figure 43.
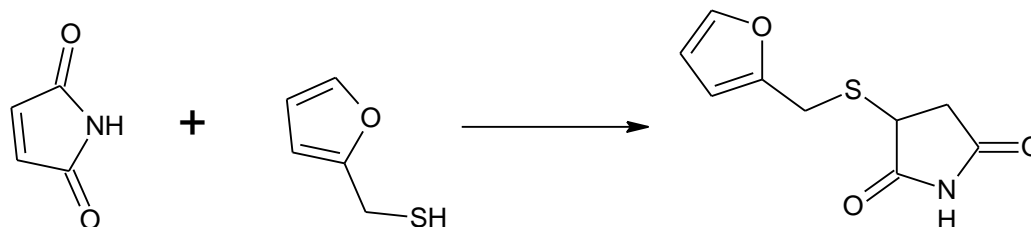
Figure 43: Thiol-Michael addition between maleimide and 2-furanmethanethiol.

Therefore the introduction of a thiol group must either occur after Diels Alder has taken place or only after the present thiol group has been protected. As described in Figure 44, this will ensure Diels Alder takes place with no competing reactions. With the commercially availability of 2-furanmethanethiol, the choice to protect its thiol group was chosen. As such, 2-furanmethane thiol was first protected with either a benzoyl or boc group in all instances before it was used in a Diels Alder reaction.
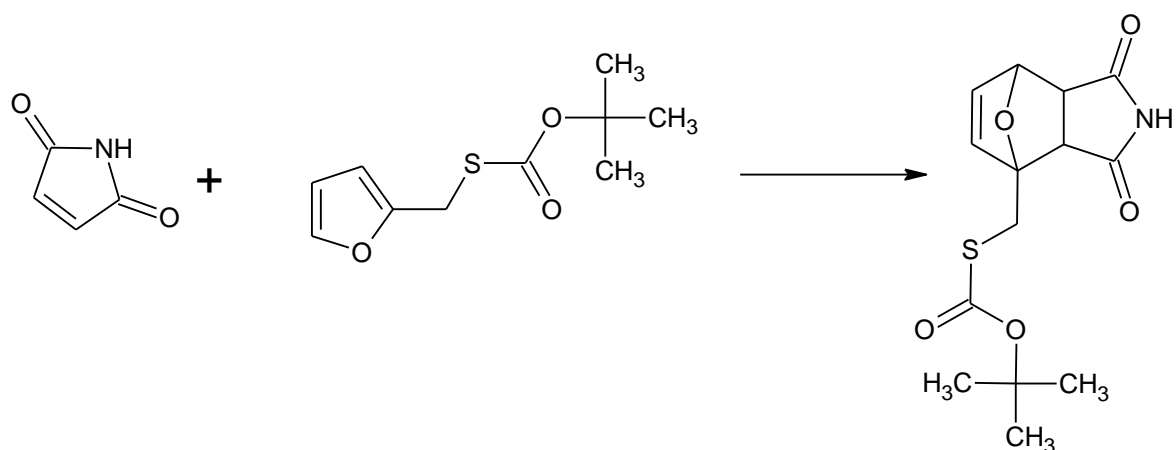
Figure 44: Diels Alder reaction between maleimide and boc protected 2-furanmethane thiol.

In order to observe the effects of the thermally labile linkers activity on cell proliferation, the presence of a known cytotoxic agent is required. Gemcitabine is the most common first line chemotherapeutic agent for treating pancreatic cancer (Hoskins *et al*. 2010). This makes it the best candidate to fill criteria as the pharmaceutical agent component of a suitable thermally labile linker. Gemcitabine (2',2'-difluoro-2'-deoxycytidine) is a prodrug that is converted intracellularly to the monophosphate by deoxycytidine kinase and then the diphosphate by pyrimidine nucleoside monophosphate kinase at the 5 position hydroxyl group (Song *et al*. 2016a). The three and five position hydroxyl group shown in Figure 45, must be free to covalently bond to the phosphate group of the neighbour nucleic acids. As a result these groups must be present and unsubstituted by the time the thermally labile linker is covalently bonded to the hybrid nanoparticles via a thiol-gold bond.
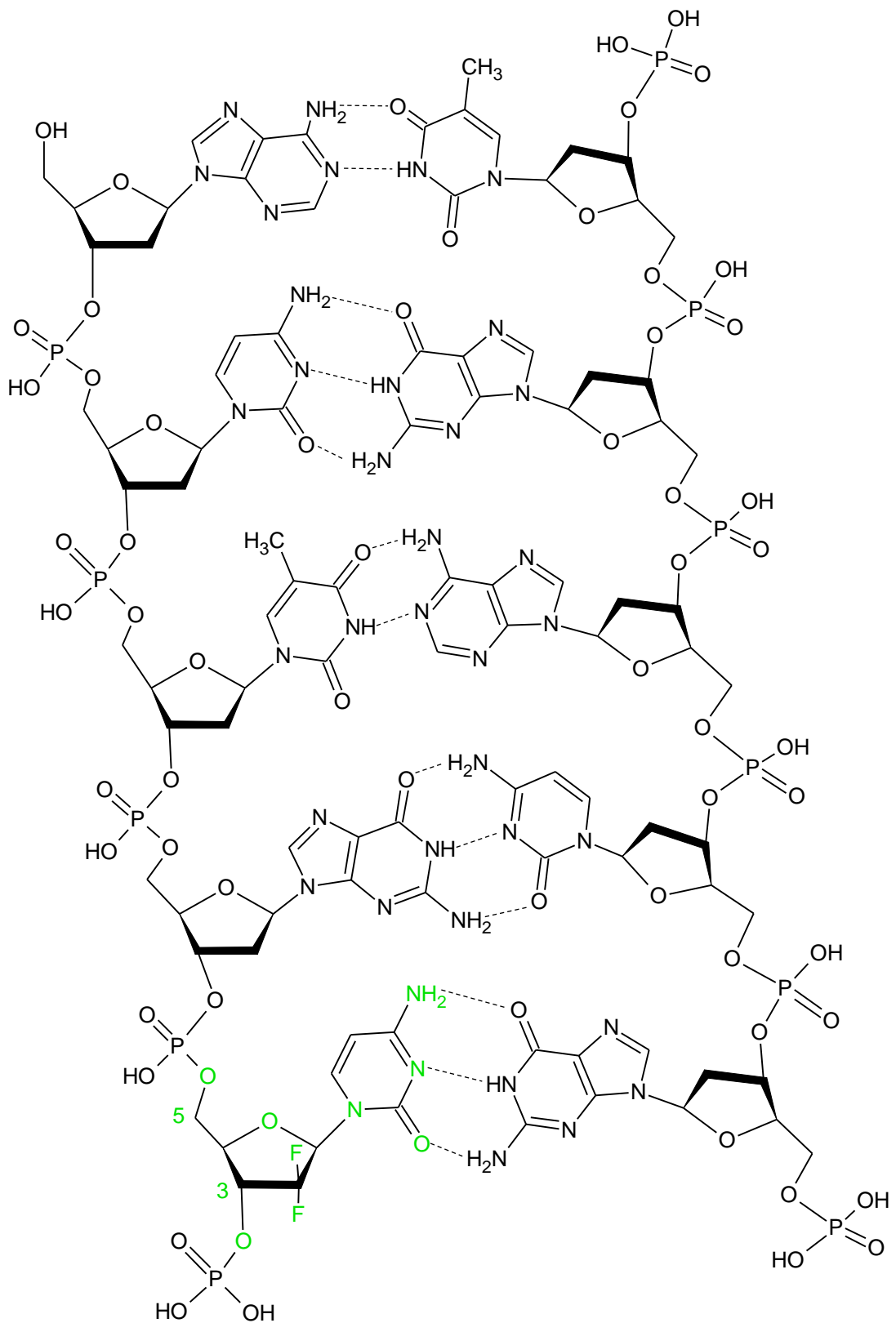
Figure 45: Diagram depicting a section of DNA where the highlighted active form of gemcitabine (2', 2'-difluoro-2'-deoxycytidine triphosphate) has substituted deoxycytidine triphosphate during DNA synthesis.

1.4. Current research on thermoresponsive drug delivery systems

The slight hyperthermia experienced by cancerous cells is caused by their accelerated growth and metabolic activity. A recent study in the exploitation of this trait involves Celsion Corporations development of a liposomal formulation called ThermoDox which is in its stage III trials. This formulation capitalises on the leaky vasculature of cancerous tissues which allows for the accumulation of liposomal formulations (Alexander *et al*. 2013; Nagy *et al*. 2009). The polymeric structure of ThermoDox is stable at 37 °C but undergoes a phase transition above 40 °C which facilitates the release of doxorubicin an antitumour drug directly at the intended site of action (Alexander *et al*. 2013). Magnetic iron oxide nanoparticles (IONP's) with surface attached Diels Alder cycloadducts were used to facilitate the release of a fluorescent dye called tetramethylrhodamine-5-C2- maleimide (RhD) which acted as a model drug. Heat generated by the IONPs subjected to an alternating magnetic field increased their surface temperature to 80 °C which allowed the retro Diels Alder reaction to occur. This caused the release of 85 % of the attached RhD compound over a 48 h time period. The Diels Alder reaction is known to proceed at temperatures of 90 °C and above but the close proximity of the Diels Alder reaction was hypothesised to allow the initiation of the retro Diels Alder at lower temperatures (N'Guyen *et al*. 2013).

1.5. Substituent effects on reactivity and reversibility of the Diels Alder reaction

The Diels Alder reaction can be promoted further with the presence of certain substituents. Electron withdrawing groups attached to the sp^2 carbon(s) of dienophiles, such as the carbonyl groups in maleimide, cause the dienophile to be more electron poor than ethene. The Diels Alder cycloadduct formed from the reaction between furan and maleimide proceeds with ΔG = -1.1 kcal mol^{-1} for the exo isomer and -3.6 kcal mol^{-1} for the endo isomer (Boutelle & Northrop 2011b). A similar reaction between 2-methoxyfuran and maleimide in Figure 46, has a ΔG value of -6 kcal mol^{-1} for its endo adduct. This difference of 2.4 kcal mol^{-1} makes the cycloadduct of 2-methoxyfuran and maleimide favourable for adduct formation (Boutelle & Northrop 2011b).
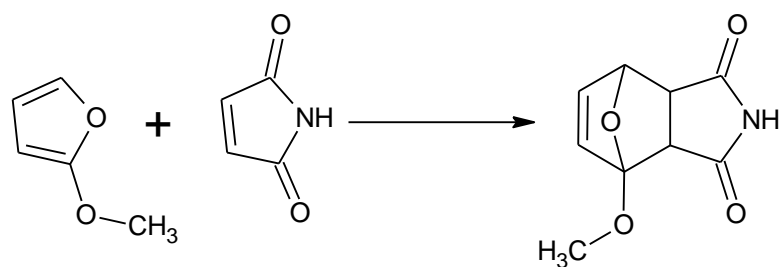
Figure 46: Diels Alder reaction between 2-methoxyfuran and maleimide.

This is because of the strong electron donating property of the methoxy group acting on the diene (furan) promoting adduct formation at the cost of completely hindering reversibility. As such, the use of a methoxy substituted furan for this projects aims was deemed highly unfavourable. The presence of alkyl chain substituents on the furan also promotes the adduct formation, at a lesser extent when compared to a strong methoxy electron donating group. The Diels Alder cycloadduct shown in Figure 47, formed from 2-methylfuran and maleimide has a ΔG value of -2.4 kcal mol^{-1} for the endo isomer, which is a difference of 1.3 kcal mol^{-1} when compared Diels Alder reaction of furan and maleimide (Boutelle & Northrop 2011b).
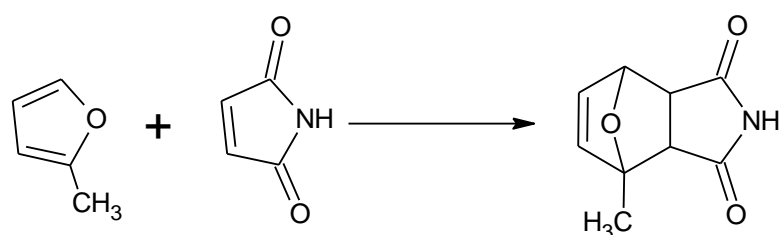
Figure 47: Diels Alder reaction between 2-methylfuran and maleimide.

The effect is a Diels Alder reaction that can proceed to produce a stable cycloadduct that is still capable of retro Diels Alder at elevated temperatures. This trait is highly beneficial for fulfilling the requirements in synthesizing a thermally labile linker. Electron withdrawing groups such as aldehydes as substituents on the diene may raise the ΔG energy enough for it to be positive. This is the case with the Diels Alder cycloaddition of 2-furaldehyde and maleimide shown in Figure 48. No adduct formation has been recorded and it is speculated that any adducts formed immediately undergo retro Diels Alder (Boutelle & Northrop 2011b).
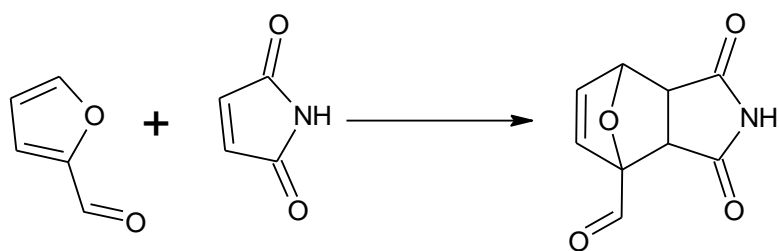
Figure 48: Diels Alder reaction of 2-furaldehyde and maleimide.

All of these examples clearly prove that the presence of substituents affect the Diels Alder and its reversibility. However the position of the substituent, not just the type also affects the forward and backwards Diels Alder reaction. Substitution on the 3 position of furans also has an effect on the formation of the cycloadduct. The Diels Alder reaction of 2 and 3-methylfuran with maleimide will proceed to form a cycloadduct, but the 3 position substitution will yield an adduct that is more stable than the 2 position. This is reflected in its endo isomers higher free energy (ΔG) of -3.6 kcal mol^{-1} at the 3 position compared to -2.4 kcal mol^{-1} for the 2-position (Boutelle & Northrop 2011b). The 2-position within furan is more electropositive than the 3 position. Therefore the presence of electron donating groups such as methoxy will favour the Diels Alder more at the 3-position (Boutelle & Northrop 2011b).

1.6. Aims and objectives

The aim of this project involves the attachment of a clinically relevant drug (gemcitabine) to the surface of gold coated iron oxide nanoparticles via a thermally labile linker. This linker would contain a Diels Alder adduct capable of facilitating the release of attached drugs at elevated temperatures. The heat required for this process would be generated by the gold coated iron oxide nanoparticles. The bioavailability, chemical stability and surface plasmon resonance properties of gold as a coating of magnetic iron oxide nanoparticles will prove invaluable in a potential novel drug formulation for treating pancreatic cancer. By utilizing the thermal reversibility of Diels Alder cycloadducts, the thermal release of drug compounds can proceed due to the heat generated by the surface plasmon resonance of gold coated iron oxide nanoparticles. These hybrid nanoparticles serve as theranostic agents capable of both diagnostic and therapeutic activity. In terms of synthesizing a thermally labile linker based on a Diels Alder adduct, it is preferable to use a 3-substituted furan. However the increased free energy of a cycloadduct formed from a 3 substituted

furan with maleimide will also lead to higher temperature requirements to initiate retro Diels Alder. One of the criteria a Diels Alder adduct will need, to meet the requirements as a suitable thermally labile linker, is to readily undergo retro Diels Alder at 45 °C. Therefore a balance has to be struck to ensure that the forward Diels Alder reaction to produce a cycloadduct is thermodynamically possible and the resulting cycloadduct is capable of undergoing retro Diels Alder at the required temperature range. The synthesis of a suitable thermally labile linker, attached to a clinically relevant drug (gemcitabine) and to the surface of gold coated iron oxide nanoparticles was carried out. Characterisation of the products of each chemical reaction step and final linker was carried out with nuclear magnetic resonance (NMR), fourier transform infrared spectroscopy (FTIR) and thin layered chromatography (TLC). The charge and particle size changes were monitored throughout hybrid nanoparticle synthesis with a zeta sizer and inductive coupled plasmon – atomic emission spectroscopy (ICP-AES) was used to characterise the atomic gold and iron ratio of hybrid nanoparticles. The synthesis process for this novel drug formulation, drug release experiments and *in vitro* experiments on pancreatic cancer cells, will be displayed in the next chapters of this study.

CHAPTER 2: SYNTHESIS OF THERMALLY LABILE

DRUG LINKERS

2.0. Introduction

Hybrid iron oxide-gold (HNPs) have shown potential as drug carriers for pancreatic cancer therapy (Sailor et al. 2012; C. M. Barnett et al. 2013). In order to further investigate the potential of these particles the drugs must first be conjugated onto the surface of the particles. This conjugation may be due to physical or chemical bonding. Physical binding of onto the surface of the HNPs has been previously reported. This study showed that positively charged drug molecules were capable of binding onto the HNP with reversible effect under heating (Eskandari & Ghourchian 2012). However, electrostatic binding may work in some circumstances but many factors such as change in pH, addition of electrolytes and temperature may contribute to the breakdown of bonds (Eskandari & Ghourchian 2012). Hence, it is desirable to develop a means of chemical binding onto the HNPs to ensure stability. It is well reported that thiolated molecules can bind to gold nanoparticles using dative covalent binding (Salihov *et al*. 2015; Zhu *et al*. 2006; Arora *et al*. 2014). A typical covalent bond involves the sharing of electrons between two atoms where each atom supplies one electron to form the bond. In dative covalent bonds, both of the electrons are supplied by one atom (Atkins 2006a). The presence of thiols or disulphides on a drug compound will allow the formation of a dative bond with the gold surface of HNPs. Drug molecules containing thiols or disulphide bonds may exploit this chemistry, however, this is non-reversible and hence it may hinder the active site of the molecule and inhibit activity. Drug molecules which do not contain such functional groups may be chemically attached to the surface of the HNPs via linker. The linker molecules themselves may be developed to be stimuli responsive i.e. Linker breakdown occurs upon alteration of conditions such as pH or temperature (Zhu *et al*. 2006; Gobbo & Workentin 2012; Engel & Kickelbick 2013).

Hybrid iron oxide-gold (HNPs) have shown potential as drug carriers for pancreatic cancer therapy (Sailor et al. 2012; C. M. Barnett et al. 2013). The first task is the conjugation of drugs to their surface in order to improve our understanding of their drug carrier potential. HNPs have a negative charge and can form electrostatic bonds with positively charged drugs (Eskandari & Ghourchian 2012). The effects of enzymatic action, presence of electrolytes and changes in pH can affect the zeta potential which in turn could prematurely release the loaded drug or make the formulation unsuitable for long term storage

(Eskandari & Ghourchian 2012). Due to the cytotoxic nature of chemotherapeutic drugs, it is imperative that a method of drug loading is utilised that promotes stability. It has already been reported that thiolated materials are capable of forming dative covalent bonds with gold coated iron oxide nanoparticles (Salihov *et al*. 2015; Arora *et al*. 2014; Zhu *et al*. 2006). A typical covalent bond involves the sharing of electrons between two atoms where each atom supplies one electron to form the bond. In dative covalent bonds, both of the electrons are supplied by one atom (Atkins 2006a). Drug compounds lacking a thiol group for an Au-S dative covalent bond, may be chemically attached to one, via a linker. The properties of the linker could also be designed in order to further promote the activity of released drugs under specific conditions such as changes in temperature (Zhu *et al*. 2006; Gobbo & Workentin 2012; Engel & Kickelbick 2013). Using a temperature sensitive linker would be ideal due to the surface plasmon resonance (SPR) property of gold. SPR is a phenomenon involving the oscillation of surface electrons caused by the conversion of absorbed electromagnetic energy of a specific wavelength into light of a different wavelength. Gold undergoes SPR at the near infrared range of the electromagnetic spectrum (H. Zhang *et al*. 2013). As a result, exposure to near infrared radiation will cause a rise in the surrounding temperature around the HNPs. The use of a Diels Alder cycloadduct was selected as a potential thermally labile linker to fit this criteria and promote drug release following the HNPs exposure to near infrared radiation.

The substituted groups present on furans and maleimides is retained after cycloaddition which further displays the customisable nature of these cycloadducts. In fact, all structural atoms present on reagents undergoing the Diels Alder reaction are present within the cycloadduct. These cycloadducts will reverse back into their original diene and dienophile reagents in elevated temperatures (Gandini 2005). This reaction has been exploited in drug delivery predominantly in polymer chemistry.

One such example is with the use of Diels Alder adducts to construct dendrimers by (Szalai *et al*. 2007). Their aim was to synthesize self-assembly systems with thermal responsiveness. They noted its reliability to form up to 4th generational dendrimers based on the furan-maleimide Diels Alder reaction shown in Figure 49. A 1,1'-(methylenedi-4,1-phenylene)- bismaleimide served as the dendrimer core and as a reactive dienophile.
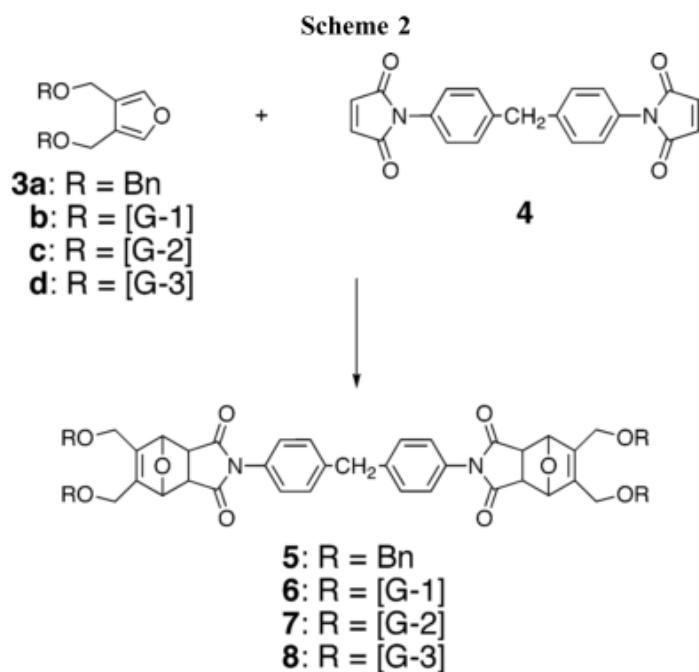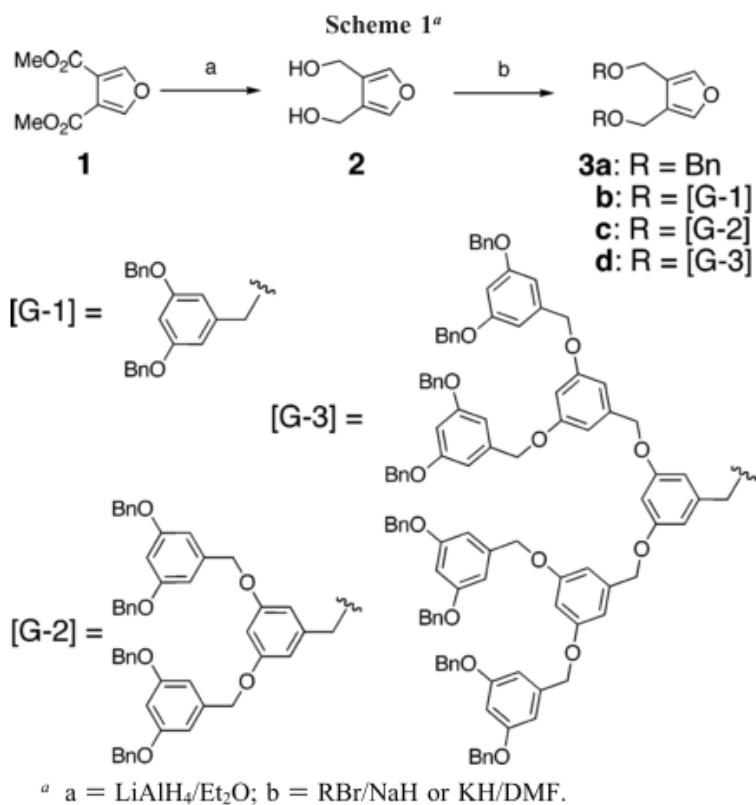
Figure 49: Reaction scheme of the synthesis of first, second, third and fourth generation dendrimers attached to a substituted furan and the subsequent reaction with a bismaleimide core (Szalai et al. 2007).

These dendrimers degraded at temperatures of 95 °C and reassembled over three days at 60 °C displaying the reversibility of the Diels Alder reaction for potential use in "self-healing" dendrimers (Szalai *et al*. 2007).

The Diels Alder reaction can also be exploited for preparing thermally reversible cross linked polymers. These polymers have been synthesised by mixing a molar equivalent of poly(furfuryl methacrylate) (PFMA) and 1,1'-(Methylenedi-4, 1-phenylene)bismaleimide (BM) in dichloromethane at room temperature (Kavitha & Singha n.d.).

A rigid film of the cross linked polymer shown in Figure 50, was cut with a knife and then heated to 120 °C. This allowed the polymer to improve its mobility due to its cross linking Diels Alder adducts reversing, filling in the notch left by the knife mark.
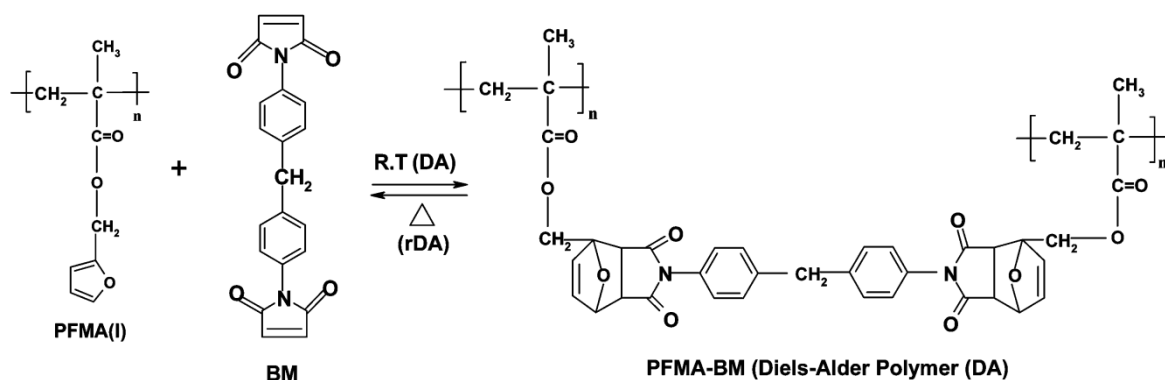
Figure 50 : Preparation of thermally amendable cross linked polymers using the Diels Alder reaction
(Kavitha & Singha n.d.).

Upon cooling the cross linker reformed via the Diels Alder reaction and evidence of damage caused by the knife had disappeared, showing the self-repairing potential of polymers utilizing Diels Alder adducts as cross linkers (Kavitha & Singha n.d.).

In this study a Diels Alder cycloadduct was attached to gemcitabine, a clinically used chemotherapeutic agent via an alkylated ester linker. The diene component of the Diels Alder adduct possessed a free thiol group that facilitated dative covalent bonding to the gold surface of hybrid nanoparticles. The rate of the retro Diels Alder reaction shown in Figure 51, directly translates to the rate of the drug delivery. Therefore the faster retro Diels Alder takes place, the quicker the loaded drug is released from the surface of the

hybrid nanoparticle formulation. As a result the ability of a suitable Diels Alder adduct to readily undergo retro Diels Alder, due to the heat generated via SPR is critical.
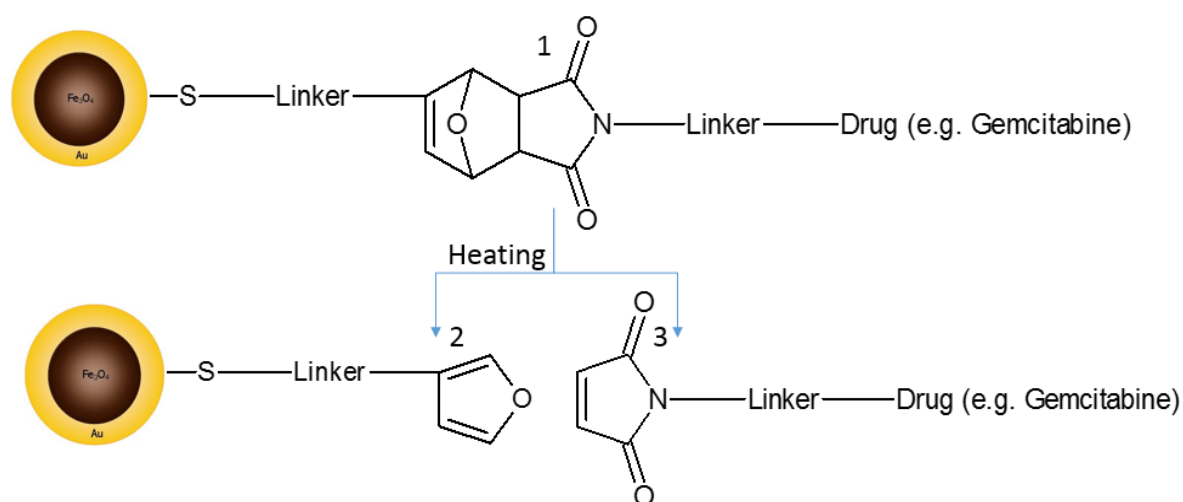
Figure 51: Schematic of a Diels Alder cycloadduct linker that undergoes retro Diels Alder in elevated temperatures to facilitate in drug release from the HNP surface. The heat required for this is generated via SPR of the gold coated HNPs after exposure to NIR radiation.

The synthesis of a suitable thermally labile linker was carried out over multiple reaction steps. The monitoring of the synthesis and breakdown of the linker were carried out using commonly used analytical techniques described below.

2.0.1 Fourier transform infra-red spectroscopy

FTIR spectroscopy is a non-destructive analytical technique used to measure the absorbance of infrared radiation of a given sample in order to ascertain its composition and structure of components (Lachenal 1995; Williams & Fleming 2007). When molecules are exposed to infra-red radiation the atoms absorb specific frequencies and vibrate due to the received energy (Williams & Fleming 2007). On a typical IR spectrum the frequency is displayed in wavenumbers 400-4000 cm^{-1}, which is the inverse of frequency (1/frequency) in cm^{-1} (Andersen *et al*. 2016). The percentage transmission of specific wavenumbers provides a strong indication to the functional groups of the analyte.

Covalent bonds are not like the rigid bridges we commonly see in literature and text books (Hart 2003; Williams & Fleming 2007). The diagrams shown are often a depiction of two nuclei being held together by the mutual attraction to a pair of electrons. When molecules are exposed to infra-red radiation their atoms vibrate in different ways called vibrational

modes. The methylene group (R=CH$_2$) C-H bonds will produce the vibration modes shown in Figure 52. With enough energy provided these nuclei can move and vibrate without their covalent bonds breaking (Williams & Fleming 2007).
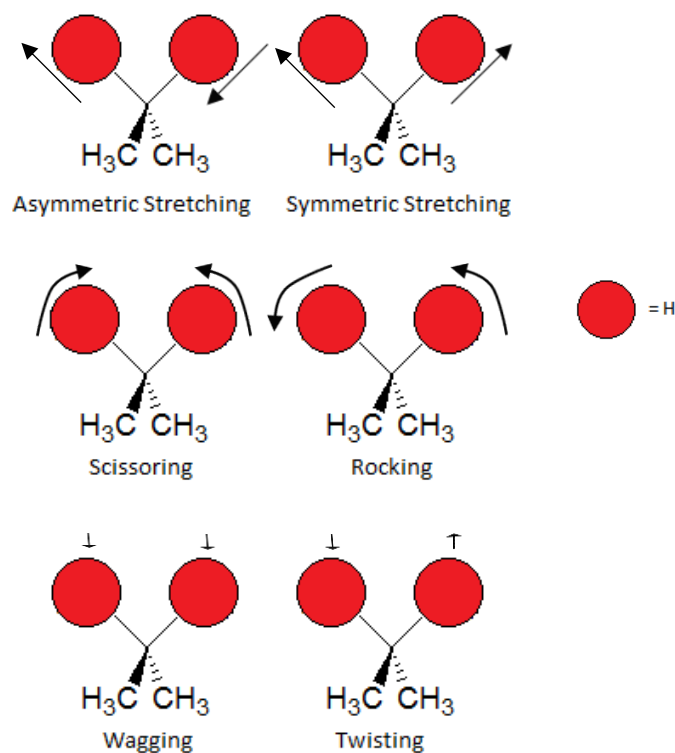
Figure 52: Vibrational modes of a methylene group -CH$_2$-.

The energy that causes the nuclei to vibrate depends on the mass of the two bonded nuclei and their bond length (Williams & Fleming 2007). Vibrating nuclei of similar masses tend to vibrate at lower frequencies (e.g. N-O at roughly 1500 cm^{-1}) than bonded nuclei of significant mass differences (e.g. O-H at roughly 3300+ cm^{-1}) (Williams & Fleming 2007). Bonds are easier to bend than stretch or compress. Stretching frequencies are therefore higher than bending ones and will have higher wavenumbers.

Some covalent bond vibrational modes (such as O-H) may produce broad absorptions due to hydrogen bonding (Williams & Fleming 2007). Hydrogen bonding involves parts of the electrons in the (O-H) bond for example, being shared with the hydrogen bond acceptor. This periodically causes the O-H bond strength to change which in turn, changes the vibrational energy of that bond. This effect broadens the range of vibrational energies the O-H bond has, which causes the broad absorptions seen on IR spectra (Williams & Fleming 2007). This also explains why other bond types with weaker hydrogen bonding (N-H) have

smaller broad peaks compared to (O-H). One disadvantage that IR spectroscopy has, is that it cannot be used to observe single atoms. Single atoms have no bonds, they do not vibrate and absorb infra-red radiation in order to produce an absorption signal (Williams & Fleming 2007). In homonuclear diatomic molecules (molecules comprised of one element) like O_2 there is no IR absorption signal on an IR spectrum because stretching does not cause a dipole moment (Williams & Fleming 2007). While IR spectroscopy is useful for discerning the structure of an analyte, it is often used with other analytical techniques such as mass spectrometry and nuclear magnetic resonance spectroscopy to correctly ascertain the structural identity of analytes.

FTIRs use an interferometer which fires a beam that is split into two identical beams. One beam travels through the sample and the other is redirected at a 90 ° angle. These beams are then reflected back and combined. Because one beam travelled through a sample, its travel time has changed which causes interference when combined with the other beam (Dean *et al*. 2002a). Light behaves like a wave and therefore the fusion of the two beams generates an interference pattern unique to each compound. In FTIR the wavelength of the beams is a mixture of frequencies across the IR spectrum. The resultant interference pattern contains information across this range, allowing analysis to take place across the IR spectrum simultaneously. This greatly reduces the time required to analyse a sample compared to dispersive spectrometers (Dean *et al*. 2002a).

2.0.2 Nuclear magnetic resonance spectroscopy

Nuclear magnetic resonance (NMR) is a capable and versatile analytical spectroscopic technique utilised to ascertain the physical structure(s) and purity of a sample (Torres & Price 2016). NMR can be used to determine the percentage composition of a mixture of known compounds. Alternatively it can be used to match unknown compounds against a literature source, library of spectral data or by deducing a likely structure based on the spectral data. NMR spectroscopy works by analysing the free induction decay, which is a signal generated by the spinning of atomic nuclei within an applied magnetic field. Different atomic nuclei within the same magnetic field will spin at different frequencies (Veeman 1997; Torres & Price 2016). This causes recognisable chemical shifts on NMR spectra. Protons (H^+) within a compound will have the same magnetic spin, however the presence

of electrons will cause these spins to provide different resonance signals (Schanda & Ernst 2016).

The motion of electrons opposes the applied magnetic field causing nuclear shielding. In order to achieve magnetic resonance, the strength of the applied magnetic field has to increase to overcome nuclear shielding (Torres & Price 2016). This cause shifts (in ppm) which explains why electronegative groups such as hydroxyls, have higher ppm values and peaks that appear further down on an NMR spectra than hydrocarbons. Some atomic nuclei such as C^{12} do not spin at all, due to an equal number of protons and neutrons. Atomic nuclei of H^1, C^{13}, N^{15} and F^{19} have a spin frequency of ½ (Lens & Hemminga 1998). These are often used for NMR spectroscopy because the analysis of their spin states is straightforward.

In H-NMR the protons can either be aligned with or opposing the applied magnetic field (Jones & Mulloy n.d.; Lens & Hemminga 1998; Torres & Price 2016). Since each proton can be described as a small magnet, its own magnetic field can deshield neighbouring protons, marginally shifting its NMR spectra peak downwards or it can enhance its nuclear shielding shifting it slightly up field (Jones & Mulloy n.d.; Lens & Hemminga 1998). This leads to the appearance of a split peak on a spectra. This is called spin- spin coupling or J-coupling (Dean *et al*. 2002b). Increasing the number of nearby protons will lead to more J-couplings causing further peak splits. The number of peaks to signify one proton environment is n+1, where n is the number of neighbouring protons to the hydrogen in question (Dean *et al*. 2002b). NMR can also be used to identify the presence and ratio of isomers within a sample. One example is with the Diels Alder reaction where products may be a mixture of endo and exo isomers. The orientation of protons changes between the two forms which is clearly visible on NMR spectrum (Goussé *et al*. 1998). This property further aids in the structural identification of analytes and proved invaluable for this work.

2.0.3. Thin layer and column chromatography

Chromatography is the term used to describe several techniques for separating materials within a mixture (Dean *et al*. 2002c). The mixture is dissolved in a solution called the mobile phase. This carries the mixture through a porous material called the stationary phase. Different components of the mixture will have a different affinity to the mobile and

stationary phase causing them to travel through the porous stationary phase at different speeds (Dean *et al*. 2002c). The properties of the mobile phase can be changed by using different solvent mixtures in order to fine tune separation of mixtures. If the stationary phase is of sufficient length then each component of the mixture can be collected individually. This is the prime objective of column chromatography, which is a technique used to purify mixtures containing a desired compound(s) after chemical synthesis. Column chromatography is often employed in the purification of reaction mixtures in order to separate the desired products from other materials (Dean *et al*. 2002c). A column like the one in Figure 53 is packed with a stationary phase such as silica gel, followed by the addition of the dried reaction mixture. The mobile phase is then added to carry the different components of the mixture down the column.
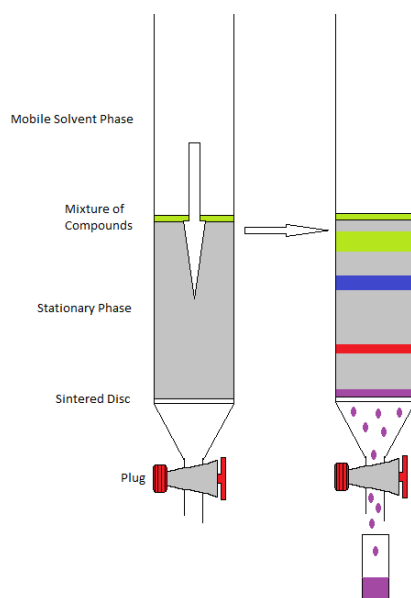
Figure 53: Diagram depicting column chromatography separation of a mixture of compounds.

Each component has their own unique affinity for the mobile and stationary phase. When the mobile phase reaches the bottom of the column it can be collected as a fraction along with any dissolved material. Evaporation of the desired fractions is then carried out to isolate the purified compound (Dean *et al*. 2002c).

Thin layer chromatography is another example of a chromatography technique. It is performed on sheet of aluminium, glass or paper, coated with a material that acts as the stationary phase. Examples of these materials include silica gel, aluminium oxide and cellulose (John *et al*. 2015; Pikul *et al*. 2013; Dean *et al*. 2002c). In organic chemical

synthesis TLC serves two main functions. The first is to monitor the progression of a reaction and the second is to ensure the end product is free of impurities. This is shown in Figure 54 where the starting materials, reaction mixture and product is spotted onto the baseline of the plate.
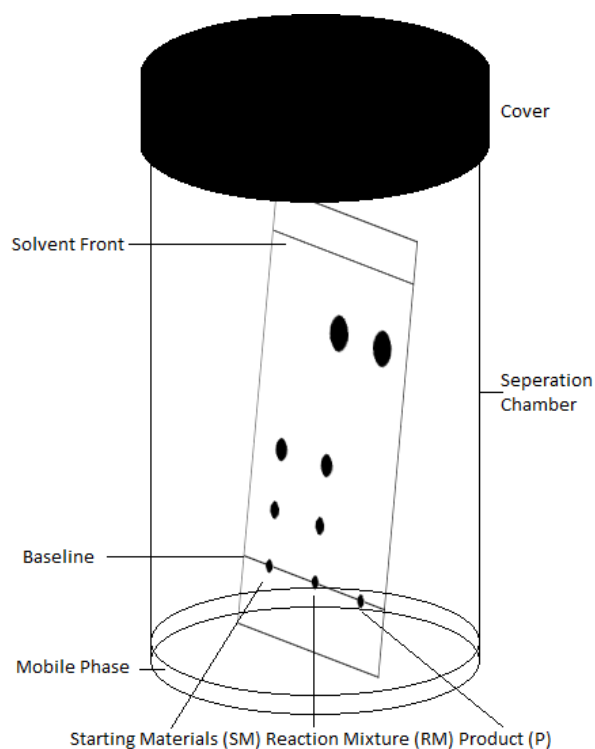
Figure 54: Diagram of a typical TLC plate for monitoring reaction progress.

Carrying out TLC involves taking a spotted TLC place and placing it within a separation chamber containing the mobile phase (Dean *et al*. 2002c). The mobile phase will travel up the plate via capillary action. The mobile phase must be below the baseline to prevent the dissolution of the sample mixtures. Upon meeting the spots, it will carry up the components of each spot up the plate, separating them out depending on their affinity for the mobile and stationary phase. When the mobile phase has nearly reached the top, the plate is removed to prevent inaccurate results (Dean *et al*. 2002c). The point where the mobile phase reached is then immediately marked and referred to as the solvent front. This is done to allow an accurate calculation of the retention factor value (Rf) of each spot on the plate (Dean *et al*. 2002c) . Rf value is calculated as:

$$Rf = \frac{\text{Distance travelled by compound}}{\text{Distance from baseline to solvent front}}$$

The characteristics of TLC and column chromatography are very similar. TLC can be described as an upside-down version of column chromatography. As a result, TLC is often used to correctly identify the most suitable mobile phase in order to carry out a subsequent column chromatography with good separation of materials (Dean *et al*. 2002c). This makes both TLC and column chromatography vital in the monitoring and purification of reaction mixtures in this study. Other forms of chromatography include, gas chromatography for the separation and analysis of non-decomposing vaporised substances and ion chromatography, which separates ions and polar materials (Gras et al. 2017; Chi et al. 2017).

2.0.4. Mass spectrometry

Mass spectrometry is an analytical technique that involves ionising a sample with a filament in order to generate ions. These secondary ions are then accelerated and magnetically deflected and detected by a mass analyser. These charged ions will be deflected depending on their mass/charge ratio. As the charge is a known constant, the mass can be determined based the amount of deflection these charged particles experience. The collision of primary ions or electrons on a compound would break bonds producing secondary ions. As a result every compound will produce their own unique fragmentation pattern which can be used to identify them. A mass spectrum may look chaotic at first, but certain patterns quickly become apparent to experienced users. For example, one way of elucidating the spectra of a hydrocarbon would be to look for two peaks that differ by 14. Peak differences of 14 are common in organic chemistry which are attributed to two fragments differing in the possession of a CH_2.

Mass spectrometry is often used in conjunction with other analytical techniques. Examples of such techniques includes gas chromatography-mass spectrometry (GC-MS) and inductively coupled plasma – mass spectrometry (ICP-MS). Standalone mass spectrometry, GC-MS and ICP-MS all require the sample to be under a high vacuum. The ambient surrounding air contains various gases that would add to the resulting mass spectrum as these would be ionised by the mass spectrometry filament. Secondly, the secondary ions generated by the samples ionisation may collide against background gas molecules. This might give rise to charge neutralisation reactions for example. Ultimately the presence of gas molecules may alter the true mass/charge ratio of secondary ions reducing the

sensitivity and accuracy of the analysis. For this reason, mass spectrometry is rarely carried out with ambient or high pressure analytical techniques such as liquid chromatography or HPLC.

2.1. Aims and objectives

The aim of this study is to design and fabricate a thermally labile chemical linker to enable gemcitabine conjugation onto the surface of hybrid iron oxide-gold nanoparticles based on the retro Diels-Alder reaction. The linker will be synthesised and then characterised using NMR Spectroscopy, FTIR Spectroscopy and TLC.

2.2. Materials and methods

2.2.1. Materials used

Material	Supplier
Maleimide	Lancaster Synthesis, UK
Furan	Alfa Aesar, UK
Benzoyl Chloride	Sigma-Aldrich Co., UK
Triethylamine	Fisher Scientific, UK
Boc Anhydride	Alfa Aesar, UK
Maleic Anhydride	Alfa Aesar, UK
Beta Alanine	Alfa Aesar, UK
Gamma amino butyric acid	Alfa Aesar, UK
Epsilon aminocaproic acid	Alfa Aesar, UK
Gemcitabine	Fluorochem, UK
N-hydroxysuccinimide	Alfa Aesar, UK
1-ethyl-3-(3-dimethylaminopropyl)-carbodiimide	Alfa Aesar, UK
Diisopropylethylamine	Sigma-Aldrich Co., UK
2-furanmethanethiol	Alfa Aesar, UK
Trifluoroacetic acid	Sigma-Aldrich Co., UK
N-Dicyclohexyl-carbodiimide	Acros Organics, UK
EDC HCl	Fluorochem, UK
Furfurylamine	Alfa Aesar, UK
Organic Solvents	Fisher Scientific, UK
Deuterated Solvents	Cambridge Isotope Laboratories., USA
Sodium Chloride	Fisher Scientific, UK
Magnesium Sulphate	Fisher Scientific, UK

Sodium Bicarbonate	Fisher Scientific, UK
Potassium Carbonate	Fisher Scientific, UK
Celite	Sigma-Aldrich Co., UK
1,4 Dioxane	Alfa Aesar
Anhydrous DMF	Sigma-Aldrich Co., UK
Anhydrous Acetonitrile	Fisher Scientific, UK
Silica Gel	Fisher Scientific, UK
Potassium Hydroxide	Fisher Scientific, UK

2.2.2. Methods

2.2.2.1. Diels alder synthesis of 3, 6 – Endo/exo-tetrahydropthalide

The synthesis of 3, 6 – Endo/exo-tetrahydropthalide is described in Figure 55. Maleimide (1 g, 10.3 mmol) was dissolved in diethyl ether (15 mL) and stirred at room temperature within a sealed tube. Furan (1.05 g, 15.5 mmol) was added and the sealed tube was sealed shut. The mixture was stirred at 95 °C for 12 h before being allowed to cool in an ice bath. The formed precipitate was filtered, rinsed with cold diethyl ether three times (20 mL × 3) and dried under suction yielding 3,6 – endo/exo-tetrahydropthalide as a white powder (0.154 g, 9 % yield) (Zhu *et al*. 2006).
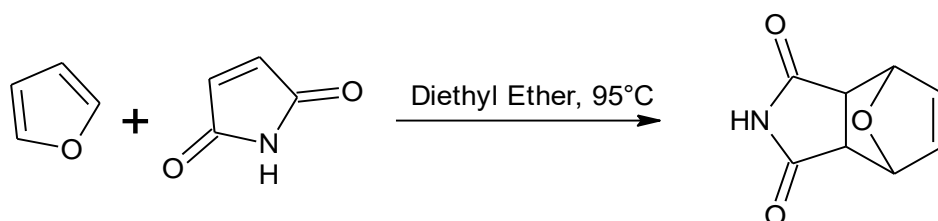
Figure 55: Reaction scheme for the Diels Alder Synthesis of 3, 6 – Endo/exo-tetrahydropthalide.

2.2.2.2. Synthesis of S-(Furan-2-ylmethyl) benzothioate

The synthesis of S-(Furan-2-ylmethyl) benzothioate is described in Figure 56. Benzoyl chloride (7.03 g, 50 mmol) was dissolved in toluene (125 mL). The mixture was stirred while 2-furanmethane thiol (5.71 g, 50 mmol) was added. The mixture was cooled to 0 °C and triethylamine (6.33 g) was added dropwise over 1 h before the mixture was allowed to stir for a further 1 h. The resultant slurry was filtered and the filtrate was diluted with toluene. This mixture was then washed with distilled water and dried with magnesium sulphate before being filtered.

The filtrate was then evaporated with the use of a rotary evaporator leaving a dark brown oil as the product (2.953 g, 36 % yield) (Uno *et al*. 2012).
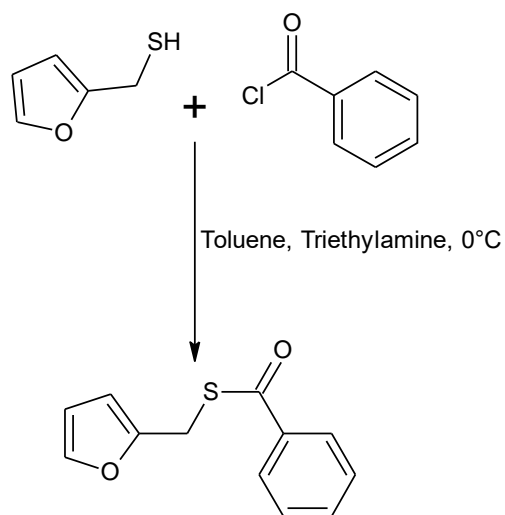
Figure 56: Reaction Scheme for the synthesis of S-(Furan-2-ylmethyl) benzothioate.

2.2.2.3. Synthesis of S-[(3,5-dioxo-10-oxa-4-azatricyclodec-8-en-1-yl)methyl] benzenecarbothionate

The synthesis of S-[(3,5-dioxo-10-oxa-4-azatricyclodec-8-en-1-yl)methyl] benzenecarbothionate is described in Figure 57. Maleimide (0.245 g, 2.5 mmol) and S-(Furan-2-ylmethyl) benzothioate (0.546 g, 2.5 mmol) was dissolved in diethyl ether (10 mL) in a sealed tube at room temperature. The mixture was heated to 95 °C and left to stir for 12 hours. The mixture filtered then washed with cold diethyl ether (20 mL × 3) and the solid product was left to dry under suction within a fume hood producing a light brown powder (0.12 g, 29 % yield).
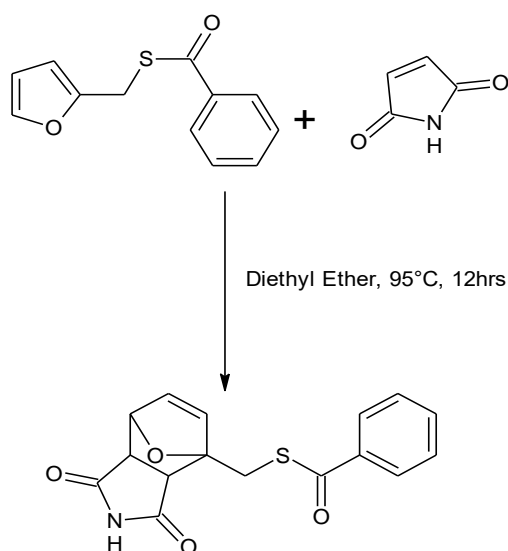
Figure 57: Reaction scheme for the synthesis of S-[(3,5-dioxo-10-oxa-4-azatricyclodec-8-en-1-yl)methyl] benzenecarbothionate.

73

2.2.2.4. Synthesis of 3-maleimidopropanoic acid

The synthesis of 3-maleimidopropanoic acid is described in Figure 58. Maleic anhydride (0.98 g, 10 mmol) was dissolved in glacial acetic acid (20 mL) followed by β-alanine (0.89 g, 10 mmol). The mixture was vigorously stirred resulting in a slurry that was stirred for 8 h at room temperature under a nitrogen atmosphere. The white precipitate was collected by filtration and washed with water (20 mL × 2). The white solid was then dispersed in 20 mL of water and refluxed at 110 °C. Once a clear solution had formed after 15 mins, the mixture was further refluxed for an additional 30 mins. The solution was then left to cool to room temperature before most of the water was evaporated with the use of a rotary evaporator. A white precipitate formed which was washed with chilled water and filtered. The resultant white powder was then dried under high vacuum. 3-maleimidopropanoic acid was obtained as a white powder (1.51 g, 89 % yield) (Song *et al*. 2009a).
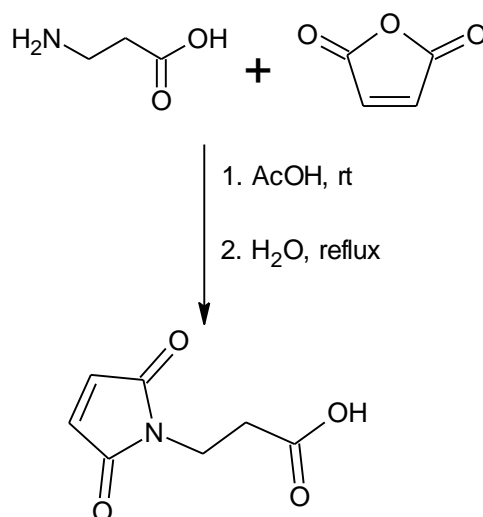
Figure 58: Reaction scheme for the synthesis of 3-maleimidopropanoic acid.

2.2.2.5. Synthesis of 4-maleimidobutyric acid

The synthesis of 4-maleimidobutyric acid is described in Figure 59. Maleic anhydride (0.98 g, 10 mmol) was dissolved in glacial acetic acid (20 mL) followed by γ-aminobutyric acid (1.03 g, 10 mmol). The mixture was vigorously stirred resulting in a slurry in fifteen minutes, which was stirred for a further 8 h at room temperature under a nitrogen atmosphere. The white precipitate was collected by filtration and washed with water (20 mL × 2). The white solid was then dispersed in 20 mL of water and refluxed at 110 °C. Once a clear solution had formed after 15 mins, the mixture was further refluxed for an additional 30 mins. The solution was then left to cool to room temperature before most of the water was evaporated with the use of a rotary evaporator. A white precipitate formed which was washed with chilled water and filtered. The resultant white powder was then dried under high vacuum. 4-maleimidobutyric acid was obtained as a white powder (1.72 g, 94 % yield) (Song *et al*. 2009a).
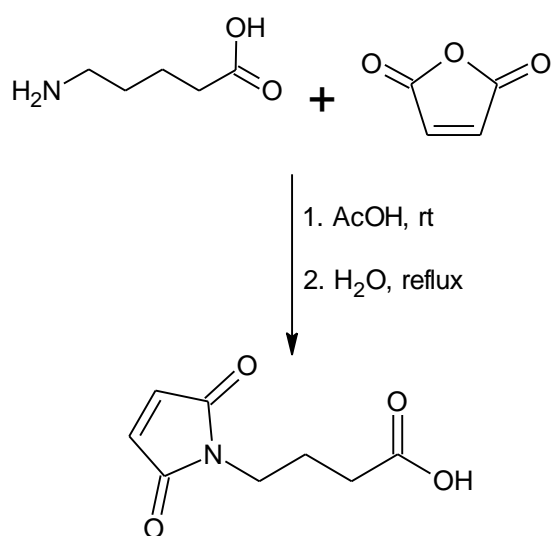
Figure 59: Reaction scheme for the synthesis of 4-maleimidobutyric acid.

2.2.2.6. Synthesis of 6-maleimidohexanoic acid

The synthesis of 6-maleimidohexanoic acid is described in Figure 60. Maleic anhydride (1.176 g, 12 mmol) was dissolved in glacial acetic acid (20 mL) followed by ε-aminocaproic acid (1.31 g, 10 mmol). A slurry formed within minutes and the mixture was left to stir for 6 h at 120 °C. The mixture was allowed to cool to room temperature and then poured into water (20 mL) before being extracted with ethyl acetate (40 mL × 3). The organic layers were washed with brine (15 mL) and dried with magnesium sulphate. The mixture was then filtered and the filtrate was evaporated under reduced pressure to give the crude product. The crude residue was purified into a white solid by column chromatography in 1:6 ethyl acetate/petroleum ether (v/v) (1.26 g, 60 % yield) (Han *et al*. 2013). Subsequent synthesis of this compound was carried out with the same procedure used for the synthesis of 3-maleimidopropanoic acid by (Song *et al*. 2009a) with improved yields.
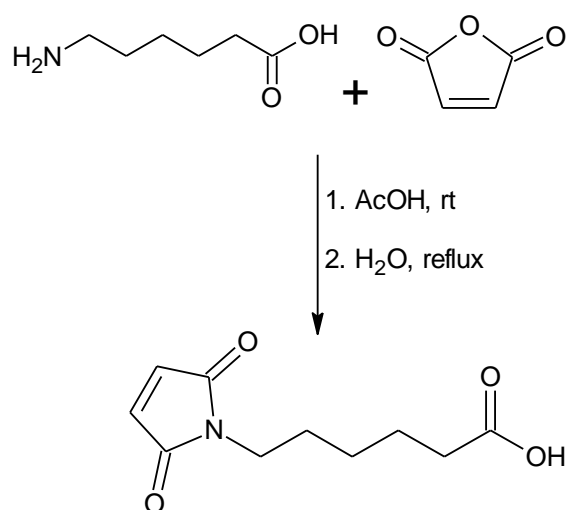
Figure 60: Reaction scheme for the synthesis of 6-maleimidohexanoic acid.

2.2.2.7. Synthesis of 3', 5'-O-Bis (tert-Butoxycarbonyl) gemcitabine

The synthesis of 3', 5'-O-Bis (tert-Butoxycarbonyl) gemcitabine is described in Figure 61. Boc Anhydride (4.36 g, 20 mmol) was dissolved in 1, 4 dioxane (40 mL) and added dropwise to a solution of gemcitabine hydrochloride (0.6 g, 2 mmol) in a stirred solution of 1M KOH (40 mL) over 10 minutes. The mixture was stirred for 40 minutes at room temperature while being closely monitored with TLC. After TLC confirmed a 50:50 ratio of the desired product and 3'-O-Bis (tert-Butoxycarbonyl) gemcitabine, the reaction mixture was extracted with ethyl acetate (80 mL × 3), washed with brine (20 mL × 2) and dried with magnesium sulphate. The mixture was then filtered to remove the magnesium sulphate and the filtrate was evaporated with the use of a rotary evaporator leaving a clear oily residue.

The oily residue was dissolved in 1,4 dioxane (40 mL) in a round bottom flask followed by the addition of boc anhydride (4.36 g, 20 mmol) and 1M KOH (40 mL). The mixture was stirred at room temperature and closely monitored with TLC. After 30 minutes of stirring, TLC analysis confirmed no more 3'-O-Bis(tert-Butoxycarbonyl)gemcitabine remained within the reaction vessel. The reaction mixture was extracted with ethyl acetate (80 mL × 3), washed with brine (20 mL × 2) and dried with magnesium sulphate. The mixture was then filtered to remove the magnesium sulphate and the filtrate was evaporated with the use of a rotary evaporator leaving a slightly yellow oily residue.

3',5'-O-Bis(tert-Butoxycarbonyl)gemcitabine was obtained as a white solid (0.326g, 63 %) after purification with column chromatography with 1:1 acetone/dichloromethane solvent system (Guo & Gallo 1999).
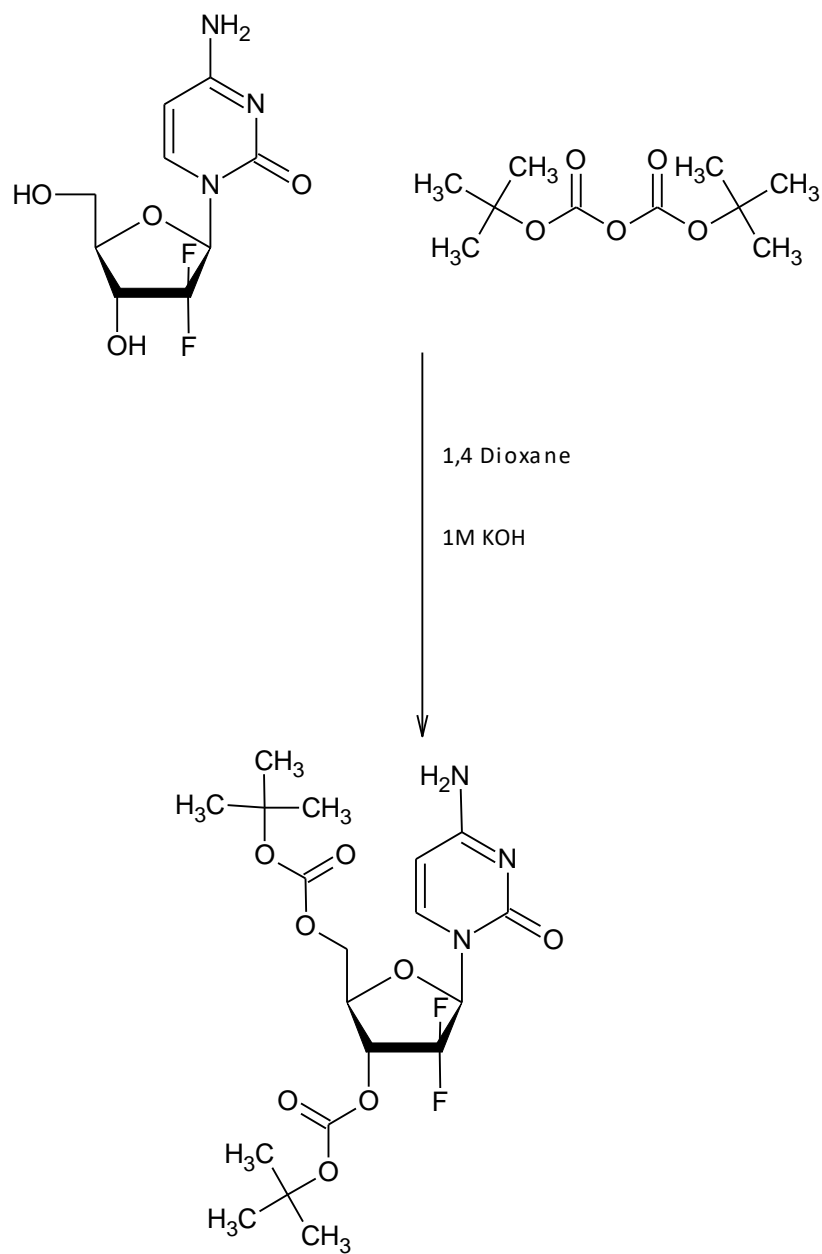
Figure 61: Reaction scheme for the synthesis of 3', 5'-O-Bis (tert-Butoxycarbonyl) gemcitabine.

2.2.2.8. Synthesis of 3-maleimido propionic acid N-hydroxysuccinimide ester

The synthesis of 3-maleimido propionic acid N-hydroxysuccinimide ester is described in Figure 62. B-alanine (2.32 g, 26 mmol) is dissolved in anhydrous DMF (35 mL) followed by the addition of maleic anhydride (2.9 g, 29 mmol). The mixture was stirred under nitrogen for 3 h at room temperature before being cooled to 0 °C for 30minutes. N-hydroxysuccinimide (3.7 g, 32 mmol) was added followed by 1-ethyl-3-(3-dimethylaminopropyl)-carbodiimide (11 g, 71 mmol). The mixture was stirred for 30 mins at 0 °C before the mixture was allowed to gently return to room temperature. The mixture was then left to stir overnight under nitrogen at room temperature.

The solvent was evaporated with the use of a rotary evaporator and the residue was dissolved in chloroform (300 mL) and washed with saturated sodium bicarbonate (100 mL). The organic layer was dried with magnesium sulphate and filtered. The filtrate was then evaporated yielding a crude brown powder.

3-maleimido propionic acid N hydroxysuccinimide ester was obtained as a white powder (3.5 g, 51 %) after purification with column chromatography 10:1 (chloroform: methanol) (Song *et al*. 2009b).
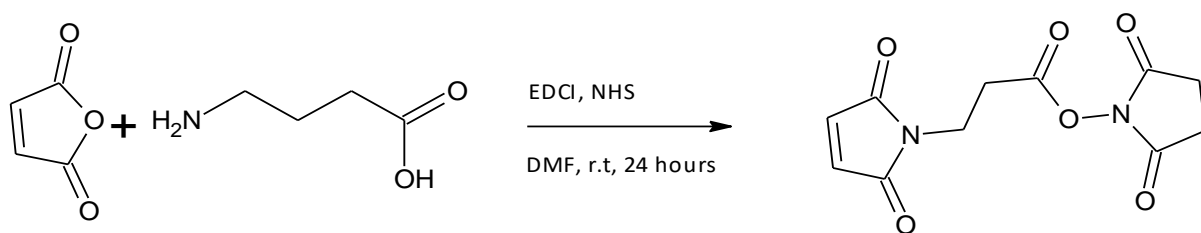
Figure 62: Reaction scheme for the synthesis of 3-maleimido propionic acid N-hydroxysuccinimide ester.

2.2.2.9. Synthesis of 4-maleimidobutyric acid N-hydroxysuccinimide ester

The synthesis of 4-maleimidobutyric acid N-hydroxysuccinimide ester is described in Figure 63. Maleic anhydride (2.9 g, 29 mmol) was dissolved in anhydrous DMF (35 mL) followed by the addition of 4-amino butyric acid (2.68 g, 26 mmol). The mixture was stirred under argon for 3 hours at room temperature before being cooled to 0 °C for 0.5 h. N-hydroxysuccinimide (3.7 g, 32 mmol) was added followed by 1-ethyl-3-(3-dimethylaminopropyl)-carbodiimide (11 g, 71 mmol). The mixture was allowed to stir for 0.5 h at 0 °C before the mixture was allowed to gently return to room temperature. The mixture was then left to stir overnight under argon at room temperature.

The solvent was evaporated with the use of a rotary evaporator and the residue was dissolved in chloroform (300 mL) and washed with saturated sodium bicarbonate (100 mL). The organic layer is dried with magnesium sulphate and filtered. The filtrate was then evaporated yielding a crude dark green film.

4-maleimido butyric acid N-hydroxysuccinimide ester was obtained as a white powder (4.8 g, 66 %) after the crude dark red product was purified with column chromatography 10:1 (chloroform: methanol) (Song *et al*. 2009b).
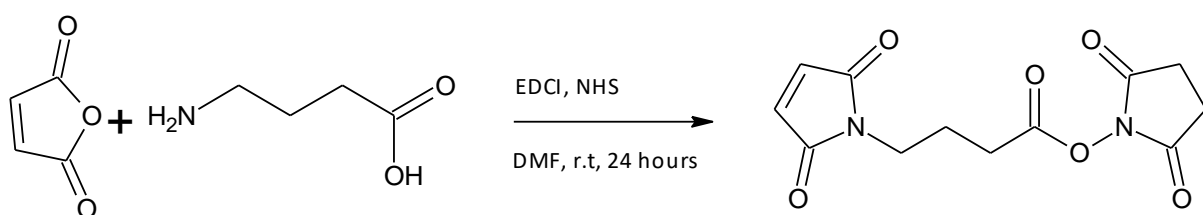
Figure 63: Synthesis of 4-maleimidobutyric acid N-hydroxysuccinimide ester.

2.2.2.10. Synthesis of 6-aminohexanoic acid N-hydroxysuccinimide ester

The synthesis of 6-aminohexanoic acid N-hydroxysuccinimide ester is described in Figure 64. Into a solution of 6-aminohexanoic acid (3.41 g, 26 mmol) in anhydrous DMF, was added maleic anhydride (2.9 g, 29 mmol). The mixture was stirred under argon for 3 hours at room temperature before being cooled to 0 °C for 0.5 h. N-hydroxysuccinimide (3.7 g, 32 mmol) was added followed by 1-ethyl-3-(3-dimethylaminopropyl)-carbodiimide (11 g, 71 mmol). The mixture was allowed to stir for 0.5 h at 0 °C before the mixture was allowed to gently return to room temperature. The mixture was then left to stir overnight under argon at room temperature.

The solvent was evaporated with the use of a rotary evaporator and the residue was dissolved in chloroform (300 mL) and washed with saturated sodium bicarbonate (100 mL). The organic layer was dried with magnesium sulphate and filtered. The filtrate was then evaporated yielding a crude dark yellow powder.

6-aminohexanoic acid N hydroxysuccinimide ester was obtained as a white powder (5.2 g, 65 %) after the crude red product was purified with column chromatography 10/1 (chloroform: methanol) (Song *et al*. 2009b).
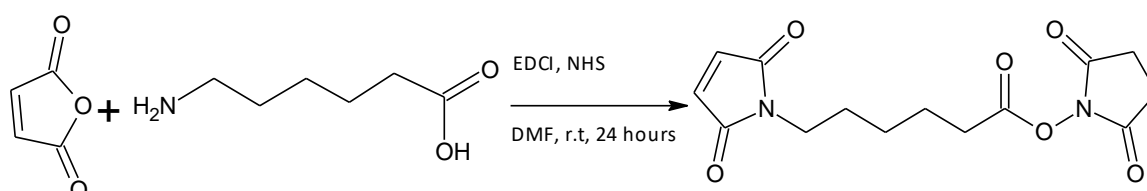
Figure 64: Reaction scheme for the synthesis of 6-aminohexanoic acid N-hydroxysuccinimide ester.

2.2.2.11. Amide coupling reaction of 3-maleimido propionic acid N-hydroxysuccinimide ester with 3′, 5′-O-Bis (tert-Butoxycarbonyl) gemcitabine

The amide coupling reaction between 3-maleimidopropanoic acid N-hydroxysuccinimide ester and 3′, 5′-O-Bis (tert-Butoxycarbonyl) gemcitabine is described in Figure 65. Into a round bottom flask, anhydrous DMF (20 mL) was added followed by 3-maleimidopropionic acid N hydroxysuccinimide ester (1.41 g, 53 mmol). 3′, 5′-O-Bis (tert-Butoxycarbonyl) gemcitabine (2.753 g, 53 mmol) was added followed by diisopropylethylamine (3.7 mL, 0.027 mmol). The reaction mixture was stirred at 40 °C for 24 h under argon. The solvent was evaporated with a rotary evaporator leaving a green residue. This compound is known as Boc-Gem-Mal.

Boc-Gem-Mal was obtained as a pale green powder (1.45 g, 44 %) after the crude dark green product was purified with column chromatography 10:1 (chloroform: methanol).
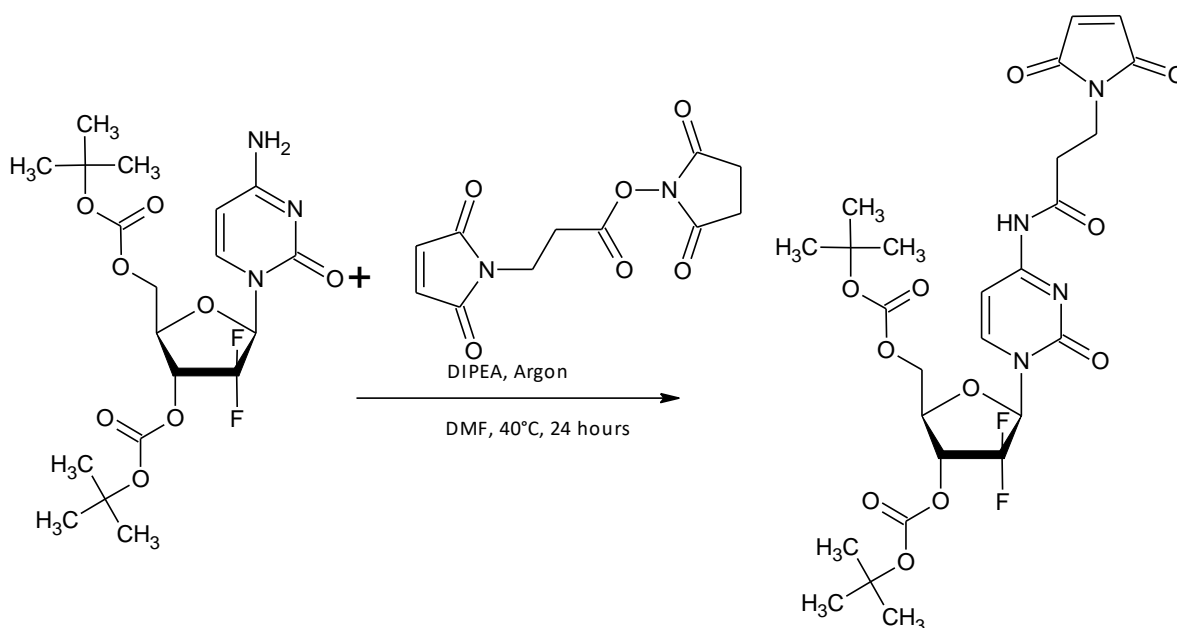
Figure 65: Chemical reaction between 3′, 5′-O-Bis (tert-Butoxycarbonyl) gemcitabine and 3-maleimido propionic acid N hydroxysuccinimide ester.

2.2.2.12. Synthesis of *O-tert*-butyl S-(furan-2-ylmethyl) carbonothionate

The boc protection of 2-furanmethane thiol is described in Figure 66. Into a round bottom flask, 2-furanmethane thiol (1 g, 8.8 mmol) and boc anhydride (1.8 g, 8.8 mmol) was dissolved in anhydrous acetonitrile (35 mL) followed by the addition of potassium carbonate (2.4 g, 17.5 mmol). The mixture was stirred at room temperature for 24 h under a nitrogen atmosphere.

The mixture was diluted with ethyl acetate (200 mL) and filtered through a celite path. The filtrate was washed with saturated sodium bicarbonate (40 mL), dried with magnesium sulphate and filtered. The resulting filtrate was evaporated leaving *O-tert*-butyl S-(furan-2-ylmethyl) carbonothionate as a brown oil (1.76 g, 93 %) (Temperini *et al*. 2010).
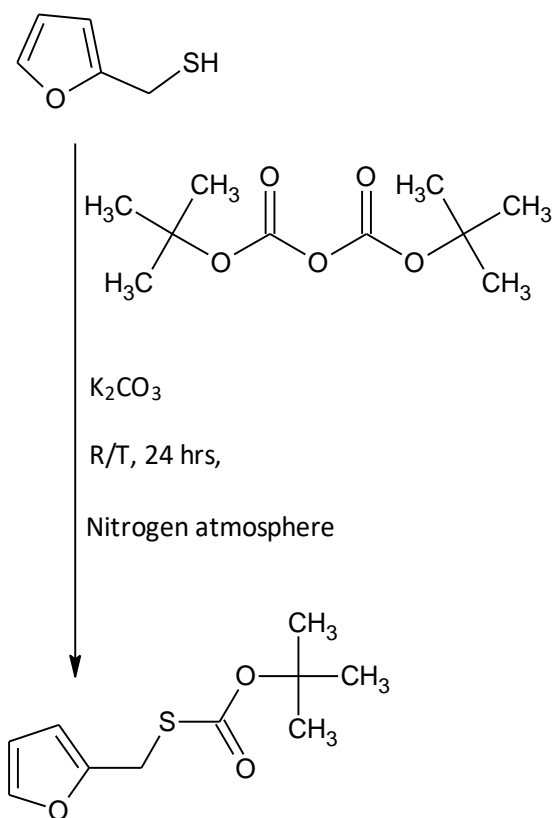
Figure 66: Reaction scheme for synthesis of *O-tert*-butyl S-(furan-2-ylmethy)carbonothionate.

2.2.2.13. Diels Alder reaction of *O-tert*-butyl S-(furan-2-ylmethyl)carbonothionate with 4-maleimidobutyric acid N-hydroxysuccinimide ester

The Diels Alder reaction of *O-tert*-butyl S-(furan-2-ylmethyl)carbonothionate and 4-maleimidobutyric acid N-hydroxysuccinimide ester is described in Figure 67. *O-tert*-butyl S-(furan-2-ylmethyl)carbonothionate (1.5 g, 9 mmol) was added into a sealed tube followed by diethyl ether (35 mL). 4-maleimido butyric acid N hydroxysuccinimide ester (2.4 g, 9 mmol) was added and the mixture was stirred at room temperature for 7 days under nitrogen. The Boc protected Diels Alder linker (BDA) was obtained as a brown greasy solid (2.14 g, 48.3 % yield) after purification with column chromatography (50/50) (petroleum ether: ethyl acetate).
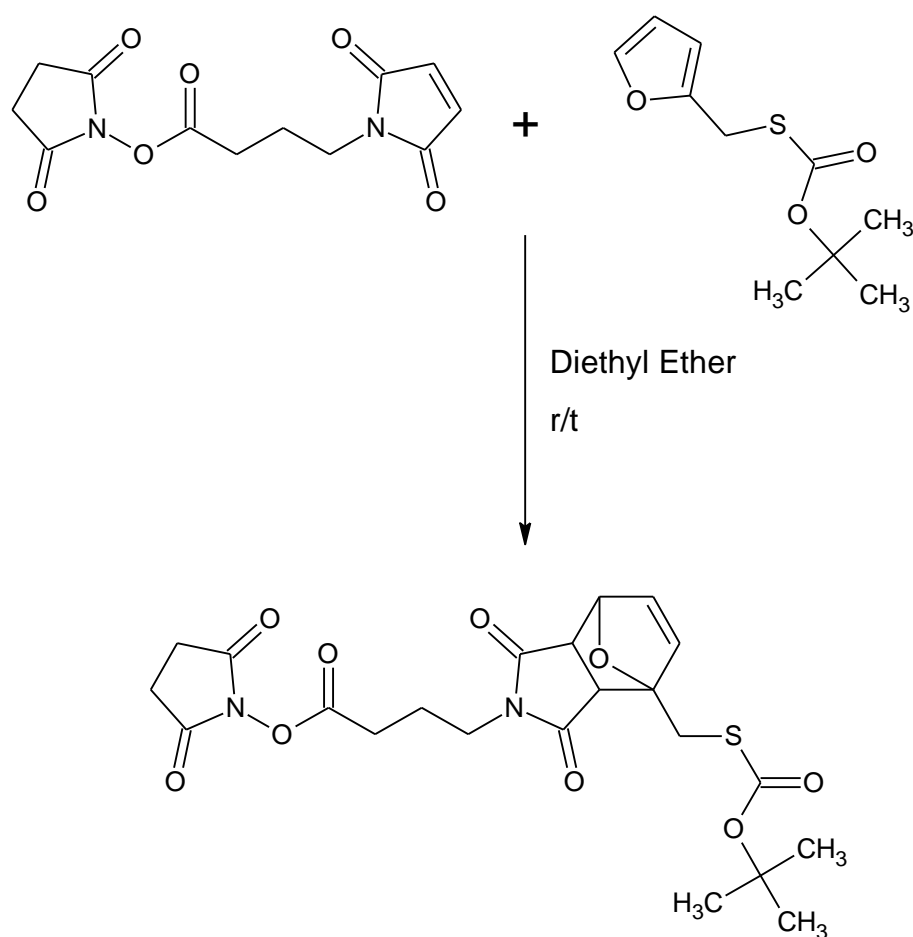
Figure 67: Diels Alder reaction between 4-maleimidobutyric acid N-hydroxysuccinimide ester and boc protected 2-furanmethane thiol.

2.2.2.14. Synthesis of boc protected Diels Alder/gemcitabine linker

The synthesis of a boc protected thiolated thermally labile drug (Boc-TTLD) is described in Figure 68. Into a round bottom flask, BDA (3.94 g, 8.2 mmol) was dissolved in dry dichloromethane (30 mL) and stirred. 3', 5'-O-Bis (tert-Butoxycarbonyl) gemcitabine (3.82 g, 8.2 mmol) was added followed by diisopropylethylamine (5.82 mL, 41 mmol). The reaction mixture was stirred at 0 °C for 108 h under an argon atmosphere. The solvent was removed under reduced pressure leaving a dark orange residue. Boc-TTLD was obtained as a pale green powder (4.31 g, 62 % yield) after purification with column chromatography 10:1 (chloroform: methanol).
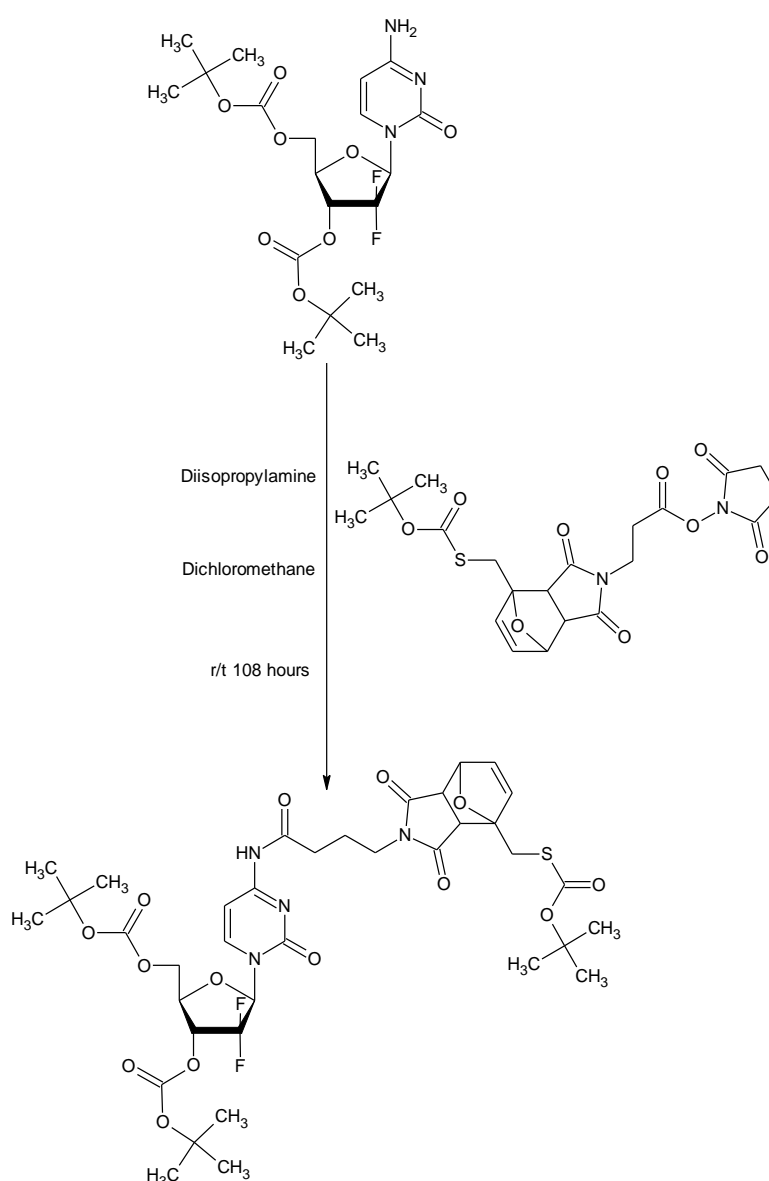
Figure 68: Reaction between 3', 5'-O-Bis (tert-Butoxycarbonyl) gemcitabine and BDA to produce Boc-TTLD.

2.2.2.15. Deprotection of Boc-TTLD

The removal of boc groups from Boc-TTLD is described in Figure 69. Into a round bottom flask, the previously synthesised Boc-TTLD (4.31 g, 5.1 mmol) was dissolved in a 185 mL solution of 15 % trifluoroacetic acid in dichloromethane (v/v) and stirred at 0 °C for 2 h. The volatile solvents were removed under reduced pressure leaving a dark red residue. Purification with column chromatography (1:1 acetone, dichloromethane) yielded a pale orange powder (1.3 g, 47 % yield). This thiolated thermally labile drug compound will be referred to as TTLD.
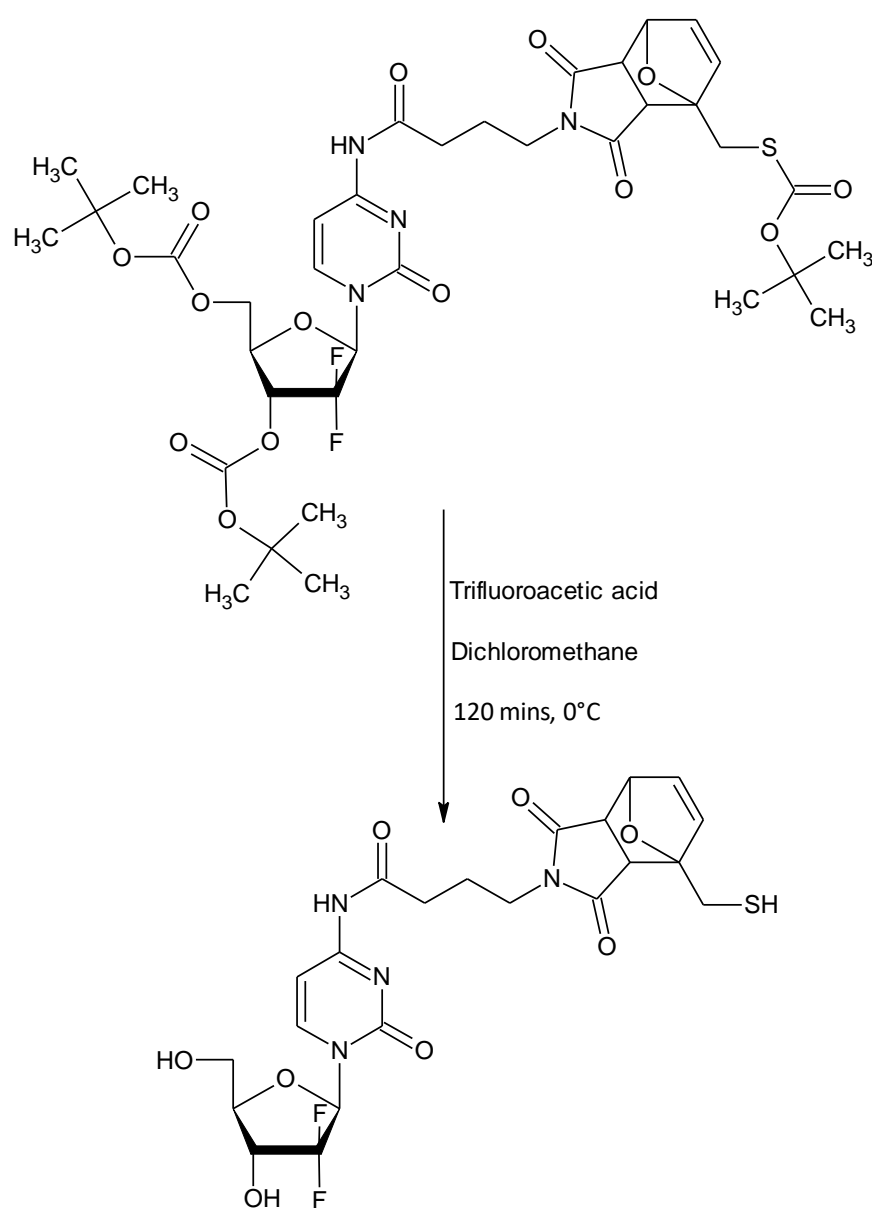
Figure 69: Reaction scheme for the TFA deprotection of Boc-TTLD to produce TTLD.

2.2.3. Characterisation of synthesised compounds

2.2.3.1 Nuclear magnetic resonance spectroscopy procedure

^{1}H NMR was carried out throughout all reactions from start to completion to monitor the consumption of starting materials and emergence of products. The samples were dissolved in appropriate deuterated 0.5 mL solvent solutions and analysed at 25 °C using 16 scans with a Bruker Avance 300 MHz NMR Spectrometer or a Bruker Avance III HD 400 MHz NMR Spectrometer (Bruker, Germany).

2.2.3.2 Fourier infrared spectroscopy procedure

FTIR analysis of purified reaction products was carried out using a Thermo Scientific Nicolet™ iS™ 5 FTIR fitted with an attenuated total reflectance adapter (Thermofisher, UK). A background correction scan was carried out to subtract data from the surrounding air. Following this a 10 mg solid sample of the compound was placed onto a diamond crystal tip and analysed with 16 scans to collect transmittance data.

2.2.3.3 Thin layer chromatography procedure

The individual starting materials and reaction mixture were analysed with thin layer chromatography by spotting a sample on a silica gel coated sheet of aluminium as shown in Figure 70. These TLC plates were then placed in a shallow pool of an eluent solution to observe the separation of materials within the reaction mixture.
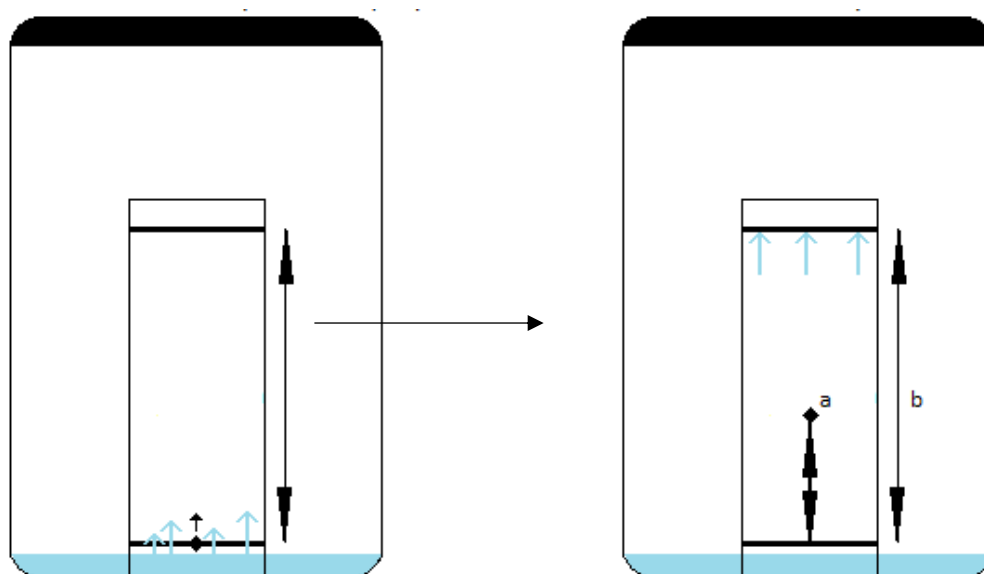
Figure 70: Illustration of TLC procedure.

The Rf value was calculated as the distance travelled by the unknown substance (a) divided by the distance travelled by the solvent through the TLC plate (b). Data acquired with this method was used to decide the best solvent system for column chromatography.

2.2.3.4 Mass spectrometry procedure

Mass spectrometry of the final thiolated thermally labile drug molecule (TTLD) dissolved in dichloromethane was carried out at Swansea University with a Xevo G2-XS Time of Flight Mass Spectrometer.

2.2.3.5 Retro Diels Alder breakdown of the thermally labile linker at elevated temperatures

The rate of the retro Diels Alder at elevated temperatures is directly related to the rate of drug release from the HNP surface. Therefore, the ability for the linker to reverse must be tested before attachment to the HNP occurs. This was carried out by heating the previously synthesised linker in several solutions of deuterated acetone in a round bottom flask at various temperatures. A 2 mL sample of the reaction mixture was added to a NMR tube, sealed with parafilm and cooled down by immersion into ice cold water for 5 min. The samples were then analysed with proton NMR spectroscopy.

Aliquot samples were analysed at the 0, 5, 10, 15, 30, 60, 120 and 180 min mark and multiple round bottom flasks of the reaction mixture were heated to 37 °C, 45 °C and 70 °C in batches of threes.

2.3. Results

2.3.1. Analytical data of 3, 6 – Endo/exo-tetrahydropthalide

2.3.1.1 ^{1}H NMR spectrum of 3, 6 – Endo/exo-tetrahydropthalide

The NMR spectrum in Figure 72 for 3, 6 – Endo/exo-tetrahydropthalide in Figure 71 showed the following peaks: 7.97 (broad singlet, [7] 1H), 6.54 (doublet, J=0.8Hz, [4, 5] 2H), 5.34 (doublet, J=0.9Hz, [3, 6] 2H), 2.92 (singlet, [1-2] 2H). The proton NMR spectrum of 3, 6 – Endo/exo-tetrahydropthalide has a peak at δ6.54 for the two protons across the double bond of the cycloadduct. The two protons closest to the bridge oxygen has been shifted up field to δ5.34. The peak at δ2.92 arises from the two protons opposite the double bond of the cycloadduct. A small broad peak can also be observed at δ7.97 belonging to the proton of the amide.
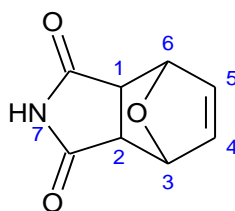
Figure 71: Chemical structure of 3, 6 – Endo/exo-tetrahydropthalide.
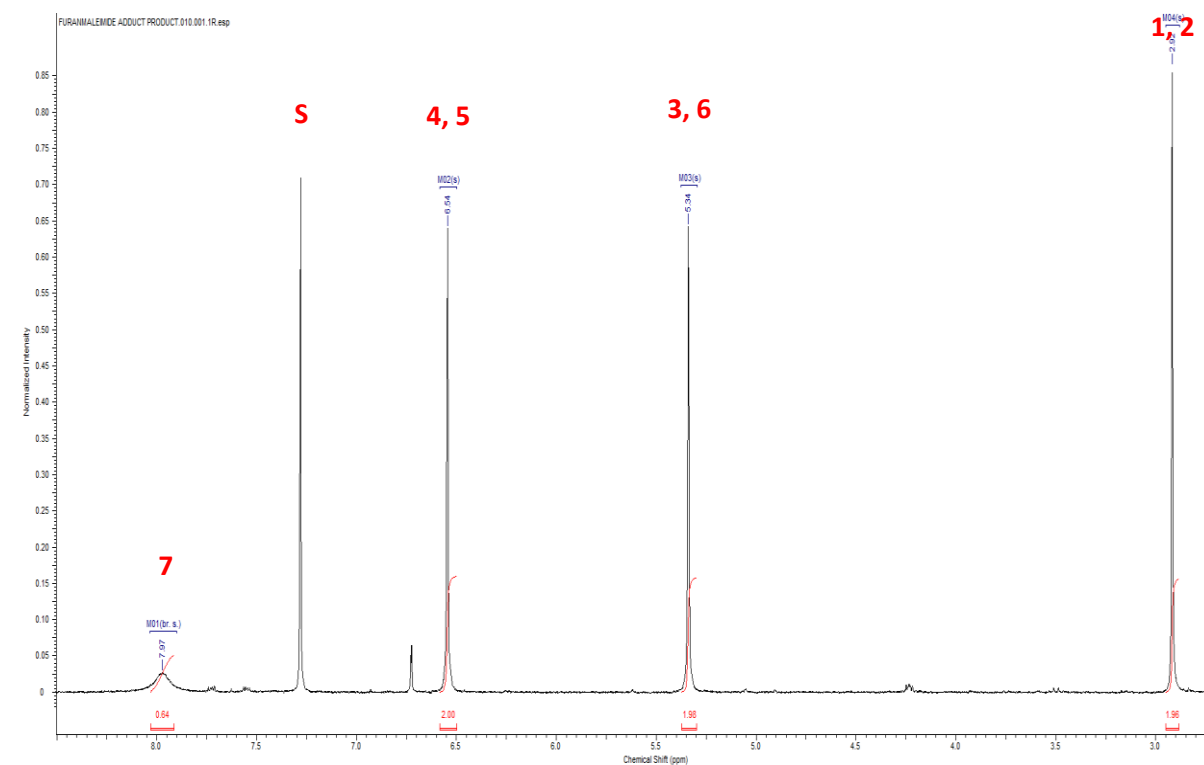
Figure 72: ^{1}H NMR spectrum of 3, 6 – Endo/exo-tetrahydropthalide in CDCl$_3$ carried out using 300MHz NMR at 25 °C.

2.3.2. Analytical data of S-(Furan-2-ylmethyl) benzothioate

2.3.2.1 ^{1}H NMR spectrum of S-(Furan-2-ylmethyl) benzothioate

The NMR spectrum in Figure 74 for 3, 6 – Endo/exo-tetrahydropthalide in Figure 73 showed the following peaks: 7.98 (multiplet, [1, 5], 2H), 7.59 multiplet, [3], 1H), 7.46 (multiplet, [2, 4], 2H), 7.37 (multiplet, [8], 1H), 6.33 (multiplet, [6, 7], 2H), 4.38 (singlet, [9], 2H). The peaks between δ7.4-8.0 are from the aromatic peaks of the benzoyl protecting groups. Another peak at δ6.33 can be observed, belonging to the two protons of carbon 2,3 of the furan. The peak at δ7.37 is also from the furan, shifted up field due to its proximity to oxygen. The CH_2 protons next to the sulphur have a peak at δ4.38.
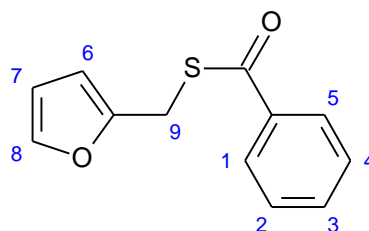
Figure 73: Reaction Scheme for the synthesis of S-(Furan-2-ylmethyl) benzothioate.
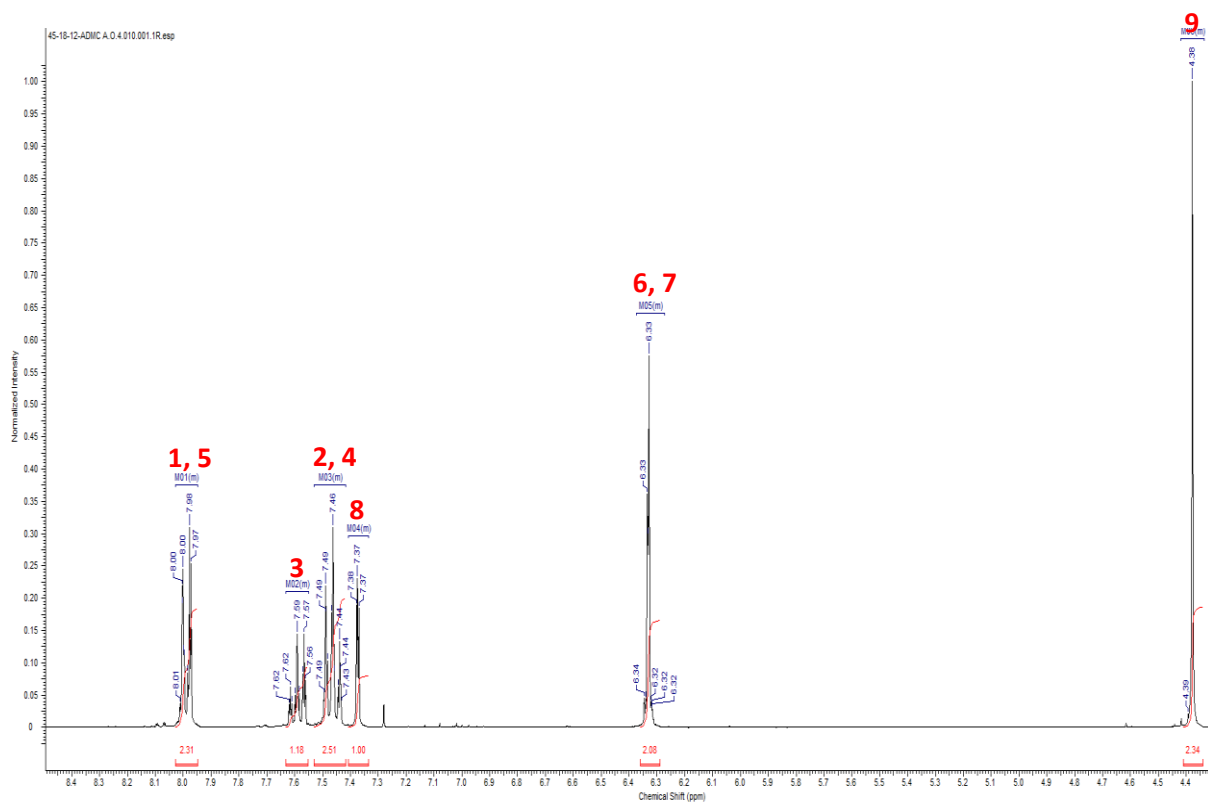
Figure 74: ^{1}H NMR spectrum of S-(Furan-2-ylmethyl) benzothioate in CDCl$_3$ carried out using 300MHz NMR at 25 °C.

2.3.3. Analytical data of ¹H NMR spectrum of S-[(3,5-dioxo-10-oxa-4-azatricyclodec-8-en-1-yl)methyl] benzenecarbothionate

2.3.3.1. ¹H NMR spectrum of S-[(3,5-dioxo-10-oxa-4-azatricyclodec-8-en-1-yl)methyl] benzenecarbothionate

The NMR spectrum in Figure 76 for S-[(3,5-dioxo-10-oxa-4-azatricyclodec-8-en-1-yl)methyl] benzenecarbothionate in Figure 75 showed the following peaks: 8.02 (multiplet, [7,11], 2H), 7.89 (broad singlet, [1], 1H), 7.62 (multiplet, [9], 1H), 7.49, (multiplet, [8,10], 2H), 6.52 (d-doublet, J=5.6Hz [5 endo/exo], 1H), 6.37 (doublet, J=5.7Hz, [4 endo/exo], 1H), 5.3 (doublet, J=1.7z , [3], 1H), 4.02 (doublet, J=14.7Hz [2-endo], 1H), 3.71 (doublet, J=14.7Hz [6-endo], 1H), 3.09 (doublet, J=14.7Hz [2-exo], 1H), 3.04 (doublet, J=14.7Hz [6-exo], 1H). The aromatic peaks of the benzoyl group δ8.02-7.5 are still present indicating that the sulphur remained protected throughout the cycloaddition. A mixture of the endo and exo isomer formed. The protons opposite the oxygen bridge produced greatly overlapping split peaks at δ6.55/δ6.37 for the endo signals and δ6.52/δ6.36 for the exo isomer. Another pair of highly overlapped peaks at δ5.3 for the proton signal closest to the bridge oxygen, is also indicative of a successful Diels Alder reaction. Evidence of an endo/exo mixture is further observed at δ4.02/δ3.71 which are the endo peaks for the protons opposite the cycloadduct double bond. The exo peaks are at δ3.09 and δ3.04. There is no peak for the CH₂ next to the sulphur. This may be due to the lack of nearby protons to resonate with. The broad peak at δ7.89 is for the secondary amine.
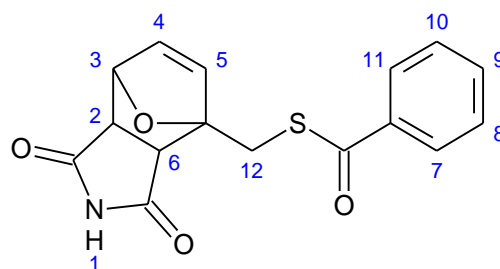
Figure 75: Reaction Scheme depicting the Diels Alder reaction between S-(Furan-2-ylmethyl) benzothioate and Maleimide to produce S-[(3,5-dioxo-10-oxa-4-azatricyclodec-8-en-1-yl)methyl] benzenecarbothionate.
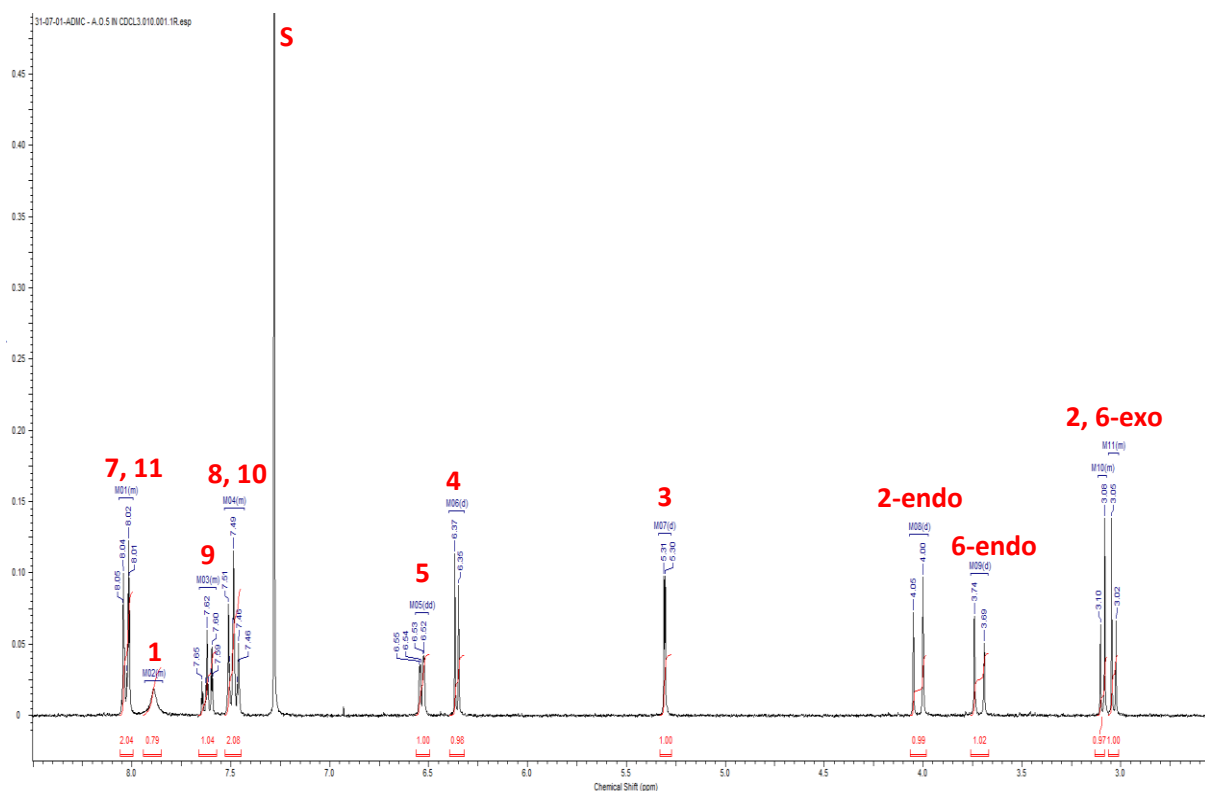
Figure 76: ^{1}H NMR spectrum of S-[(3,5-dioxo-10-oxa-4-azatricyclodec-8-en-1-yl)methyl] benzenecarbothionate in CDCl$_3$ carried out using 300MHz NMR at 25 °C.

2.3.3.2 FTIR of S-[(3,5-dioxo-10-oxa-4-azatricyclodec-8-en-1-yl)methyl] benzenecarbothionate

FTIR analysis of S-[(3,5-dioxo-10-oxa-4-azatricyclodec-8-en-1-yl)methyl] benzenecarbothionate shown in Figure 77, was carried out in order to identify functional groups indicative of a successful Diels Alder reaction between a benzoyl protected furan and maleimide. The peaks of note are displayed in Table 1. The aromatic stretches at 3000 cm^{-1} (C-H) and 1450 cm^{-1} (C=C) indicate that the benzoyl group is still present on the cycloadduct. The secondary amine stretch at 3100 cm^{-1} is also present, indicating a successful Diels Alder reaction.
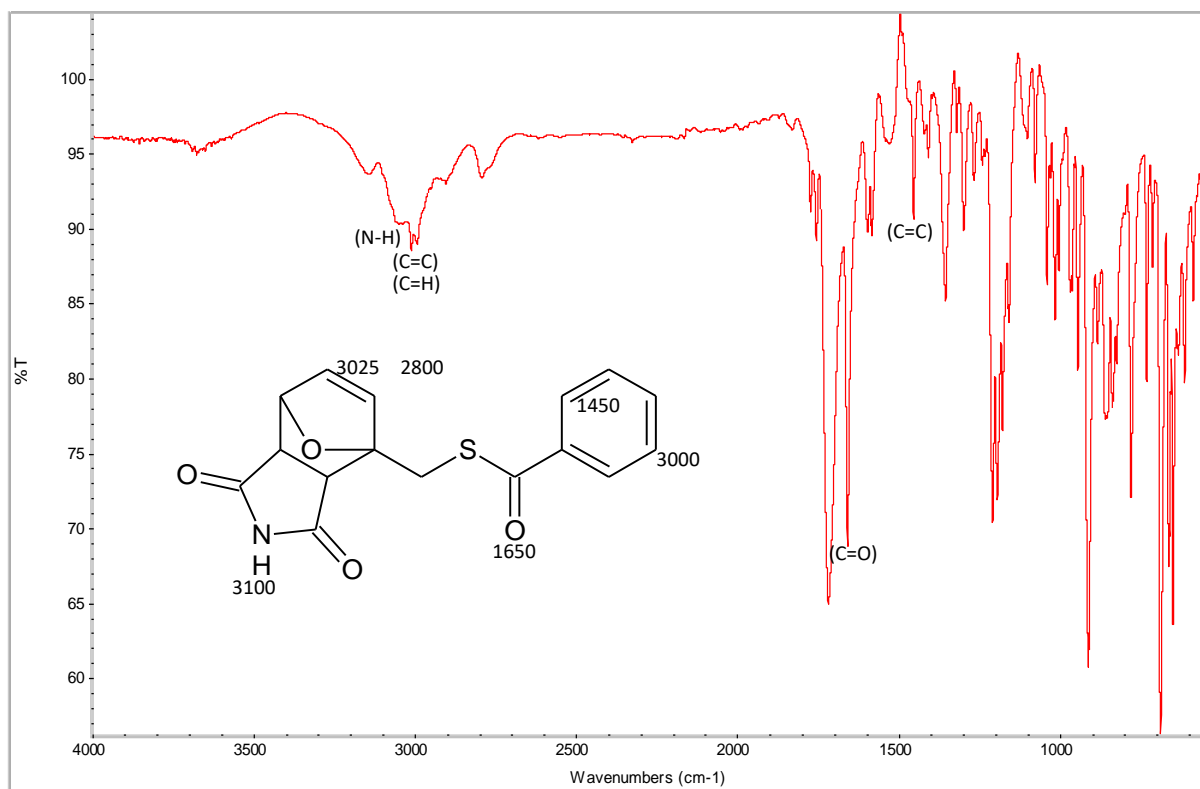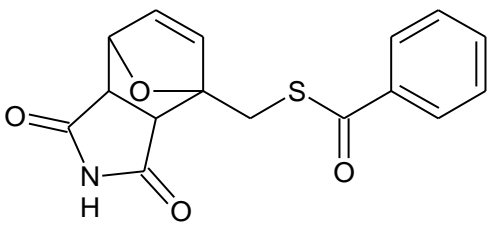
Figure 77: FTIR (16scans) of S-[(3,5-dioxo-10-oxa-4-azatricyclodec-8-en-1-yl)methyl] benzenecarbothionate.

Table 1: FTIR peak absorbance assignments for -[(3,5-dioxo-10-oxa-4-azatricyclodec-8-en-1-yl)methyl] benzenecarbothionate.

Compound (3)		Wavenumber (cm^{-1})	Bond Type	Assignment
		1450	Aromatic stretch	(C=C)
		1650	Conjugated Ketone	(C=O)
		2800	Alkyl stretch	(C-H)
		3000	Aromatic stretch	(C-H)
		3025	Alkene stretch	(C=C)
		3100	Secondary amine stretch	(N-H)

2.3.3.3. TLC analysis of S-[(3,5-dioxo-10-oxa-4-azatricyclodec-8-en-1-yl)methyl] benzenecarbothionate

TLC analysis of the S-[(3,5-dioxo-10-oxa-4-azatricyclodec-8-en-1-yl)methyl] benzenecarbothionate mixture post workup was carried out to clarify its purity. An

illustration of the TLC plate is displayed in Figure 78. The Rf value of this compound is 0.36 in a Petroleum Ether – Ethyl Acetate (1:1) solvent system.
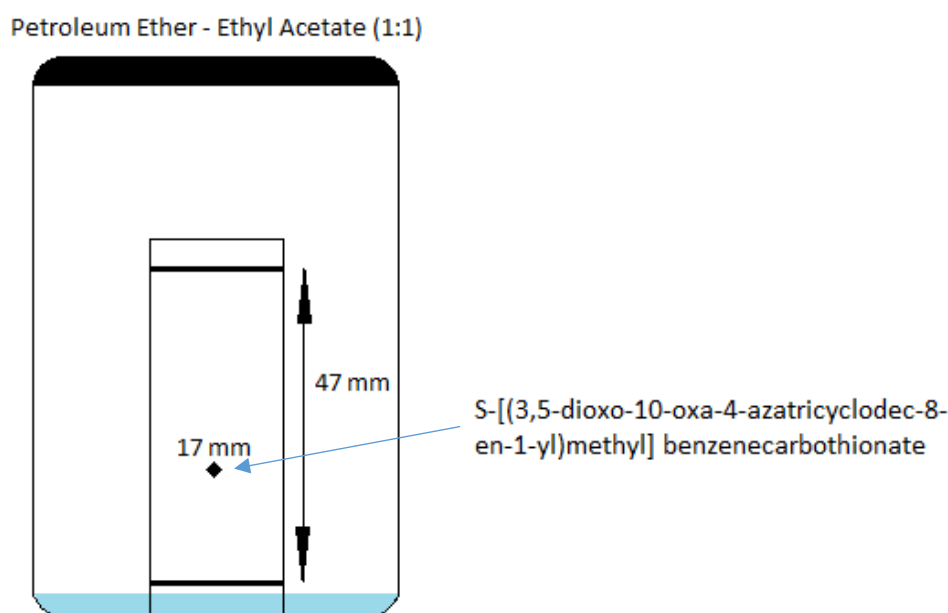
Figure 78: TLC plate of S-[(3,5-dioxo-10-oxa-4-azatricyclodec-8-en-1-yl)methyl] benzenecarbothionate post workup.

2.3.4. Analytical data of 3-maleimidopropanoic acid

2.3.4.1. ^{1}H NMR spectrum of 3-maleimidopropanoic acid

The NMR spectrum in Figure 80 for 3, 6 – Endo/exo-tetrahydropthalide in Figure 79 showed the following peaks: 7.69 (broad singlet, [1], 1H), 6.02 (singlet, [4, 5] 2H), 2.99 (triplet, J=6.8Hz [3], 2H), 2.56 (triplet, J=6.8Hz [2], 2H). The NMR spectrum of 3-maleimidopropanoic acid contained two triplets for the CH_2 of the alkyl chain, with one up field due to its proximity to the acid group. These are found at δ2.56 and δ2.99. The tall peak at δ6.02 is attributed to the two protons of the maleimide. There is a broad singlet at δ3.35 which indicative of a trace water contamination.
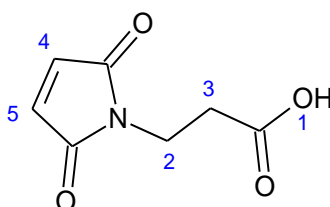
Figure 79: Reaction scheme for the synthesis of 3-maleimidopropanoic acid
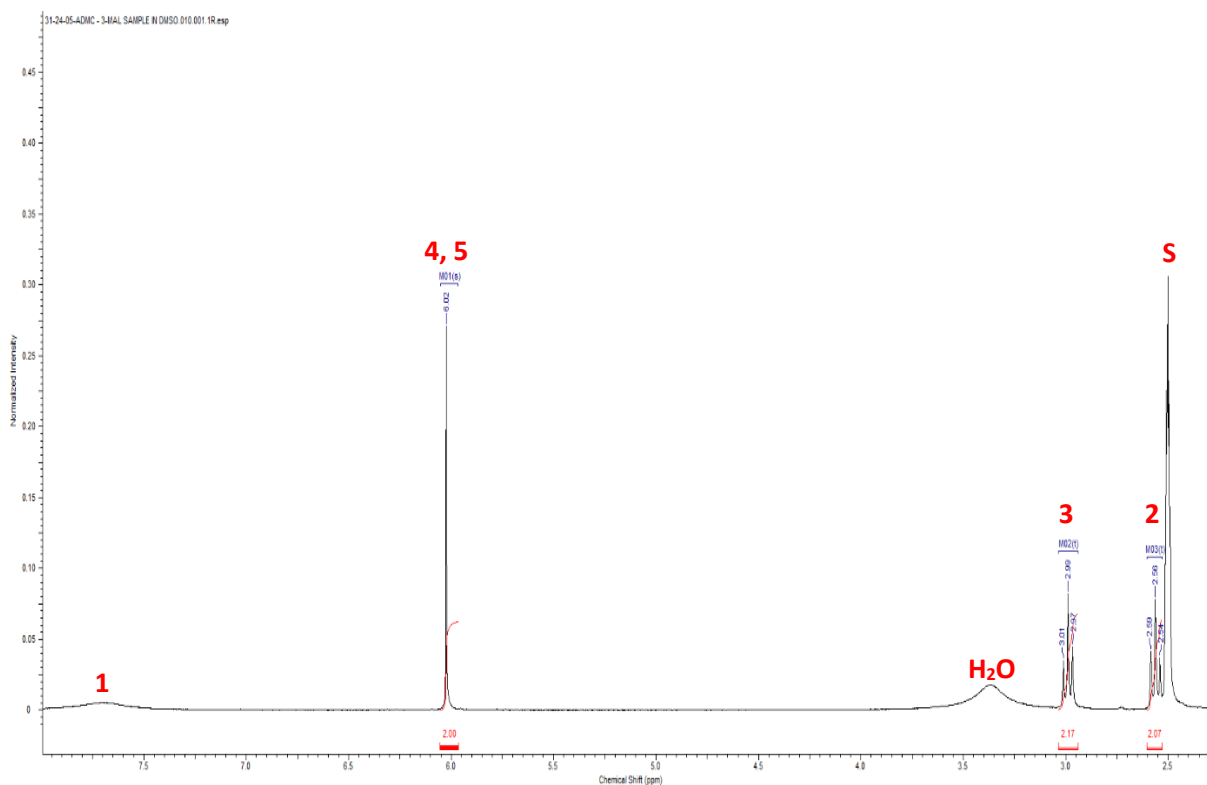
Figure 80: ^{1}H NMR spectrum of 3-maleimidopropanoic acid in DMSO_d carried out using 300MHz NMR at 25 °C.

2.3.4.2 FTIR of 3-maleimidopropanoic acid

FTIR analysis of 3-maleimidopropanoic acid was carried out to identify peaks indicative of a successful synthesis reaction. The peaks of note are displayed in Table 2. The peaks at 3250 cm^{-1} (O-H) and 1690 cm^{-1} (C=O) in Figure 81 are attributed to the carboxylic acid group of 3-maleimidopropanoic acid. There are also two peaks for the alkyl CH$_2$ absorbance at 2980 cm^{-1} and 2940 cm^{-1} (C-H).
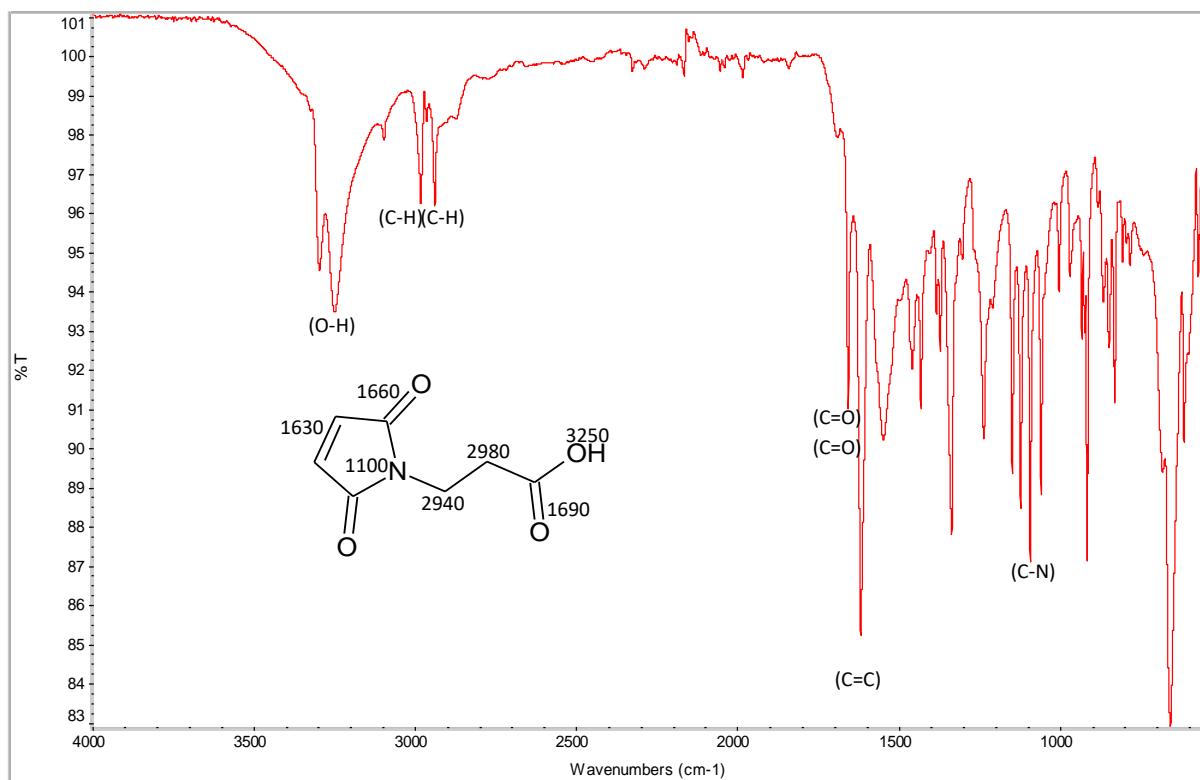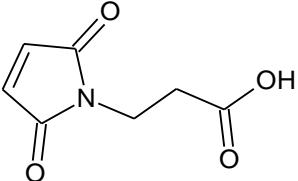
Figure 81: FTIR of 3-maleimidopropanoic acid.

Table 2: FTIR peak absorbance assignments for 3-maleimidopropanoic acid.

3-maleimidopropanoic acid	Wavenumber (cm^{-1})	Bond Type	Assignment
	1100	Tertiary amine	(C-N)
	1630	Alkene stretch	(C=C)
	1660	Tertiary amide stretch	(C=O)
	1690	Carboxylic acid stretch	(C=O)
	2940	Alkyl stretch	(C-H)
	2980	Alkyl stretch	(C-H)
	3250	Carboxylic acid	(O-H)

2.3.4.3. TLC analysis of 3-maleimidopropanoic acid

TLC analysis of the 3-maleimidopropanoic acid mixture post workup was carried out to clarify its purity. An illustration of the TLC plate is displayed in Figure 82. The Rf value of this compound is 0.41 in a Petroleum Ether – Ethyl Acetate (1:6) solvent system. A single spot eliminated the need for further purification.

Petroleum Ether - Ethyl Acetate (1:6)

63 mm

26 mm

3-maleimidopropanoic acid
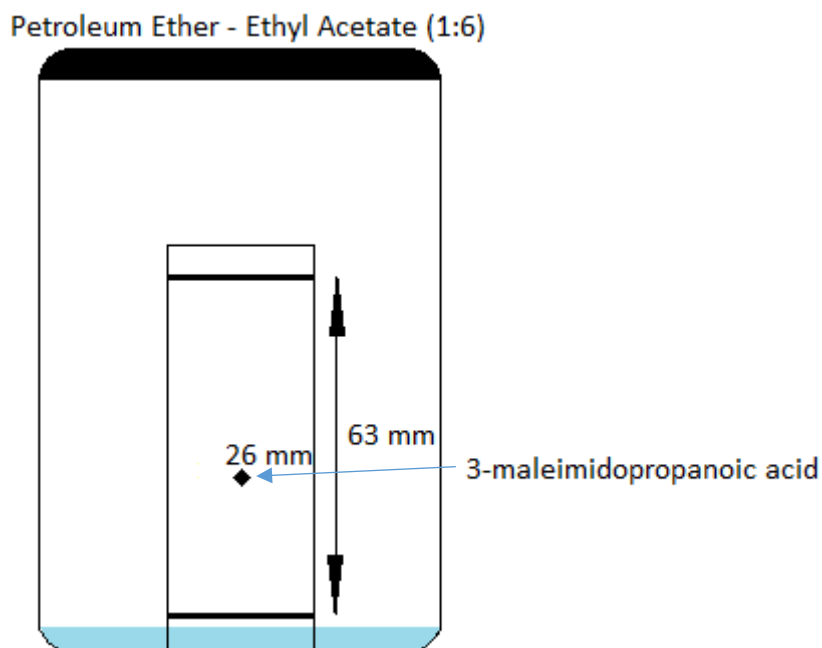
Figure 82: TLC plate of 3-maleimidopropanoic acid post workup.

2.3.5. Analytical data of 4-maleimidobutyric acid

2.3.5.1 ^{1}H NMR spectrum of 4-maleimidobutyric acid

The NMR spectrum in Figure 84 for 4-maleimidobutyric acid in Figure 83 showed the following peaks: 6.03 (singlet, [5, 6] 2H), 2.81 (triplet, [4], 2H), 2.33 (triplet, J=7.3Hz [3], 2H), 1.74 (quintet, J=7.4Hz [2], 2H). The NMR spectrum of 4-maleimidobutyric acid contains a two triplets at δ2.81 and δ2.33 for the terminal CH_2 of the alkyl chain and a quintet at δ1.74 for the central CH_2 of the alkyl chain. The tall singlet at δ6.03 is indicative of the maleimide protons. There are two trace solvent contaminants which are water and acetone, indicated by their peaks at δ3.35 and δ2.1 respectively.
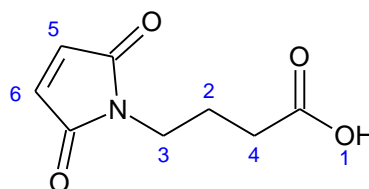
Figure 83: Reaction scheme for the synthesis of 4-maleimidobutyric acid.

97
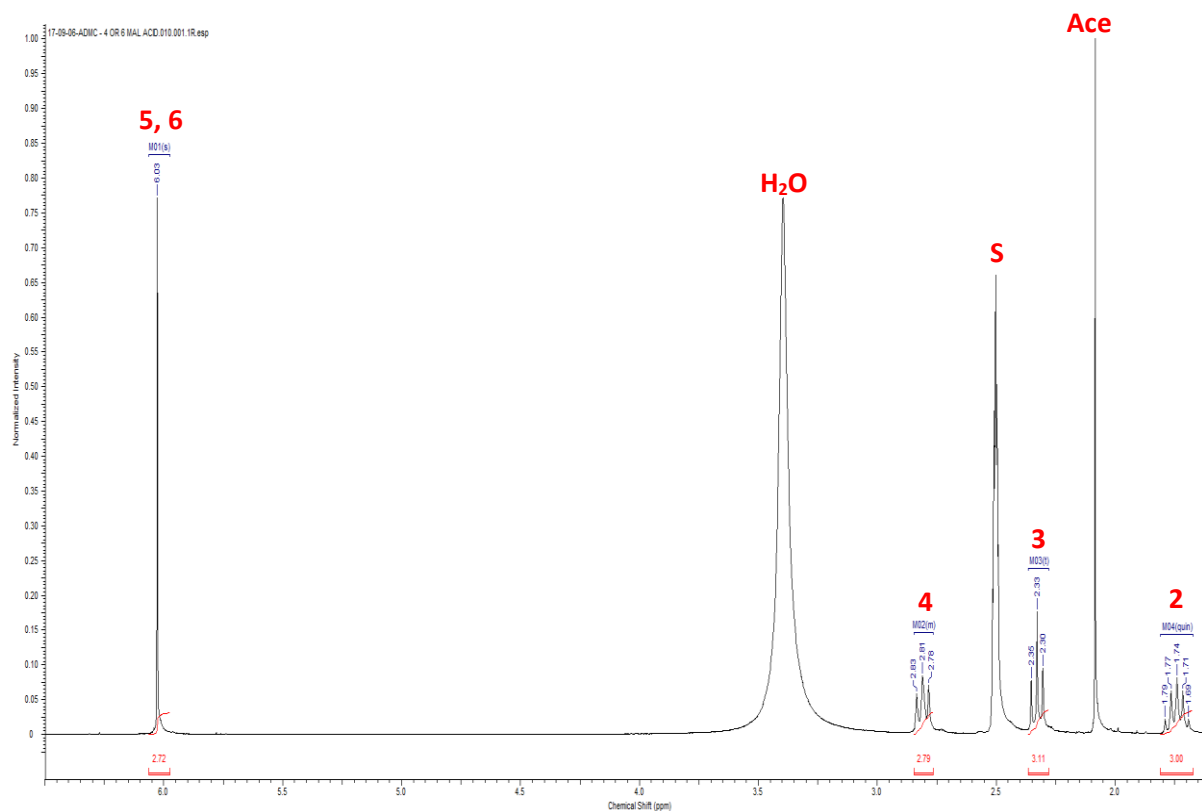
Figure 84: ¹H NMR spectrum of 4-maleimidobutyric acid in DMSO_d carried out using 300MHz NMR at 25 °C.

2.3.5.2. TLC analysis of 4-maleimidobutyric acid

TLC analysis of the 4-maleimidobutyric acid mixture post workup was carried out to clarify its purity. An illustration of the TLC plate is displayed in Figure 85. The Rf value of this compound is 0.39 in a Petroleum Ether – Ethyl Acetate (1:6) solvent system. A single spot eliminated the need for further purification.
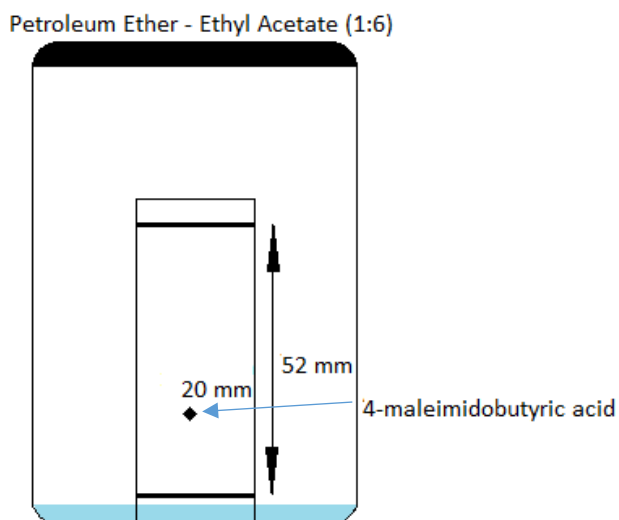
Figure 85: TLC plate of 4-maleimidobutyric acid post workup.

2.3.6. Analytical data of 6-maleimidohexanoic acid

2.3.6.1. ^{1}H NMR spectrum of 6-maleimidohexanoic acid

The NMR spectrum in Figure 87 for 6-maleimidohexanoic acid in Figure 86 showed the following peaks: 6.70 (singlet, [7, 8], 2H), 3.54 (triplet, J=7.2Hz [4], 2H), 2.61 (triplet, J=7.4Hz [6], 2H), 1.78 (quintet, J=7.6Hz [5], 2H), 1.71 (quintet, [3]) 2H), 1.41 (quintet [2], 2H). The NMR spectrum of 6-maleimidopropanoic acid contains two triplets for the terminal CH_2 protons of the alkyl chain, which are located at $\delta 3.54$ and $\delta 2.61$. The central alkyl CH_2 protons have a peak at $\delta 1.41$. The neighbouring CH_2 closer to the tertiary amine is shifted up field to at $\delta 1.71$. The other neighbouring CH_2 closer to the acid group is also shifted up field to a greater extend $\delta 1.78$ as these protons experience more deshielding from the carboxylic group than they would from a tertiary amine. The two protons on the maleimide form a tall singlet at $\delta 6.7$. NMR analysis also indicated the presence of a trace ethyl acetate contaminant, attributed to its signals at δ 4.12, $\delta 2.05$ and $\delta 1.26$.
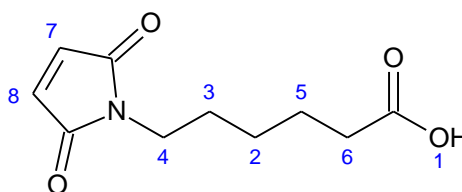
Figure 86: Reaction scheme for the synthesis of 6-maleimidohexanoic acid.
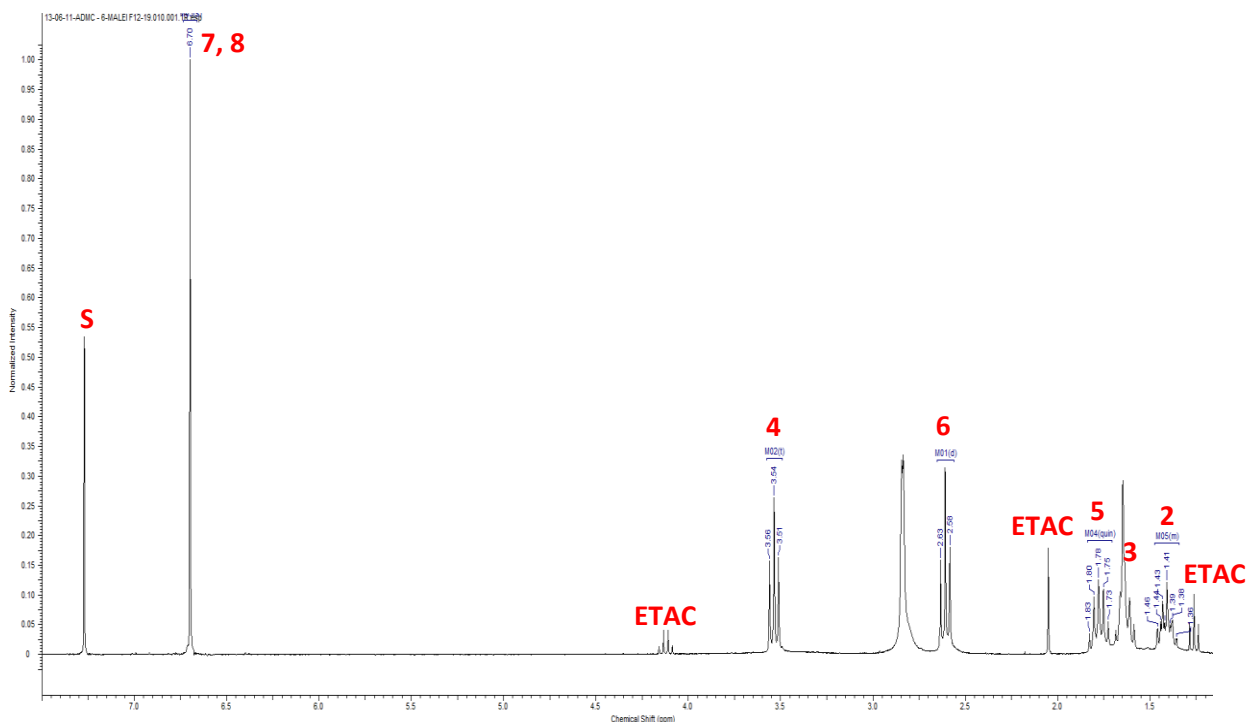
Figure 87: 1H NMR spectrum of 6-maleimidohexanoic acid in CDCL3 carried out using 300MHz NMR at 25 °C.

2.3.6.2. TLC analysis of 6-maleimidohexanoic acid

TLC analysis of the 6-maleimidohexanoic acid mixture post workup was carried out to clarify its purity. An illustration of the TLC plate is displayed in Figure 88. The Rf value of this compound is 0.36 in a Petroleum Ether – Ethyl Acetate (1:6) solvent system. A single spot eliminated the need for further purification.
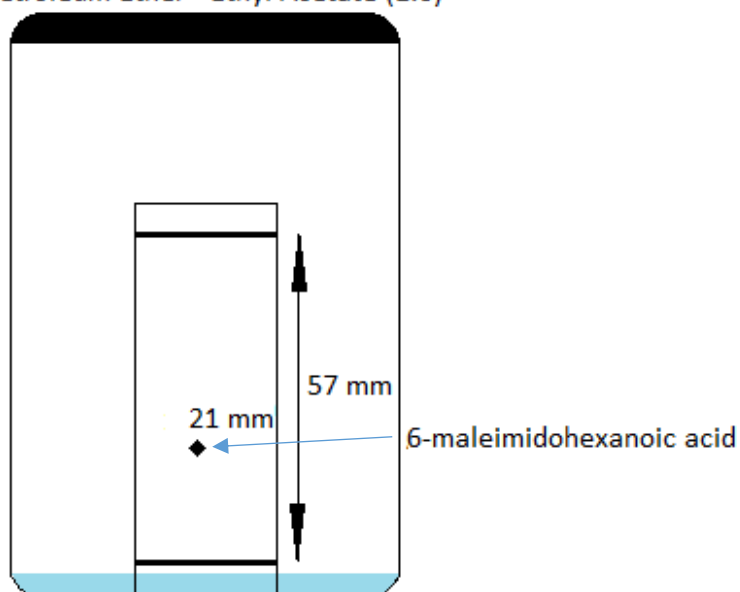
Figure 88: TLC plate of 6-maleimidohexanoic acid post workup.

2.3.7. Analytical data of 3', 5'-O-Bis (tert-Butoxycarbonyl) gemcitabine

2.3.7.1. ^{1}H NMR spectrum of 3', 5'-O-Bis (tert-Butoxycarbonyl) gemcitabine

The NMR spectrum in Figure 90 for 3', 5'-O-Bis (tert-Butoxycarbonyl) gemcitabine in Figure 89 showed the following peaks: 7.61 (doublet J=7.5Hz [6], 1H), 6.35 (doublet [7], 1H), 5.95 (singlet J=7.5Hz [5] 1H), 5.3 (singlet [4], 1H), 4.52, 4.46 (multiplet [3], 2H), 4.42 (doublet [2], 1H), 1.5 (singlet [9], 9H), 1.48 (singlet [8], 9H). NMR analysis of 3',5'-O-Bis(tert-Butoxycarbonyl)gemcitabine showed the presence of a very tall pair of singlets at $\delta 1.5$ and $\delta 1.48$ which are each attributed to the nine protons of the two boc groups. Further evidence of successful boc protection of both hydroxyl groups was indicated by the peaks at δ 5.3, δ 4.52, δ 4.46 and δ 4.42 which match the literature source results for the reaction procedure (Guo & Gallo 1999). The peaks for the pyrimidine protons ($\delta 7.61$ and $\delta 5.95$) remain unchanged from literature sources (Guo & Gallo 1999) which confirm that boc protection of the primary amine group had not occurred. Trace amount of water ($\delta 2.87$) and ethyl acetate (δ 4.06, δ 1.98 and δ 1.21) were also observed in the NMR spectrum.
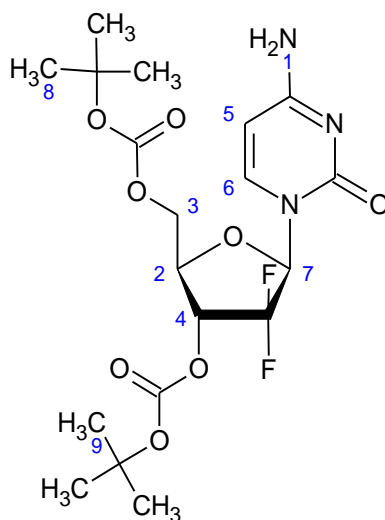
Figure 89: Reaction scheme for the synthesis of 3', 5'-O-Bis (tert-Butoxycarbonyl) gemcitabine.
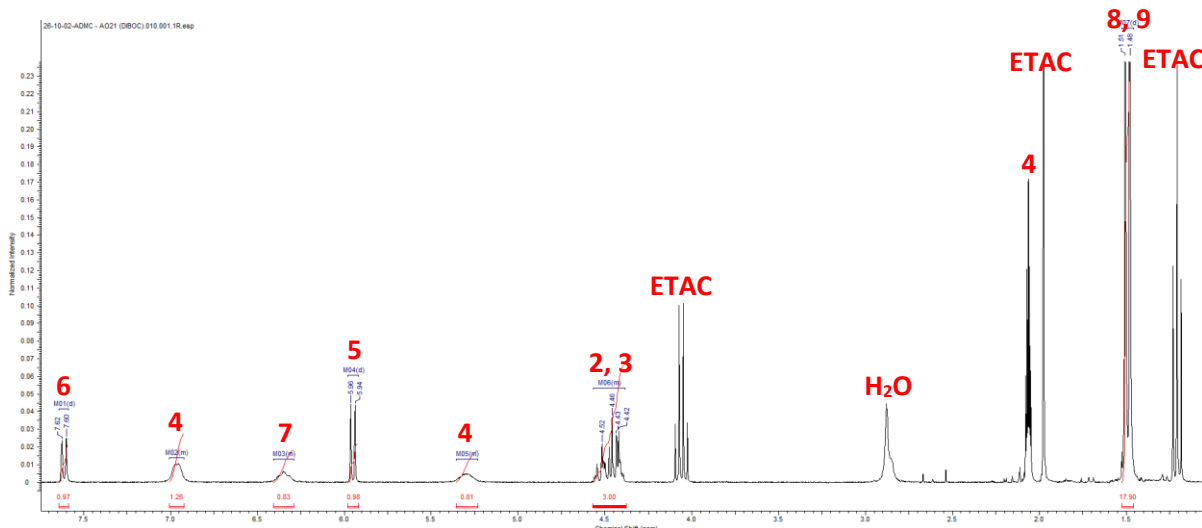
Figure 90: 1H NMR spectrum of 3', 5'-O-Bis (tert-Butoxycarbonyl) gemcitabine in Acetone_d carried out using 300MHz NMR at 25 °C.

2.3.7.2 FTIR of 3', 5'-O-Bis (tert-Butoxycarbonyl) gemcitabine

FTIR analysis of 3', 5'-O-Bis (tert-Butoxycarbonyl) gemcitabine in Figure 91 was carried out in order to ensure boc protection had successfully taken place. Noteworthy peaks are displayed in Table 3. FTIR analysis of 3', 5'-O-Bis (tert-Butoxycarbonyl) gemcitabine shows a primary amine bend at 1650 cm^{-1} which indicates that the primary amine is unaffected by the boc protection. An indicator that both hydroxyl groups were successfully boc protected is the lack of a broad peak in the 3200+ cm^{-1} region.
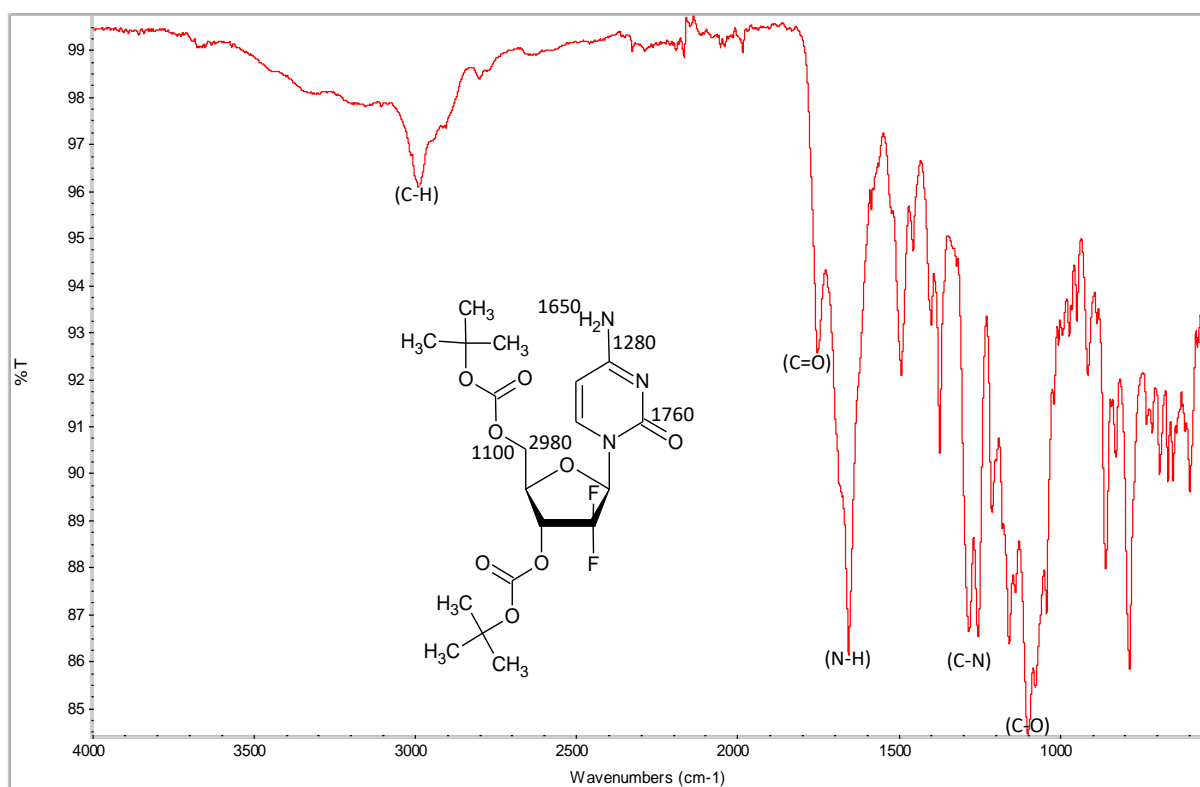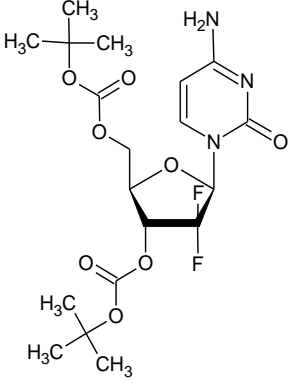
Figure 91: FTIR of 3', 5'-O-Bis (tert-Butoxycarbonyl) gemcitabine.

Table 3: FTIR peak absorbance assignments for 3',5'-O-Bis(tert-Butoxycarbonyl)gemcitabine.

3',5'-O-Bis(tert-Butoxycarbonyl)gemcitabine	Wavenumber (cm⁻¹)	Bond Type	Assignment
	1100	Aliphatic ether stretch	(C-O)
	1280	Aromatic amine stretch	(C-N)
	1650	Primary amine bend	(N-H)
	1760	Carbonyl stretch	(C=O)
	2980	Alkyl stretch	(C-H)

2.3.7.3. TLC analysis of 3',5'-O-Bis(tert-Butoxycarbonyl)gemcitabine

TLC analysis of the 3',5'-O-Bis(tert-Butoxycarbonyl)gemcitabine mixture post workup was carried out to clarify its purity. An illustration of the TLC plate is displayed in Figure 92. The Rf value of this compound is 0.47 in a dichloromethane - acetone (1:1) solvent system. Three spots were visible in the resultant TLC plate for the tri boc (Rf = 1) and mono boc (Rf = 0.26) gemcitabine, which prompted the use of column chromatography for further purification.
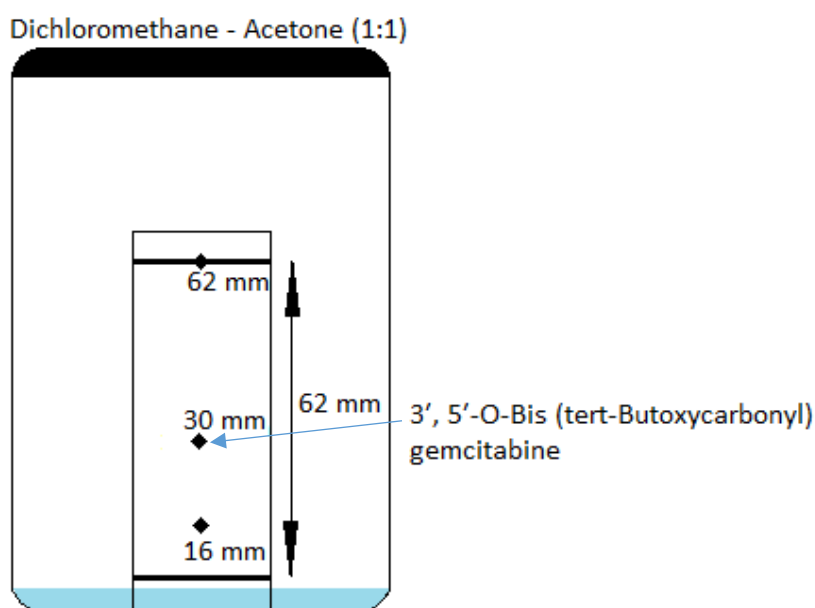
Figure 92: TLC plate of 3',5'-O-Bis(tert-Butoxycarbonyl)gemcitabine post workup.

Column chromatography of the reaction mixture illustrated in Figure 61 was carried out. The pooled fractions from that column were dried and the resulting white powder was analysed by TLC showing a pure compound as illustrated in Figure 93.
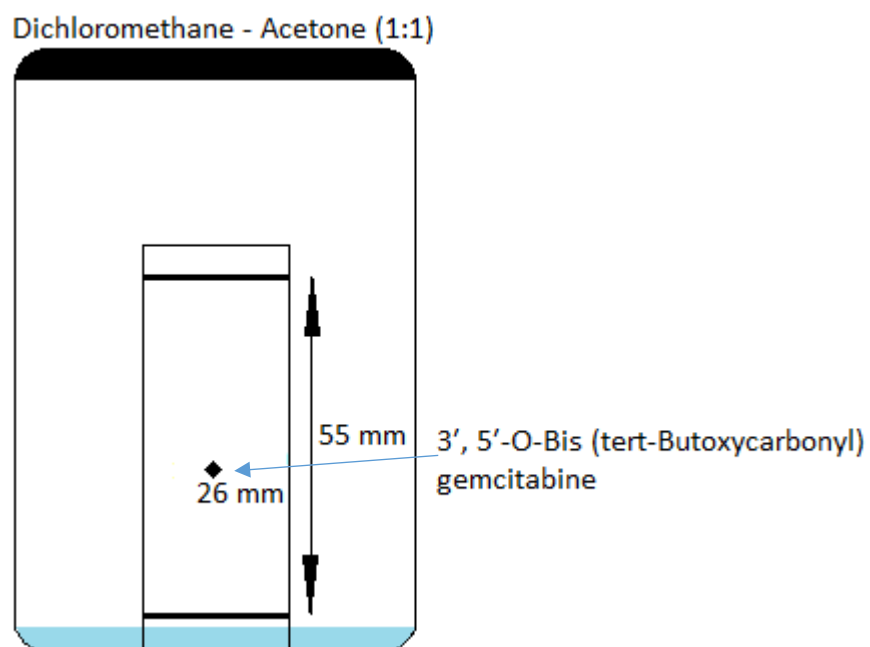
Figure 93: TLC plate of 3',5'-O-Bis(tert-Butoxycarbonyl)gemcitabine post column chromatography.

2.3.8. Analytical data of 3-maleimido propionic acid N-hydroxysuccinimide ester

2.3.8.1. ^{1}H NMR spectrum of 3-maleimidopropionic acid N-hydroxysuccinimide ester

The NMR spectrum in Figure 95 for 3-maleimido propionic acid N-hydroxysuccinimide ester in Figure 94 showed the following peaks: 7.05 (singlet [5, 6], 2H), 3.74 (triplet J=6.9Hz [2], 2H), 3.04 (triplet J=6.9Hz [1] 2H), 2.79 (singlet [3, 4], 4H). The NMR spectrum of 3-maleimido propionic acid N-hydroxysuccinimide ester has two expected triplets at δ3.74 and δ3.04 for the CH_2 protons of the alkyl chain. The two maleimide protons were observed as a tall singlet at δ7.05 while the four succinimide protons formed a broad singlet at δ2.79.
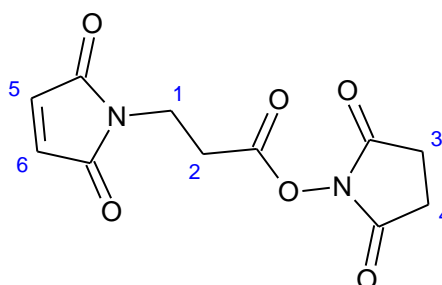
Figure 94: Reaction scheme for the synthesis of 3-maleimido propionic acid N-hydroxysuccinimide ester.
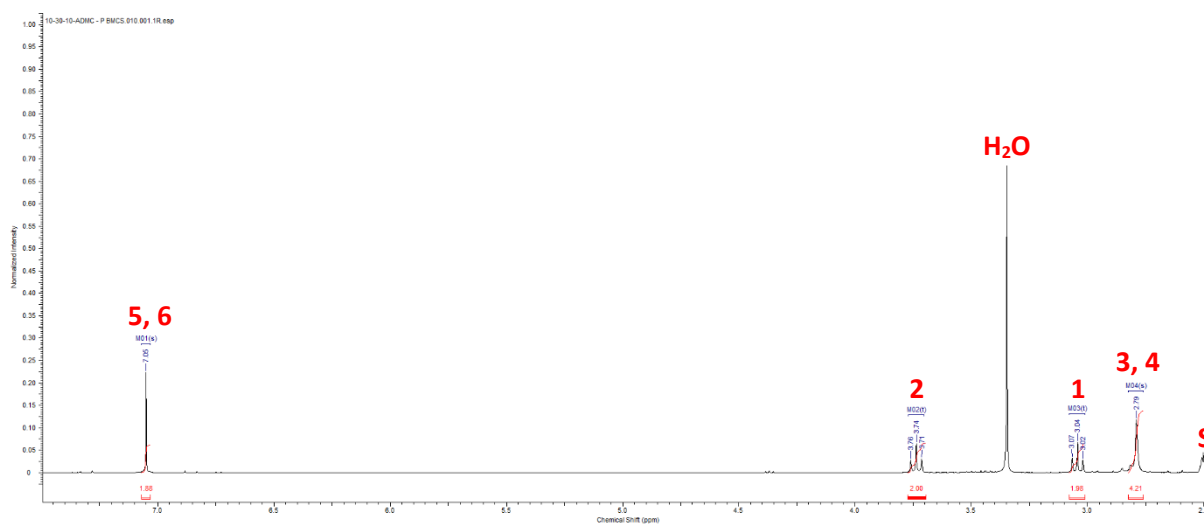
Figure 95: ^{1}H NMR spectrum of 3-maleimido propionic acid N-hydroxysuccinimide ester in DMSO_d carried out using 300MHz NMR at 25 °C.

2.3.8.2. FTIR of 3-maleimidopropionic acid N-hydroxysuccinimide ester

FTIR of 3-maleimidopropionic acid N-hydroxysuccinimide ester was carried out to ensure its successful synthesis by identifying functional groups indicative of this outcome. The successful synthesis of 3-maleimido propionic acid N-hydroxysuccinimide ester is confirmed by the maleimide alkene stretch at 3100 cm^{-1}, the tertiary amine stretch at 1670 cm^{-1} and the alkyl stretches at 2940 cm^{-1} and 2850 cm^{-1} shown in Figure 96. Noteworthy peaks are displayed in Table 4.
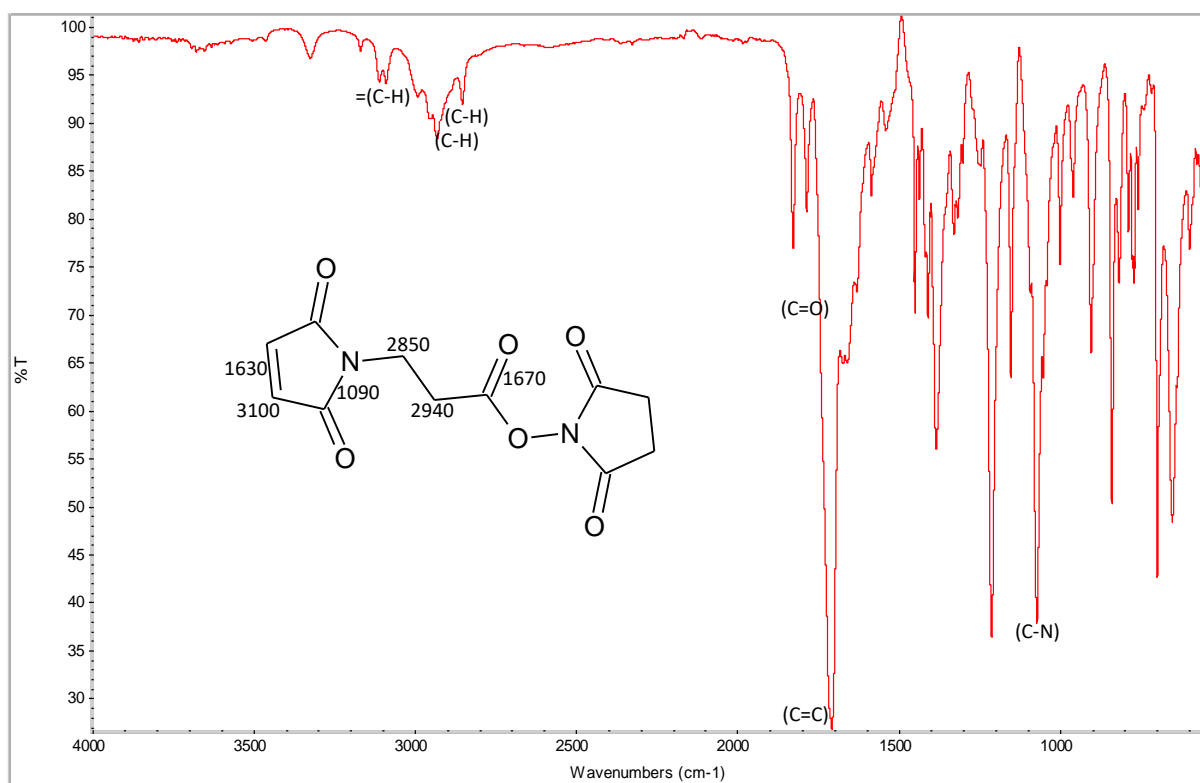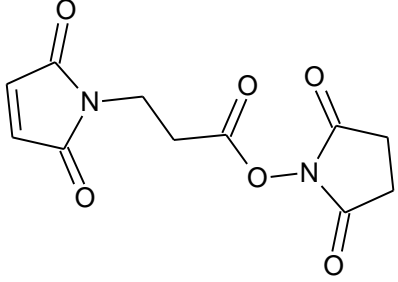
Figure 96: FTIR of 3-maleimidopropionic acid N-hydroxysuccinimide ester.

Table 4: FTIR peak absorbance assignments for 3-maleimidopropionic acid N-hydroxysuccinimide ester.

3-maleimidopropionic acid	Wavenumber (cm⁻¹)	Bond Type	Assignment
N-hydroxysuccinimide ester	1090	Tertiary amine stretch	(C-N)
	1630	Alkene stretch	(C=C)
	1670	Tertiary amide stretch	(C=O)
	2850	Alkyl stretch	(C-H)
	2940	Alkyl stretch	(C-H)
	3100	Alkene stretch	=(C-H)

2.3.8.3. TLC analysis of 3-maleimidopropionic acid N-hydroxysuccinimide ester

TLC analysis of the 3-maleimidopropionic acid N-hydroxysuccinimide ester mixture post workup was carried out to clarify its purity. An illustration of the TLC plate is displayed in Figure 97. The Rf value of this compound is 0.76 in a chloroform - methanol (9:1) solvent system. Two spots were visible in the resultant TLC plate which prompted the use of column chromatography for further purification.
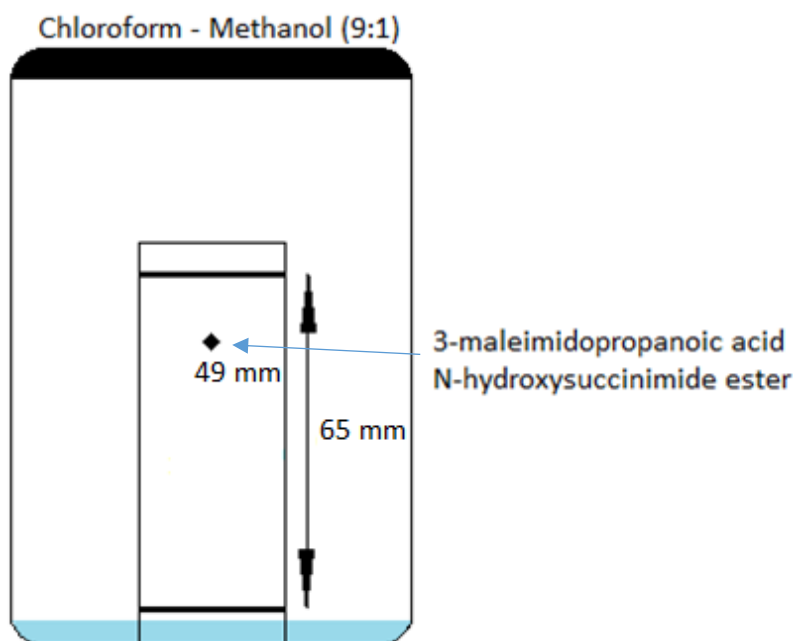
Figure 97: TLC plate of 3-maleimidopropionic acid N-hydroxysuccinimide ester post work up.

Column chromatography of the reaction mixture illustrated in Figure 62 was carried out. The pooled fractions from that column were dried and the resulting brown powder was analysed by TLC showing a pure compound as illustrated in Figure 98.

Figure 98: TLC plate of 3-maleimidopropionic acid N-hydroxysuccinimide ester post column chromatography.

2.3.9. Analytical data of 4-maleimidobutyric acid N-hydroxysuccinimide ester

2.3.9.1 ^{1}H NMR spectrum of 4-maleimidobutyric acid N-hydroxysuccinimide ester

The NMR spectrum in Figure 100 for 4-maleimidobutyric acid N-hydroxysuccinimide ester in Figure 99 showed the following peaks: 7.01 (singlet [6, 7], 2H), 3.48 (triplet J=7.0Hz [2], 2H), 2.80 (singlet [4, 5], 4H), 2.72 (triplet J=7.4Hz [3] 2H), 1.83 (quintet J=7.2Hz [1] 2H). NMR analysis of 4-maleimidobutyric acid N-hydroxysuccinimide ester indicated two triplets at δ3.48 and δ2.72 for the terminal CH_2 protons of the alkyl chain. The central CH_2 protons are observed as a quintet at δ1.83. Similar to the NMR spectrum of 3-maleimido propionic acid N-hydroxysuccinimide ester (Figure 95), there is a tall singlet attributed to the two maleimide protons (δ7.01) and a broad singlet for the four protons of the succinimide (δ2.72). There is also a trace acetone signal at δ2.1.
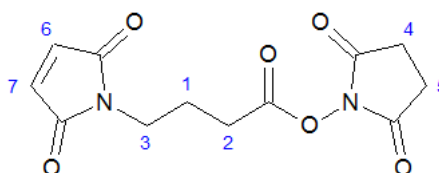
Figure 99: Synthesis of 4-maleimidobutyric acid N-hydroxysuccinimide ester.
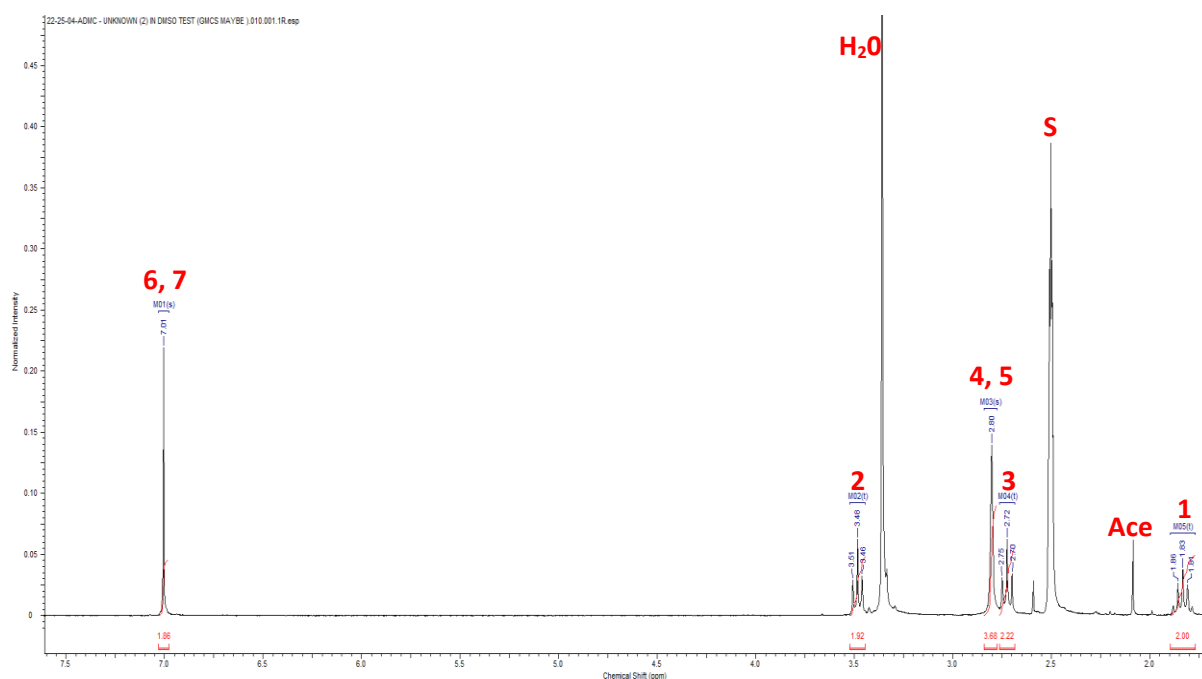
Figure 100: ^{1}H NMR spectrum of 4-maleimidobutyric acid N-hydroxysuccinimide ester in DMSO_d carried out using 300MHz NMR at 25 °C.

2.3.9.2 FTIR of 4-maleimidobutyric acid N-hydroxysuccinimide ester

FTIR analysis of 4-maleimidobutyric acid N-hydroxysuccinimide ester produced a spectrum in Figure 101, which is very similar to that of 3-maleimidopropanoic acid N-hydroxysuccinimide ester. Table 5 displays the noteworthy signals. NMR analysis produced spectra that clearly distinguishes between the two compounds, which highlighted the importance of NMR spectroscopy as a means of correctly analysing these compounds. Due to the structural similarity of 3-maleimidopropanoic acid N-hydroxysuccinimide ester in Figure 94 and 4-maleimidobutyric acid N-hydroxysuccinimide ester Figure 99, their FTIR spectrum are nearly identical. There is a maleimide alkene stretch at 3100 cm^{-1}, a tertiary amine stretch at 1670 cm^{-1} and the alkyl stretches at 2940 cm^{-1} and 2850 cm^{-1}.
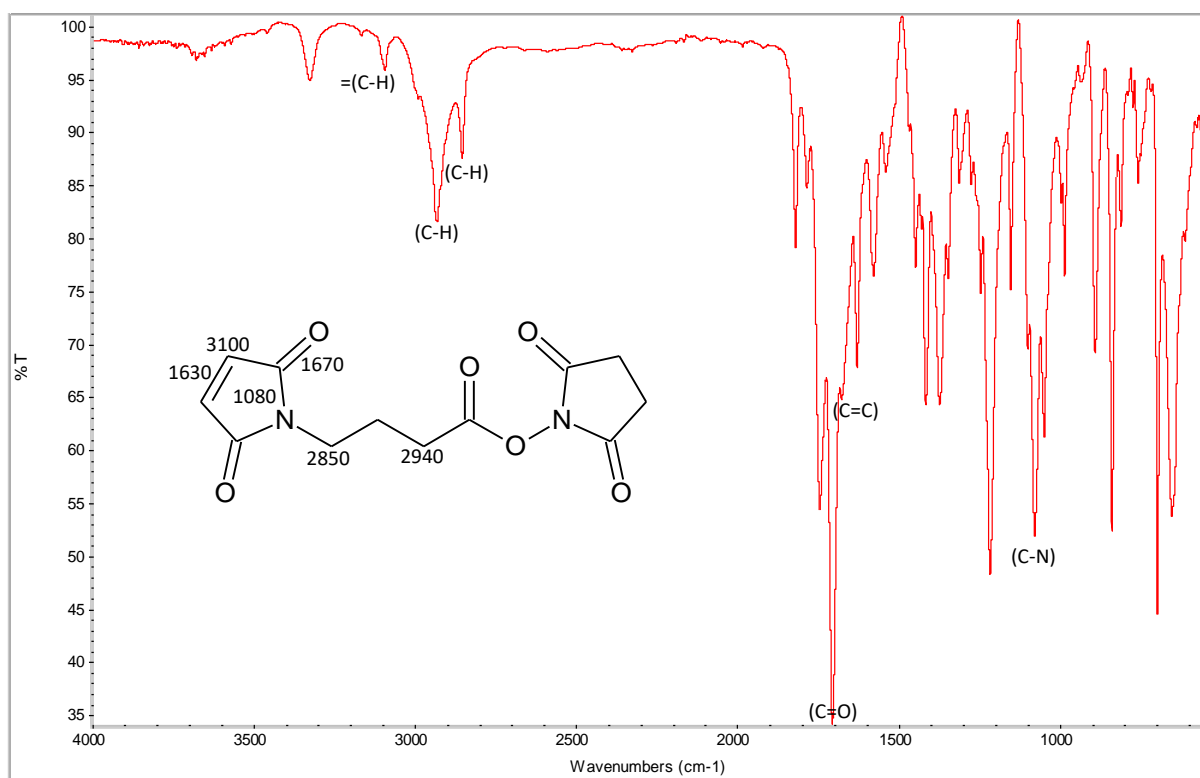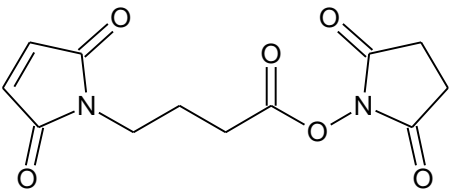
Figure 101: FTIR of 4-maleimidobutyric acid N-hydroxysuccinimide ester.

Table 5: FTIR peak absorbance assignments for 4-maleimidobutyric acid N-hydroxysuccinimide ester.

4-maleimidobutyric acid N-hydroxysuccinimide ester	Wavenumber (cm^{-1})	Bond Type	Assignment
	1080	Tertiary amine stretch	(C-N)
	1630	Alkene stretch	(C=C)
	1670	Tertiary amide stretch	(C=O)
	2850	Alkyl stretch	(C-H)
	2940	Alkyl stretch	(C-H)
	3100	Alkene stretch	=(C-H)

2.3.9.3. TLC analysis of 4-maleimidobutyric acid N-hydroxysuccinimide ester

TLC analysis of the 4-maleimidobutyric acid N-hydroxysuccinimide ester mixture post workup was carried out to clarify its purity. An illustration of the TLC plate is displayed in Figure 102. The Rf value of this compound is 0.71 in a chloroform - methanol (9:1) solvent system. Two spots were visible in the resultant TLC plate which prompted the use of column chromatography for further purification.
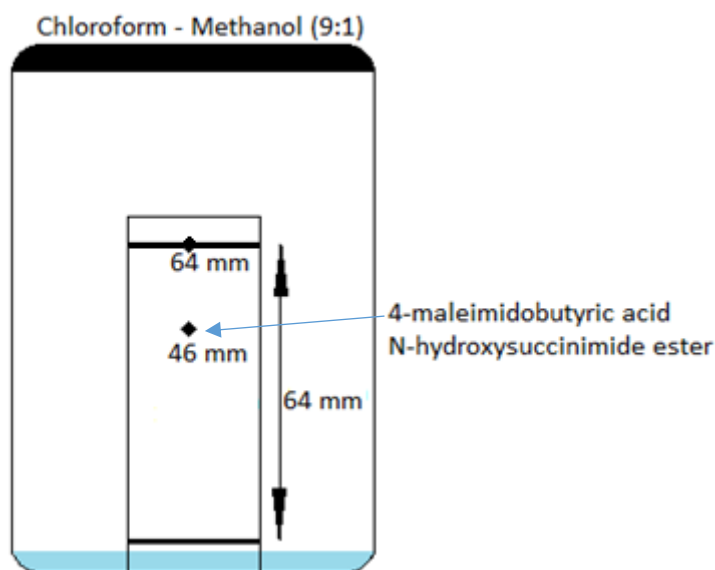
Figure 102: TLC plate of 4-maleimidobutyric acid N-hydroxysuccinimide ester post work up.

Column chromatography of the reaction mixture illustrated in Figure 63 was carried out. The pooled fractions from that column were dried and the resulting dark green solid was analysed by TLC showing a pure compound as illustrated in Figure 103.

Figure 103: TLC plate of 4-maleimidobutyric acid N-hydroxysuccinimide ester post column chromatography.

2.3.10. Analytical data of 4-maleimidobutyric acid N-hydroxysuccinimide ester

2.3.10.1 ^{1}H NMR spectrum of 6-aminohexanoic acid N-hydroxysuccinimide ester

The NMR spectrum in Figure 103 for 6-maleimidohexanoic acid N-hydroxysuccinimide ester in Figure 104 showed the following peaks: 6.70 (singlet [8,9], 2H), 3.54 (triplet J=7.2Hz [3], 2H), 2.84 (singlet [6,7], 4H), 2.61 (triplet J=7.4Hz [5] 2H), 1.78 (quintet J=7.6Hz [2] 2H), 1.65 (quintet J=7.6Hz [4] 2H) 1.41 (quintet [1] 2H). As observed with the 3 and 4-length N-alkylated esters (Figure 36, 38), the NMR spectrum of synthesis of 6-maleimidohexanoic acid N-hydroxysuccinimide ester contains a broad singlet for the four succinimide protons (δ2.84) and a tall singlet for the two maleimide protons (δ6.7). The alkyl chain CH_2 signals as expected contains two terminal triplets at δ3.54 and δ2.61. Three quintets are also observed for the central three CH_2 signals at δ1.78, δ1.65 and δ1.41. There is a trace water contaminant at δ1.65 and signals indicating a trace amount of ethyl acetate present (δ4.12, δ2.05 and δ1.26).
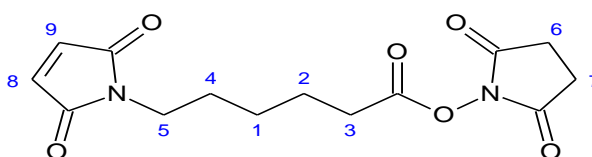
Figure 104: Reaction scheme for the synthesis of 6-aminohexanoic acid N-hydroxysuccinimide ester.
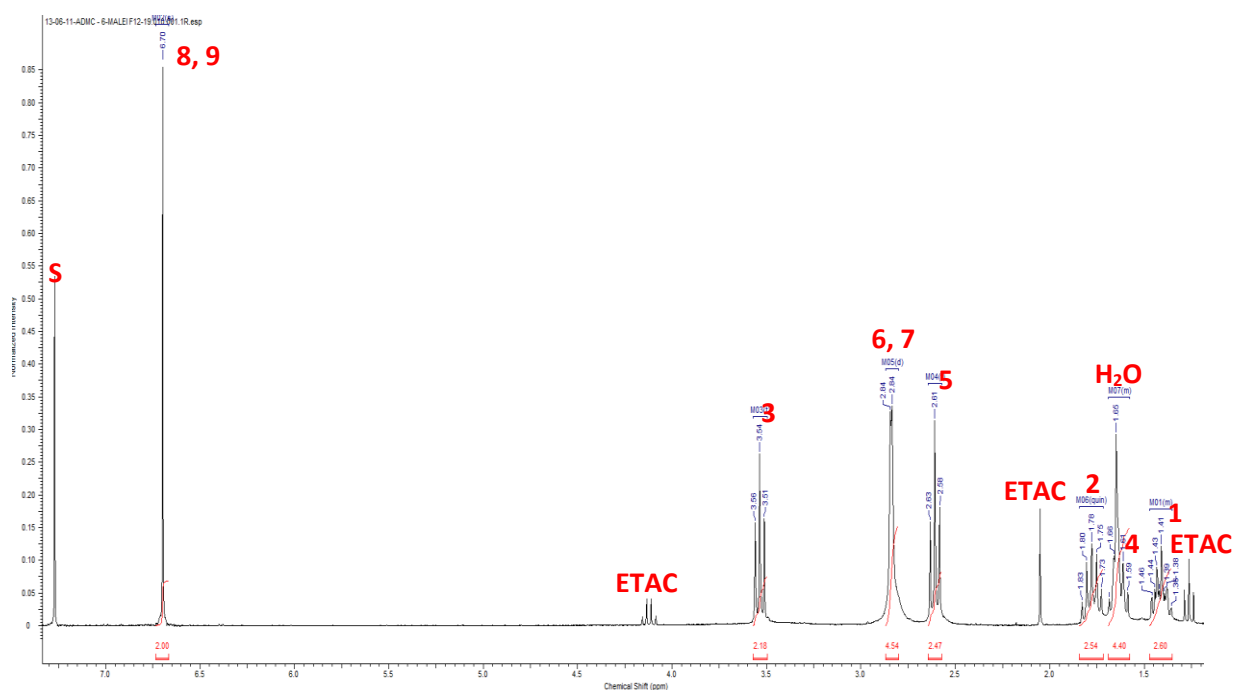
Figure 105: ^{1}H NMR spectrum of 6-aminohexanoic acid N-hydroxysuccinimide ester in DMSO_d carried out using 300MHz NMR at 25 °C.

114

2.3.10.2. FTIR of 6-maleimidohexanoic acid N-hydroxysuccinimide ester

As expected, the FTIR analysis of 6-maleimidohexanoic acid N-hydroxysuccinimide ester in Figure 106 produced a spectrum that was very similar to that of the 3 and 4 alkyl length analogues. Table 6 lists the noteworthy peaks. The FTIR spectrum of 6-maleimidohexanoic acid N-hydroxysuccinimide ester therefore has IR absorbance's similar to those of 3-maleimidopropanoic acid N-hydroxysuccinimide ester and 4-maleimidobutyric acid N-hydroxysuccinimide ester due to their similar chemical structure. These are the maleimide alkene stretch at 3100 cm^{-1}, the tertiary amine stretch at 1670 cm^{-1} and alkyl stretches at 2940 cm^{-1} and 2850 cm^{-1}.
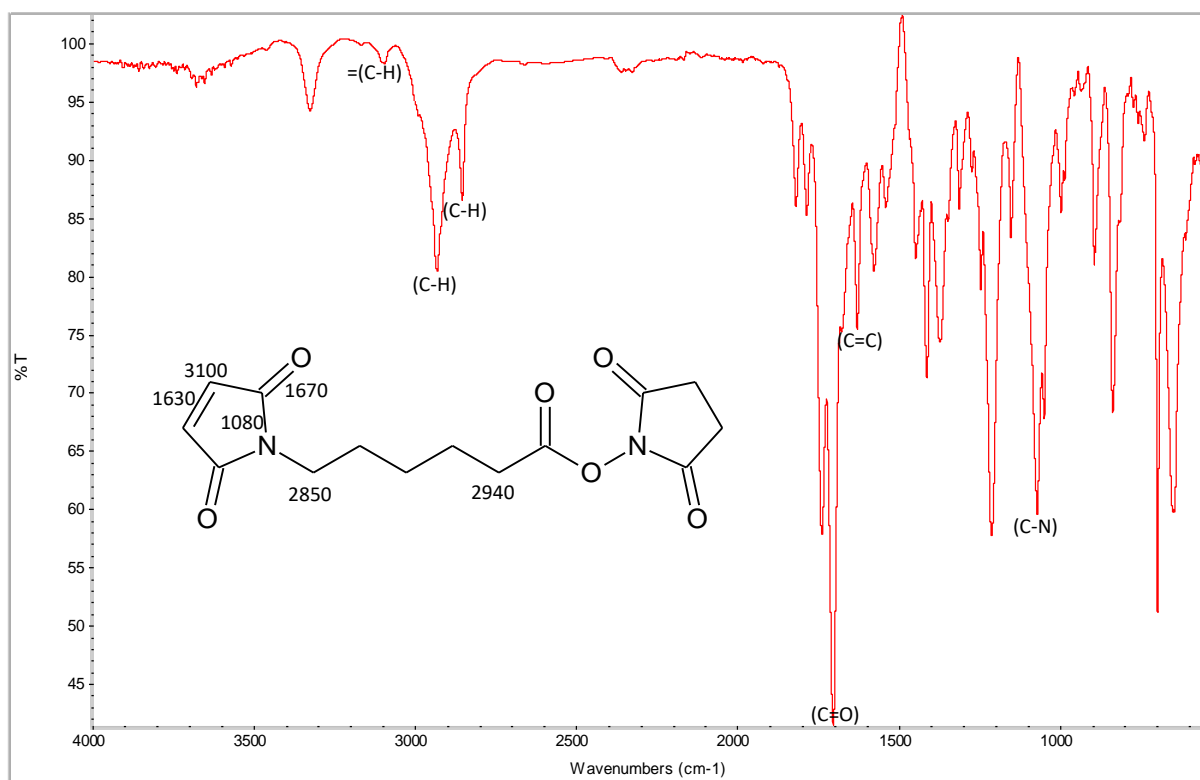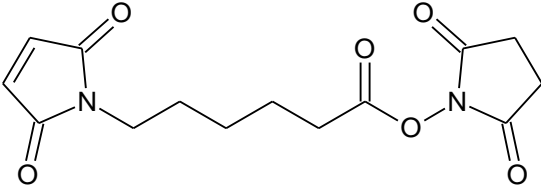
Figure 106: FTIR of 6-maleimidohexnoic acid N-hydroxysuccinimide ester.

Table 6: FTIR peak absorbance assignments for 6-maleimidohexanoic acid N-hydroxysuccinimide ester.

6-maleimidohexanoic acid N-hydroxysuccinimide ester	Wavenumber (cm^{-1})	Bond Type	Assignment
	1080	Tertiary amine stretch	(C-N)
	1630	Alkene stretch	(C=C)
	1670	Tertiary amide stretch	(C=O)
	2850	Alkyl stretch	(C-H)
	2940	Alkyl stretch	(C-H)
	3100	Alkene stretch	=(C-H)

2.3.10.3. TLC analysis of 6-maleimidohexanoic acid N-hydroxysuccinimide ester

TLC analysis of the 6-maleimidohexanoic acid N-hydroxysuccinimide ester mixture post workup was carried out to clarify its purity. An illustration of the TLC plate is displayed in Figure 107. The Rf value of this compound is 0.52 in a chloroform - methanol (9:1) solvent system. Two spots were visible in the resultant TLC plate which prompted the use of column chromatography for further purification.
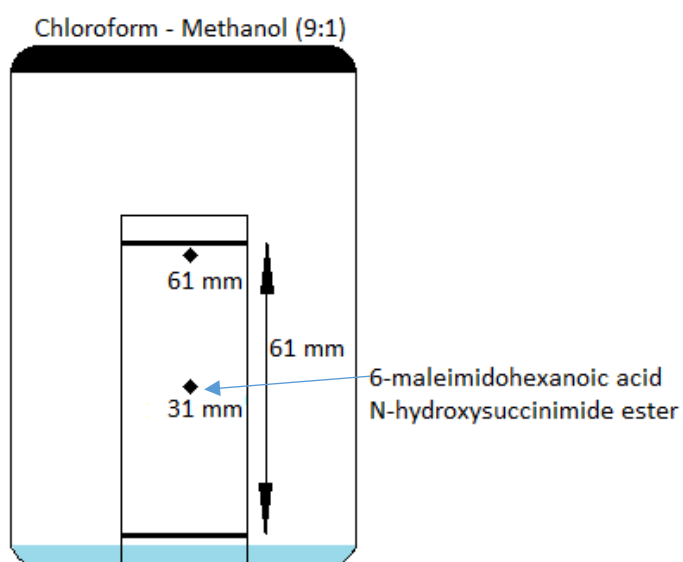
Figure 107: TLC plate of 6-maleimidohexanoic acid N-hydroxysuccinimide ester post work up**.**

Column chromatography of the reaction mixture illustrated in Figure 64 was carried out. The pooled fractions from that column were dried and the resulting yellow highly viscous oil was analysed by TLC showing a pure compound as illustrated in Figure 108.
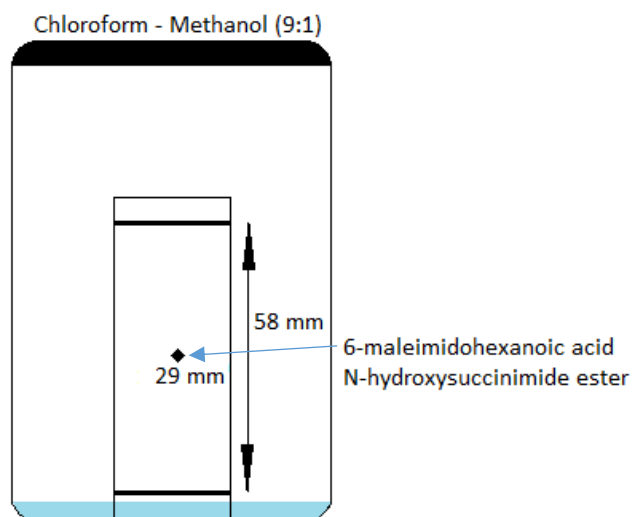
Figure 108: TLC plate of 6-maleimidohexanoic acid N-hydroxysuccinimide ester post column chromatography.

2.3.11. Analytical data of Boc-Gem-Mal

2.3.11.1 ^{1}H NMR spectrum of Boc-Gem-Mal

The NMR spectrum (Figure 110) of Boc-Gem-Mal (Figure 109) showed the following peaks: 7.90 (doublet [8], 1H), 7.26 (doublet [7], 1H), 6.75 (singlet [9,10], 2H), 6.23 (multiplet [11] 1H), 5.20 (multiplet [4] 2H), 4.45-4.29 (multiplet [2,3] 3H), 3.72 (triplet [6], 2H), 2.76 (triplet [5] 2H) 1.36 (singlet [12] 9H), 1.35 (singlet [13] 9H). Evidence of a successful amide coupling reaction would be observed by noting the disappearance of the signals at δ7.61 and δ5.95 for 3',5'-O-Bis(tert-Butoxycarbonyl)gemcitabine's pyrimidine protons. These protons were up shifted to δ7.9 and δ7.26 due to their proximity to the newly formed amide group. The other protons remained relatively unchanged indicating the boc groups remained and therefore no reaction had taken place at the hydroxyls. A trace amount of water can be observed at δ2.74.
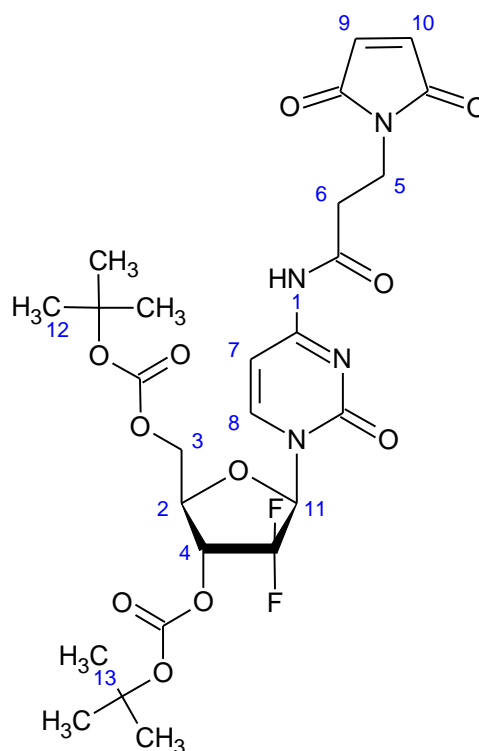
Figure 109: Reaction scheme depicting the reaction between 3', 5'-O-Bis(tert-Butoxycarbonyl)gemcitabine and 3-maleimido propionic acid N hydroxysuccinimide ester to produce Boc-Gem-Mal.
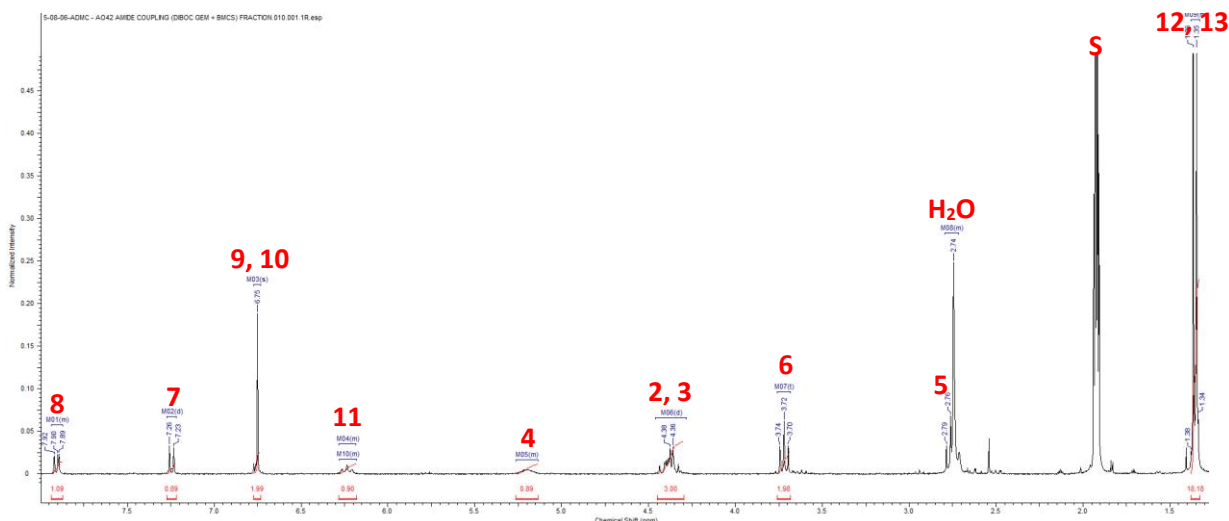
Figure 110: ^{1}H NMR spectrum of Boc-Gem-Mal in DMSO_d carried out using 300MHz NMR at 25 °C.

2.3.11.2. TLC analysis of Boc-Gem-Mal

TLC analysis of the starting materials (3',5'-O-Bis(tert-Butoxycarbonyl)gemcitabine and 3-maleimido propionic acid N hydroxysuccinimide ester) and the post workup Boc-Gem-Mal mixture was carried out to observe its purity. An illustration of the TLC plate is displayed in Figure 111. The Rf value of this compound is 0.7 in a chloroform - acetone (1:1) solvent system. The presence of the starting material was evident by their comparative spots in the resultant TLC plate which prompted the use of column chromatography for further purification.
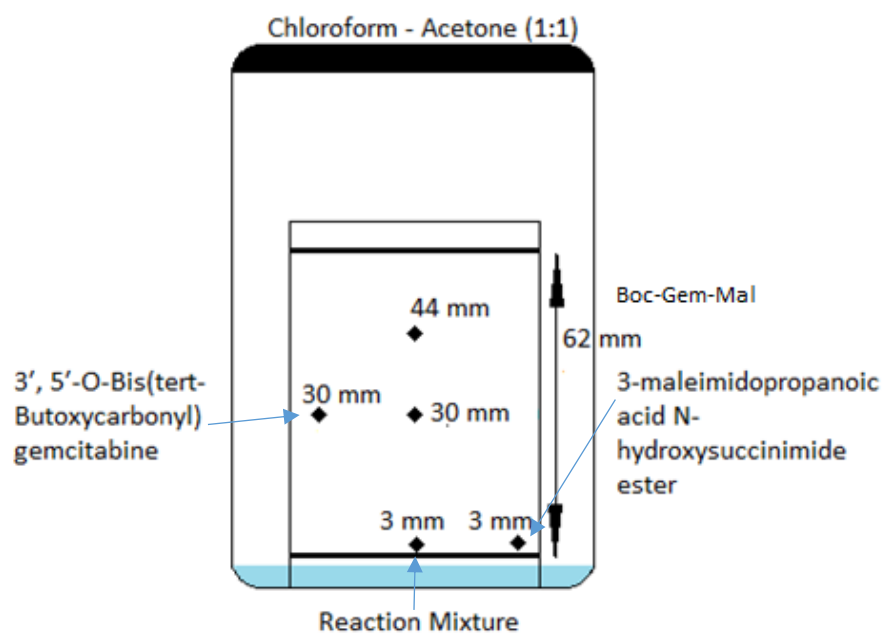
Figure 111: TLC plate of Boc-Gem-Mal post workup.

Column chromatography of the reaction mixture illustrated in Figure 65 was carried out. The pooled fractions from that column were dried and the resulting light green powder was analysed by TLC showing a pure compound as illustrated in Figure 112.
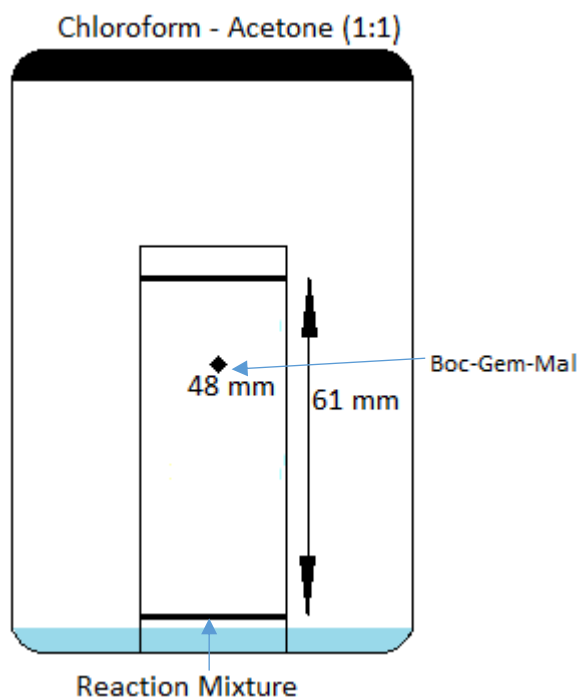
Figure 112: TLC plate of Boc-Gem-Mal post column chromatography.

2.3.12. Analytical data of *O-tert*-butyl S-(furan-2-ylmethyl) carbonothionate

2.3.12.1. ^{1}H NMR spectrum of *O-tert*-butyl S-(furan-2-ylmethyl) carbonothionate

The NMR spectrum (Figure 114) of *O-tert*-butyl S-(furan-2-ylmethyl) carbonothionate (Figure 113) showed the following peaks: 7.34 (multiplet [3], 1H), 6.3 (multiplet [1], 1H), 6.23 (multiplet J=3.2Hz [2], 1H), 4.06 (singlet [4] 2H), 1.5 (singlet [5] 9H). Successful boc protection of 2-furanmethane thiol was noted by the presence of a very tall singlet at δ1.5 for the nine boc group's protons. The furan proton neighbouring the oxygen is upshifted to δ7.34 compared to the other two which have a similar chemical shift of δ6.3 and δ6.23. There is a trace water contamination at δ1.52.
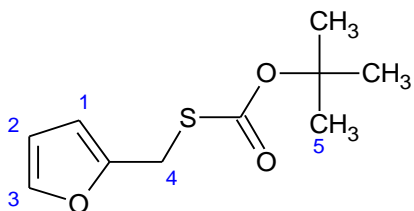
Figure 113: Reaction scheme for the synthesis O-tert-butyl S-(furan-2-ylmethyl) carbonothionate.
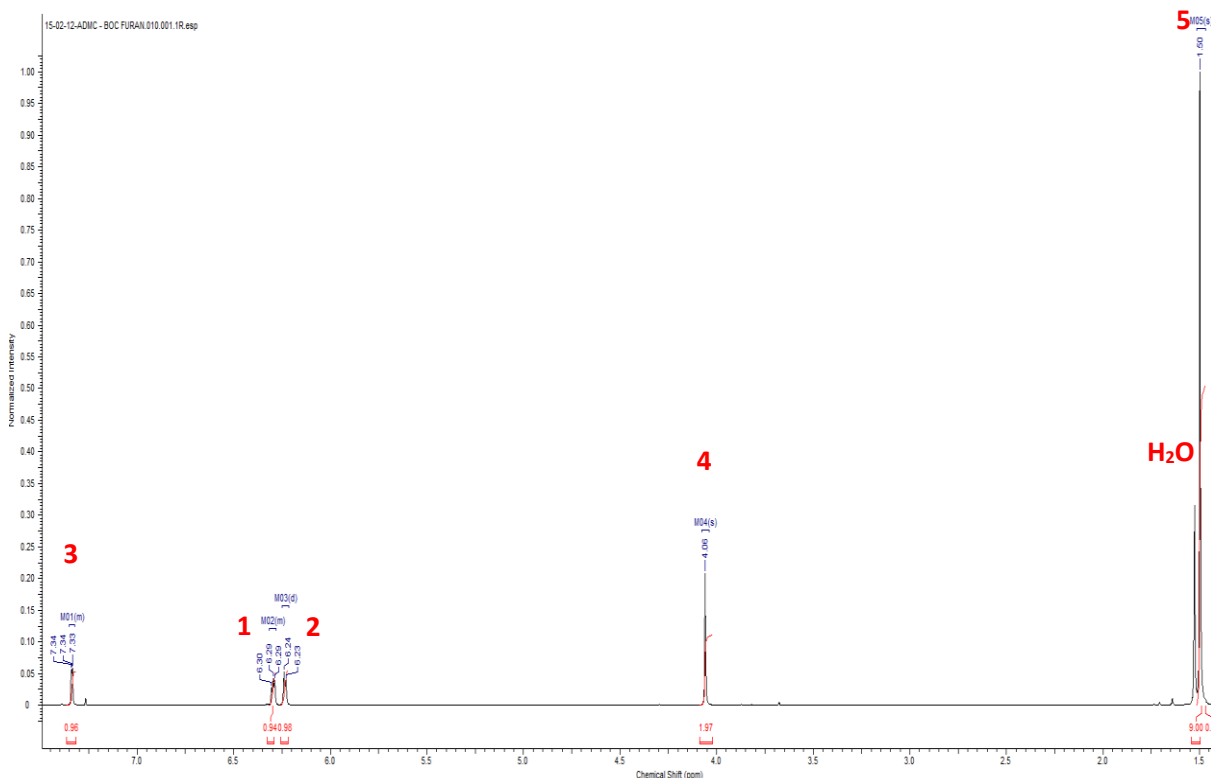
Figure 114: ^{1}H NMR spectrum of *O-tert*-butyl S-(furan-2-ylmethyl) carbonothionate in CDCl$_3$ carried out using 300MHz NMR at 25 °C.

2.3.12.2. FTIR of *O-tert*-butyl S-(furan-2-ylmethyl) carbonothionate

FTIR analysis of the product yielded a spectrum which corroborated the NMR analysis that 2-furanmethanethiol had been successfully boc protected. Table 7 lists the noteworthy peaks indicative of a successful boc protection of 2-furanmethane thiol. A thiol group has a signal around 2550-2600 which is absent from the IR spectral analysis. The presence of a the conjugated alkene stretch at 1650 cm^{-1} (C=C) of the furan and the lack of a thiol (S-H) stretch at around 2550 cm^{-1} in Figure 115 indicates the successful boc protection of 2-furanmethane thiol.
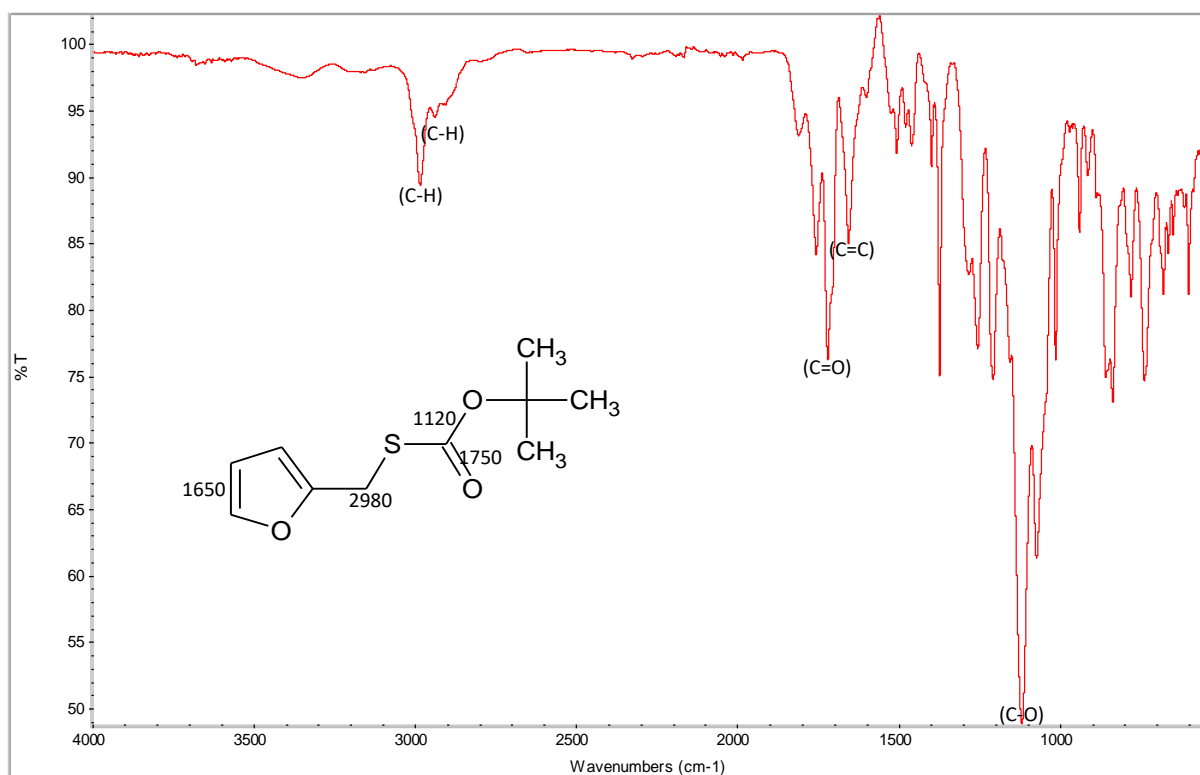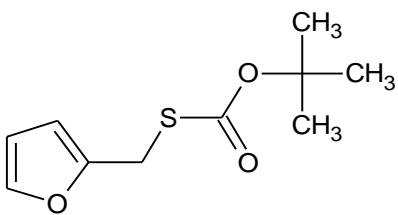
Figure 115: FTIR of *O-tert*-butyl S-(furan-2-ylmethyl) carbonothionate.

Table 7: FTIR peak absorbance assignments for *O-tert*-butyl S-(furan-2-ylmethyl) carbonothionate.

O-tert-butyl S-(furan-2-ylmethyl) carbonothionate	Wavenumber (cm^{-1})	Bond Type	Assignment
	1120	Aliphatic ester stretch	(C-O)
	1650	Conjugated alkene stretch	(C=C)
	1750	Ester stretch	(C=O)
	2980	Alkyl stretch	(C-H)

2.3.12.3. TLC analysis of O-*tert*-butyl S-(furan-2-ylmethyl) carbonothionate

TLC analysis of the *O-tert*-butyl S-(furan-2-ylmethyl) carbonothionate mixture post workup was carried out to clarify its purity. An illustration of the TLC plate is displayed in Figure 116.The Rf value of this compound is 0.87 in a petroleum ether – ethyl acetate (1:1) solvent system. Only one Spot was visible indicating a pure compound requiring no further purification.
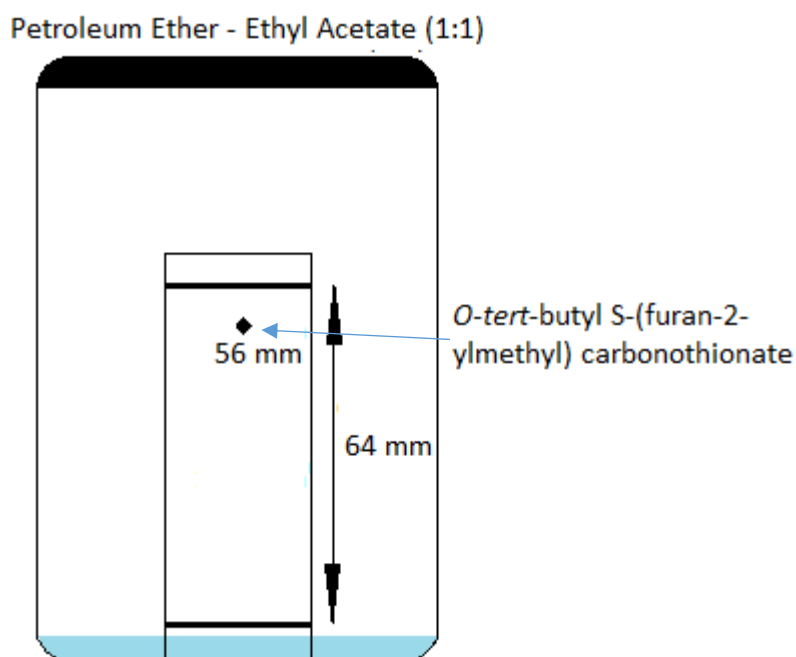
Figure 116: TLC plate of *O-tert*-butyl S-(furan-2-ylmethyl) carbonothionate post workup**.**

2.3.13. Analytical data of BDA

2.3.13.1. ^{1}H NMR spectrum of BDA

The NMR spectrum (Figure 118) of BDA (Figure 117) showed the following peaks: 6.53 (multiplet [4-endo], 1H), 6.41 (multiplet J=3.2Hz [4-exo], 1H), 6.31 (multiplet [3-endo] 1H), 6.24 (multiplet [3-exo] 1H), 5.24 (doublet J=1.7Hz [2], 1H), 4.06 (singlet [11] 2H), 3.61 (triplet [7], 2H), 3.59 (multiplet J=6.2Hz [1-endo], 1H), 3.44 (doublet J=6.2Hz [5-endo], 1H), 3.01 (singlet [1-exo] 1H), 2.95 (doublet [5-exo] 1H), 2.84 (singlet [9,10] 4H), 2.64 (triplet [8], 2H), 2.01 (quintet [6], 2H), 1.5 (singlet [12], 9H). The cycloadduct acquired by the Diels Alder reaction of *O-tert*-butyl S-(furan-2-ylmethyl) carbonothionate and 4-maleimidobutyric acid N-hydroxysuccinimide ester, produced an NMR spectrum containing a lot of signals due to the complexity of the compound. However, specific peaks indicative of a successful Diels Alder reaction were present including the emergence of new signals between δ6.53-δ6.24 for the endo/exo alkene protons of the cycloadduct. The disappearance of the maleimide signal of 4-maleimidobutyric acid N-hydroxysuccinimide ester at δ7.01 also confirmed this. As a result these two protons were downshifted to δ3.69/δ3.44 and δ3.01/δ2.95 for the endo/exo isomer respectively. The proton signals for the succinimide ester remained relatively unchanged when compared to those of 4-maleimidobutyric acid N-hydroxysuccinimide ester. There is a trace water peak at δ1.51 and ethyl acetate peaks at δ4.12, δ2.05 and δ1.26.
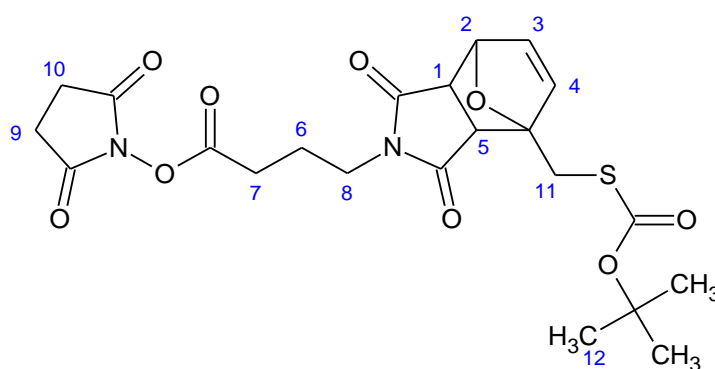
Figure 117: Reaction scheme for the Diels Alder reaction between 4-maleimidobutyric acid N-hydroxysuccinimide ester and *O-tert*-butyl S-(furan-2-ylmethyl) carbonothionate to produce BDA.
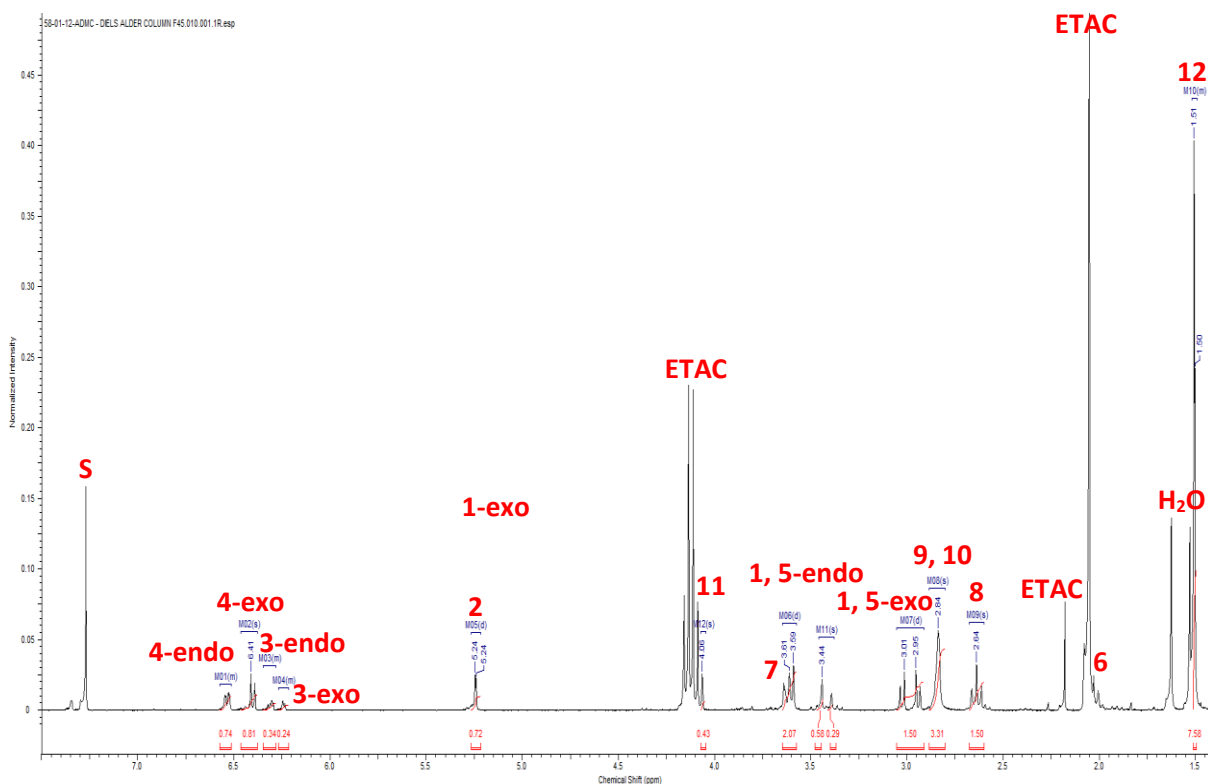
Figure 118: 1H NMR spectrum of BDA in CDCl3 carried out using 400MHz NMR at 25 °C.

2.3.13.2. TLC analysis of BDA

TLC analysis of the BDA mixture post workup was carried out to clarify its purity. An illustration of the TLC plate is displayed in Figure 119.The Rf value of this compound is 0.42 in a petroleum ether – ethyl acetate (1:1) solvent system. Two spots were visible indicating the work up mixture required further purification.
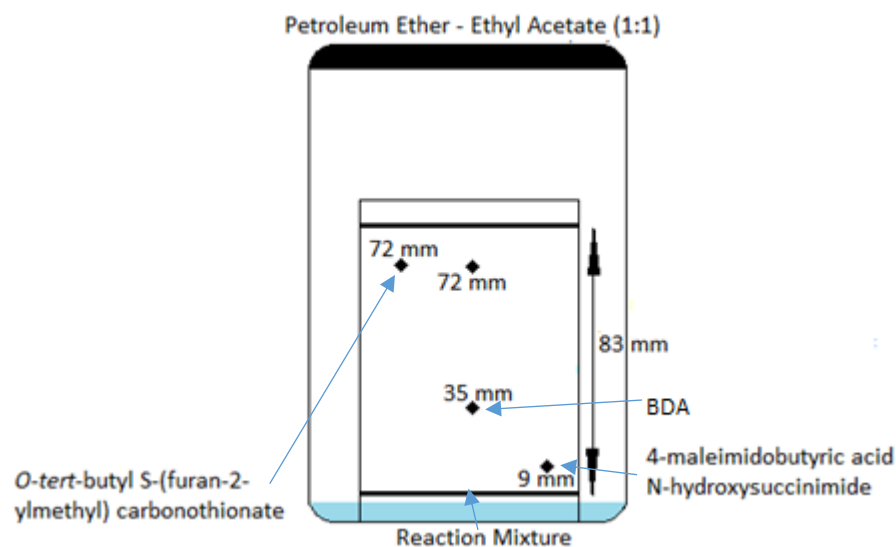
Figure 119: TLC plate of BDA post workup.

Column chromatography of the reaction mixture illustrated in Figure 67 was carried out. The pooled fractions from that column were dried and the resulting brown greasy solid was analysed by TLC showing a pure compound as illustrated in Figure 120.
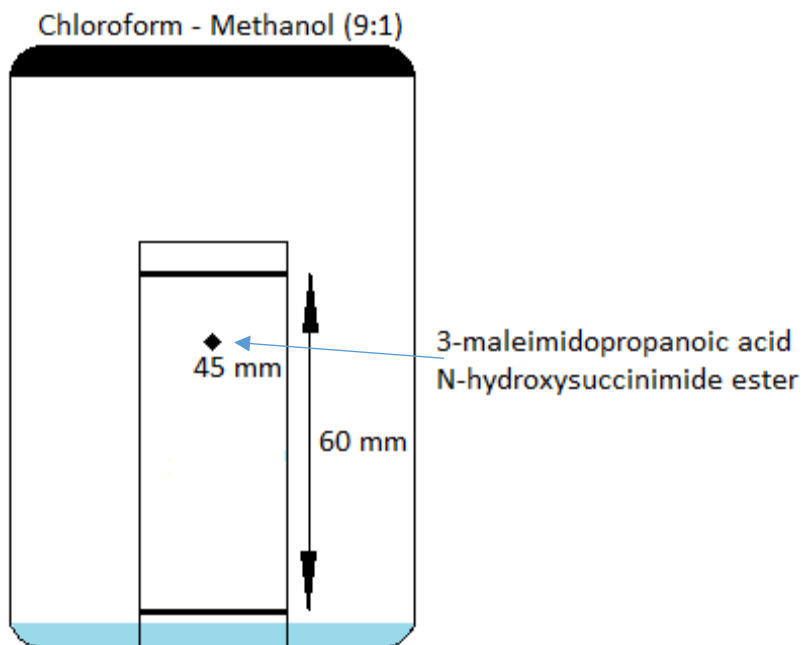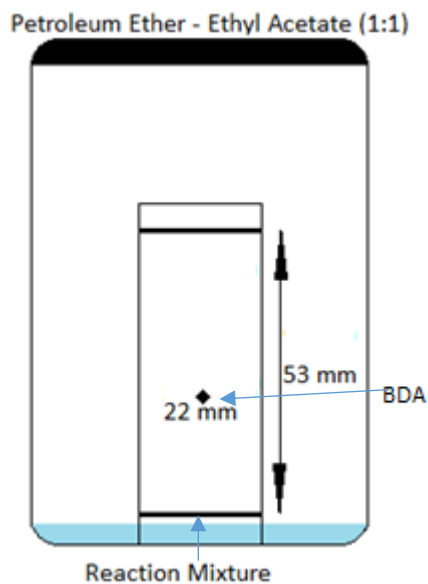

Figure 120: TLC plate of BDA post column chromatography.

2.3.14. Analytical data of Boc-TTLD

2.3.14.1 ^{1}H NMR spectrum of Boc-TTLD

The NMR spectrum (Figure 122) of Boc-TTLD (Figure 121) showed the following peaks: 7.89 (singlet [14], 1H), 7.29 (doublet J=7.2Hz [13], 1H), 6.48 (br-singlet [5-endo], 1H), 6.41 (br-singlet J=3.2Hz [5-exo], 1H), 6.27 (doublet J=4.2Hz [4-endo] 1H), 6.24 (multiplet [17] 1H), 6.16 (multiplet [4-exo] 1H), 5.5 (br-singlet [3-endo], 1H), 5.20 (br-singlet [12], 1H), 5.0 (br-singlet [3-exo], 1H), 4.45-4.31 (multiplet [10,11] 3H), 3.44 (triplet J=14.3Hz [8], 2H), 3.40 (br-singlet [2-endo], 1H), 3.29 (doublet J=14.5Hz [6-endo], H), 2.97 (br-singlet [2-exo], 1H) 2.89 (doublet J=6.4Hz [6-exo], 1H), 2.44 (triplet [9] 2H), 1.78 (triplet [7] 2H), 1.35 (doublet [16,18,19] 27H). Successful amide coupling of the Diels Alder adduct in Figure 54 with 3', 5'-O-Bis (tert-Butoxycarbonyl) gemcitabine was indicated by the chemical shifts of the gemcitabine's pyrimidine protons, which had shifted from δ7.61 and δ5.95 to δ7.89 and δ7.29, while the other 3', 5'-O-Bis (tert-Butoxycarbonyl) gemcitabine proton signals remained relatively unchanged. This reaction was carried out 0 °C due to the cycloadducts ability to undergo retro Diels Alder. Assurances of this was evident in the presence of signals at δ6.48/δ6.27 and δ6.41/δ6.16 for the endo and exo isomers respectively. This coupled with the lack of a signal for the maleimide protons show that no detectable retro Diels Alder had taken place over the 108 hour reaction and that the synthesis of a boc protected thermally labile linker with an attached gemcitabine was successful.
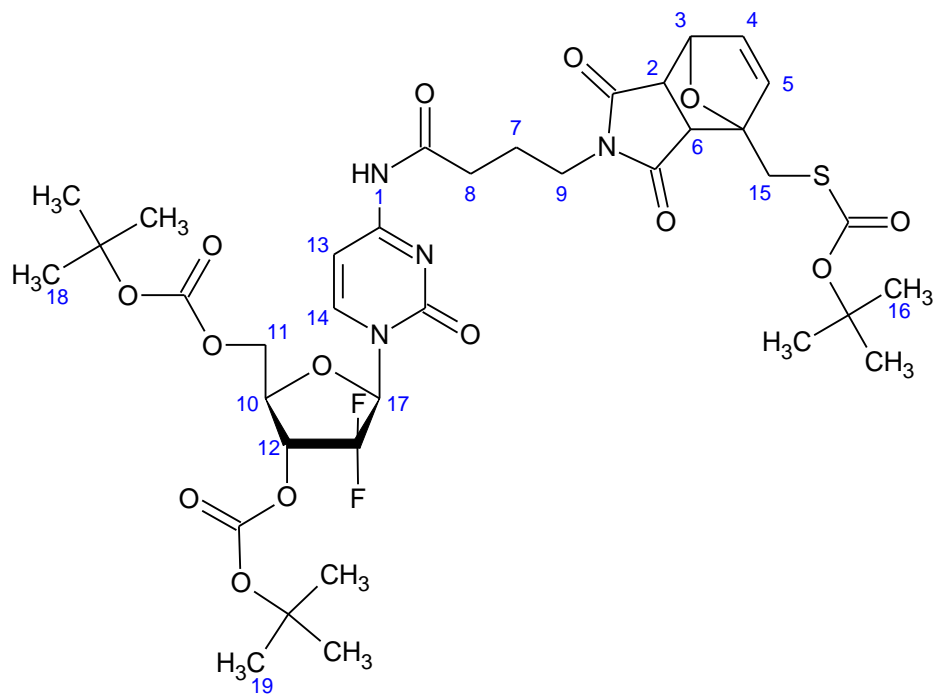
Figure 121: Reaction scheme for the amide coupling between 3',5'-O-Bis(tert-Butoxycarbonyl)gemcitabine and BDA to produce Boc-TTLD
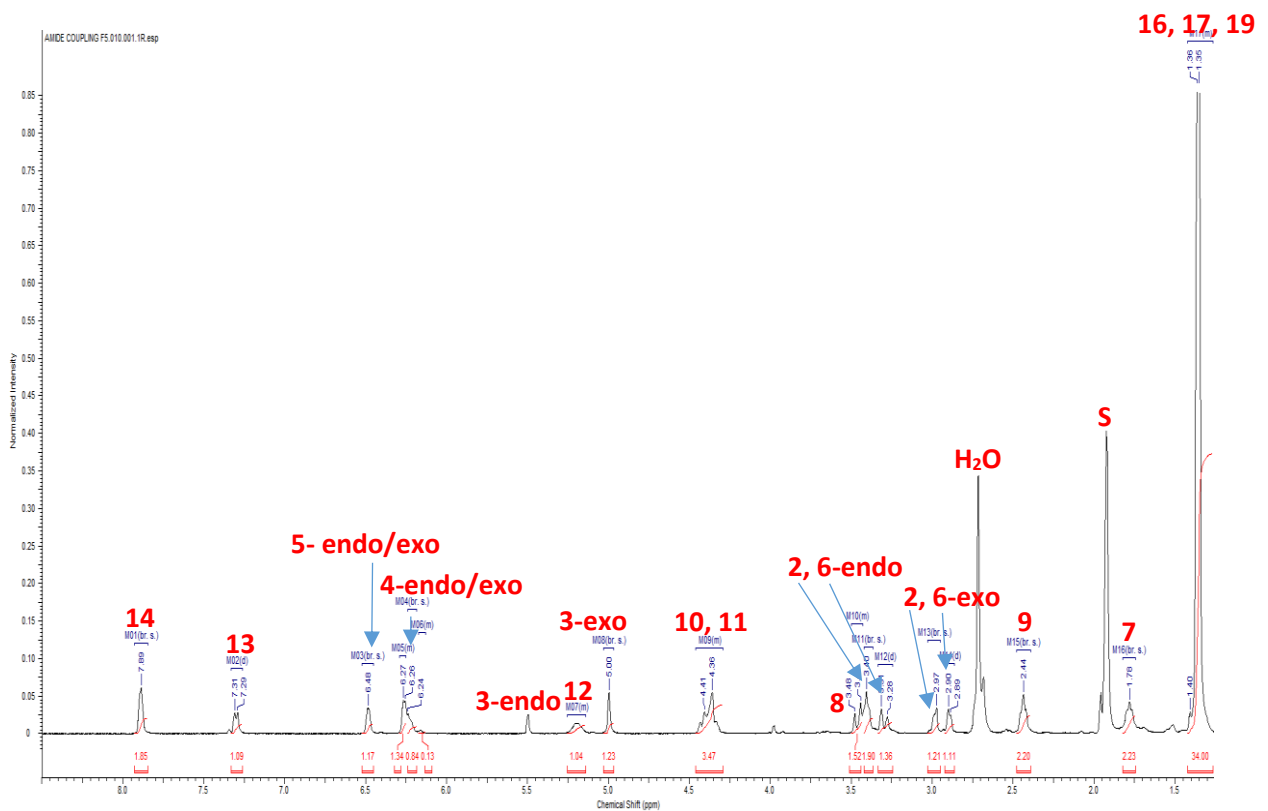
Figure 122: 1H NMR spectrum of Boc-TTLD in acetone_d carried out using 400MHz NMR at 25 °C.

2.3.14.2. TLC analysis of Boc-TTLD

TLC analysis of the Boc-TTLD mixture post workup was carried out to clarify its purity. An illustration of the TLC plate is displayed in Figure 123. The Rf value of this compound is 0.61 in a petroleum ether – ethyl acetate (1:1) solvent system. Three spots for the two starting materials and product were visible indicating the work up mixture required further purification.
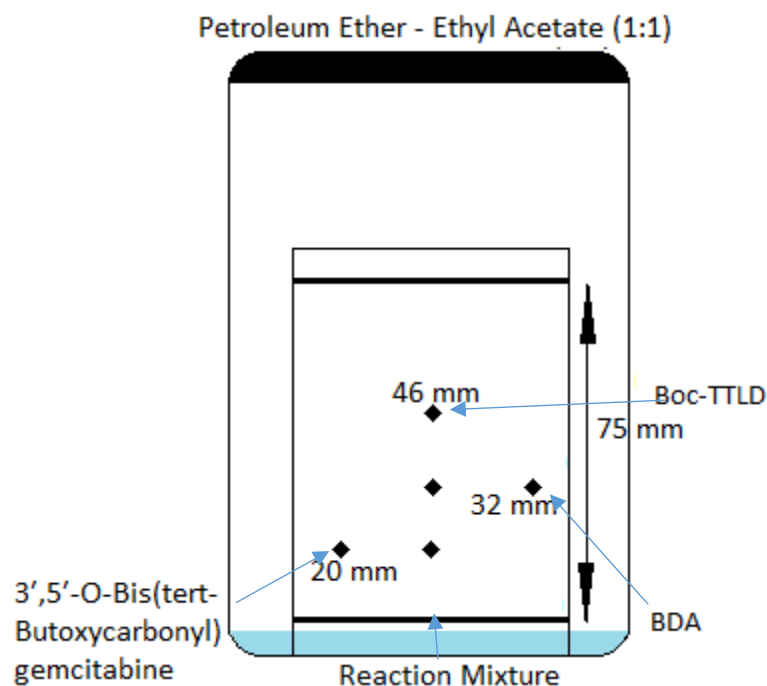
Figure 123: TLC plate of Boc-TTLD post work up.

Column chromatography of the reaction mixture illustrated in Figure 68 was carried out. The pooled fractions from that column were dried and the resulting dark orange solid was analysed by TLC showing a pure compound as illustrated in Figure 124.
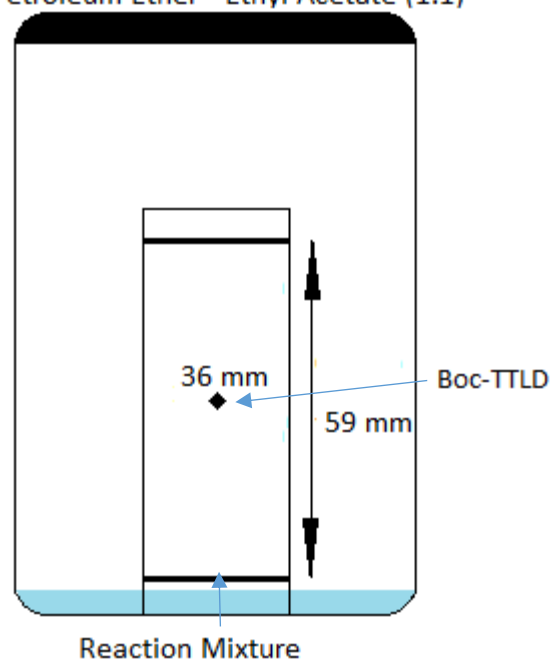
Figure 124: TLC plate of Boc-TTLD post column chromatography.

2.3.15. Analytical data of TTLD

2.3.15.1 ^{1}H NMR spectrum of TTLD

The NMR spectrum (Figure 126) of TTLD (Figure 125) showed the following peaks: 8.31 (doublet J=7.2Hz [15], 1H), 7.38 (doublet J=7.2Hz [14], 1H), 6.63 (singlet J=0.9Hz [6], 1H), 6.41 (doublet [5], 1H), 6.28 (triplet [16], 1H), 5.14 (doublet [4] 1H), 4.48 (multiplet [13] 1H), 4.02 (doublet [12a,11], 2H), 3.89 (doublet J=3.8Hz [12b], 1H), 3.56 (triplet [10] 2H), 3.54 (triplet [3], 1H), 3.46 (doublet [7], 1H), 3.11 (doublet [2], 2H), 2.56 (triplet [9], 2H), 2.29 (triplet [1], 1H), 1.91 (quintet [8], 1H). TFA deprotection of the boc protected thermally labile linker was carried out to remove the boc groups. This was successfully achieved and noted by the disappearance of the very tall singlet at δ1.5 ensuring the complete removal of the boc protecting groups. The pyrimidine protons remained and had shifted to δ8.31 and δ7.45. This was a confirmed indicator of the boc groups' removal based on the literature data of 3', 5'-O-Bis (tert-Butoxycarbonyl) gemcitabine in the paper by (Guo & Gallo 1999) and that the amide bond remained. The cluster of peaks for CH and CH_2 protons around δ4.5 had shifted downwards to δ4.02 and δ3.89. The CH proton has also shifted down field from δ5.2 to δ4.48. These proton signal shifts around the hydroxyl groups indicate the removal of the boc groups that were previously present. The emergence of a triplet at δ2.29 for the SH proton further indicates the boc group protecting the thiol group has been removed.
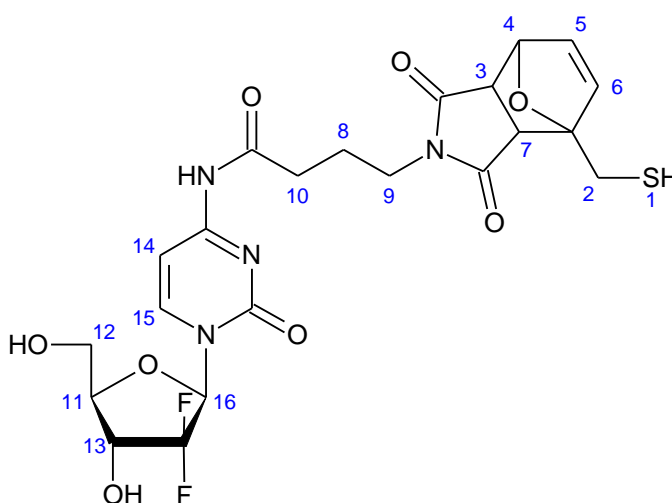
Figure 125: Reaction scheme for the TFA Deprotection of Boc-TTLD to produce TTLD.
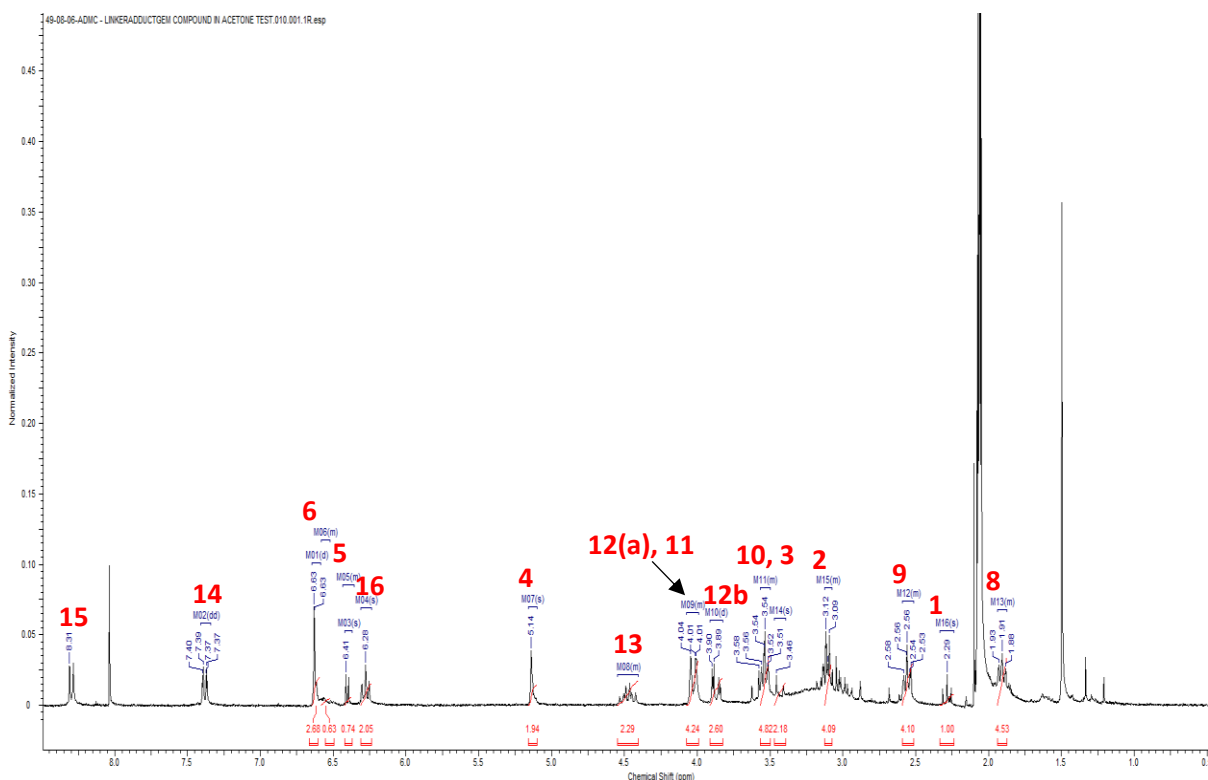
Figure 126: ^{1}H NMR spectrum of Boc-TTLD in acetone_d carried out using 400MHz NMR at 25 °C.

2.3.14.2. TLC analysis of TTLD

TLC analysis of the TTLD mixture post workup was carried out to clarify its purity. An illustration of the TLC plate is displayed in Figure 127. The Rf value of this compound is 0.55 in a dichloromethane - acetone (1:1) solvent system. Two spots were visible indicating the work up mixture required further purification.
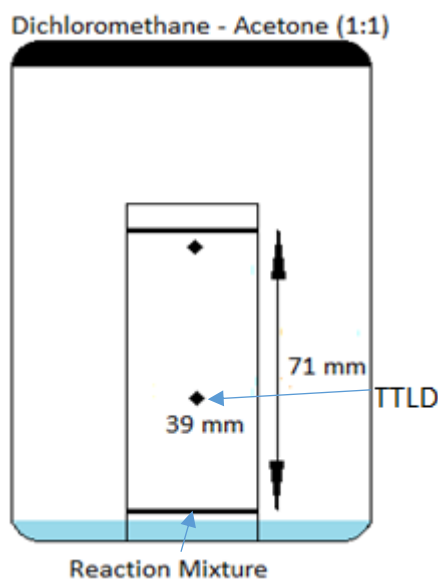
Figure 127: TLC plate of TTLD post work up.

Column chromatography of the reaction mixture illustrated in Figure 69 was carried out. The pooled fractions from that column were dried and the resulting orange solid was analysed by TLC showing a pure compound as illustrated in Figure 128.
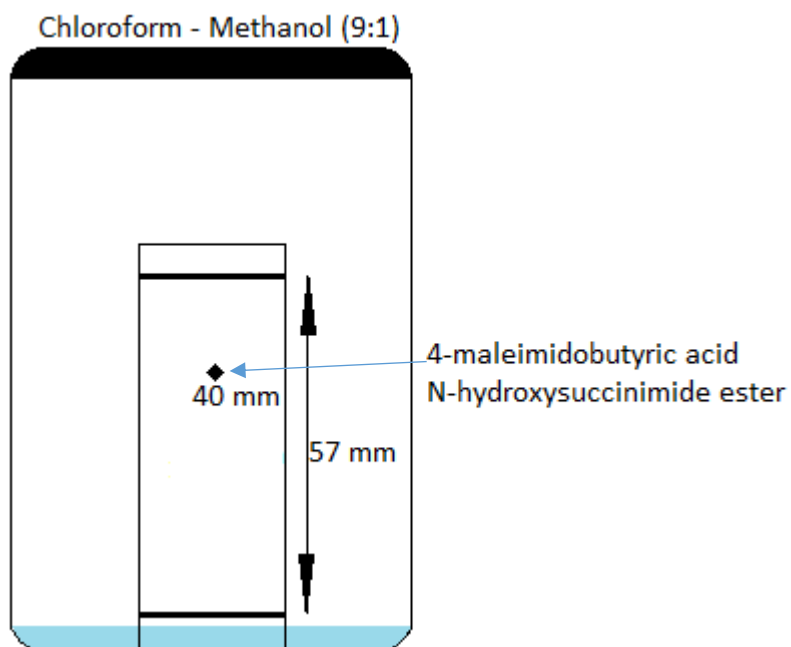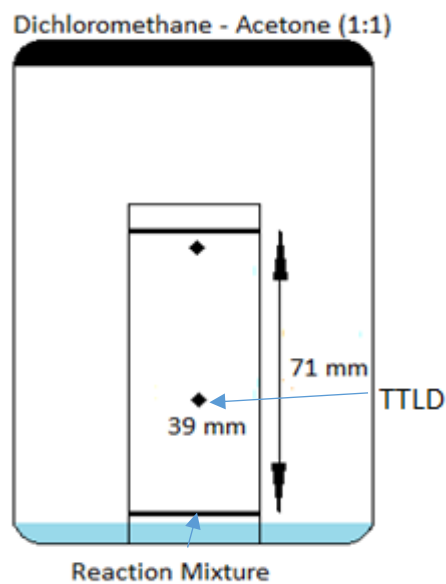

Figure 128: TLC plate of TTLD post column chromatography.

2.3.14.3. Mass spectrometry analysis of TTLD

Mass spectrometry of the synthesised TTLD compound was carried out and the relevant area of the resultant spectrum is shown in Figure 129. The formula mass of TTLD is 542.51 g mol^{-1}.
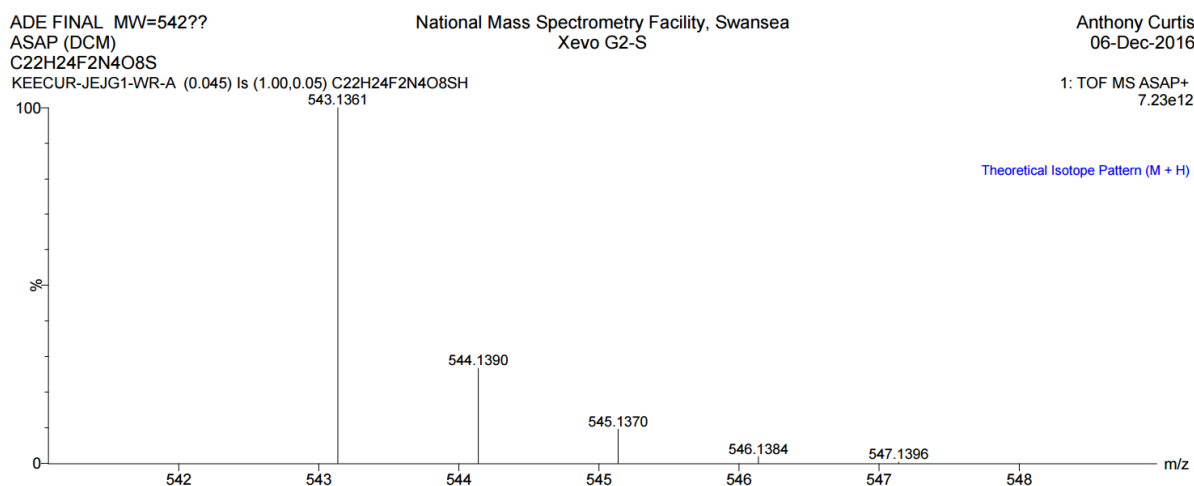
Figure 129: Mass spectrum of TTLD.

The most abundant peak occurs at an m/z value of 543.136 which is the mass/charge that a protonated (M+H+) form of TTLD would have. This evidence supported by NMR analysis and FTIR is a further affirmation that the synthesis of TTLD was successfully carried out.

2.3.16. Analytical data for the retro Diels Alder (drug release simulation) experiment of TTLD

2.3.16.1 ^{1}H NMR spectrum for the retro Diels Alder (drug release simulation) experiment of TTLD

The peak at δ6.41 (maleimide proton) shown in Figure 130 was monitored as its reduction was an indication of retro Diels Alder taking place. The integration of this peak was compared to another at δ4.48. The chemical shifts for the peaks in the NMR spectra shown in Figure 131 differ from what is stated due to a technical problem with the NMR equipment during the experiment.
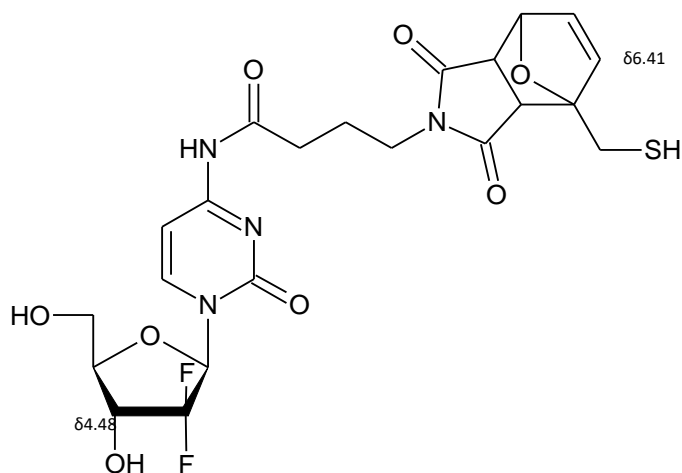
Figure 130: Chemical structure of TTLD.
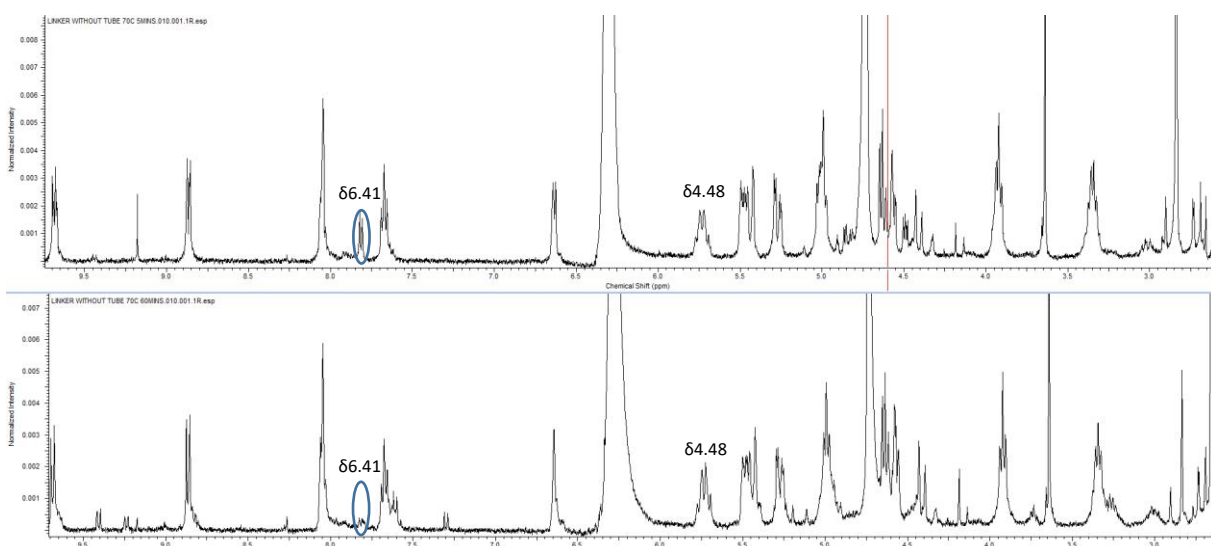
Figure 131: Comparison of the NMR of the thermally labile linker at the 5 minute and 60 minute mark. Note the reduction of the peak highlighted.

Figure 132 is a graph displaying the change in the integration of the peak at δ6.41 over time (progression of retro Diels Alder), at 20 °C, 37 °C, 45 °C and 70 °C. The application of heat triggers the retro Diels Alder reaction with increasing amounts depending on the temperature. These values could be used to demonstrate the release profile of a drug loaded HNP. At room temperature (20 °C) there is no detectable retro Diels Alder reaction which demonstrates the TTLD's stability at ambient temperatures.
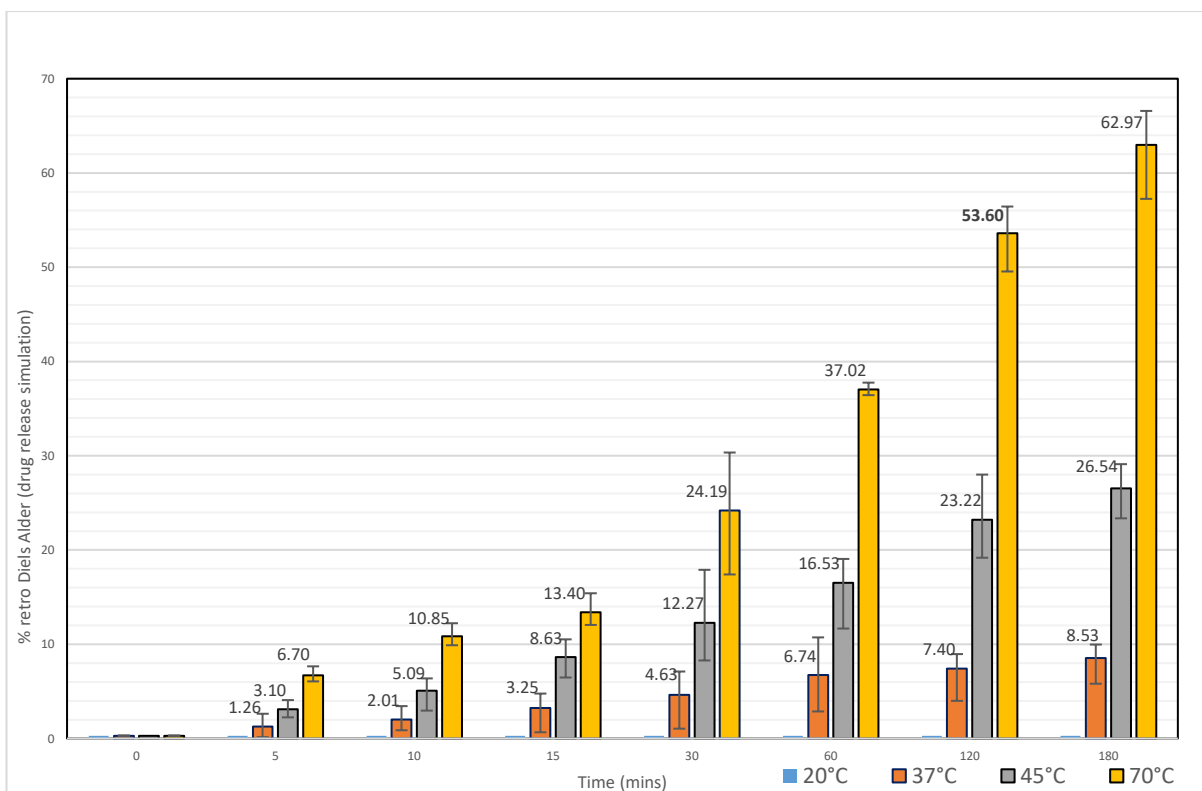
Figure 132: Progression of the retro Diels Alder reaction of TTLD over time at 20 °C, 37 °C, 45 °C and 70 °C.

One thing to note is that this reaction takes place within a closed system. As a result there is a combination of the forward and reverse reaction occurring. Within a tumour, the released drug/maleimide compound would travel away from the HNP surface preventing a Diels Alder reaction from taking place again. Therefore the rate of retro Diels Alder is expected to be higher in vivo than within the closed system of a round bottom flask.

2.4. Discussion

The synthesis of TTLD with an attached gemcitabine molecule was successful after a series of synthesis reactions. NMR, IR and mass spectrometry analysis of TTLD indicated the complete boc deprotection of the thiol and hydroxyl groups. Coincidentally a very strong garlic odour can be detected from the compound which is a common trait amongst thiol compounds (Node *et al*. 2001). Low aqueous solubility is a major problem for the development of new drug formulations (Savjani *et al*. 2012). Removal of the hydrophobic boc protecting groups improved the water solubility of TTLD which is an ideal attribute for a drug formulation to have (Savjani *et al*. 2012). The presence of the carbonyl and hydroxyl groups aid in enhancing the solubility of TTLD by increasing its hydrogen bonding with water molecules (Savjani *et al*. 2012).

The repeated synthesis of TTLD requires the production of 4-maleimidobutyric acid N-hydroxysuccinimide ester and the boc protection of 2-furanmethanethiol (66 % and 93 % yields respectively) (1st generation). The subsequent Diels Alder reaction has an average yield of 48 % for the cycloadduct (2nd generation). The boc protection of gemcitabine has an average yield of 63 % (2nd generation) and its amide coupling reaction with the aforementioned cycloadduct had a 62 % yield (3rd generation). The TFA deprotection step (4th generation) resulted in a yield of 47 % for TTLD. This 4 generational reaction synthesis therefore has an overall yield of 25 % when based on the lowest yield 1st generation reaction (synthesis of 4-maleimidobutyric acid N-hydroxysuccinimide ester).

The retro Diels Alder experiments to simulate drug release, were successful in displaying the potential of TTLD for drug release at elevated temperatures. At the human body temperature (37 °C), the rate of retro Diels Alder was very slow where only 9 % of the cycloadduct had undergone retro Diels Alder after 180 mins. Increasing the temperature by 8 °C (from 37 °C to 45 °C) and the same amount of release would occur within 15 mins. The extent of the surface plasmon resonance heating effects, have already been observed and documented in literature (Curtis *et al*. 2015). A 5 µg mL^{-1} HNP solution when exposed to a 1064 nm laser, caused a temperature increase of up to 7 °C on a 2 % agar phantom after a 60 sec exposure time when measured with a thermal camera (Curtis *et al*. 2015). The agar phantom used (2 %) has been considered a good mimic for biological tissue (Li *et al*. 2011). This heating effect diminishes away from the site of laser contact where no

heating is experienced beyond 5 mm. At a 4 mm heating range, the temperature still rises by 7 °C which would bring the overall temperature of cancerous cells within range to 49 °C (Curtis *et al*. 2015). Figure 133 displays the "drug release" as indicated by the percentage retro Diels Alder at 45 °C where 0.45 % of the TTLD will undergo retro Diels Alder after 1 min of laser irradiation. This effect will be higher at 49 °C. This laser study reported that the exposed area returned to ambient temperatures within 4 min (Curtis *et al*. 2015). Therefore multiple 1 min exposures every 4 min would lead to a cumulative release of TTLD.
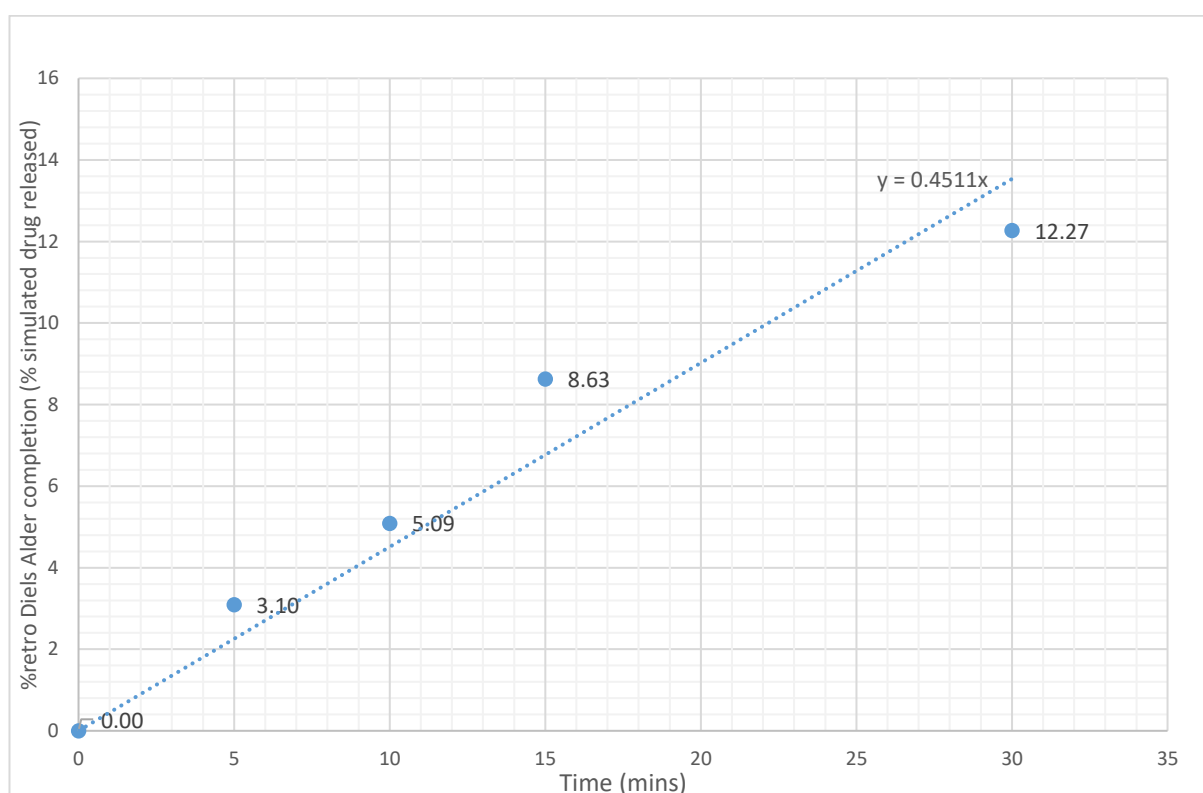
Figure 133: Graph depicting the % retro Diels Alder over time at 45 °C as a simulation for drug release over time.

The 0.45 % per min retro Diels Alder result was acquired by heating TTLD within a closed system (sealed round bottom flask). Therefore both the Diels Alder and retro Diels Alder was taking place establishing an equilibrium between the products and reactants, in which the more heat resistant exo isomer would have been forming over time (Peterson *et al*. 2011). In a clinical setting, any gemcitabine molecules released due to the retro Diels Alder reaction, would migrate away from the HNP surface and carry out its pharmacodynamics purpose. This would prevent the Diels Alder reattachment to the HNP surface. Therefore it can be argued that the drug release recorded is lower than the potential *in vitro* release rate, which will be determined in chapter 3.

Gemcitabine is usually administered intravenously over 0.5 h where significant amounts fail to reach its intended target due to 1st pass metabolism and uptake into healthy tissues (Pliarchopoulou & Pectasides 2009). This causes the systemic side effects commonly associated with chemotherapy. The attachment of TTLD to HNPs followed by a direct injection into the solid tumour would eliminate the side effects associated with chemotherapy (Becker *et al*. 2013). The HNP drug formulation would accumulate inside cells and a clinical patient could receive multiple 1 min doses of infrared radiation with 2 min cooling down phases at the tumour site, which would release the drug payload from the HNP surface. This highlights the thermally labile nature of this linker and its potential as a heat triggered drug formulation. At room temperature (20 °C) there was no detectable retro Diels Alder taking place which gives credence to the stability of TTLD at room temperature for long term storage.

2.5. Conclusion

Synthesis and characterisation of TTLD, plus the data acquisition highlighting its potential as a promising formulation, for heat triggered drug release was successfully completed. The next task involved the attachment of TTLD to HNPs with a thiol-gold dative covalent bond, in order to gauge the effects of SPR on the drug release rates of this formulation and ultimately on cell proliferation with *in vitro* studies.

CHAPTER 3: SYNTHESIS, DRUG LOADING AND RELEASE STUDIES OF HYBRID NANOPARTICLE FORMULATIONS

3.0. Introduction

Hybrid nanoparticles (HNPs) comprising of an iron oxide core with a gold coating are capable of strong covalent binding with thiol groups due to the dative covalent bond that forms between their gold shell and the sulphur atoms (Hoskins, Yue Min, Gueorguieva, et al. 2012; Jazayeri et al. 2016; Wang et al. 2013). As discussed previously, HNPs are theranostic agents due to the imaging properties of their iron oxide core which can be used for diagnosis purposes and their therapeutic properties, due to the surface plasmon resonance (SPR) attribute from the gold coating, which will be used to facilitate the controlled release of drug compounds via a thermally labile linker (Savka I. Stoeva *et al.* 2005; C.-H. Wu *et al.* 2014; Santhosh & Ulrih 2013b). Production of these HNPs occurs via a multi-step process, starting with the synthesis of iron oxide nanoparticles using an established co-precipitation method (Hoskins, Yue Min, Gueorguieva, et al. 2012a) with subsequent gold coating. This leads to the synthesis of HNPs reported to have long term stability for over 6 months at room temperature as well as stability in pH ranges which mimic physiological conditions i.e. lysosomes (pH 4.6) and blood (pH 7.4) (C. M. Barnett et al. 2013). The stability of the previously synthesised thiolated thermally labile drug (TTLD) which when released at various pH's needs to be studied to ensure this formulation is clinically robust in cellular and systemic environments. This release leads to the formulation of a gemcitabine-maleimide analogue (Gem-Mal). Figure 134 shows the chemical structure of these two compounds.
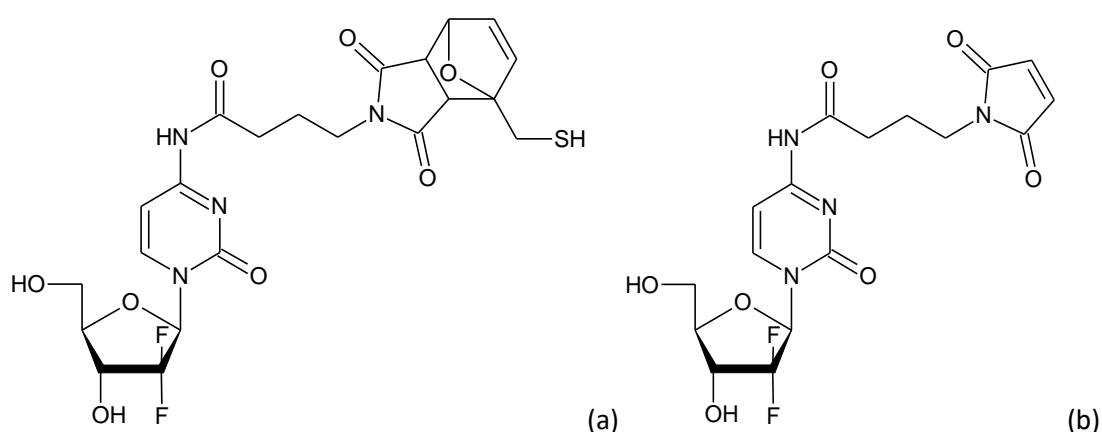
Figure 134: Chemical structure of TTLD (a) and its release form Gem-Mal (b).

The thermal effects arising from the surface plasmon resonance properties of HNPs is already an established fact, where a 50 µg mL^{-1} suspension of HNPs in 2 % agar phantom

raised the temperature to 82 °C (Curtis *et al*. 2015). This study also noted that thermal rise was dependant on laser exposure time and the HNPs concentration. Therefore a lower concentration and/or shorter laser exposure time would increase the temperature to the desired value of 44 °C.

The effect of this heating on cell proliferation has also been observed in a study that involved exposing HNPs to pancreatic cancer cells. Confirmation of the successful uptake of the HNPs was determined by washing the cells with PBS and imaging them with TEM (Guo et al. 2013). The result of this study concluded that the HNPs themselves had no effect on cell proliferation, which meant these HNPs have no cytotoxic properties (Guo *et al*. 2013). The images in Figure 135, explain this further where the cells (A) remained unaffected after a 7.9 W cm^{-2} exposure for 5 min followed by a 24 h rest in image (D) (Guo *et al*. 2013).
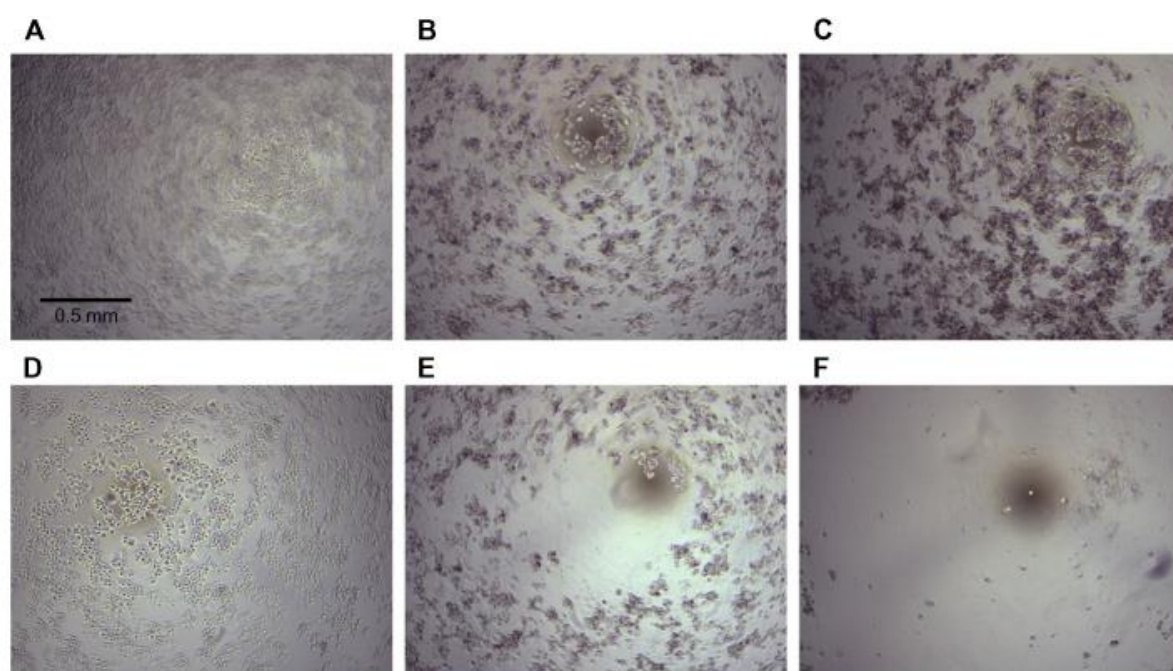
Figure 135: PaNc-1 cells exposed to 0, 25, and 50 µg mL-1 dose of nanoparticles, respectively, without laser irradiation (A–C) and with laser irradiation at 7.9 W cm-2 power density (D–F) (Guo *et al*. 2013).

The uptake of the 25 µg mL^{-1} and 50 µg mL^{-1} suspensions in image B and C in Figure 135, clearly shows the presence of the HNPs within the cells. After exposure to the same 7.9 W cm^{-2} laser for 5 min, there is a clear loss of cell proliferation for the 25 µg mL^{-1} image (B) after 24 h (E) where the authors of this study stated the cell proliferation fell to 22 %. With the 50 µg mL^{-1} suspension (C), this effect is more pronounced with a cell proliferation of

only 2.3 % after a 5 min exposure to the 7.9 W cm^{-2} laser followed by a 24 h rest. The relationship between temperature and laser intensity is shown in Figure 136.
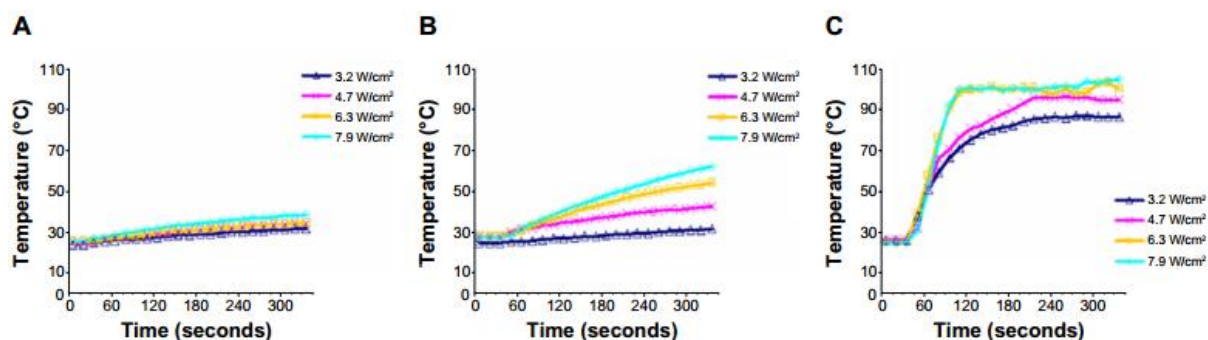
Figure 136: Photothermal response of 0 (A), 25 (B), and 50 (C) μg mL-1 nanoparticle samples at 3.2, 4.7, 6.3, and 7.9 W cm-2 (Guo *et al*. 2013).

The graphical data in Figure 136, shows a significant difference in temperature increase when HNPs are exposed to laser light, compared to the control (A) and the temperature increases over time. The effect of HNP concentration and laser intensity is also shown due to the sharper rise and plateauing of the detected temperature in the 50 μg mL^{-1} compared to the 25 μg mL^{-1} (Guo *et al*. 2013). This clearly shows that the surface plasmon resonance properties of HNPs can be exploited for destroying pancreatic cancer cells and that the HNPs concentration affects the extent of cellular destruction. Due to the close proximity of cancerous tumours to healthy tissue, it would not be feasible to heat up pancreatic tumours to a high enough temperature to cause cell death, without damaging nearby healthy tissue. However, if the cancer cells are not heated high enough, they will survive and regrow. The use of TTLD attached to HNPs will bridge these two conflicting problems. The use of SPR will be utilised to heat up TTLD to a high enough temperature to trigger the release of Gem-Mal, but not too high to damage nearby healthy tissue. The pancreatic cancer cells, already stressed by constant replication and exposure to elevated temperatures should also be quite susceptible to the sudden presence of a large concentration of Gem-Mal following the retro Diels Alder of TTLD. This threefold exploitation of pancreatic cancer weaknesses should prove effective.

Another study that evaluated the potential of hybrid iron oxide-gold nanoparticles as heat triggers for pancreatic cancer therapy looked at both the *in vitro* and *in vivo* outcome of administered HNPs and production of heat shock proteins (HSP-27 and HSP-70) which are produced under heat related stressful conditions in cells (Oluwasanmi *et al*. 2016). These

proteins are classed as molecular chaperones that assist various protein folding processes such as the folding of newly synthesised proteins and the refolding of misfolded proteins (Sonuç Karaboğa *et al*. 2016). The elevation levels of these proteins after laser irradiation of absorbed 5 µg mL^{-1} and 50 µg mL^{-1} HNP suspensions in Figure 137 were determined by ELISA and indicate that the cells are stressed by the increase in the heat generated by surface plasmon resonance of the gold surface (Oluwasanmi *et al*. 2016).
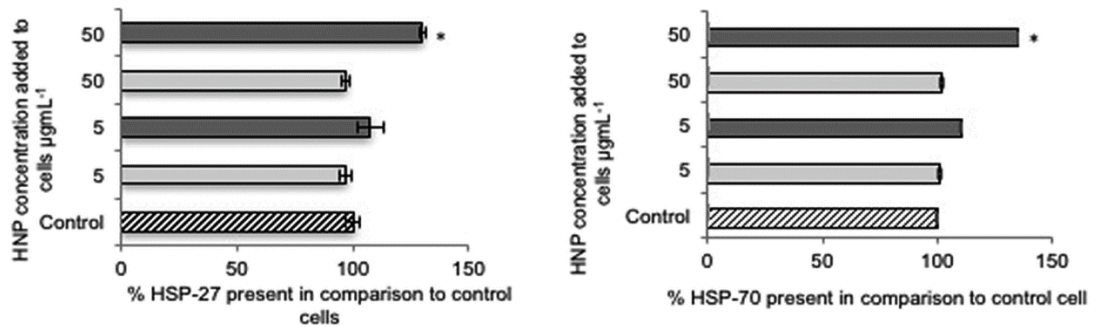
Figure 137: Comparison of HSP-27 and HSP-70 levels with the addition 5 µg mL-1 and 50 µg mL-1 HNP suspensions before and after 60 seconds of laser exposure (Oluwasanmi *et al*. 2016).

The effect of this heating on cell viability was also determined with trypan blue exclusion in which the results from this study was in line with those from the ELISA measurement of heat shock proteins in Figure 138. Cell viability remained at 100% after the 5 µg mL^{-1} HNP suspension was absorbed without laser irradiation and decreased slightly after a single 60 second laser exposure and more so after multiple irradiation cycles. The decrease in cell viability after single and multiple laser exposure was more significant in the 50 µg mL^{-1} HNP suspensions where cell viability fell to 85 % after multiple laser irradiations of 50 µg mL^{-1} absorbed HNPs (Oluwasanmi *et al*. 2016).
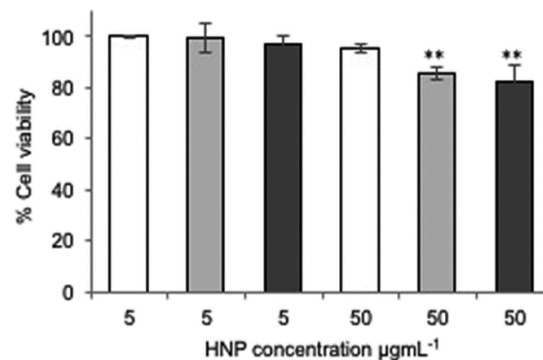
Figure 138: Effect of HNP concentration on cell viability. From left to right: 5 µg mL-1 without laser exposure, with a 60 second laser exposure, multiple irradiations and 50 µg mL-1 without laser exposure, with a 60 second laser exposure, multiple irradiations (Oluwasanmi *et al*. 2016).

144

The heat dissipation of HNPs within tumours was also carried out on Bx-PC3 xenograft mice. With the use of a thermal imaging camera, the extent of heat dissipation within and beyond the treated tumour was determined. In Figure 139-(D1) we can see a sharp temperature rise upon laser exposure which reaches its maximum after 10 seconds for the tumour previously treated with an injected 50 µg mL^{-1} HNP suspension. Without the presence of HNPs in Figure 139-(B1-3) there is no tissue heating being observed. Upon injection of the 50 µg mL^{-1} HNP the heat maps in Figure 139-(C1-3) clearly show that the elevated temperatures is confined more to the tumour only (Oluwasanmi *et al*. 2016).
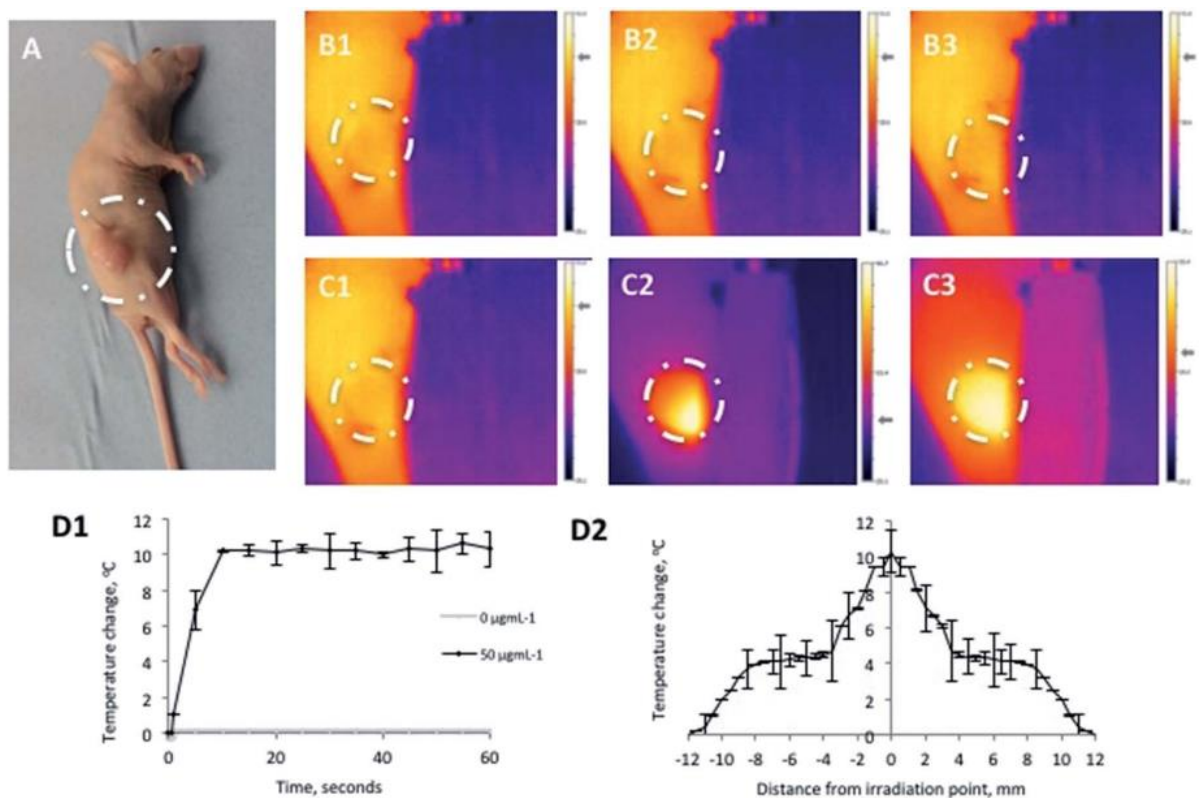
Figure 139: Effect of in situ laser irradiation of HNPs injected I.T. in pancreatic xenograft models. (A) Nu/Nu xenograft (BxPC-3) tumour bearing mouse, (B & C) heat dissipation maps of tumours absent (B) and with 50 mg mL1 HNPs I.T. (C) at (1) t 1⁄4 0 s, (2) t 1⁄4 30 s and (3) t 1⁄4 60 s. (D) Quantification of (1) thermal rise at irradiation point and (2) heat dissipation away from laser focal point measured using a thermal imaging camera (n 1⁄4 3 SD) (Oluwasanmi *et al*. 2016).

This study confirms that in an *in vivo* environment, HNPs can be utilised to increase the temperature of tumours after laser irradiation. The 50 µg mL^{-1} HNP suspension was utilised due to the improved reduction in cell viability shown in Figure 138 compared to the 5 µg mL^{-1} HNP suspension. At 5 µg mL^{-1} HNP suspension the HNPs are not close enough to generate a high increase in bulk temperature and the cells seem capable of tolerating HNP

concentrations of 50 μg mL^{-1}. The combined action of a rise in bulk temperature and the heat triggered release of anticancer agents should produce an enhanced effect on the reduction of cell viability (Oluwasanmi *et al*. 2016).

The synthesis of HNPs, their drug loading and drug release studies were carried out and quantified by various commonly used analytical techniques such as, zeta potential measurements, transmission electron microscopy, high performance liquid chromatography, inductively coupled plasma-optical emission spectroscopy and UV-Vis spectroscopy. HNPs were analysed at every major step of their synthesis by measuring their zeta potential, their gold and iron content and their morphology using transmission electron microscopy. Drug loading and drug release studies were monitored with HPLC. The procedures used for these techniques will be described below.

3.0.1. Zeta potential

Zeta potential of a nanoparticulate dispersion is a measure of the electric potential energy or voltage of these nanoparticles at their surface and compared with the charge of the bulk solution (Montes Ruiz-Cabello *et al*. 2014). The effects of zeta potential is more prominent in solutions comprising of very small particles where their size promotes extended dispersion that can be further augmented with electrostatic interactions. With a large enough zeta potential, dispersed particulates will be electrostatically repulsed and resist aggregation. Zeta potentials between ±0-10 mV, 10-20 mV, 20-30 mV and 30+ mV are considered "highly unstable", "relatively stable", "moderately stable", and "highly stable" respectively (Patel & Agrawal 2011; Bhattacharjee 2016). The zeta potential of particulate dispersions is very important for pharmaceutics where producing non-aggregating and easily dispersible formulations is highly regarded. However at increased zeta potential, biocompatibility issues are experienced. Therefore a balance of zeta potential and biological activity is required when designing pharmaceutical products.

3.0.2. Transmission electron microscopy

Electron microscopy like other microscopic techniques is used for observing the surface of materials at a detail too high for the naked eye. Conventional optical microscopes use a series of lenses to magnify the images of materials to a size visible with the naked eye. However these lenses diffract visible light and are limited by the Abbe diffraction limit,

which is the point where a microscope cannot distinguish two objects close to each other (Nature 2009). This diffraction limit is based on wavelength and is the highest magnification point where light can be diffracted enough to resolve two objects side by side. Blue objects for example can be resolved at a higher magnification than red ones due to blue lights shorter wavelength. This limit still allows for the imaging of objects as small as chloroplasts of 5 μm width (Sadava 2008). The use of electron microscopes is necessary to resolve images up to the 1 nm range and is made possible due to the wavelength of electrons being far smaller than of visible light (Sadava 2008). The two most commonly used forms of electron microscopy are transmission electron microscopy (TEM) and scanning electron microscopy (SEM). TEM involves passing a beam of electrons through a sample and using the detection of unaffected electrons (that passed through unimpeded), reflected and scattered electrons to produce an image on a fluorescent screen (Dean *et al*. 2002c). SEM also involves the use of an electron beam. The main difference is that this beam is scanned across the surface of the sample. This allows the topography of the sample to be mapped (Dean *et al*. 2002c).

3.0.3. High performance liquid chromatography

High performance liquid chromatography (HPLC) is a chromatographic technique that is involved in the separation and analysis of components within a mixture (Neue 2007; Dean *et al*. 2002c). It involves the passing of sample mixtures in a solvent (mobile phase) through a column of an adsorbent (stationary phase) with high pressure. With the same mobile and stationary phase, each component in a mixture will travel through the column at different speeds (Dean *et al*. 2002c).

The specific time taken for a specific mixture component to travel through the column is called its retention time. This retention time can be changed depending on various factors. One such effect is the polarity of the column adsorbent. Columns containing polar adsorbents will have a higher affinity for polar components in a separation mixture. This is the case with normal-phase HPLC systems. These polar components will then travel slower than the column leading to longer retention times. Conversely if a non-polar solvent is used then the non-polar components of the mixture will have a greater affinity for the mobile phase (solvent) and travel through the column quicker which shortens their retention time. Reverse-phase HPLC systems use a non-polar stationary phase and an aqueous polar

147

mobile phase instead. Longer columns will increase the retention time, as it increases the distance components must travel before reaching the end. Changing the relationship between the mobile phase (solvent) and stationary phase (column) will affect the retention time as well. For example, if the flow rate is increased the retention time will decrease as more material can be carried through the column at any one time. This is also the case with increasing the pressure of the solvent as it passes through the column. These factors are relevant in an optimised HPLC system. If the column is degraded the retention time will decrease overall and the extent of this retention time decrease, will depend on the mixture components affinity for the stationary phase.

After a component from a mixture has travelled through the column it is often analysed with an analytical technique. Some techniques that can be used in conjunction with HPLC include the commonly used UV/Vis spectroscopy, fluorescence spectroscopy, mass spectrometry and electrochemical detectors (Dost & İdeli 2012; Khare *et al*. 2016; Ansari & Häubl 2016; Campos *et al*. 2016). In drug formulation, HPLC is commonly used for drug quantification studies. These may measure the extent of drug incorporation or the binding onto a structure or to measure drug release from a system.

3.0.4. Inductive coupled plasma – optical emission spectroscopy

Inductively coupled plasma – optical emission spectroscopy (ICP-OES) is an analytical technique used for detection and measurement of metals by analysing the emission of electromagnetic radiation from excited metal atoms and ions (Parham *et al*. 2009). Emission of these electromagnetic waves is achieved by exposing metal atoms to a plasma source. The excited electrons return to ground state emitting electromagnetic radiation at specific wavelengths for that atomic species (Lee *et al*. 2003). The sample must be a solution which may require acid digestion to aid in ionisation of the sample within the plasma (Y. Yang *et al*. 2016). This solution is then injected as a fine aerosol by combining it with a stream of argon gas which acting as a nebulizer (Todolí & Mermet 2006). This aerosol is carried through an argon plasma of around 7000 °C to excite the outer electrons of the metals within the sample. This technique is commonly used in inorganic chemistry to quantify metallic composition in systems such as concentration or iron and gold in hybrid nanoparticles.

3.0.5. UV/Vis spectroscopy

UV/Vis spectroscopy is an analytical technique used to measure the absorbance of visible light and near ultraviolet radiation of materials, typically organic compounds with conjugation and transition metals (Dean *et al*. 2002c). Predicting the frequencies of least absorbances is possible because the colour of an object corresponds to the frequencies of light least absorbed or reflected (Dean *et al*. 2002c). Atoms and molecules exposed to the visible light and near ultraviolet range of the electromagnetic spectrum enter electronic transition states, as their electrons absorb the energy of the UV/Vis light and move to higher excited transition state (Atkins 2006b). This makes UV/Vis spectroscopy a form of absorbance spectroscopy (Dean *et al*. 2002c; Razzazan *et al*. 2016). UV/Vis spectroscopy is carried out by dissolving the material of interest in a solvent within a cuvette. After a blank calibration is carried out, the sample is exposed to light and UV radiation and the absorbance over a determined range of wavelengths is calculated. A diagram of UV-Vis analysis is shown in Figure 140.
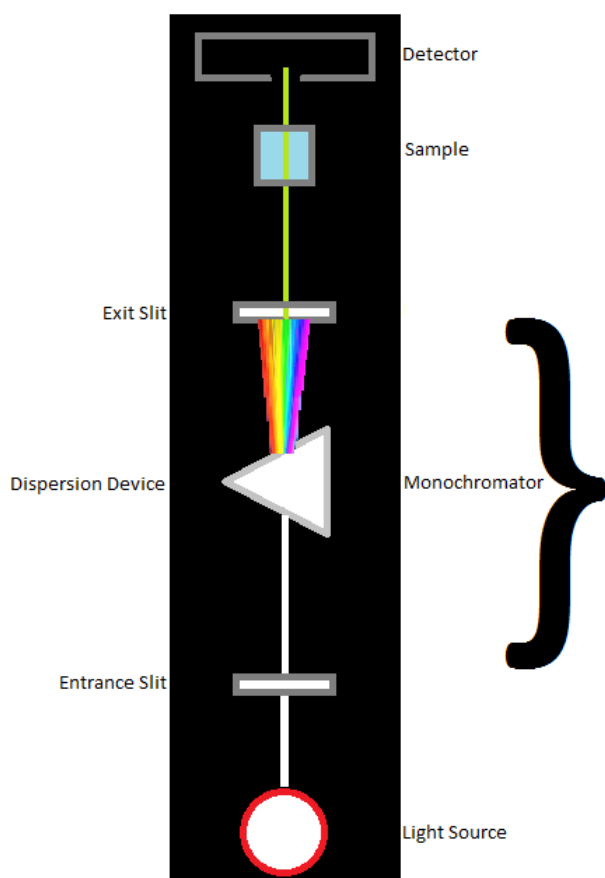
Figure 140: Diagram of UV-Vis schematic.

The amount of absorbance is proportional to the concentration of the sample which makes this technique valuable for producing calibration curves and determining the concentration of unknown samples (Dean *et al.* 2002c). This relationship is described using the Beer Lamberts law:

$$A = \varepsilon\, l\, c$$

Where A is the absorbance, ε is the molar absorptivity, l is the path length (e.g. width of cuvette) and c is the concentration of the sample (Atkins 2006c). The molar absorptivity is value of the absorbance under standard conditions such as (A when l and c = 1) in a calibration series for a specific dissolved species (Atkins 2006c). Once this is established, the concentration of unknowns can be acquired by rearranging the above equation:

$$c = \frac{A}{\varepsilon\, l}$$

This technique is commonly used in drug quantification, especially in conjunction with HPLC. In this study, UV-Vis will be used in order to determine the state of gold coating onto the HNPs and indicate the SPR wavelength which is equivalent to the λ_{max} value.

3.1 Aims and objectives

The aim of the following study was to synthesize hybrid nanoparticles capable of surface modification with TTLD, a gemcitabine analogue with a thiolated thermally labile linker with and without a thiol capped polyethylene glycol (Thiol-PEG). The HNP-drug system developed will be tested *in vitro* for their ability to act as thermally responsive drug delivery vehicles for delivery of a novel gemcitabine analogue. The degree of loading and heat triggered release will be determined with HPLC.

3.2 Materials and methods

3.2.1 Materials used

Material	Supplier
RPMI Media	Fisher Scientific (UK)
Hydrochloric Acid	Fisher Scientific (UK)
Sodium Hydroxide	Fisher Scientific (UK)
Acetonitrile	Fisher Scientific (UK)
O-[2-(3-Mercaptopropionyl amino) ethyl]-O'-methylpolyethylene glycol	Sigma Aldrich (UK)
Potassium Nitrate	Sigma Aldrich (UK)
Iron (II) Sulphate	Sigma Aldrich (UK)
Sulphuric Acid	Sigma Aldrich (UK)
Polyethylene Imine	Sigma Aldrich (UK)
Chloroauric Acid	Alfa Aesar (UK)
Sodium Borohydride	Sigma Aldrich (UK)
Hydroxylamine	Sigma Aldrich (UK)
Dialysis Bag	Medicell (UK)
Nitric Acid	Fisher Scientific (UK)
Formvar	Sigma Aldrich (UK)
Copper grids	Agar Scientific (UK)
Chloroform	Sigma Aldrich (UK)

3.2.2. Methods

3.2.2.1. Synthesis of iron oxide nanoparticles

Sodium hydroxide (1.03 g, 0.026 mols) and potassium nitrate (1.82 g, 0.018 mols) were dissolved in deionised water (180 mL) in a 3 neck round bottomed flask with a fitted condenser. A syringe adaptor was used to bubble nitrogen into the mixture for 15 min before the mixture was heated to 90 °C for a further 20 min. A solution of Iron (II) Sulphate (3.89 g, 0.026 mols) in sulphuric acid (20 mL, 0.01 M) was prepared with the use of sonication to aid in dissolution. This solution was then combined with the previous mixture and heated to 90 °C with nitrogen bubbling through for a further 1 h. The nitrogen pump was removed after 1 h of stirring and the mixture was left to stir for an additional 24 h at 90 °C. The iron oxide nanoparticles (IONPs) were magnetically separated and washed with deionised water 10 times before being suspended in 100 mL deionised water and refrigerated for future use. (Hoskins, Yue Min, Gueorguieva, et al. 2012).

3.2.2.2. PEI coating of iron oxide nanoparticles

The previously synthesised iron oxide nanoparticle (IONP) suspension (10 mL) was added to 100 mL of poly(ethyleneimine) (PEI) (5 mg mL^{-1}) and sonicated for 2 h with a MSE Soniprep 150 Plus Disintegrator. The excess PEI was removed by repeatedly washing and magnetically separating the PEI coated IONPs (IONP-PEI) with deionised water. The IONP-PEI were then suspended in 10 mL deionised water (Hoskins, Yue Min, Gueorguieva, et al. 2012a).

3.2.2.3. Synthesis of gold seed solution

Chloroauric acid $HAuCl_4$ (375 µL, 4 %) and Na_2CO_3 (500 µL, 0.2 M) were dissolved in 100 mL of water chilled to 5 ˚C. After 5 min of stirring, 5 mL of sodium borohydride solution (0.5 mg mL^{-1}) was added over 5 min (1 mL per min). The observation was a colour change from pale yellow to deep red indicating the presence of 2 nm gold seeds. The gold seed solution was stirred for a further 10 min before being immediately utilised or refrigerated (Hoskins, Yue Min, Gueorguieva, et al. 2012).

3.2.2.4. Synthesis of gold coated iron oxide nanoparticles

The previously synthesised IONP-PEI suspension (10 mL) was added to the gold seed solution (100 mL) and stirred for 2 h at room temperature. The nanoparticles were washed and magnetically separated with deionised water before being suspended in a 100 mL solution of PEI (MW 2000) (0.1 mg mL^{-1}) and sonicated for 10 min. The gold seeded particles (Au-seed-IONP's) were then washed 10 times with deionised water before being suspended in 10 mL of deionised water. In order to reduce gold onto the nanoparticle surfaces, the 10 mL suspension of the Au-seed-IONP's was suspended in a solution of sodium hydroxide (0.01M, 110 mL) and stirred. HAuCl$_4$ (0.5 mL, 1 %) was added followed by 0.2M hydroxylamine (0.75 mL) and stirred at room temperature. This step was repeated with 10 min intervals 4 times with 1 % HAuCl$_4$ (0.5 mL) and 0.2 M hydroxylamine (0.25 mL) followed by additional stirring for 30 min. The final solution was then washed 5 times with deionised water and the gold coated iron oxide nanoparticles (HNPs) were suspended in 10mL deionised water (Hoskins, Yue Min, Gueorguieva, et al. 2012a).

3.2.3. Characterisation of synthesised nanoparticles

3.2.3.1. Zeta potential measurement procedure

The surface charge of nanoparticles throughout their synthetic route was measured by introducing very dilute suspensions into folded capillary zeta cells and inserting these cells into a Malvern Zetasizer Nano ZS. The zetasizer was then programmed to analyse samples 100 times at 25 °C (n=3). The overall average zeta potential is used when describing the zeta potential of nanoparticles from now on, unless otherwise stated.

3.2.3.2. Transmission electron microscopy procedure

TEM imaging of the synthesis stages for HNPs was carried out using the Jeol Jem-1230 transmission electron microscope using anaLYSIS software, at the University of Keele. This allowed visualisation of the nanoparticulate size and morphology. Prior to imaging, formvar coated copper grids were prepared. Glass slides were dipped in formvar, and dried using mild heat from a light source. The edges were filed to help raise the film before the glass slides were gently submerged to separate the film from the glass slide surface. The grids were then carefully placed on the floating formvar film. The next step involved taking a

fresh glass slide and slowly slipping the slide under the film so that it attaches to the glass slide surface. The slide was then dried using mild heat from a light source. The samples were pipetted (10 µL) onto the grids and allowed to air dry before imaging with a JEOL, JEM-1230.

3.2.3.3. Inductively coupled plasma – optical emission spectroscopy procedure

Inductively Coupled Plasma – Optical Emission Spectroscopy (ICP-OES) was used to measure the metal content of the HNPs. Samples were prepared first by adding 0.4 mL of suspended nanoparticles to a 1.6 mL solution of 1:1 hydrochloric acid/nitric acid (1:5 dilution of 0.4 mL nanoparticles) to make up a 2 mL mixture, which was gently heated for a few min until dissolution of nanoparticles was achieved. 0.01 mL of this solution was then added to 9.99 mL of deionised water (1:5000 v/v from original 0.4 mL nanoparticle sample). This 10 mL solution was then analysed by an Agilent Technologies 700 series ICP-OES. All intensities were therefore multiplied by 5000 to acquire the concentration of the original 0.4 mL nanoparticle sample based on a calibration curve (R^2 = 0.9997) for iron and (R^2 = 0.9981) for gold. Iron and gold was analysed at a wavelength of 261.187 nm and 242.794 nm respectively.

3.2.3.4. UV-Vis spectroscopy procedure

Uv-Vis spectroscopy characterisation of HNPs was executed by filling a cuvette of path length 10 mm with a solution of the nanoparticles in water. Initially a blank analysis of just water was carried out to eliminate the absorbance of background material in the water. The samples were then analysed with a Varian Cary 50 Bio Uv-Vis spectrophotometer (64 scans) over a wavelength range of 400-700 nm (1 nm, stepwise), in order to determine the lambda max of the HNPs within this range.

3.2.3.5. Drug loading of HNPs procedure

Into a sample tube, 5 mg of HNPs (based on iron mass only) was added followed by 25 mg (based on gemcitabine mass only) of the thiolated thermally labile drug (TTLD) both with and without 25 mg of the O-[2-(3-Mercaptopropionyl amino) ethyl]-O'-methylpolyethylene glycol (PEG-Thiol). The mixture was diluted to 5 mL with deionised water and stirred for 2 h at room temperature. The drug loaded HNPs were magnetically separated and washed

with 5 mL of deionised water. The overall 10 mL "waste solution" was retained and analysed using reverse phase HPLC for drug content. The peak area was used to calculate drug content from a calibration curve (R^2 = 1). Drug attachment onto HNP surface was deduced by subtraction of the unbound drug content from the starting drug weight.

3.2.3.6. High performance liquid chromatography procedure

High Performance Liquid Chromatography (HPLC) was carried out by first injecting an unknown sample solution, comprised of an unknown mixture in a 1:1 v/v water:acetonitrile solvent, into a HPLC vial. The vial(s) were loaded into a Perkin Elmer Flexar LC Autosampler. The flow rate for the solvent phase solution which was isocratically eluted, was 1 mL min^{-1} (1:1 v/v water:acetonitrile) for all samples unless otherwise stated and the sample injection amount is 10 µL. Sample fractions were analysed with UV-Vis spectroscopy in which the lambda max value selected was 268 nm, where gemcitabines pyrimidine is strongly absorbed by UV-Vis spectroscopy. This lambda max is used for all HPLC analysis unless otherwise stated. The retention time of the released drug is 0.77 min with the use of a Pinnacle DB C18 reverse phase column (100 mm length, 1.9 µm particle size, 140 Å pore size, 2.1 mm internal diameter), and the amount of drug released was calculated with comparisons to a previously produced calibration curve of standard drug solution concentrations. The R^2 value of this calibration curve is 1.

3.2.3.7. *In vitro* drug release studies procedure

A dialysis membrane (12-14 kDa, 0.04 mm wall thickness, 31.7 mm diameter, 24 Å pore size) was filled with 2 mL of HNP-drug or HNP-drug-PEG solution. The filled membrane was placed into 200 mL water or cell media at varied pH (7.4, 5.6) under *sink* conditions. The solutions were stirred and the rate of drug release measured at varied temperature. This procedure was applied to the following experimental parameters in Table 8:

Table 8: Experimental parameters for the dialysis drug release studies

pH	Drug Loaded HNPs	Drug + PEG Loaded HNPs
pH 7 (Water)	20°C, 37°C, 44°C	20°C, 37°C, 44°C
pH 5.6 (Cell Media)	20°C, 37°C, 44°C	20°C, 37°C, 44°C
pH 7.4 (Cell Media)	20°C, 37°C, 44°C	20°C, 37°C, 44°C

Aliquots (1 mL) of the solution were taken at various time points (1 min, 2 min, 5 min, 10 min, 15 min, 30 min, 1 h, 2 h, 3 h, 4 h, 24 h, 48 h, 72 h and 96 h) and placed in HPLC vials. Fresh 1 mL of deionised water/cell culture media of appropriate pH was placed back into the conical flask. Total drug release was analysed using HPLC as described in section 3.2.3.6.

3.2.3.8. Stability assessment procedure of HNPs

Into a vial containing 3 mL of a 1:1 (v/v) solution of deionised water and acetonitrile, was added 3 mg of TTLD attached to 0.6 mg of HNPs. This process was repeated seven more times producing eight identical drug/NP suspensions. Four vials were stored at room temperature away from direct sunlight and the other four was refrigerated away from direct sunlight. Every day the vials were shaken and every seven days a 0.1 mL aliquot of each vial was acquired and analysed with HPLC to calculate the amount of GEM-MAL that had released from the HNP surface.

3.3. Results

3.3.1. Synthesis and characterisation of HNPs

The synthesis of HNPs was successful, based analytical results from a combination of zeta potential measurements, ICP-OES analysis and TEM imaging. These were carried out at every synthesis step from iron oxide nanoparticle synthesis to the final gold coated hybrid nanoparticles. Uv-Vis analysis was carried out on both the iron oxide nanoparticles and the gold coated nanohybrids as well.

3.3.1.1. Zeta potential measurement results

The average zeta potential of the uncoated IONPs was measured to be -14.8 mV with a deviation of 4.37 mV as shown in Figure 141.
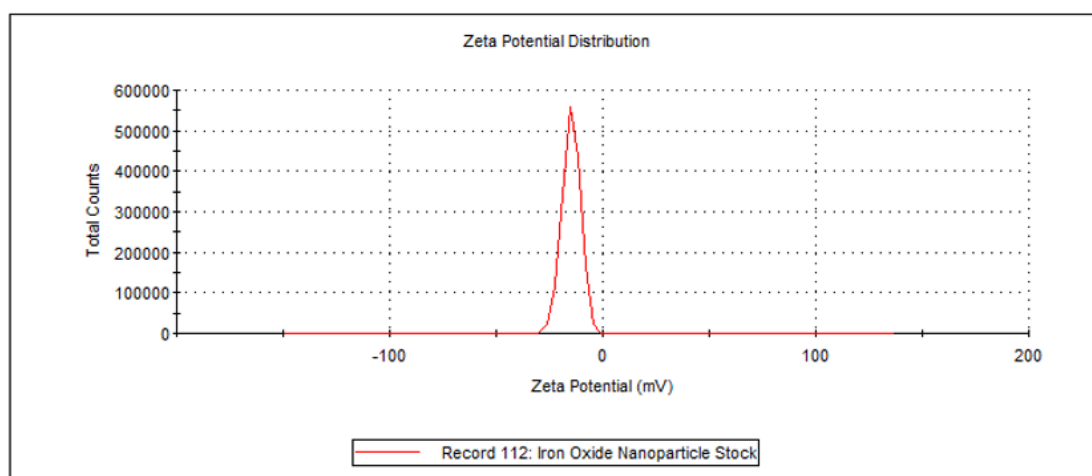
Figure 141: Zeta potential distribution graph showing the average and range of zeta potentials over 100 runs at 25°C for IONP's.

PEI coating of the IONP's led to a change in the surface charge from -14.8 mV to +23.7 mV (3.93 mV deviation) shown in Figure 142.

		Mean (mV)	Area (%)	Width (mV)
Zeta Potential (mV): 23.7	Peak 1:	23.7	100.0	3.93
Zeta Deviation (mV): 3.93	Peak 2:	0.00	0.0	0.00
Conductivity (mS/cm): 0.00151	Peak 3:	0.00	0.0	0.00
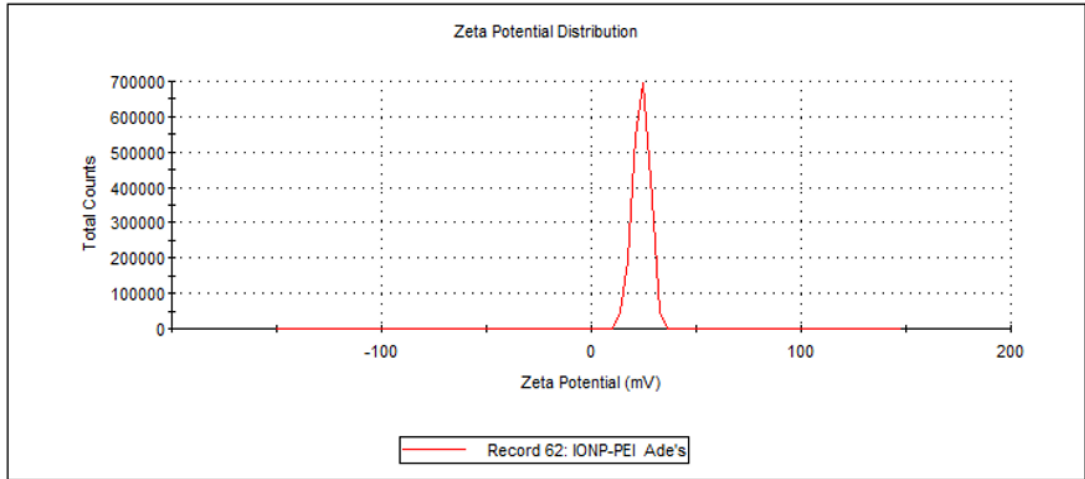
Figure 142: Zeta potential distribution graph showing the average and range of zeta potentials over 100 runs at 25°C for IONP-PEI.

Gold reduction on the surface of the PEI coated IONPs reduced the overall surface charge due to the negative charge of the gold atoms leading to a zeta potential of 16.2 mV (3.95 mV deviation) for the final HNPs in Figure 143.

		Mean (mV)	Area (%)	Width (mV)
Zeta Potential (mV): 16.2	Peak 1:	16.2	100.0	3.95
Zeta Deviation (mV): 3.95	Peak 2:	0.00	0.0	0.00
Conductivity (mS/cm): 0.00985	Peak 3:	0.00	0.0	0.00
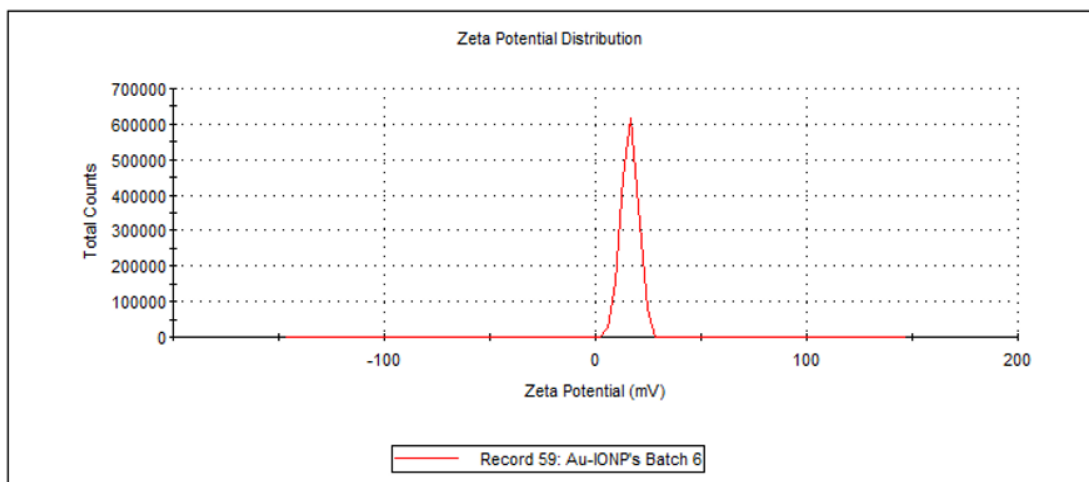
The zeta potential measurements and shift in surface charge at each step of the synthetic route suggest HNP synthesis had been successful. The negative charge of -14.8 mV for the IONPs is due to sulphate association resulting from the synthesis route and is indicative of successful IONP synthesis (C. Barnett et al. 2013). Addition of the PEI coat was successful, as shown by a change in the surface charge, from -14.8 mV to 23.7 mV. This overall positive charge is due to the positive amine functional groups within the cationic PEI backbone (C. Barnett et al. 2013). Gold seeding and the final gold reduction step reduced the surface charge to 16.2 mV due to the electronegative charge of colloidal gold (C. Barnett et al. 2013).

3.3.1.2. Transmission electron microscopy results

The TEM image in Figure 144 of the IONPs were acquired which confirmed their size to be approximately 150 nm in diameter shown at a magnification of x40000.
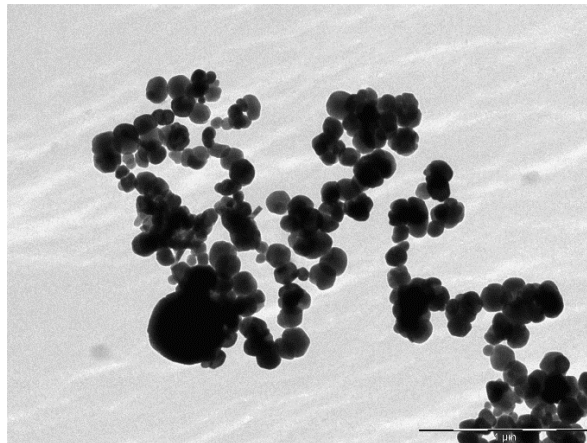
Figure 144: TEM image of IONPs at a magnification of x40000.

TEM images of the gold seeded IONPs were acquired which confirmed their presence on the surface of IONPs as shown in Figure 145(a) at a magnification of x40000 where the seeds are visible on the surface. In Figure 145(b) these same nanoparticles were magnified to x250000 and here, the 2 nm gold seeds can be clearly observed attached onto the IONP surface.

A   **B**
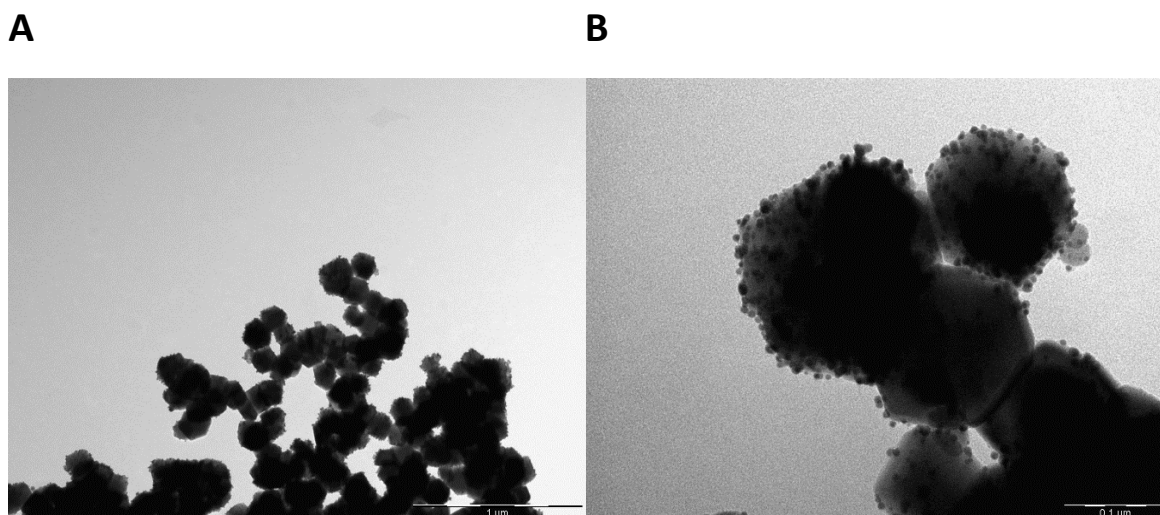
Figure 145: TEM image of gold seeded IONP's at A) x40000 and B) x250000.

The acquisition of TEM images at x40000 and x250000 was carried out for all batches of synthesised HNPs to ensure gold seeding was successful before gold reduction took place.

After the gold reduction step, the gold seeds are no longer present in any meaningful amount on the surface and the gold has formed a solid smooth shell around the iron oxide nanoparticle as shown in Figure 146 at x40000 magnification. The average size of the HNPs is roughly 150 nm. These images suggest that HNP synthesis was successful.
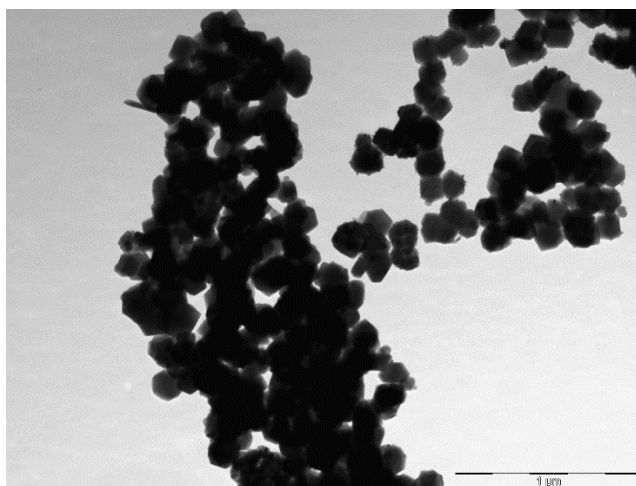
Figure 146: TEM image of HNPs.

3.3.1.3 UV-Vis spectroscopy results

UV-Vis spectroscopy of HNPs between 400 nm and 700 nm shown in Figure 147 led a λ_{max} of 573 nm which is within the observed λ_{max} of 540 nm to 575 nm from literature sources (Hoskins, Yue Min, Gueorguieva, et al. 2012a; Robinson et al. 2010). This result coupled with the zeta potential measurements earlier, indicates that complete gold shell coating had been achieved and the HNP synthesis was successful. The calculation of the λ_{max} for HNPs is important as it provides the optimal wavelength to expose HNPs to which will lead to the largest conversion of this electromagnetic energy to thermal energy. In the event that using the specific λ_{max} of gold is improbable, the UV-Vis spectrum will still provide information on suboptimal yet highly effective wavelengths for the exploitation of the surface plasmon resonance property of gold. ICP-OES will be used to further confirm the successful production of HNPs.
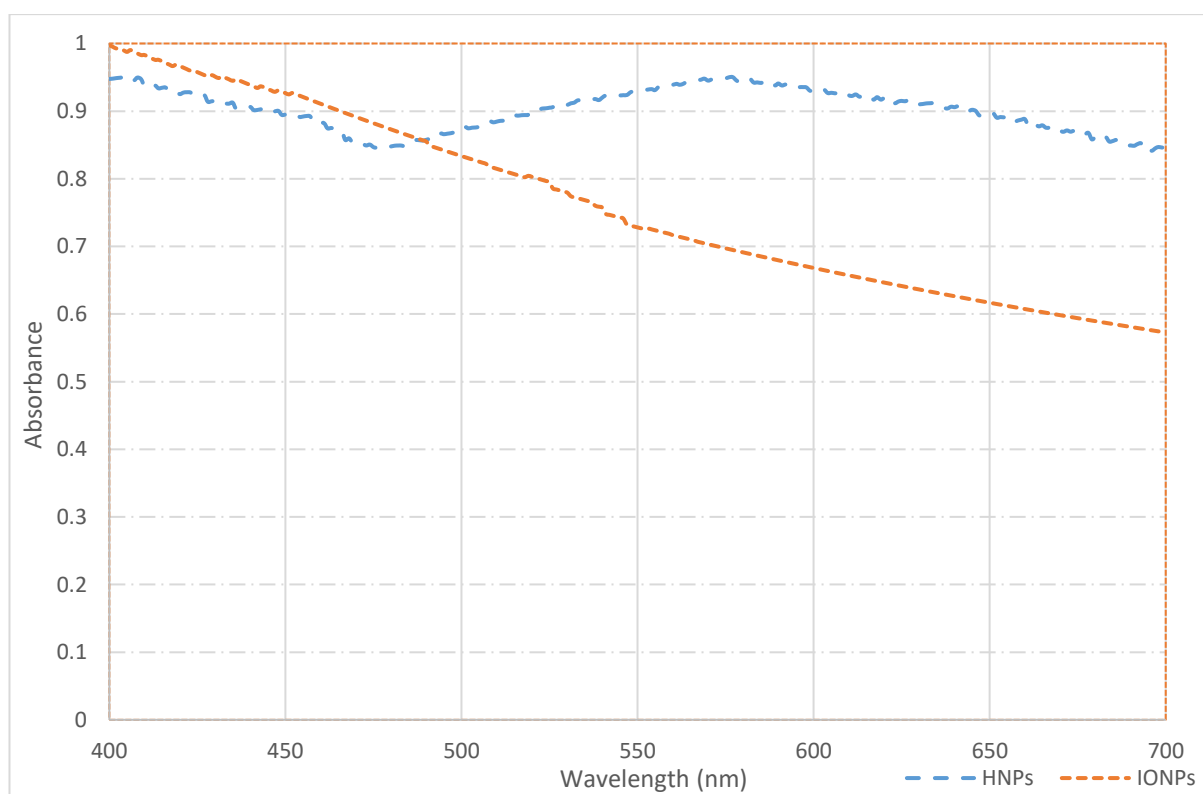
Figure 147: UV-Vis spectrum of IONPs and HNPs.

3.3.1.4. Inductively coupled plasma – optical emission spectroscopy results

In order to quantify the elemental composition of the HNPs, the gold and iron concentrations were measured using ICP-OES. A calibration curve was first produced from a range of 0.05 ppm to 10 ppm from standard solutions and with a blank solution, producing the calibration curve for iron in Figure 148 and gold in Figure 149. The equation of these graphs was used to resolve the unknown concentration of iron and gold in HNPs. Iron and gold was analysed at a wavelength of 261.187 nm and 242.794 nm respectively.
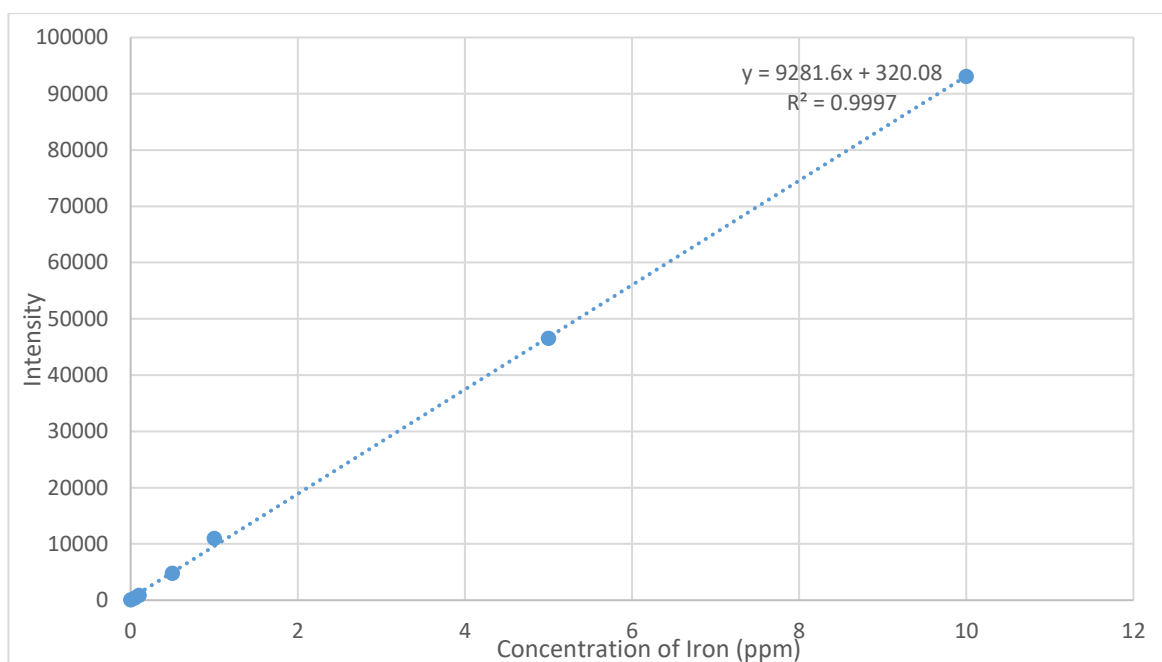
Figure 148: Calibration curve of dissolved iron concentration vs optical emission spectroscopy intensity.
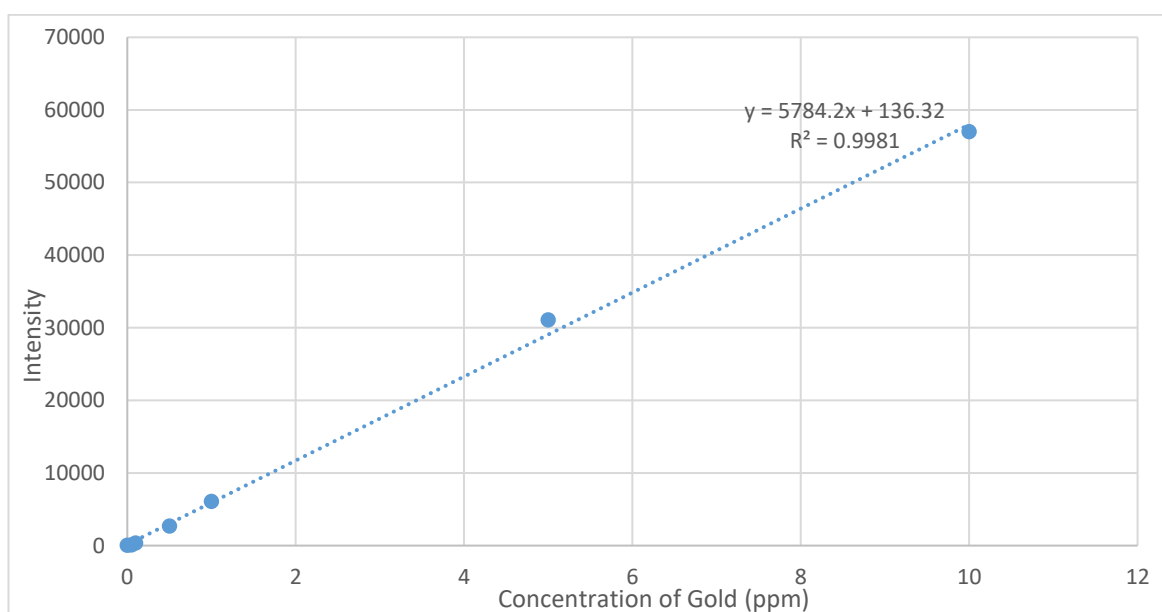
Figure 149: Calibration curve of dissolved gold concentration vs optical emission spectroscopy intensity.

The equation for the calibration curve for gold is:
$$y = 5784.2x + 136.32$$

The equation for the calibration curve for iron is:

$$y = 9281.6x + 320.08$$

An overview of the gold and iron content of the Au-IONP synthesis path is shown in Table 9 below.

Table 9: The Au-IONP Synthesis Steps

Synthesis Step	Gold Intensity	Iron Intensity	Gold Concentration (mg mL^{-1})	Iron Concentration (mg mL^{-1})	Gold:Iron Ratio
IONPs	66	30835	0	15.44	-
Gold Seed Step	2864	6386	2.24	3.32	2:3
Gold Reduction Step	2246	22398	1.82	11.89	2:13

The iron oxide nanoparticles analysed, only contained a negligible amount of gold after elemental analysis, which can arise from numerous sources. Introduction of a gold seed solution to the PEI coated IONPs post wash, led to the gold content rising forming a ratio of 2:3 for gold and iron concentrations respectively. After the gold reduction step the gold content fell as the smooth outer shell was formed. This ultimately led to a ratio of 2:13 for the gold and iron concentrations levels respectively in the synthesised Au-IONPs. The sample for the gold reduction ICP-OES analysis came from a sample suspension that was diluted from 10 mL to 2 mL causing the Fe concentration to increase. Ultimately, the aim of the ICP-OES analysis, was to determine the ratio of iron and gold in a suspension of known volume.

3.3.2. HNP drug loading

3.3.2.1. Drug loaded onto HNPs

A calibration curve was generated via the analysis of known drug concentrations using HPLC connected to a UV detector at a lambda max of 268 nm for the detection of TTLD (Jaidev *et al*. 2015; Razzazan *et al*. 2016). Examples of Uv-Vis spectrums generated by HPLC analysis for TTLD and gemcitabine is shown in Figure 150 and 151 respectively (H. Song et al. 2014).
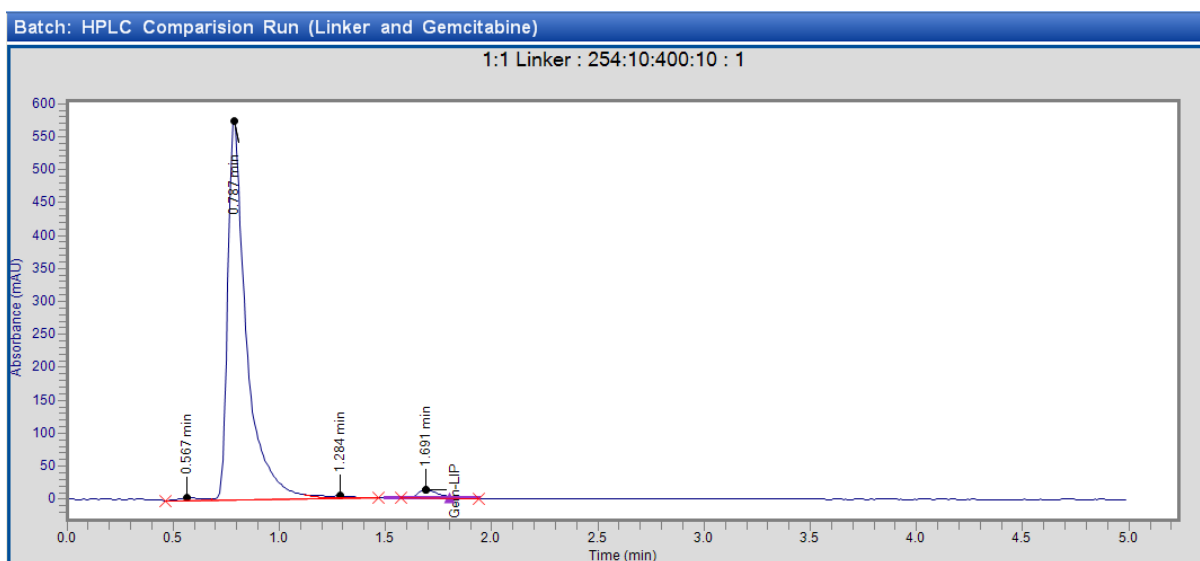
Figure 150: Uv-Vis spectra generated by HPLC analysis of TTLD at 268 nm.
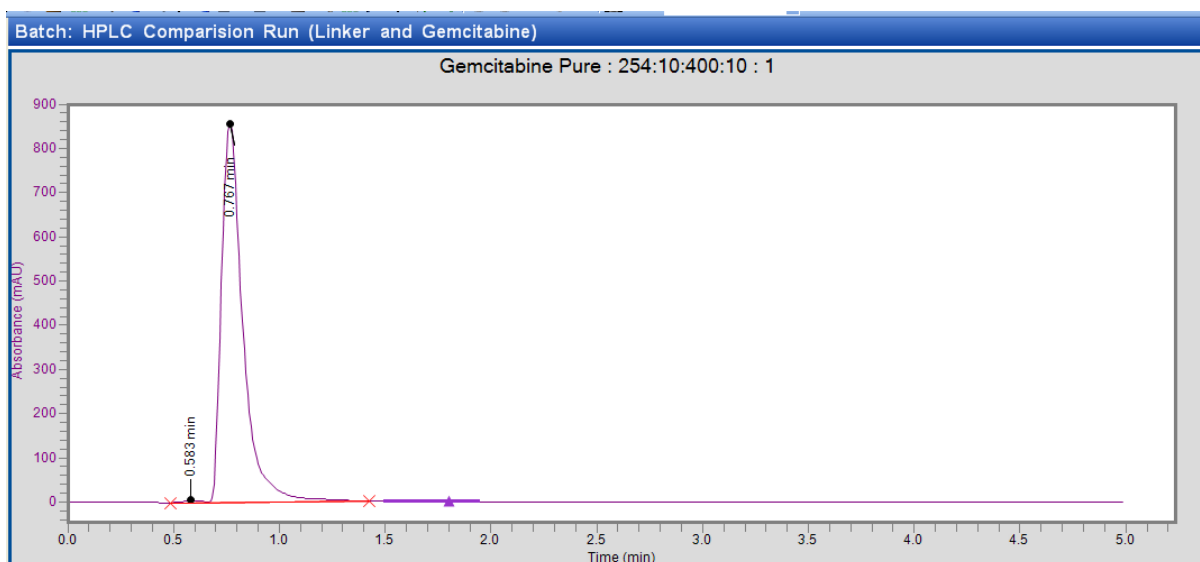
Figure 151: Uv-Vis spectra generated by HPLC analysis of gemcitabine at 268 nm.

The y-axis displays the absorbance at 268 nm over time (x-axis). With the use of HPLC, a calibration curve based on the area under the curve of the peak, at a retention time of 0.77

min for gemcitabine was plotted in Figure 152. This was performed in order to acquire the relationship equation between the peak area and drug concentration. The equation of this curve is: $y = 22702849.34x$
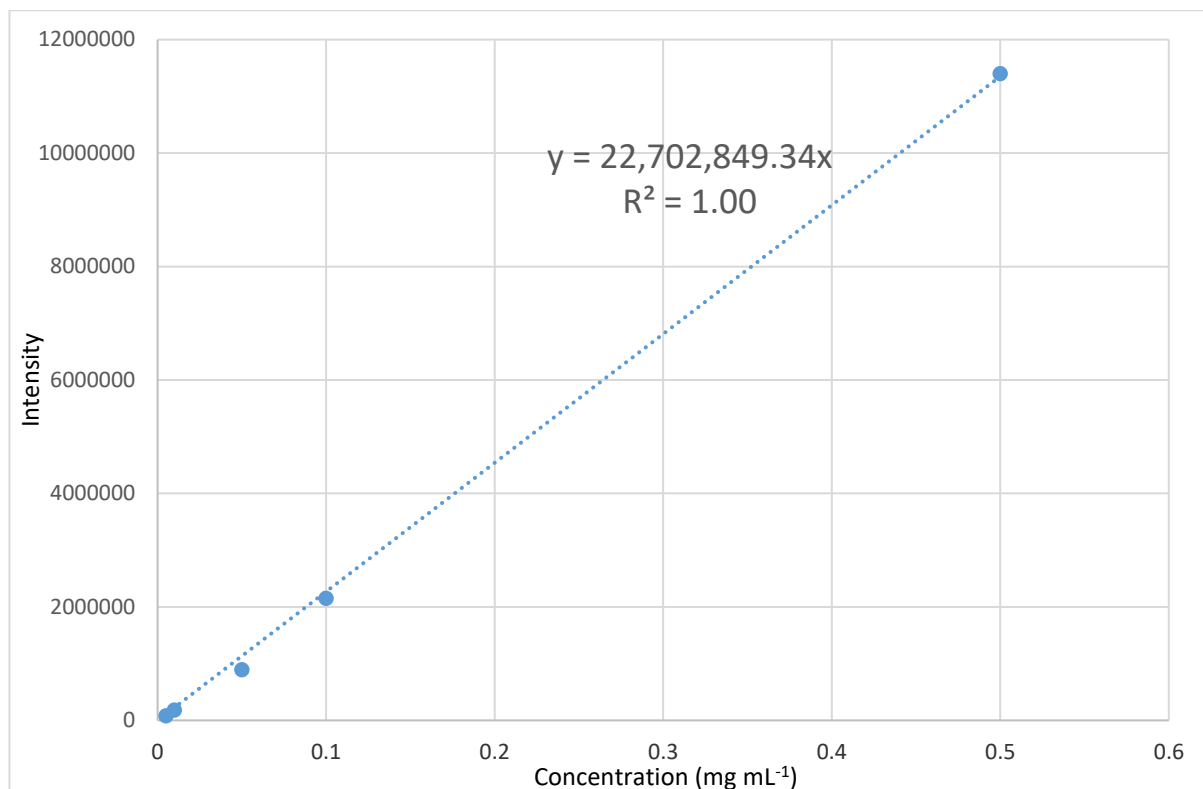
Figure 152: Graph of the calibration curve for drug concentration against HPLC retention peak area.

Drug loading of the HNPs was carried out in 5 mL of deionised water. The reaction mixture was washed once with another 5 mL of deionised water (1:2 v/v dilution). Based on the equation of the calibration curve ($y = 22702849.34x + c$), where c = 0, the concentration and therefore mass of the drug in the "wash solutions" was acquired. The amount of the leftover drug was used to ascertain the amount of drug loading that has occurred and the results are displayed in Table 10.

Table 10: The drug loading calculations for TTLD only and TTLD+PEG loaded HNPs.

	TTLD Mass (mg)	Calculated Intensity	Dilution Factor	Mass of TTLD remaining	% Drug Loading
TTLD without PEG-Thiol	25	504423	2x	0.45	98
TTLD with PEG-Thiol	25	1526264	2x	1.4	94

3.3.3. Drug release studies

3.3.3.1. *In vitro* drug release at 20 °C

Drug release at increasing temperature was carried out at pH 7 (water), 5.6 (cell media) and 7.4 (cell media). These three pH were chosen due to their biological and pharmaceutical relevance. Human blood has a pH of 7.4 and this environment is an important factor when attempting to mimic biological conditions (Ameri et al. 2016; C. M. Barnett et al. 2013). At a pH of 7 the TTLD+HNP formulation will be in neutral conditions to determine if drug release is pH sensitive. One of the processes involved in gemcitabines uptake is by receptor mediated endocytosis into endosomes. These early stage endosomes can release their contents and/or fuse together to form late stage endosomes where the interval pH ranges from 5-6. Therefore pH 5.6 was chosen to mimic the potential environment that the TTLD+HNP formulation would experience intracellularly. The same experimental procedures were used for the TTLD+PEG loaded HNPs. The graph in Figure 153 shows the percentage release of detected Gem-Mal over time from the TTLD and TTLD+PEG loaded HNPs formulations, at 20°C and pH 7.
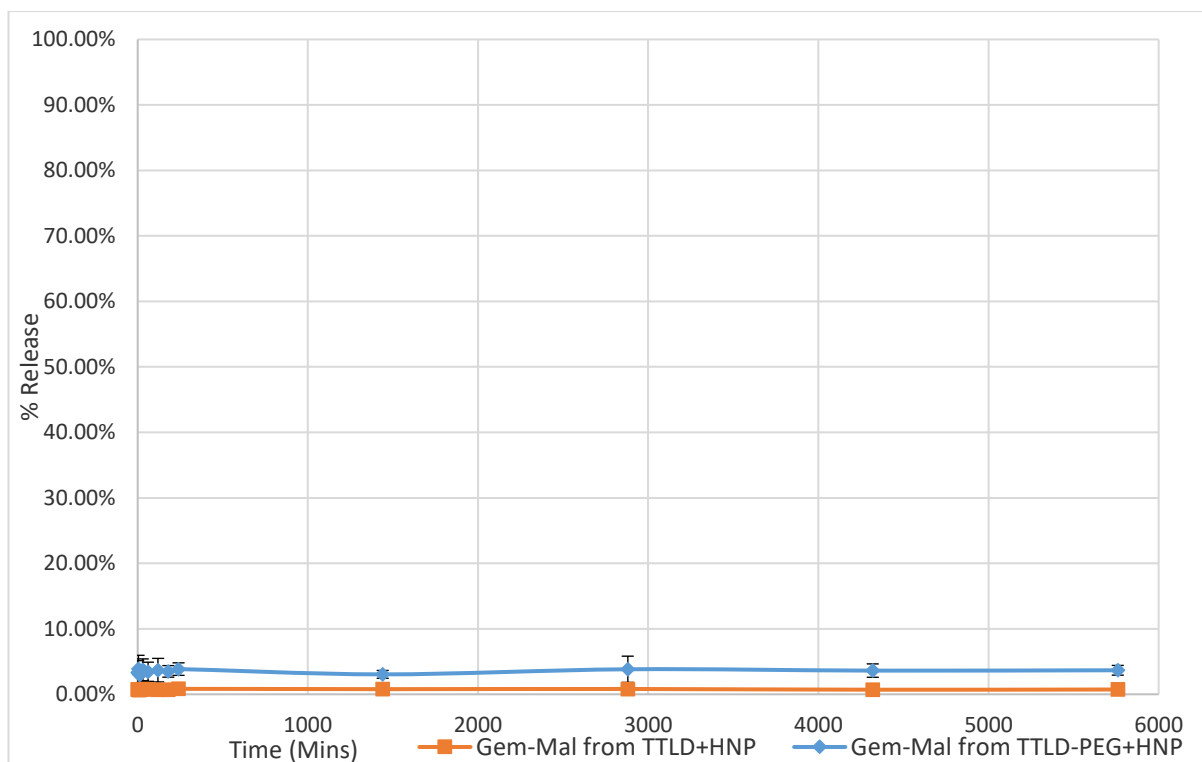
Figure 153: Graph of TTLD and TTLD+PEG loaded HNPs release over 96 h at pH 7 (water) and at 20°C (n=3, ±0.13 % and 0.42 % respectively). No statistical difference observed between Gem-Mal from TTLD+HNP and Gem-Mal from TTLD-PEG+HNP, nor any change over time (P < 0.05).

The graph in Figure 153 for TTLD loaded and TTLD+PEG loaded HNPs, show no major Gem-Mal release over the time period tested (P < 0.05). This indicates that the linker does not undergo retro Diels Alder breakdown at low temperatures over time, a physiological pH and that the formulation was still intact. The tiny amounts of Gem-Mal release observed in the PEGylated sample may be attributed to TTLD compounds that was not covalently bonded to the gold HNP surface but was instead entangled around the long chain PEG during drug loading, which became separated upon dialysis. Small amounts of TTLD approaching during drug loading may have been physically hindered from reaching the HNP surface.

The graph in Figure 154 is of the TTLD and TTLD+PEG formulation release study at 20°C at pH 7.4 with cell media. Just like the graphical data of pH 7 (water) no major release was observed over the time period tested.
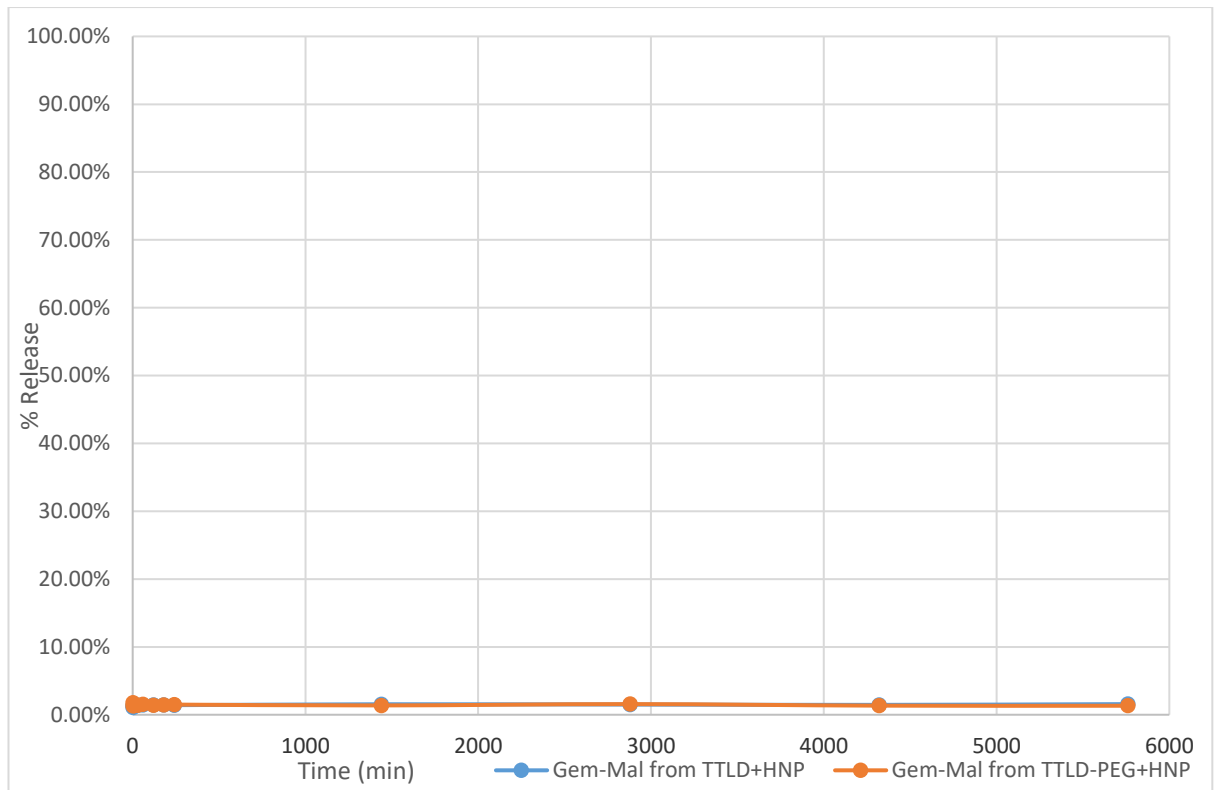
Figure 154: Graph of TTLD and TTLD+PEG loaded HNPs release over 96 h at pH 7.4 (cell media) and at 20°C (n=3, ±0.01 % and 0.06 % respectively). No statistical difference observed between Gem-Mal from TTLD+HNP and Gem-Mal from TTLD-PEG+HNP, nor any change over time (P < 0.05).

The graph in Figure 155 shows how the percentage Gem-Mal release changes over time when the pH is at 5.6 at 20 °C.
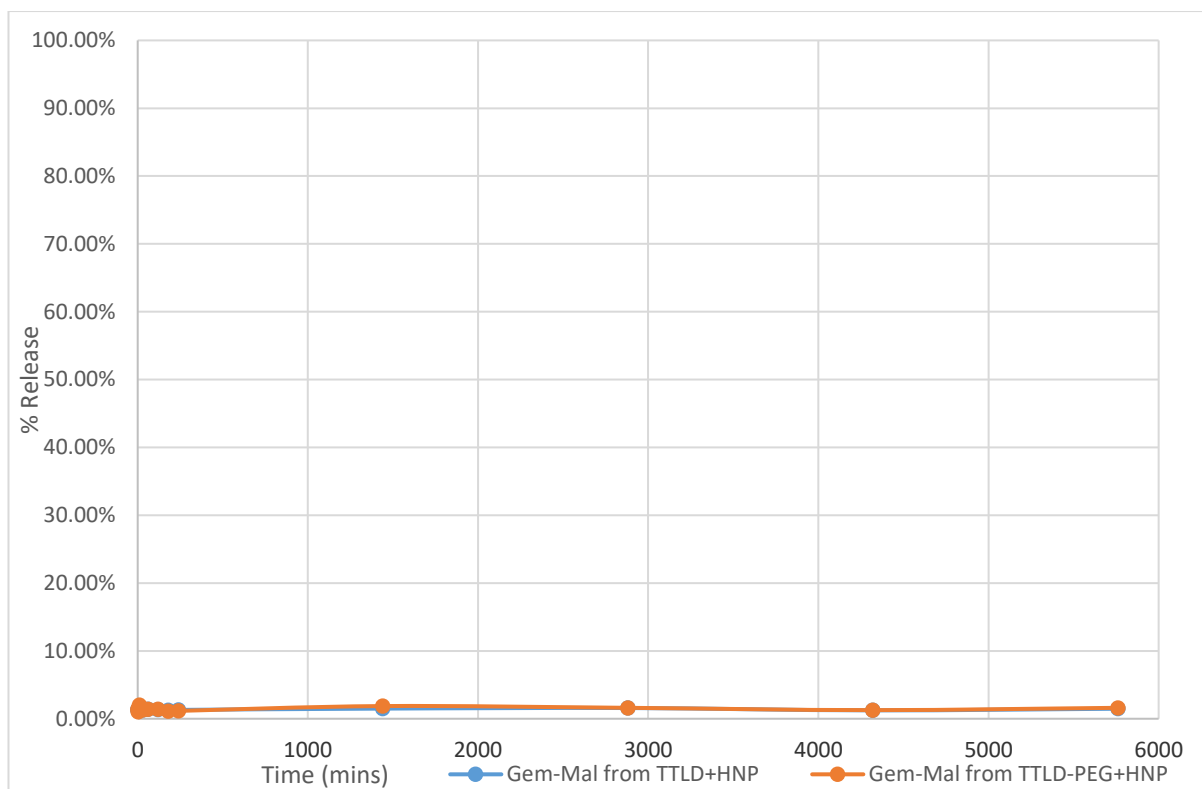
Figure 155: Graph of TTLD and TTLD+PEG loaded HNPs release over 96 h at pH 5.6 (cell media) and at 20°C (n=3, ±0.02 % and 0.03 % respectively). No statistical difference observed between Gem-Mal from TTLD+HNP and Gem-Mal from TTLD-PEG+HNP, nor any change over time (P < 0.05).

An initial burst release was observed with between 1 to 2 % of the Gem-Mal released within the first 1 min in the PEGylated and non-PEGylated formulations respectively is likely attributed to dislodged TTLD instead of surface attached TTLD and is not attributed to pH or temperature. Hence, it can be concluded that at 20 °C and at a pH of 5.6, no retro Diel-Alder was taking place and that the linker remained intact with the gemcitabine remaining fully bound onto the HNP surface (P < 0.05).

3.3.3.2. *In vitro* drug release at 37 °C

Subsequently, drug release was carried out at 37 °C in order to mimic what may happen at body temperature. These studies were carried out at varied pH (7, 7.4, & 5.6 as previously discussed). The graph in Figure 156 shows the Gem-Mal release over time of TTLD and TTLD+PEG loaded HNPs at 37°C at pH 7.
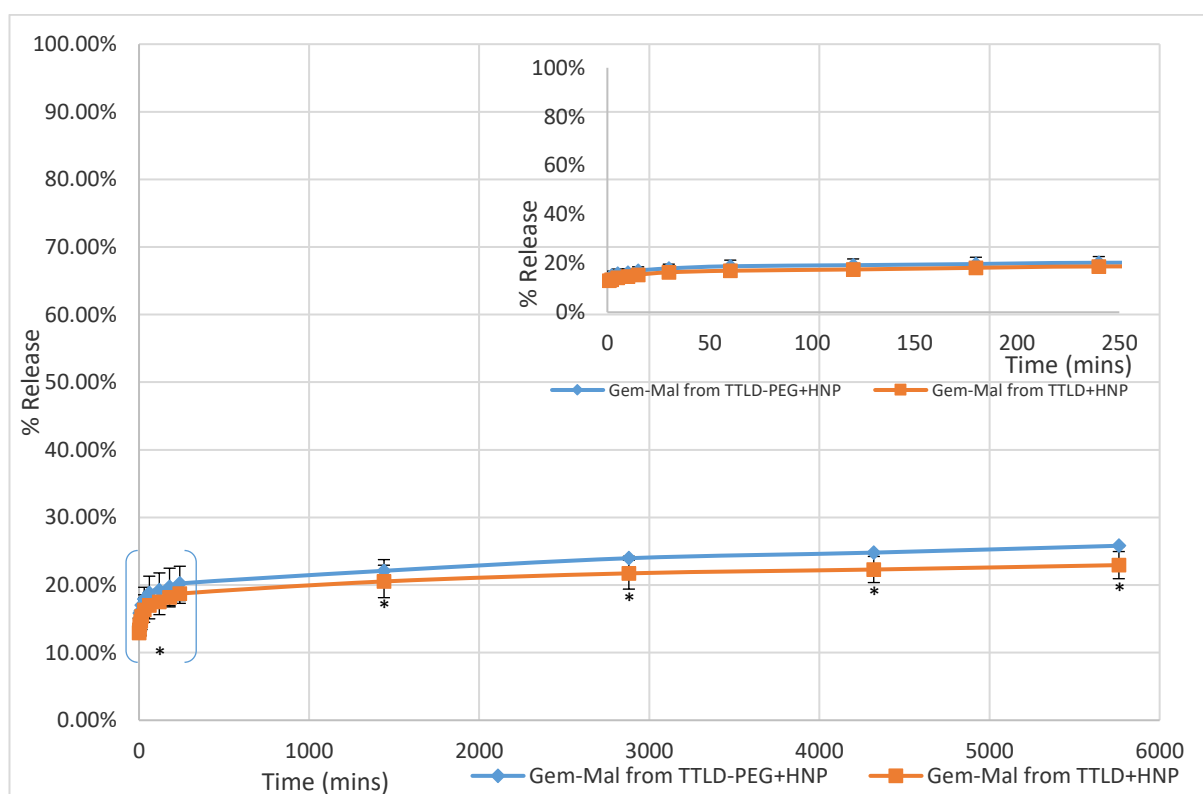
Figure 156: Graph of TTLD and TTLD+PEG loaded HNPs release over 96 h at pH 7 (water) and at 37°C (n=3), ±0.35 % and 0.78 % respectively). No statistical difference between Gem-Mal from TTLD+HNP and Gem-Mal from TTLD-PEG+HNP observed (P < 0.05). Every time point is statistically higher [*] compared to those at 20 °C (P < 0.05) (Figure 153).

Both the TTLD and TTLD+PEG formulations show a direct correlation between % Gem-Mal release vs time. There is an initial burst release where 13 % and 14 % of the Gem-Mal released within 1 min for the TTLD and TTLD+PEG formulations respectively. The rate of release gradually decreases until a linear correlation is established beyond the 60 min time point. The only difference between the experimental variables for the graph in Figure 153 with Figure 156 is the temperature. Overall at 37 °C the % Gem-Mal release increases over time for TTLD and TTLD+PEG loaded HNPs when compared to the formulation at 20 °C where no release takes place (P < 0.05). Therefore this 13-14 % burst release is an effect of

temperature only. It is worth noting that the amount of Gem-Mal released from the TTLD+PEG is about 2.5 % "released" higher than with just TTLD. This again may be due to the entangling effect mentioned earlier as there is no statistical significance between both sets of data (P < 0.05).

The same parameters for Figure 157 were repeated with the difference being the use of cell media at a pH of 7.4 instead of water at a pH of 7.
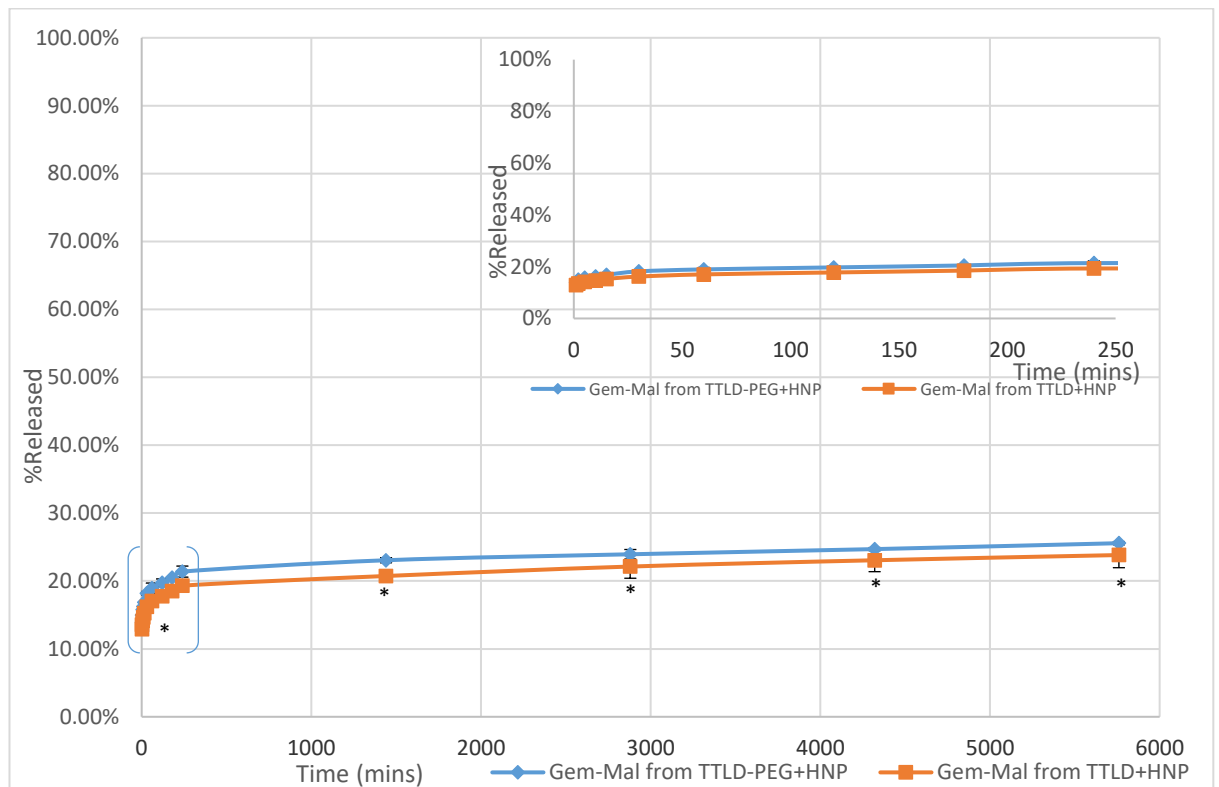
Figure 157: Graph of TTLD and TTLD+PEG loaded HNPs release over 96 h at pH 7.4 (cell media) and at 37 °C (n=3), ±0.13 % and 0.22 % respectively). No statistical difference between Gem-Mal from TTLD+HNP and Gem-Mal from TTLD-PEG+HNP observed (P < 0.05). Every time point is statistically higher [*] compared to those at 20 °C (P < 0.05) (Figure 154).

The initial burst release of Gem-Mal at pH 7.4 in 37 °C cell media is 13 % and 14 % respectively for TTLD and TTLD+PEG loaded HNPs, which is also the outcome in water at pH 7 at 37 °C. These results show that the slightly more alkaline blood pH of 7.4 will not affect the % release of Gem-Mal.

The graph below in Figure 158 is based on the same experimental conditions as those used in Figure 157, but the pH is at 5.6 and the bulk solution is cell media.
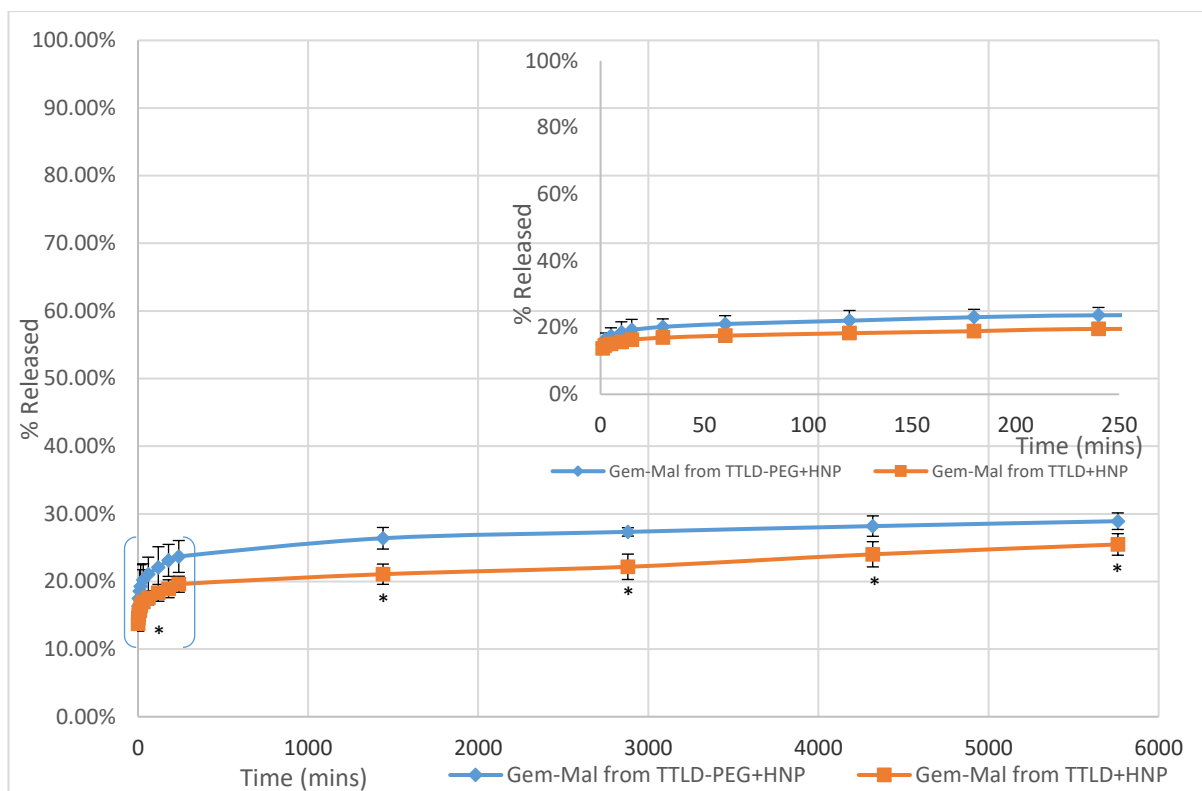
Figure 158: Graph of TTLD and TTLD+PEG loaded HNPs release over 96 h at pH 5.6 (cell media) and at 37°C (n=3, ±0.57 % and 1.03 % respectively). No statistical difference between Gem-Mal from TTLD+HNP and Gem-Mal from TTLD-PEG+HNP observed (P < 0.05). Every time point is statistically higher [*] compared to those at 20 °C (P < 0.05) (Figure 153).

The initial burst % release of Gem-Mal at pH 5.6 is 14 % for TTLD and 15 % for TTLD+PEG at pH 5.6 (cell media). This is an average difference of 1 % release compared to pH 7 (water). The decrease in pH from 7 to 5.6, coupled with the presence of PEG may be the cause for this 1 % difference in initial burst % Gem-Mal release, when comparing the pH 5.6 and 7 release data with only TTLD HNPs at 37 °C (P < 0.05) There is no statistical difference between pH 5.6 and 7 for TTLD+PEG loaded HNPs at 37 °C (P < 0.05). After 5 days of heating the percentage release is 29 % for the TTLD+PEG at pH 5.6 formulation which is 3 % higher than in water (pH 7). With the effects of cell media ruled out, it can be concluded that at a pH of 5.6 there is a tiny effect on the percentage Gem-Mal release with an elevated temperature still being the major contributing factor.

3.3.3.3. *In vitro* Gem-Mal release at 44 °C

The Gem-Mal release was analysed at 44 °C, this temperature was used to mimic the temperature of HNPs after laser irradiation. These studies were carried out at varied pH (7, 7.4, & 5.6 as previously discussed). The graph in Figure 159 demonstrates the rapid release of Gem-Mal from the HNPs surface when heated to 44°C at pH 7.
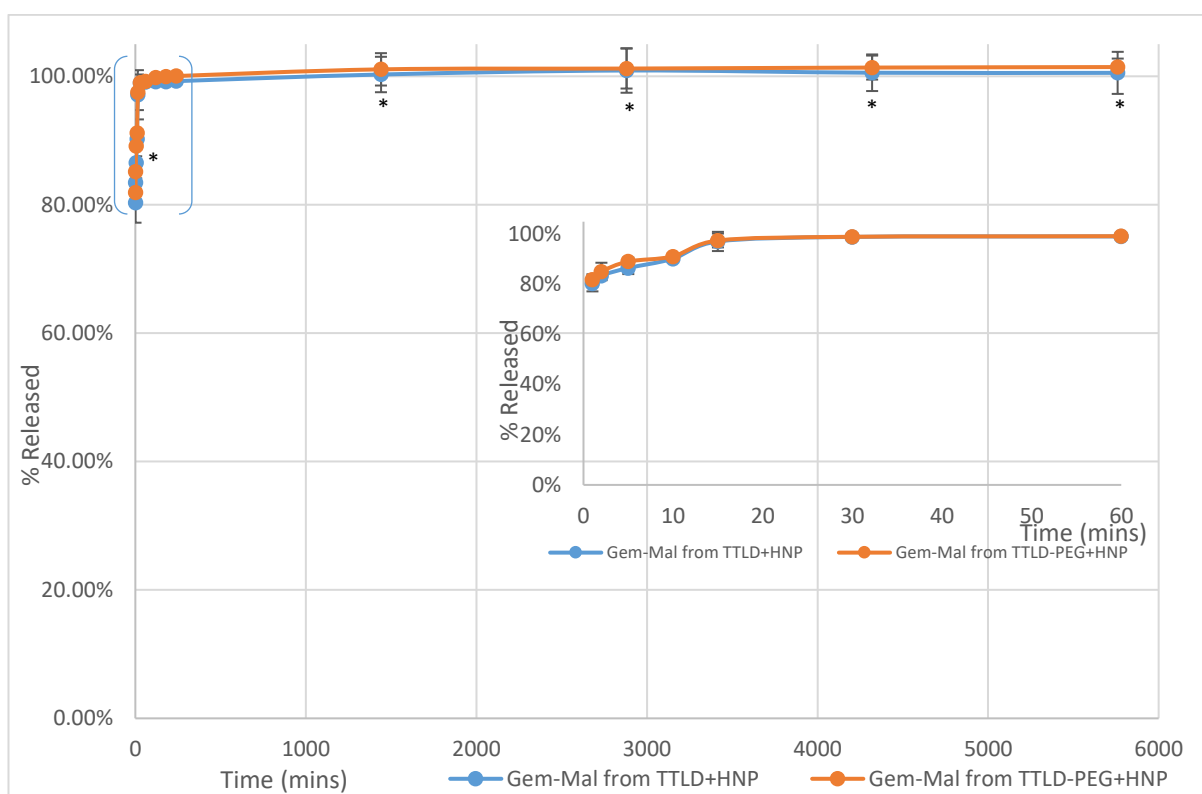
Figure 159: Graph of TTLD and TTLD+PEG loaded HNPs release over 96 h at pH 7 (water) at 44°C (n=3, ±1.55 % and 1.49 % respectively). No statistical difference between Gem-Mal from TTLD+HNP and Gem-Mal from TTLD-PEG+HNP observed (P < 0.05). Every time point is statistically higher [*] compared to those at 20 °C (P < 0.05) (Figure 159).

The TTLD+HNP formulation released 80 % of the Gem-Mal within 1 min while the TTLD+PEG+HNP released 82 % in the same time frame at 44 °C. Within 60 min over 99 % of the Gem-Mal in both formulations had released. The graph in Figure 160 expanded for the first 60 mins of this experiment displays this clearer. The TTLD+PEG remains 2-3 % higher in percentage released initially indicating that the difference between TTLD and TTLD+PEG is based on non-surface attached TTLD instantly unhooking from surface TTLD and PEG. If all non-surface attached TTLD was removed (with a more vigorous wash after drug loading) then it is likely the difference between percentage drug release from TTLD and TTLD+PEG formulations would be zero or too negligible to detect. At 44 °C the effect of temperature

is so high that it renders the marginal 2-3 % initial release between TTLD and TTLD+PEG formulations and overall percentage release/time trend statistically negligible (P < 0.05).
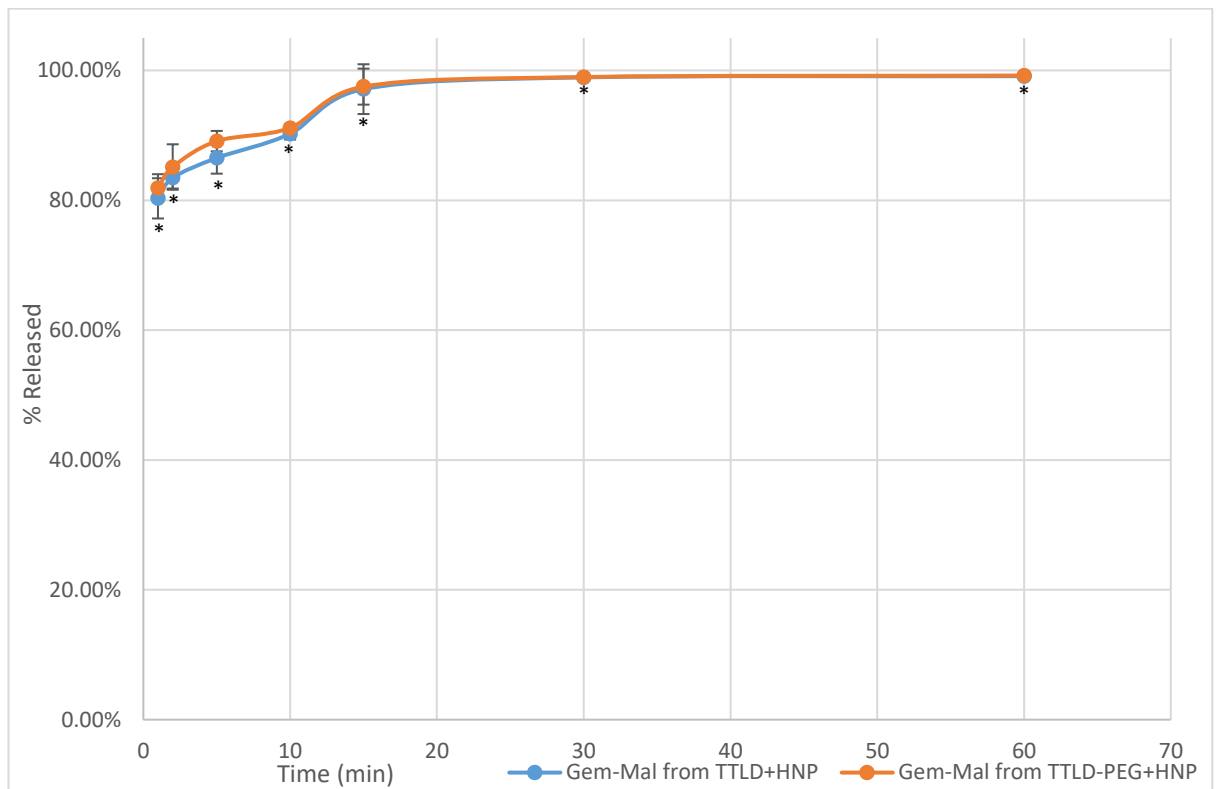
Figure 160: Graph of TTLD and TTLD+PEG loaded HNPs release over 60 min at pH 7 (water) at 44°C (n=3, ±1.55 % and 1.49 % respectively). No statistical difference between Gem-Mal from TTLD+HNP and Gem-Mal from TTLD-PEG+HNP observed (P < 0.05). Every time point is statistically higher [*] compared to those at 20 °C (P < 0.05) (Figure 153).

At a pH of 7.4 at 44 °C in Figure 161 the percentage release of Gem-Mal over time is very similar to pH 7 with TTLD and TTLD+PEG formulations (P < 0.05). The initial burst percentage release of 80 % is the same as pH 7 for TTLD and 82 % for TTLD+PEG formulations. TTLD+PEG also required 60 min of heating to reach 99 % TTLD release but the TTLD only formulation required 24 h. Note that the point at which 99 % release was achieved would have been between 4 h and 24 h. Either way both the TTLD and TTLD+PEG formulations have negligible differences in their release rate and show a rapid rate of release approaching 100 % within minutes.
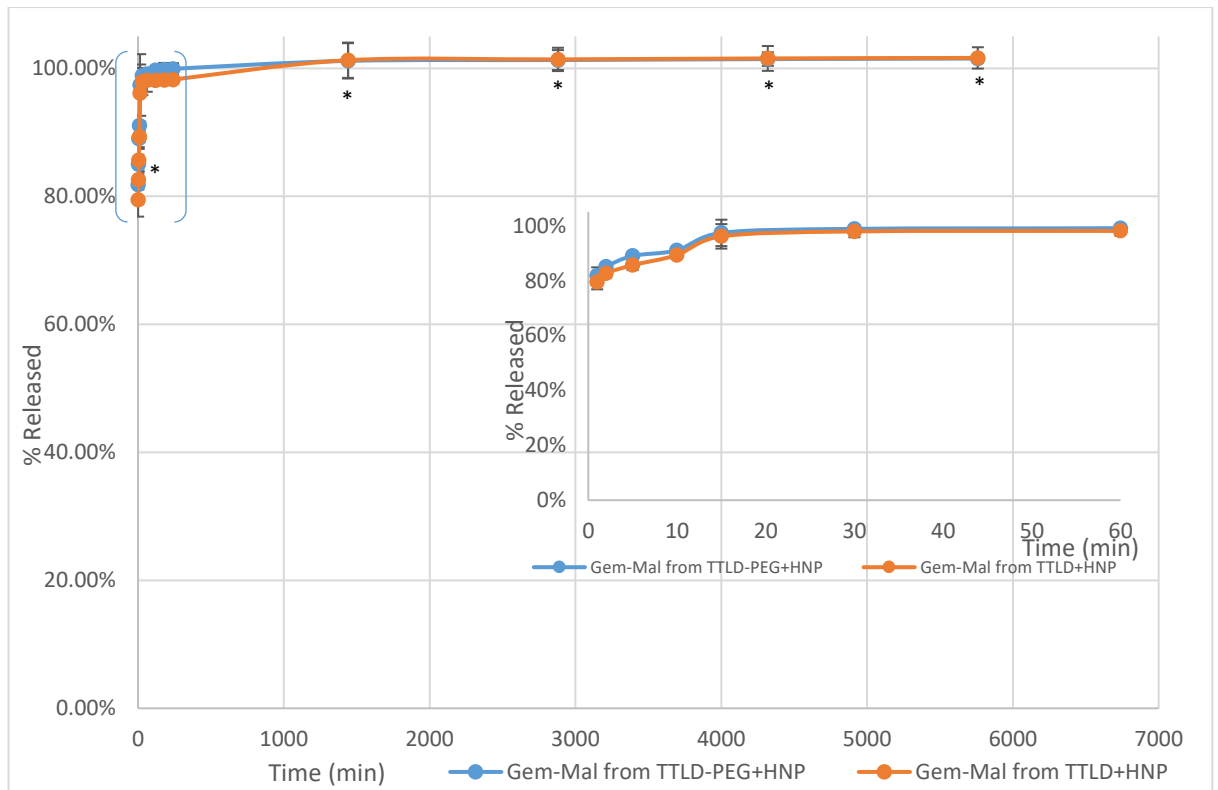
Figure 161: Graph of TTLD and TTLD+PEG loaded HNPs release over 96 h at pH 7.4 (cell media) at 44°C (n=3, ±1.59 % and 0.77 % respectively). No statistical difference between Gem-Mal from TTLD+HNP and Gem-Mal from TTLD-PEG+HNP observed (P < 0.05). Every time point is statistically higher [*] compared to those at 20 °C (P < 0.05) (Figure 151).

At a pH of 5.6 shown in Figure 162 the initial burst percentage release of Gem-Mal is 1 % higher than TTLD+PEG when compared to pH 7 and the percentage released reached 99 % within 15 min compared to the 60 min it took at pH 7. Even with these tiny differences the effect of pH is negligible at a temperature of 44 °C (P < 0.05).
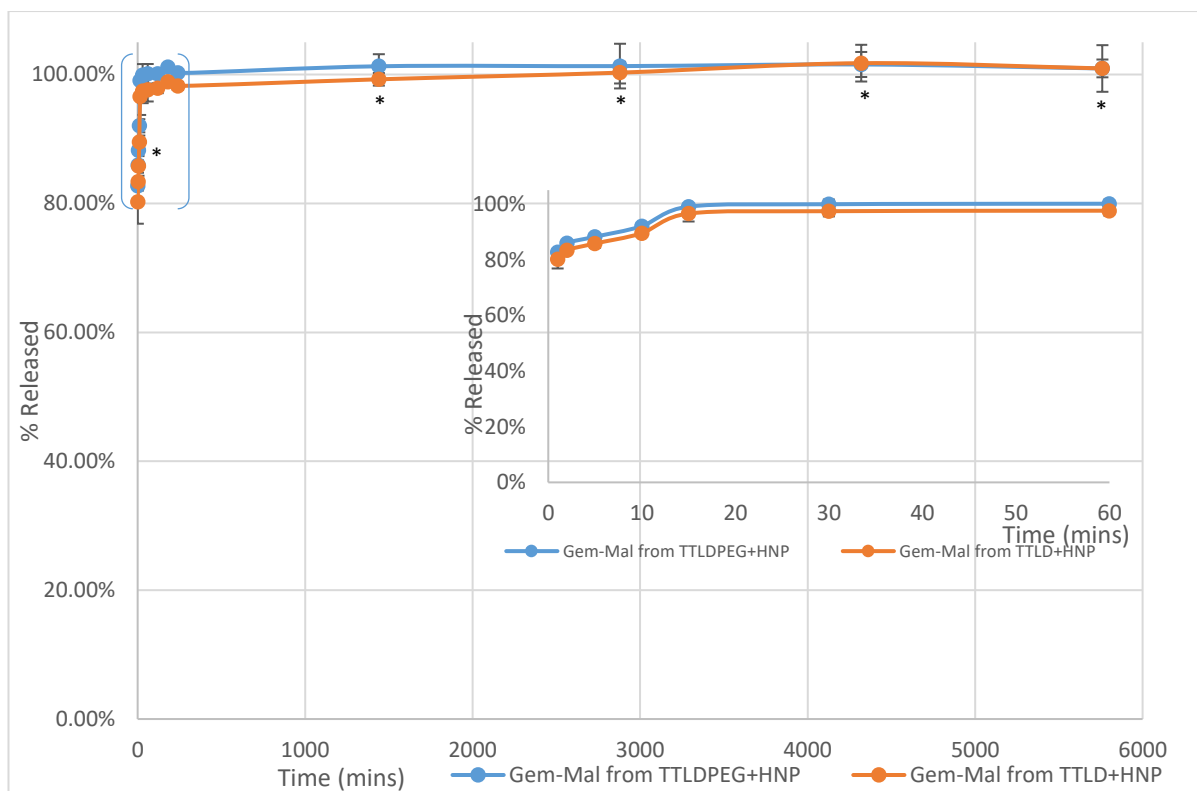
Figure 162: Graph of TTLD and TTLD+PEG loaded HNPs release over 96 h at pH 5.6 (cell media) at 44°C (n=3, ±1.84 % and 0.96 % respectively). No statistical difference between Gem-Mal from TTLD+HNP and Gem-Mal from TTLD-PEG+HNP observed (P < 0.05). Every time point is statistically higher [*] compared to those at 20 °C (P < 0.05) (Figure 152).

These findings indicate that temperature is the major factor which influences the induction of retro Diels-Alder and hence liberation of Gem-Mal molecules. Hence, these systems have potential as thermally triggered drug delivery vehicles.

3.3.4. Stability determination of TTLD+HNP formulations

The stability of the TTLD+HNP formulation was observed by storing it as a suspension at 5 °C and 20 °C over a 4 week period. The amount of Gem-Mal detected as a function of drug release during storage conditions is displayed graphically in Figure 163.
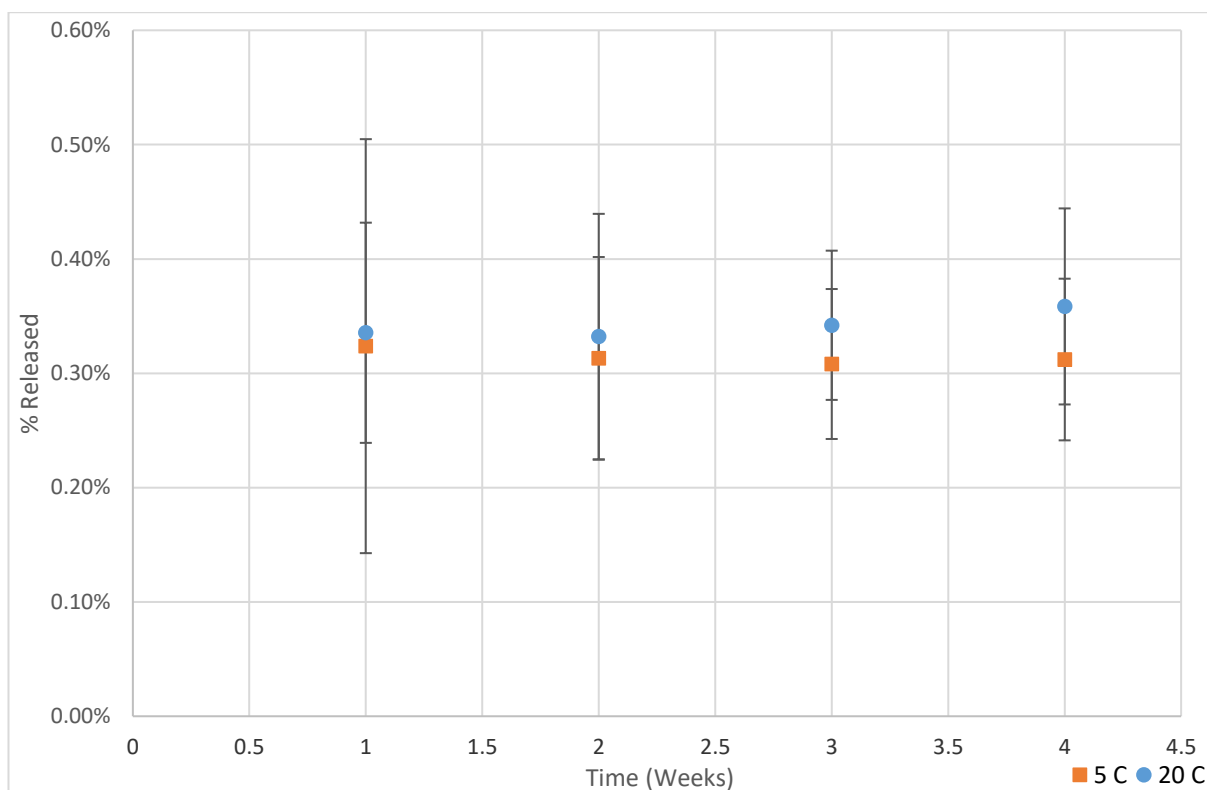
Figure 163: Graph of the release of TTLD over four weeks at 5 °C and 20 °C. No statistical significance was observed between 5 °C and 20 °C nor over time (P < 0.05).

The graphical data presented in Figure 163 does not indicate any trend between the percentage release of Gem-Mal and time for the TTLD+HNP formulation at 20 °C. There is some release shown which ranges from 0.33 % to 0.36 % but these do not follow a time dependant trend. Similar results occur at a storage temperature of 5°C. There is no statistical difference between the percentage release of Gem-Mal at 5°C or 20°C (p <= 0.01). The experimental observations at 20°C are akin to those of 5°C where the size of the errors for each average weekly results is higher than the overall range of percentage release results over the four week experiment. Hence, it can be deduced that storage of the HNP-gemcitabine formulations would result in stable systems over a 4 week period. Obviously prolonged studies are required in order to estimate the realistic shelf life of these systems over longer time periods, as well as studies at higher and sub zero temperatures.

3.4. Discussion

The synthesis of the HNPs was deduced to be successful from all the characterisation carried out. The results indicated the final HNPs to be composed of 1.82 mg mL^{-1} Fe and 11.89 mg mL^{-1} Au giving a ratio of Fe:Au 13:2.

Reports on the fabrication of HNPs have described a Fe:Au ratio of 3:1 (Hoskins, Yue Min, Gueorguieva, et al. 2012). In our study, the Fe:Au ratio was 13:2. Our iron oxide cores produced 150 nm nanoparticles. In the literature the iron oxide produced was 30 nm in diameter. Therefore with a higher surface area to volume ratio, more gold seeds can attach to the smaller reported 30 nm iron oxide cores and subsequently more gold is present after the coating step. Additionally, the gold coating thickness may have influenced the overall gold composition, a comparison between the two studies cannot be made due to lack of published information. Nevertheless, for this study the TEM images confirmed that complete gold coating had occurred and that the synthesis of HNPs had been successful.

HPLC confirmed that the gemcitabine analogue was successfully conjugated onto the HNP surface. The 98 % and 96 % drug loading of TTLD and TTLD+PEG respectively indicates that the HNP surface was not completely saturated and that more drug loading may have been achievable at a higher drug feed : particle ratio. Therefore these HNPs may be capable of carrying more than 5 mg TTLD per 1 mg HNPs. However, this was not investigated.

The aim of this study was to develop a system which acted in a stimuli responsive manner and released Gem-Mal molecules upon external trigger. In this instance upon heat. Hence the effect of temperature on Gem-Mal release was observed over varied pH which mimicked biological conditions.

At 20 °C there was a negligible change in release across the three mentioned pH values. At a temperature of 37 °C and 44 °C there is a definite increase in percentage release of Gem-Mal as seen in the graph in Figure 164.
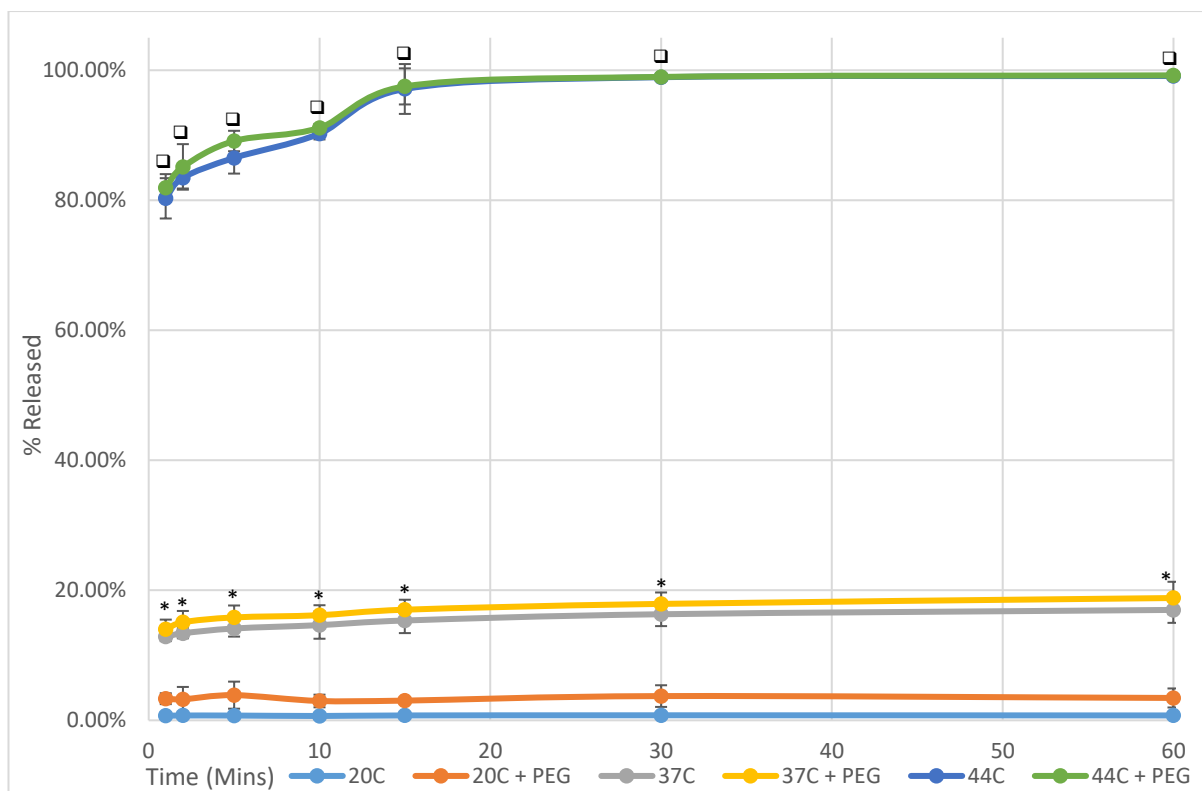
Figure 164: Comparative graph of all TTLD and TTLD+PEG formulations at 20, 37 and 44 °C, at a pH of 7 (water) over 60 min. Standard deviation of TTLD+HNP at 20 °C, 37 °C and 44 °C was 0.13 %, 0.35 % and 1.55 % respectively. Standard deviation of TTLD-PEG+HNP at 20 °C, 37 °C and 44 °C was 0.42 %, 0.78 % and 1.49 % respectively. Statistically significant data points for temperature mediated release is denoted with * and ❑ for 37 °C and 44 °C respectively when compared to 20 °C.

The initial burst release experienced at 37 °C and 44 °C must be temperature dependant due to the significant difference in percentage Gem-Mal release after 1 min of heating. This burst release behaviour is extremely beneficial for clinical use at 44 °C as it ensures the majority of the dose is released within minutes intracellularly. This prevents lengthy chemotherapeutic sessions often experienced by pancreatic cancer patients who will receive a therapeutic dose intracellularly without the systemic side effects. Overall this thermal responsive formulation is already displaying attributes that highlight its potential as a future first line treatment for pancreatic cancer. It also enables patients who are not able to be administered gemcitabine intravenously the opportunity to receive treatment intratumorally.

While a burst release is experienced at 37 °C, it is less significant (14 %) compared to the 80 % at 44 °C. This is a crucial factor as it prevents the sudden release of Gem-Mal before target laser irradiation. If this was to occur, then healthy cells surrounding the tumour site

would also experience the cytotoxic effects of the Gem-Mal compounds. Another advantage of a significantly lower percentage release at 37 °C is that the remaining TTLD is still attached to the HNP allowing them to enter the cancer cells before being released. Therefore it stands to reason that roughly 15 % of the dose is lost while the remaining 85 % of the formulation is able to enter the cell intracellularly. The TTLD that is prematurely released at 37 °C may still have cytotoxic activity like gemcitabine due to their structural similarities and *in vitro* experiments later on in this study will highlight the pharmaceutical activity of Gem-Mal against gemcitabine.

The lack of Gem-Mal release at room temperature (20 °C) is a good indicator of this formulations physical stability in storage conditions. Drug formulations should typically be inactive until introduction into the recipient occurs. This ensures that once the formulation has been packaged and stored, it no longer requires analytical testing and should remain effective and unchanged, throughout its shelf life.

Thermal responsive drug delivery systems for the transport and release of gemcitabine is already an established advancement in nanotechnology. However the mode of transport, mechanism of release and overall performance of such systems varies considerably. The use of magnetoliposomes to encapsulate gemcitabine has been shown to only have a stable lifespan of 4 days determined by dynamic light scattering, before aggregation and drug release occurs (Ferreira *et al*. 2016). This formulation is called gem-ML and this is a much shorter potential shelf life than the 4+ weeks of high stability shown for the TTLD+HNP in section 3.3.4. This means that clinically, gem-ML would have to be produced *in situ* prior to administration. Both TTLD+HNP and gem-ML formulations have been shown to reach the target temperature of 44 °C in order to induce hyperthermia in pancreatic cancer cells. As stated previously, the method of reaching this temperature for TTLD+HNP is with the use of SPR triggered by infra-red exposure. Gem-ML utilises iron oxide nanoparticles which have been encapsulated alongside gemcitabine into liposomes. These iron oxide nanoparticles will generate external heat when exposed to an alternating magnetic field allowing the formulation to be heated to 56 °C (Ferreira *et al*. 2016).

The difference between the core body temperature (37 °C) and the desired therapeutic temperature of 44 °C is only 7 °C. The aim of a thermal responsive drug delivery system is to have a strong activity at 44 °C with a considerably lower activity at 37 °C which proved

to be a difficult criteria to complete when designing and synthesizing a thermally labile linker. Gem-ML has been reported to only release 17 % of its contents after 72 hr at 37 °C compared to the 23 % release shown for the TTLD+HNP formulation, a difference of 5 %. However virtually 100 % of the HNPs would have surface attached TTLD compared to only 54 % of gem-ML encapsulation. Magnetoliposomes without encapsulated gemcitabine was shown to have cytotoxic effects bringing the percentage cell viability down to 60 % after 72 hr during incubation at 37 °C. The authors state that this is unlikely due to the inherent cytotoxic effects of iron oxide nanoparticles and more to do with the liposomes (Ferreira *et al*. 2016). The *in vitro* experimental results shown later on in this study for TTLD+HNP will be compared to those of gem-ML to fully compare the two.

Another thermally sensitive drug delivery system for gemcitabine, is a liposome called HaT-GEM, which was shown to achieve a 100 % release of its cargo at 41 °C over 2 min, with no detectable release occurring at 37 °C (May et al. 2013). While this is an impressive display of thermal stability at core body temperature, its rapid release also occurs at 39 °C where 80 % of the encapsulated gemcitabine is release after 30 min (20 % after 2 min). As this formulation is administered intravenously rather than intratumourally with TTLD+HNP, any clinical patient with fever would be at risk of rapid systemic release of gemcitabine from this formulation. At best this would render its antitumor activity inert and in some cases cause serious side effects. However, intravenous treatment compared with intratumour has obvious benefits such as lack of requirement for minimally invasive surgery, infection risk etc.

GEM-TSLnps, another liposome based drug delivery system for gemcitabine, released 25 % of its gemcitabine cargo at 37 °C after 10 mins, which is a significantly shorter release time compared to TTLD+HNP which required 60 mins to release a similar amount. Also, the amount of gemcitabine release from the GEM-TSLnps formulation seems to stabilise between 42 °C to 52 °C at 60 % release compared to the 100 % release after 30 mins for the TTLD+HNP formulation at 44 °C. This shows that TTLD+HNP proves superior in both stability at core body temperature and rapid drug release at the target therapeutic temperature of 44 °C.

GEM-TSLnps, HaT-GEM and gem-ML are the most noteworthy known thermally sensitive drug delivery systems for gemcitabine and they are all liposome based. These all suffer

from inefficient encapsulation levels, poor long term stability and either poor stability at 37 °C and/or lower rapid release profiles at 44 °C. This is due to the physical requirement of the liposomes to encapsulate their cargo and physically morph their structure at 44 °C in order to allow their cargo to escape. TTLD+HNP is a metallic nanoparticle based drug delivery system which achieved a near 100 % loading of 5 mg of a gemcitabine analogue (TTLD) per 1 mg of HNPs as well as a similar loading efficiency when TTLD was simultaneously loaded onto the HNP gold surface alongside PEG-Thiol. Attachment of TTLD and PEG-Thiol is achieved chemically rather than with physical encapsulation leading to a uniform and stronger interaction between the carriers (HNPs) and their cargo (TTLD). The release is also a chemical process that does not occur at physiological pHs of 5.6 and pH 7.4 as well as pH 7. Mode of release is purely temperature dependant in a biological setting where the thermal stability remains higher than most mentioned liposome based systems at 37 °C but has a superior rapid release profile at 44 °C.

There are no indications of a metallic nanoparticle delivery system for the transport and thermal release of gemcitabine in literature to date which suggests that TTLD+HNP is a first of its kind as a metallic based thermal sensitive drug delivery system for gemcitabine, as well as one that utilizes chemical reactions rather than physical changes to elicit temperature dependant drug release.

Studies have already shown that laser irradiation of HNPs will achieve temperatures of 44 °C which further highlights the potential of HNPs with surface modified Diels Alder cycloadducts as drug carriers and facilitators of thermally driven drug release (Curtis *et al.* 2015). Here, the effect of pH on the TTLD+HNPs formulation was minimal between a pH of 7.4 and 5.6. This finding indicates that no matter what location the nanoparticulate formulation is in i.e. Intracellular location, which drug release will only occur after thermal rise. Hence a truly triggered release system has been developed.

The stability of the TTLD+HNP formulations was observed and the results show us that at typical storage temperatures of clinical medicines (room temp/cupboards and refrigeration) the TTLD+HNP formulations remained stable over four weeks with no observable trend in percentage release. At 20 °C the percentage release is roughly 0.31 %. This differs to the 0.69 % to 0.9 % release observed in the dialysis release studies. However this is not significant (p>0.05).

Previous retro Diels Alder experimental data shown in Figure 132 as well as dialysis release studies in Figures 153-155 at 20 °C both showed that TTLD remains stable over several days. However the medium term stability of the TTLD+HNP formulation which will be indicative of the potential shelf life needed to be ascertained. Medicinal formulations are often refrigerated or stored away from sunlight within cupboards at room temperature. This is to ensure that the composition of the formulation doesn't change over time. Changes can include the degradation of excipients or modification of the active pharmaceutical ingredient, which can reduce the potency of the drug (Qun Gao *et al*. 2014). In the case of thermally triggered systems the storage temperature is particularly relevant.

The TTLD+HNP formulations remained stable over four weeks with no observable trend in percentage release. At 20 °C the percentage release is roughly 0.31 %. This differs to the 0.69 % to 0.9 % release observed in the dialysis release studies.

3.5. Conclusion

The production of HNPs and their subsequent surface modification with TTLD and/or TTLD+PEG has been successful. The rate of Gem-Mal release from these formulations at various pHs and temperatures have yielded clinically promising results. The next stage of this study will be the observation of uptake and subsequent effects of the cell proliferation of pancreatic cancer cells.

CHAPTER 4: DRUG UPTAKE AND CELL VIABILITY STUDIES OF HYBRID NANOPARTICLE FORMULATIONS

4.0. Introduction

The ultimate goal of a pharmaceutical research and development study is to prove the effectiveness and safe use of novel treatments on patients (Lemke 2008). Human testing of unknown compounds and formulations would be extremely dangerous and highly unethical without some evidence of safety and efficacy before administration. Therefore drug discovery paths often originate with the chemical study of the desired drugs behaviour, followed by its activity in different simulated biological conditions, *in vitro* activity in cellular environments and finally in *vivo* animal testing (Lemke 2008; Pathania *et al*. 2014; Megha *et al*. 2015). Drug compounds and formulations that pass through these preclinical pathways with clear evidence of benefit are then eligible for human testing before they can be made available for clinical use. The *in vitro* phase of preclinical screening is important as it involves the use of living cells or tissues to evaluate the pharmacological activity of novel drug formulations (Aulton 2007).

Biological systems are a collection of complicated chemical systems and microenvironments which can have an effect on active ingredients and their constituents. Therefore novel drug formulations have to be observed in chemical environments which can mimic these physiological conditions (Wijdeven *et al*. 2014; de la Escosura *et al*. 2015). These environments can include the various biological pHs such as blood and the gastro intestinal tract (Lemke 2008; Aulton 2007). These are often tested individually to fully understand their effects on the drug formulation being tested without the interference of other chemical variables, such as testing a novel drug in a series of biological pHs without changing the temperature, concentration etc.

One critical step in this transition from chemical interactions to biological ones is the *in vitro* testing of novel drug formulations. This involves the growth of human cells outside the body which are then exposed to the drug formulations in different conditions to determine their effects (Lemke 2008). Like with the chemical testing performed prior, the advantage of *in vitro* testing is that the cells are isolated away from other biological effects that would be present in *vivo* allowing the focus of the interactions to take intracellularly (Vinken & Blaauboer 2016; Aulton 2007). Lastly, there has been a growing worldwide move away from animal testing with bans taking place for certain groups of chemicals such as cosmetics research in the EU (Vinardell 2015). The general consensus though is that *in vivo*

experiments are crucial in ensuring the safety of humans inoculated with unproven chemicals for clinical use only when suitable *in vitro* testing is not available (Garattini & Grignaschi 2016; Vinardell 2015). As a form of compromise, the expanded use of *in vitro* experiments on a wider range of variables should reduce the amount of *in vivo* experiments needed (Vinardell 2015). Overall, the application of *in vitro* testing is a key and invaluable step in the evaluation of new drug entities for clinical use (Vinken & Blaauboer 2016).

This studys overall aim is to evaluate the *in vitro* effects of Gem-Mal, +HNP and the HNPs alone against gemcitabine and experimental controls in order to observe their effects. The desired clinical effect of the TTLD+HNP formulation is the reduction of cell viability of pancreatic cancer cells. Therefore the percentage cell viability will be used as an indicator of the effectiveness of these drug and HNP compounds. Cell viability is the term used to describe the ability of cells to maintain and grow their population, to basically remain viable. The percentage cell viability is the amount of cells that remain viable in an altered environment (such as after exposure to a cytotoxic drug) compared to the cell viability from a population of cells in optimal growth conditions (Bandele *et al*. 2012; Weyermann *et al*. 2005; Yang *et al*. 2002). The percentage cell viability changes were determined with the 3-(4,5-dimethylthiazol-2-yl)-2,5-diphenyltetrazolium bromide (MTT) assay and trypan blue exclusion assay.

Pancreatic cancer has an absolute 5 year survival rate of 3.7 %. This means that after the disease is first diagnosed the patient has a 3.7 % chance of surviving after 5 years (Liu *et al*. 2012b; Yuqing Zhang *et al*. 2013c; Tran *et al*. 2013b). This particularly deadly type of cancer has the worst prognosis of all cancer types (Yuqing Zhang *et al*. 2013c; Al Shemaili *et al*. 2014). It is the 5th most common cause of cancer death in the UK accounting for 2.6 % of all cancer cases but 5.2 % of all cancer related deaths (Maraveyas *et al*. 2012).

It is administered intravenously over a course of 30 mins slowly to prevent localised toxicity at the administration site (Pliarchopoulou & Pectasides 2009). It has a short half-life of 8-17 mins and a large portion of the dose is metabolised in the liver which leads to high dose requirements in order to attain a therapeutic response (Griffith & Jarvis 1996). Some patients do not experience a therapeutic effect after gemcitabine administration which has led to its reported effectiveness in only 23.8 % of all who receive it (Burris *et al*. 1997; Hoskins *et al*. 2010). The side effects associated with gemcitabine administration are

numerous and often serious especially with its hepatoxicity and renal toxicity effects. These side effects often prevent pancreatic cancer patients from continuing their chemotherapy.

Hybrid nanoparticles (HNPs) can be utilised for improving the chemotherapeutic treatment of pancreatic cancer. They can aid in the faster uptake and intracellular accumulation of their drug cargo and facilitate their heat triggered release in a controlled manner by exploiting the surface plasmon resonance properties from the gold coating of the HNPs. They can also be used to visually map the presence of drug-HNP formulations due to their iron oxide cores acting as MRI contrasting agents.

4.0.1. MTT assay

The MTT assay utilises colourimetry to indicate the metabolic activity of cells after exposure to an introduced substance. 3-(4,5-dimethylthiazol-2-yl)-2,5-diphenyltetrazolium bromide (MTT) is a yellow soluble dye that is enzymatically metabolised (reduced) into insoluble purple formazan crystals intracellularly. This is carried out by mitochondrial reductase within the mitochondria and within endosomes with other reducing enzymes like NADH reductase (Bernas & Dobrucki 2002; Lü et al. 2012). This means that after MTT is added, the cells have to be left to incubate for a few hours before analysis can occur (Riss *et al*. 2004). The addition of DMSO will dissolve these formazan crystals producing a purple solution. The intensity of this solution is dependent on the amount of formazan present and is therefore indicative of the metabolic activity of the cells. Dead cells cannot metabolize MTT so the MTT assay can be used to discern the population of alive cells only (Huyck *et al*. 2012). The MTT assay is run with the use of controls that form the benchmark intensity where experimental variables can be based off. The MTT assay is a standard assay which is used for almost all cell viability studies as a starting point. Colourimetry is an analytical technique used to determine the concentration of a coloured substance within a solution (Riss *et al*. 2004). For example, the MTT assay of gemcitabine inoculated BxPC-3 cells shown in Figure 165. Note the two control columns on the left have the deepest shade of purple and all other well intensities would be compared against them as an indicator of percentage cell viability with the assumption that the controls have 100 percentage cell viability.
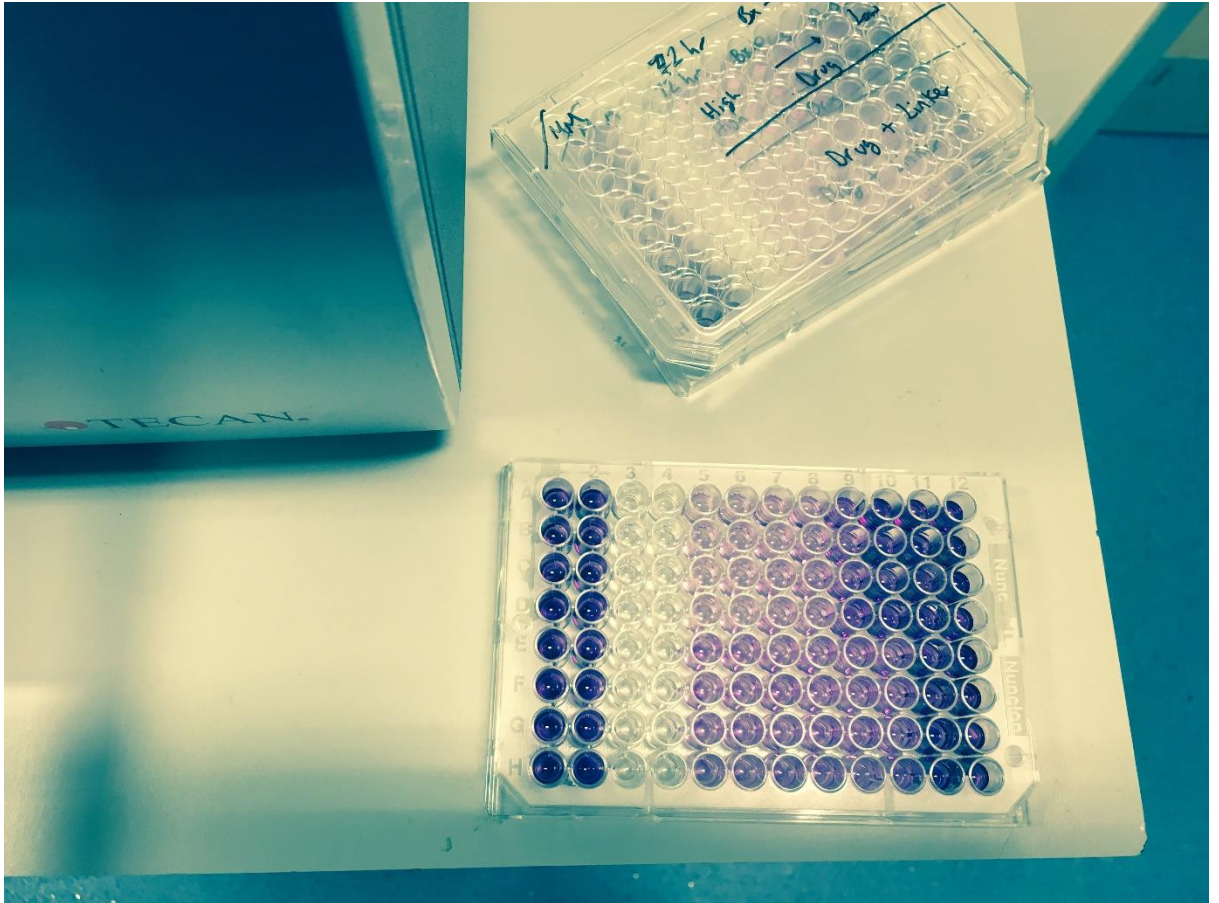
Figure 165: Photo of a 96-well plate after MTT incubation and DMSO addition with the first two columns being the positive control.

The plate in Figure 165 would be read on a plate reader where the absorbance would be determined for each well.

4.0.2. Trypan blue exclusion and cell counting

The trypan blue exclusion assay is a cell counting technique that can calculate the population of living and dead cells within a sample. It is based on the premise that trypan blue cannot enter living cells due to their structural integrity but it may enter cells which have already or are undergoing apoptosis/necrosis (Strober 2001). Once staining has occurred, the number of cells within a sample is determined. The dye free cells are considered viable and the dead cells will have a blue appearance from the trypan blue staining (Strober 2001). Basic cell counting techniques involve placing a diluted sample of the cells onto a specialised microscope slide called a haemocytometer which were historically used for blood cell counts but can be used for other cell types (Brito *et al*. 2016). These have a grid pattern where each section is a specific area and therefore volume. The

average number of cells within each grid is related to the overall cell population of the cell stock once dilution factors are incorporated into calculations (Brito *et al*. 2016). Modern automated haemocytometers can use microscopic images of a region from a microscope slide to determine the cell population using recognition software that automatically detects living and dead cells within a sample region (Grishagin 2015; Han *et al*. n.d.).

4.0.3. Drug uptake and centrifugation

The drug uptake rate of gemcitabine, Gem-Mal and the TTLD+HNP formulation is important to determine the effectiveness of the HNPs as a drug delivery vehicle (Fang *et al*. 2015). The cytotoxic activity of gemcitabine and Gem-Mal occurs intracellularly so any initial biological assays such as the trypan blue exclusion or MTT may not take into consideration whether an equal amount of each substance is present within the cells (Song *et al*. 2016b). For example, gemcitabine may be inherently more cytotoxic than Gem-Mal but have a lower uptake rate. In order to analyse the drug uptake rate of these substances, cultures of human pancreatic adenocarcinoma BxPC-3 cells will first have to be grown then dosed. After enough time has taken place for drug uptake to occur, the extracellular environment was purged of gemcitabine, Gem-Mal or TTLD+HNP by washing the wells with PBS. The cells are then counted and a volume of suspended cells of known cell population is taken for analysis. This will be done with centrifugation which is a technique used for separating the components of a mixture with centripetal forces (Zubrick 1997). This causes larger components to settle first causing sedimentation of the mixture contents. Only components soluble in the supernatant (the surface liquid layer) will be present there. Gem-Mal and gemcitabine are water soluble and will be present in the supernatant while the destroyed cells which burst due to osmotic pressure, and their organelles will settle at the bottom. The supernatant can then be removed and analysed with HPLC to acquire the gemcitabine or Gem-Mal concentration.

4.1. Aims and objectives

The aim of the *in vitro* studies is to observe the effects of Gem-Mal, the HNPs alone and the TTLD+HNP formulation against controls and gemcitabine on the percentage cell viability of BxPC-3 cells. The drug uptake rates of each substance mentioned will be

determined as well in order to ascertain the effectiveness of the HNPs to facilitate the uptake of Gem-Mal.

4.2. Materials and methods

4.2.1 Materials used

Material	Supplier
BxPC$_3$ Cells	LGC Standards, ATCC (USA)
RPMI Media	Fisher Scientific (UK)
Gemcitabine	Fluorochem (UK)
Cell Culture Flask	Fisher Scientific (UK)
96-Well Plates	Fisher Scientific (UK)
12-Well Plates	Fisher Scientific (UK)
6- Well Plates	Fisher Scientific (UK)
Dulbecco's Phosphate Buffered Saline	Sigma Aldrich (UK)
3-(4,5-dimethylthiazol-2-yl)-2,5-diphenyltetrazolium bromide	Sigma Aldrich (UK)
Dimethylsulfoxide	Fisher Scientific (UK)
Trypan Blue Stain 0.4 %	Life Technologies (UK)
Trypsin-EDTA	Life Technologies (UK)
Eppendorf Tubes	Fisher Scientific (UK)
Cell Counting Slides	Life Technologies (UK)
Streptomycin Penicillin	Life Technologies (UK)
Foetal Bovine Serum	Life Technologies (UK)
Glutaraldehyde	Sigma Aldrich (UK)

4.2.2. Methods

4.2.2.1. Preparation of Bx-PC3 cell cultures

All *in vitro* experiments and results discussed in this study were carried out using the BxPC-3 cells. Well plate cell cultures were produced by seeding BxPC-3 cells in their exponential growth phase and allowing them to incubate overnight at 37 °C within a 5 % CO_2 atmosphere in RPMI-1640 media supplemented with a 1 % streptomycin penicillin and 5 % foetal bovine serum (Fang *et al*. 2015).

4.2.2.2. Preparation of excipient solutions and well plate dosing

Throughout the *in vitro* studies, eight different concentrations of substances were used to monitor their effects on BxPC-3 cell populations over time. Preparation of these concentrations is shown in Table 11. Each Aliquot was taken from 20 mg mL^{-1} stock solutions of either gemcitabine, Gem-Mal, TTLD+HNP or HNPs alone. The amount of Gem-Mal used in these solutions was calculated based on the mass of gemcitabine within Gem-Mal. With Gem-Mal being roughly twice the mass of gemcitabine, then a stated 0.1 mg mL^{-1} of Gem-Mal would actually be 0.2 mg mL^{-1} of Gem-Mal. This ensures that their cytotoxicity comparisons are based on gemcitabine. The TTLD+HNP stock solution was calculated based on the gemcitabine content of TTLD (5 mg per 1 mg HNPs) and the HNP stock solution was based on the iron content on the HNP's derived by ICP-OES.

Table 11: Preparation of Excipient Solutions for BxPC-3 dosing.

Concentration (mg mL^{-1})	Stock Aliquot (mL)	Total Volume (mL)
0.1	22.5	4.5
0.05	11.5	4.5
0.025	5.6	4.5
0.01	2.25	4.5
0.005	1.125	4.5
0.001*	90	4.5
0.0001*	9	4.5
0.00001*	1	4.5

* Aliquot was taken from 0.05 mg mL^{-1} solution.

4.2.3. MTT assay procedure

A 96-well plate was seeded with 15,000 of BxPC$_3$ cells/well which were previously suspended in media. These were incubated inside an ESCO CelCulture CO$_2$ Incubator for 24 h at 37 °C in a 5 % CO$_2$ environment to allow the suspended BxPC$_3$ cells to attach to the well surfaces. The media was removed and the well plates were dosed in a format illustrated in Figure 166.
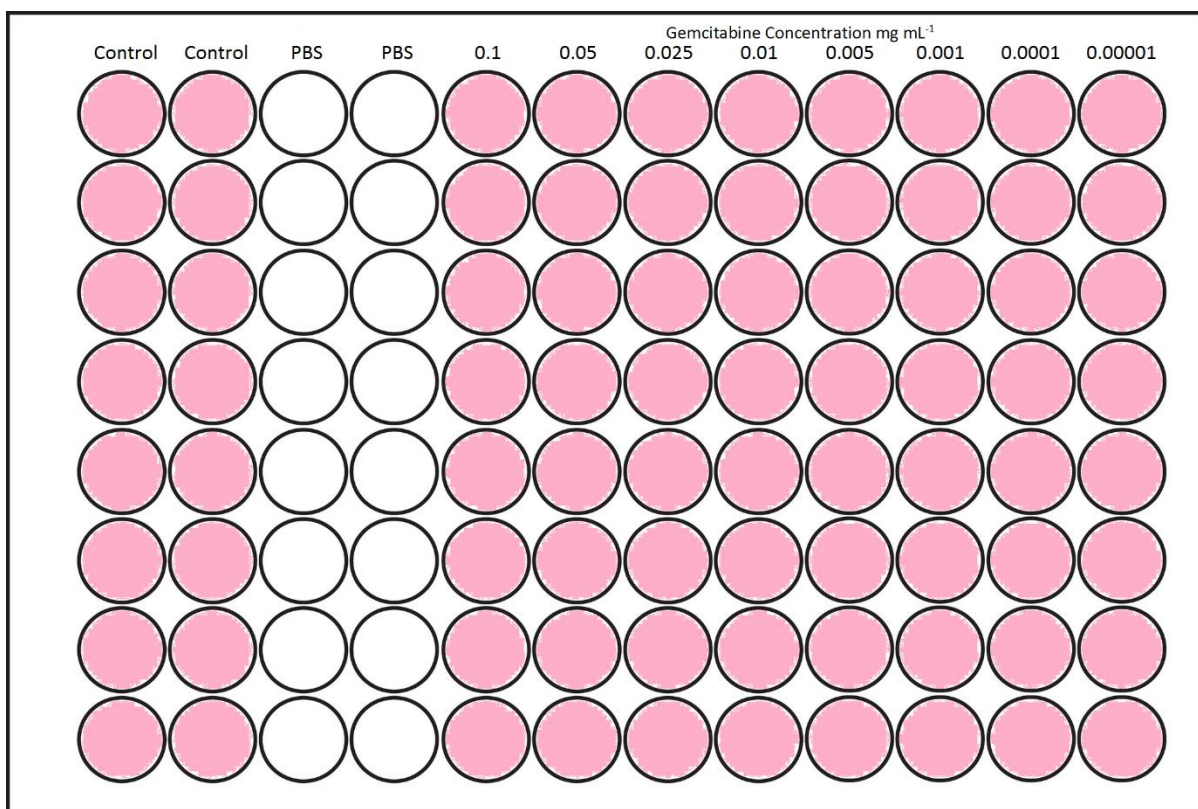
Figure 166: Diagram of the 96-well plate assembly for the MTT assay of gemcitabine dosed BxPC-3 cells setup.

The 96-well plate was incubated for 24 h at 5 % CO_2. Following this, the media and PBS was removed and replaced with a 175 µL solution of 10 % MTT in media. The plate is then incubated for 4 h to allow the uptake of MTT into the $BxPC_3$ cells. Afterwards, the media was removed and the wells were washed three times with PBS to ensure no gemcitabine remained. After this wash step, 175 µL of DMSO was added causing the well plate wells to rapidly change colour to variable shades of purple due to the dissolution of the purple formazan crystals (Gaudin *et al*. 2016). The 96-well plate was then analysed by a Tecan Infinite M200 Pro Microplate Reader at 570 nm and the percentage cell viability was calculated as an intensity percentage of the control wells values. This method was repeated two more times on two other 96-well plates to form a triplicate set of results. Two other triplicate sets of experiments were carried out at the 48 h and 72 h time point after gemcitabine addition. This led to a total of 9 individual 96-well plates for the MTT gemcitabine study. Another two studies using the same procedure as the MTT gemcitabine study were carried out for Gem-Mal and TTLD+HNP.

4.2.3.1. Trypan blue exclusion assay procedure

The trypan blue exclusion method was used to monitor the change in population over time of BxPC$_3$ cells after dosing with gemcitabine, Gem-Mal, TTLD+HNP and the HNP's alone and to determine each substances IC$_{50}$. The trypan blue procedure for gemcitabine was carried out by first seeding a 12-well plate with 0.5 mL of 25,000 cells/well BxPC$_3$ cells which were previously suspended in media. The plate was incubated for 24 h at 37 °C in a 5 % CO$_2$ atmosphere to allow the cells to adhere to the well plate surfaces. The media was removed and the BxPC-3 cells dosed with gemcitabine in the same format as shown in Figure 167. The 12-well plate was incubated for 24 h before the well plates were washed three times with PBS to remove trace gemcitabine. Following this, 75 µL of trypsin and the cells were briefly incubated before they were suspended in 0.5 mL of media (Banerjee *et al*. 2013).

Figure 167: Diagram of the 12-well plate assembly for the trypan blue exclusion assay of gemcitabine dosed BxPC-3 cells setup.

The analysis of each well plate of suspended BxPC$_3$ cells occurred as follows: Into a fresh eppendorf tube was added 75 µL of a 0.4 % trypan blue solution, followed a 75 µL aliquot of a cell suspension. The 150 µL dyed suspension was briefly shaken and a 10 µL aliquot was removed from the eppendorf tube and pipetted into a Countess Invitrogen cell counting chamber slide. The cells were counted using a Countess Invitrogen Automated Cell Counter and the live cell counts were compared to those of the control well plate cell populations to produce a percentage cell viability value for each sample concentration. This was repeated to form a set of 12-well plate triplicates for gemcitabine.

4.2.3.2. Intracellular drug uptake

In order to determine the rate of drug uptake over time of gemcitabine, Gem-Mal, TTLD+HNP and HNPs alone, BxPC$_3$ cells which had been previously seeded and incubated at 37 °C in a 5 % CO$_2$ atmosphere for 24 h. They were then dosed with 3 mL of a 0.05 mg mL^{-1} solution of gemcitabine, Gem-Mal, TTLD+HNP or HNPs alone in media in 6-well plates (50,000 cells/well) where each well was dosed with only one of the mentioned four substances with a 5th well used as the control. The 6-well plate setup is illustrated below in Figure 168.
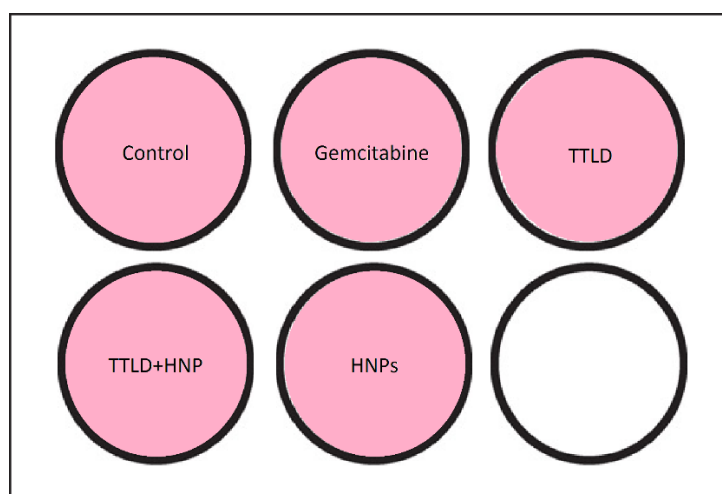
Figure 168: Diagram of the 6-well plate assembly for the drug uptake study for gemcitabine, Gem-Mal, TTLD+HNP and HNP only dosed BxPC-3 cells setup.

The BxPC-3 cells were incubated for 1 h to allow the uptake of the various substances to occur. Following this, the cell media was removed and the wells were washed three times with PBS to ensure the removal of trace amounts of the substances. The cells were suspended with 185 µL of trypsin before 815 µL of the media was added. The cells were then counted with a trypan blue assay to determine the amount of live cells per mL. An aliquot of each well plate equivalent to 100000 cells was acquired and placed into an Eppendorf tube. Deionised water was then added until the total volume of each tube was 1 mL. The presence of deionised water causes rupture of the cell membrane due to an osmotic imbalance caused by the hypotonic environment which releases the contents of the cells into the surrounding solvent. Centrifugation of this solution in a Hermule Z-323 centrifuge at 500 rpm for 5 min, drives the cell fragments to the bottom of the Eppendorf tube. The supernatant was removed and analysed via HPLC with a Pinnacle DB C18 reverse

phase column at 268 nm in a Perkin Elmer Flexar LC Autosampler with a flow rate of 1 mL min^{-1} (1:1 v/v water:acetonitrile) where a sample injection volume of 10 µL was used. The observed HPLC intensities were converted to concentrations with the calibration curve "$y = 22702849.34x$" where y is the intensity and x is the concentration in mg mL^{-1}. Each resulted calculated concentration was divided by 100000 to acquire the amount of gemcitabine per cell. This procedure was repeated two more times to generate a triplicate set of results for the uptake of gemcitabine in the unbound form, as unbound Gem-Mal, as released Gem-Mal and from the HNP's alone without any surface attachments after 1 h. This procedure was repeated again in triplicate at the 4 h and 24 h mark.

4.2.3.3. Effect of heat on cell viability

In a clinical setting, the TTLD+HNP formulation would release its Gem-Mal cargo after exposure to laser irradiation resulting in a localised elevated temperature. Previously we have shown that this release occurs at 37 °C and more significantly at the desired 44 °C temperature. Therefore a trypan blue exclusion was carried out on a previously seeded 12-well plate of BxPC-3 cells, where 8 different concentrations of gemcitabine, Gem-Mal, TTLD+HNP and the HNPs alone were added. This was repeated five times to produce 6 individual 12-well plates. The diagram in Figure 169 illustrates the well plate setup for this study.
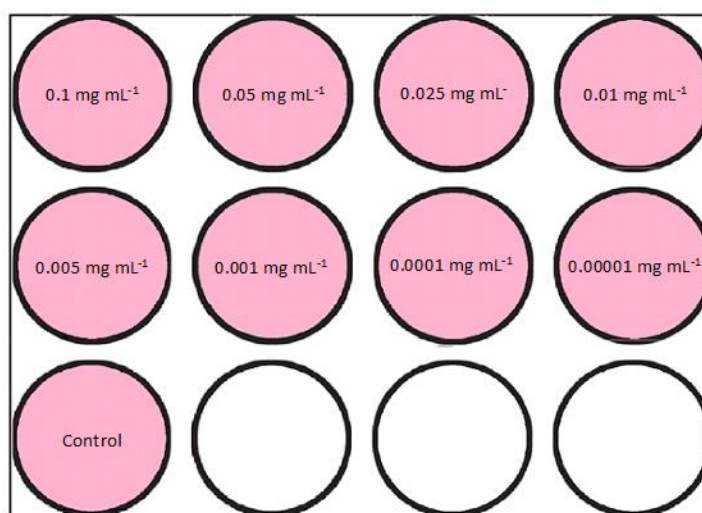
Figure 169: Diagram of the 12-well plate assembly for the increased heat exposure study for gemcitabine dosed BxPC-3 cells setup.

The 6 individual 12-well plates were incubated for 48 h to ensure that an adequate uptake of gemcitabine, Gem-Mal and TTLD+HNP occurred so that the IC_{50} of BxPC-3 (determined by trypan blue exclusion) would be reached. Half of the well plates were removed after 24 h and placed into a preheated Memmert IN-30 incubator and heated at 44 °C for 0.5 h to simulate the thermal rise generated by the SPR of laser irradiated HNP gold coatings before returning back into the 37 °C, 50 % CO_2 incubator. The other three plates were not removed throughout their 48 h incubation. The IC_{50} was determined for all 6 plates and the heat activated IC_{50} results were compared to the non-activated plates to note the effect on percentage cell viability using trypan blue exclusion.

4.3. Results

4.3.1. Cell viability

The effects of gemcitabine, Gem-Mal, TTLD+HNP and the HNP alone were observed by dosing BxPC-3 cells with known concentrations of these substances over a 72 h period with analysis taking place at the 24 h 48 h and 72 h time points. Gem-Mal is comprised of gemcitabine attached to a maleimide via an amide linker.

4.3.1.1. MTT assay for cell viability

The graph ahead in Figure 172 shows the relationship between gemcitabine concentration and time on the percentage cell viability of BxPC-3 cells. The graphs in Figure 170 and 171 use the same experimental parameters for Gem-Mal and TTLD+HNP respectively.

Figure 170: Graph depicting the effect of Gem-Mal concentration on BxPC-3 cells at various concentrations at 24, 48 and 72h time points with the MTT assay (n=3) (± 5.5 %). Data points labelled with * and ❑ show statistically significant effects on % cell viability at 48 h and 72 h compared to the previous time points 24 h and 48 h respectively ($P < 0.05$).

Only Gem-Mal achieves an IC_{50} using the MTT assay within 24 h of incubation with a concentration of 0.038 mg mL^{-1}. Gem-Mal displays increasing cytotoxicity over time as the percentage cell viability decreases from over the 24 h, 48 h and 72 h time points at all

concentrations indicating its cytotoxic properties, even when introduced extracellularly in an unbound form and taken up. ($P < 0.05$). The graph lines in Figure 170 show that Gem-Mal's detrimental effect on percentage cell viability is also the highest at the 72 h time point compared to gemcitabine and the TTLD+HNP formulation. At a concentration of 0.1 mg mL^{-1} the percentage cell viability has fallen to the lowest point in all experimental conditions of 19 %. Therefore Gem-Mal displays the most cytotoxicity at the 24 h and 72 h time points ($P < 0.05$).

The TTLD+HNP formulation does not achieve an IC$_{50}$ until its analysis at the 72 h time point which occurs at a concentration of 0.0005 mg mL^{-1} shown in Figure 171.

Figure 171: Graph depicting the effect of TTLD+HNP concentration on BxPC-3 cells at various concentrations at 24, 48 and 72h time points with the MTT assay (n=3) (± 7.8 %). Data points labelled with * and ☐ show statistically significant effects on % cell viability at 48 h and 72 h compared to the previous time points 24 h and 48 h respectively ($P < 0.05$).

At the highest concentration the cell viability decreases from 70 % at 24 h to 59 % and 31 % for the 48 h and 72 h time points respectively ($P < 0.05$). This shows that increasing the exposure time to TTLD+HNP decreases the cell viability. After 72 h there is no decrease in percentage cell viability for TTLD+HNP compared to the 24 h mark at 0.01 μg mL^{-1}. In fact

the percentage cell viability has increased from 96 % at 24 h, which might indicate that there is no pharmaceutical effect of the TTLD+HNP at 0.01 µg mL^{-1}. This is shown at the 48 h mark as well (P < 0.05). The 4 % reduction in cell viability from the 24 h to 48/72 h might be due to experimental errors and not a factor of TTLD+HNP exposure.

At the lowest concentration of 0.01 µg mL^{-1} for TTLD+HNP, there is little discernible effect on percentage cell viability. The percentage cell viability is 99 % on average at the 48 h in Figure 171, which indicates that the activity of TTLD+HNP is so low that it has marginal effects on cell viability if any at all. One theory for this, is that the formulation cannot produce an effect until it has been taken up in sufficient amounts and also released from the HNP surface. After the cells were exposed to TTLD+HNP the percentage cell viability decreased from 99 % at 0.01 µg mL^{-1} to 31 % at 0.1 mg mL^{-1}. However much of this reduction in percentage cell viability occurs between 0.01 µg mL^{-1} to 0.001 mg mL^{-1} where it falls to 41 % (P < 0.05). Between 0.001 mg mL^{-1} to 0.01 mg mL^{-1} there is a small decrease in percentage cell viability from 41 % to 34 % as well (P < 0.05). This trend of a sharp decrease in percentage cell viability between 0.01 µg mL^{-1} and 0.001 mg mL^{-1} followed by a gentle decrease is also observed at the 24 h and 48 h time points. At all three time points there is a statistical decrease in percentage cell viability from 0.001 mg mL^{-1} to 0.01 µg mL^{-1} (P < 0.05).

Unlike the TTLD+HNP formulation, gemcitabine has a noticeable effect on cell viability, even at a concentration of 0.00001 mg mL^{-1} after 24 h, which has dropped to 81 % in Figure 172.
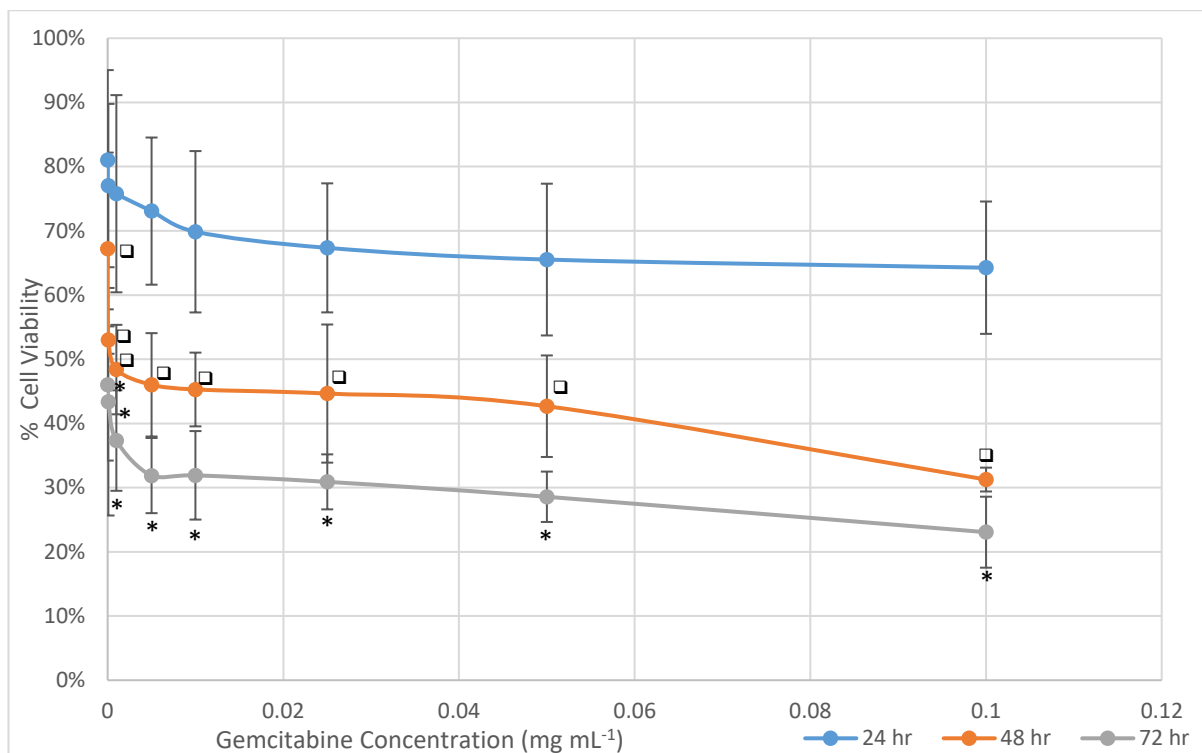
Figure 172: Graph depicting the effect of gemcitabine concentration on BxPC-3 cells at various concentrations at 24, 48 and 72 h time points with the MTT assay (n=3), (± 3.7 %). Data points labelled with * and ❑ show statistically significant effects on % cell viability at 48 h and 72 h compared to the previous time points 24 h and 48 h respectively (P < 0.05).

This drop in cell viability increases as the concentration does, where it falls from 81 % to 64 % between gemcitabine concentrations of 0.00001 mg mL^{-1} to 0.1 mg mL^{-1}, an overall decrease of 17 % (P < 0.05). TTLD+HNP ranges from 96 % cell viability to 70 %, a difference of 26 % over this concentration range at 24 h (P < 0.05). At the 72 h time point gemcitabine at 0.00001 mg mL^{-1} reduces the cell viability to 46 % and at 0.1 mg mL^{-1} the percentage cell viability is at 23 % (P < 0.05). Even at the lowest concentration, accumulation of gemcitabine within the cells is enough to cause the desired pharmaceutical activity which only improves as the concentration and exposure time increases (P < 0.05). Gemcitabine has an IC$_{50}$ of 0.0009 mg mL^{-1} after 48 h and <0.00001 mg mL^{-1} after 72 h.

The overall trend between gemcitabine and TTLD+HNP is that, lower concentrations of TTLD+HNP decreases the cell viability less than gemcitabine does. This continues to higher

concentrations where gemcitabine has a lower cell viability to TTLD+HNP at all concentrations. Gemcitabine's path will be a combination of drug uptake/accumulation into the cell versus the drug's expulsion/metabolism out of the cell. Overall gemcitabine would accumulate within the cell, even at very low concentrations of 0.00001 mg mL^{-1} decreasing percentage cell viability. TTLD+HNP has to first accumulate within the cell and then release its cargo. Previous results shown earlier in chapter 3 show that the Gem-Mal is released from the HNP surface more rapidly at 44 °C with a much retarded release at 37 °C. Therefore it's likely that even after accumulation of TTLD+HNP within the cells the pharmaceutical component of the formulation does not produce an effect until it is released from the HNP inside the cell. This release stage will stagger the activity of the TTLD+HNP formulation within the cell at low concentrations. As the concentration increases, this inhibition effect decreases as the cell viability begins to resemble those of gemcitabine. This suggests that TTLD+HNP is accumulating faster in the cells than gemcitabine, followed by a slow release within the cell. This might explain the sharp decrease in percentage cell viability of 40 % from 0.0001 mg mL^{-1} to 0.001 mg mL^{-1} for TTLD+HNP compared to a reduction of only 6 % for gemcitabine. The requirement of Gem-Mal to be released from the HNP after uptake appears to reduce its effect on cell viability.

4.3.1.2. Trypan blue exclusion for cell viability

The graphs in Figures 173, 174, 175 and 176 shows the relationship between the stated drug compound or HNP concentration and time on the cell viability of BxPC-3 cells. The trend seems to be that increased levels of gemcitabine, Gem-Mal, TTLD+HNP and the HNPs alone all reduce the cell viability of BX-PC$_3$ cells over time. There is a clear difference in all cases in cell viability after 24 h, 48 h and 72 h of exposure to gemcitabine (P < 0.05). The earliest recorded gemcitabine IC$_{50}$ is reached at the 48 h time point with a gemcitabine concentration of 0.0175 mg mL^{-1}. At the 72 h time point the IC$_{50}$ occurs at a gemcitabine concentration of 0.008 mg mL^{-1}. Gem-Mal has an IC$_{50}$ of 0.06 mg mL^{-1} at the 48 h time point and 0.012 mg mL^{-1} at the 72 h time point. The TTLD+HNP formulation has an IC$_{50}$ 0.025 mg mL^{-1} after 48 h and 0.004 mg mL^{-1} after 72 h. The HNPs alone did not reduce the cell viability enough to produce an IC$_{50}$ after 72 h indicating their biocompatibility over concentration ranges tested.
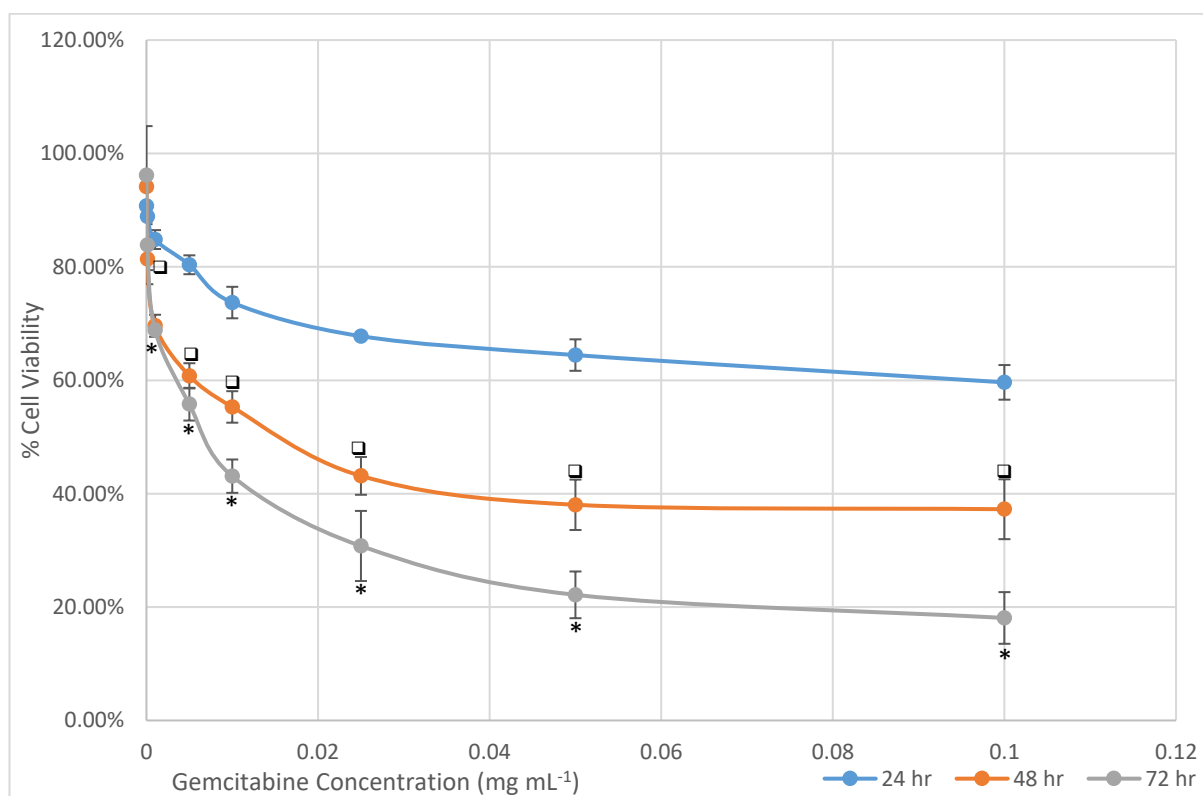
Figure 173: Graph depicting the effect of gemcitabine concentration on BxPC-3 cells at various concentrations at 24, 48 and 72h time points with the trypan blue assay (n=3, ±0 %, 5.9 % and 6.6 % respectively). Data points labelled with * and ▢ show statistically significant effects on % cell viability at 48 h and 72 h compared to the previous time points 24 h and 48 h respectively (P < 0.05).
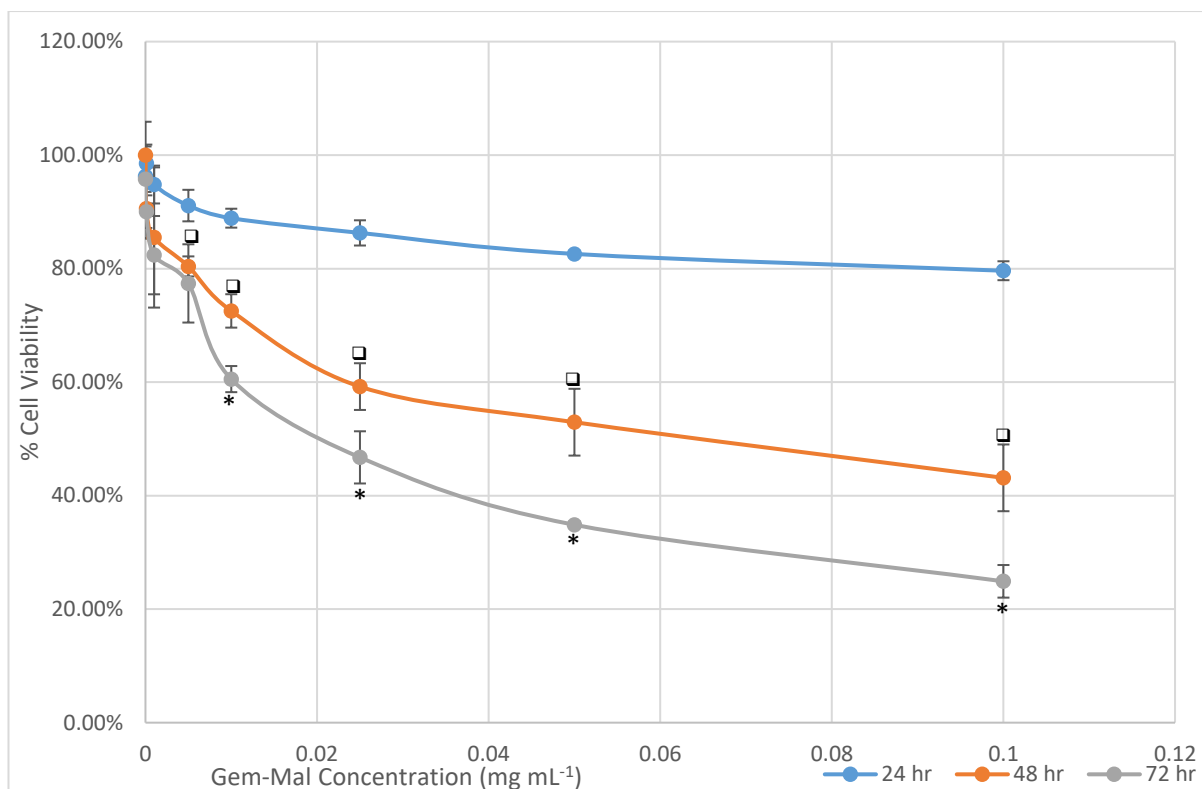
Figure 174: Graph depicting the effect of Gem-Mal concentration on BxPC-3 cells at various concentrations at 24, 48 and 72h time points with the trypan blue assay (n=3, ± 0 %, 5.8 % and 3 % respectively). Data points labelled with * and ❑ show statistically significant effects on % cell viability at 48 h and 72 h compared to the previous time points 24 h and 48 h respectively ($P < 0.05$).

Gemcitabine and Gem-Mal both have a strong effect on cell viability in both a time and concentration dependant manner. Gemcitabine has a lower IC_{50} than Gem-Mal after 48 h with a difference of 0.0425 mg mL^{-1}. Gemcitabine's IC_{50} falls to 0.008 mg mL^{-1} after 72 h while Gem-Mal's decreases to 0.02 mg mL^{-1}. Overall this shows that gemcitabine is more cytotoxic than Gem-Mal. This may be because Gem-Mal's intracellular cytotoxicity is lower than gemcitabine or that its uptake is slower which reduces its accumulation rate. Drug uptake experiments were carried out later on in this study that investigates this further.
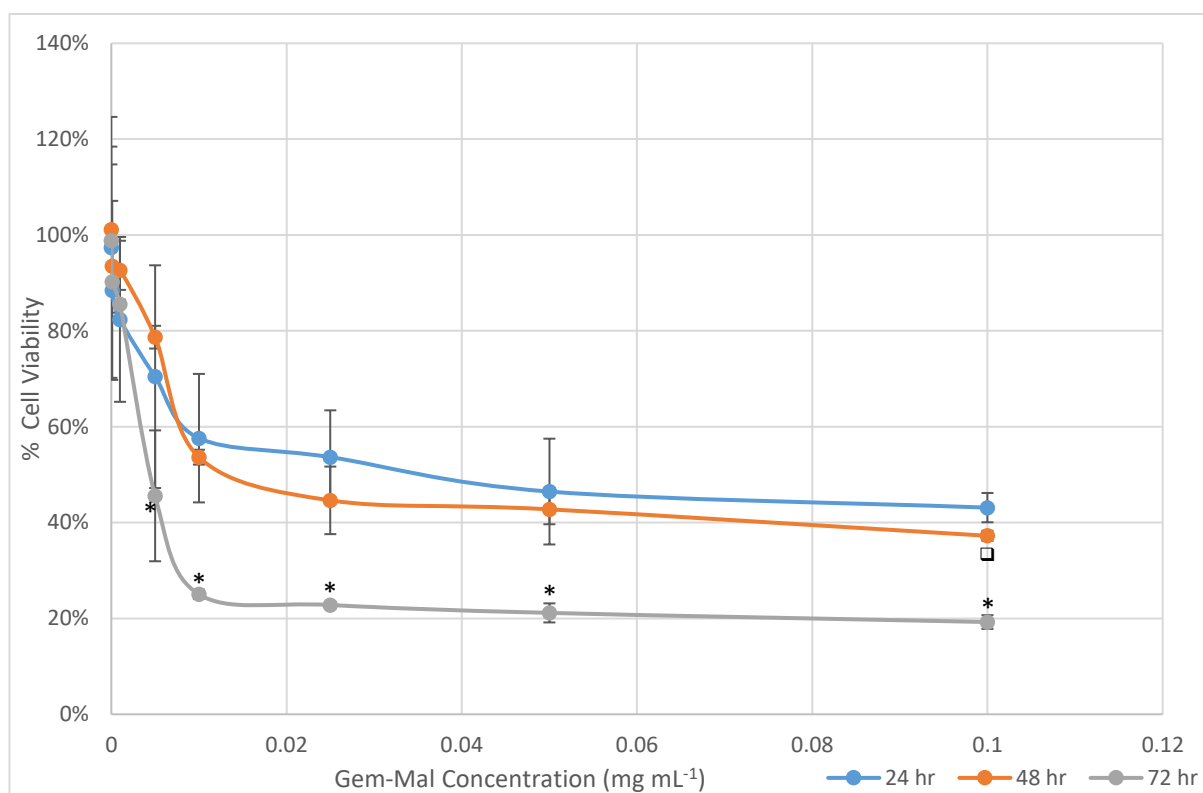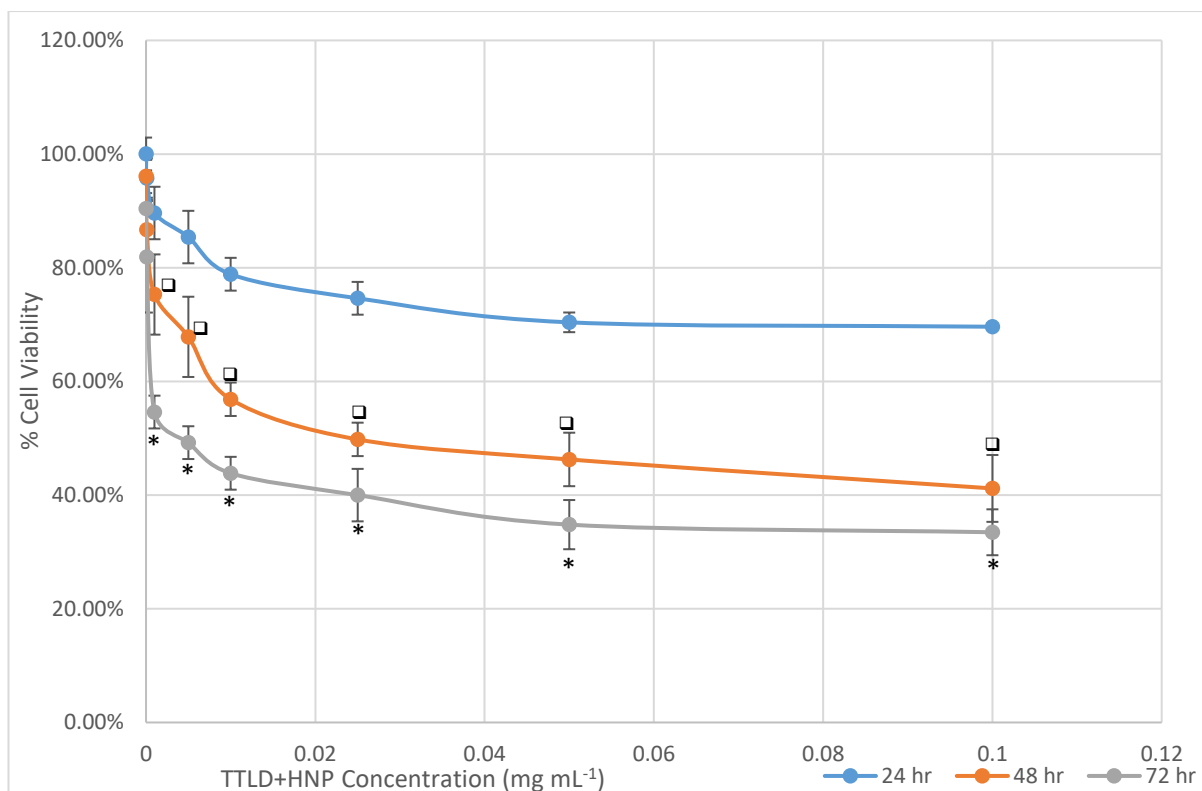
Figure 175: Graph depicting the effect of TTLD+HNP concentration on BxPC-3 cells at various concentrations at 24, 48 and 72h time points with the trypan blue assay (n=3, ±6.6 %, 5.4 % and 6.6 % respectively). Data points labelled with * and ❑ show statistically significant effects on % cell viability at 48 h and 72 h compared to the previous time points 24 h and 48 h respectively (P < 0.05).

The TTLD+HNP formulation has a lower IC_{50} of 0.025 mg mL^{-1} at 48 h compared to just the unbound Gem-Mal. This value is still 1.6 fold lower than gemcitabine's IC_{50} though, which remains the most cytotoxic substance at 48 h. This may be due to the fact that the TTLD+HNP is taken up faster than the unbound gemcitabine which increases its intracellular concentration at the 48 h time point, but the bound Gem-Mal is unable to have a cytotoxic effect until the retro Diels Alder takes place. The need for a retro Diels Alder step may have acted as a bottlenecking event intracellularly leading to a lower IC_{50}. This might explain why the IC_{50} of TTLD+HNP is lower at 0.004 mg mL^{-1} compared to gemcitabines 0.008 mg mL^{-1}. If the uptake of the TTLD+HNP's is one way then the overall concentration of the intracellular TTLD+HNP increases over time. This may lead to similar activities to unbound gemcitabine the longer the cells take up TTLD+HNP. These statements will be confirmed or repealed following the drug uptake experiments.
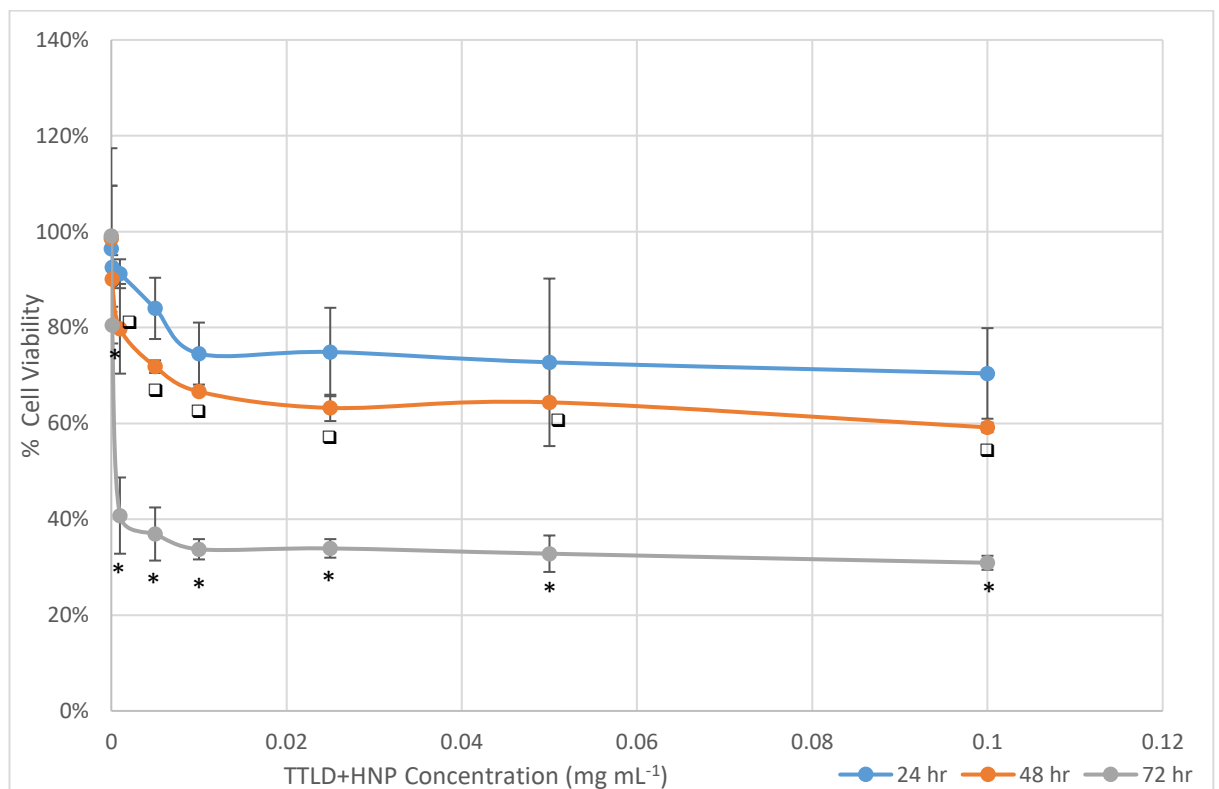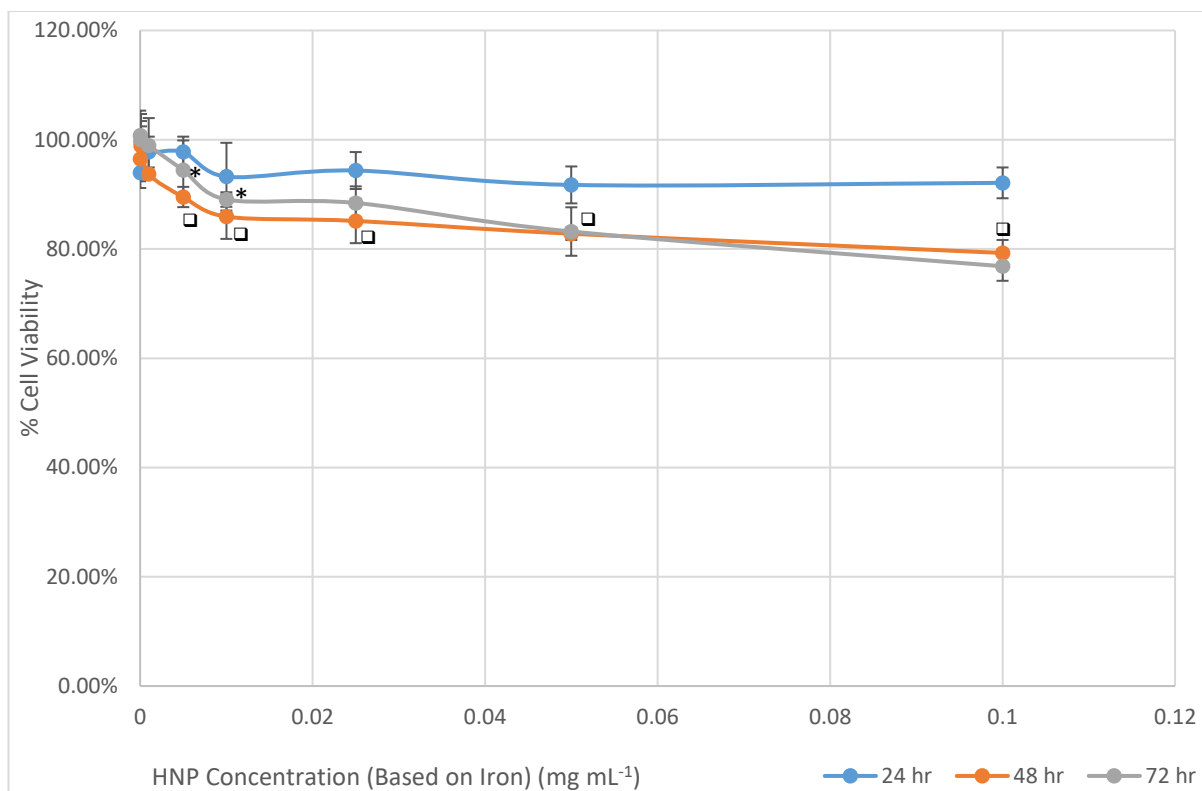
Figure 176: Graph depicting the effect of HNP concentration on BxPC-3 cells at various concentrations at 24, 48 and 72h time points with the trypan blue assay (n=3, ±2.6 %, 4.4 % and 3.6 % respectively). Data points labelled with * and ▢ show statistically significant effects on % cell viability at 48 h and 72 h compared to the previous time points 24 h and 48 h respectively (P < 0.05).

The cells appear to tolerate the presence of the HNPs even at the highest experimental concentration of 0.1 mg mL^{-1} where the percentage cell viability falls from 90 % to 77 % after 24 h and 72 h of incubation. At some lowered measured concentrations the cell viability is slightly higher at the 72 h time point compared to the 48 h time point. For example at 0.025 mg mL^{-1} the cell viability is 88 % after 72 h but 86 % for the same concentration at the 48 h time point. Each time point result is acquired from a triplicate set of individual well plate and hence experimental errors are likely the cause for the large standard deviations. The differences are large enough for the calculated error bars to overlap both results. Therefore the effects of the HNPs on percentage cell viability seems to peak at 48 h and no change in percentage cell viability occurs beyond that for concentrations of the HNPs between 0.1 mg mL^{-1} and 0.01 mg mL^{-1} (P < 0.05). Only at concentrations between 0.01 mg mL^{-1} and 0.005 mg mL^{-1} is there a statistical difference in cell viability between the 48 h and 72 h time points (P < 0.05).

4.3.2. Drug uptake results

In order to get a clearer picture of the activity of gemcitabine, Gem-Mal, TTLD+HNP have on cell viability, their intracellular concentrations were determined at set time points using reverse phase HPLC. This is because the cells may have more than one trafficking mechanisms for the internalisation and hence this effect the rate of uptake and hence ability to exhibit therapeutic effect.

4.3.2.1. HPLC determination for the cell uptake of excipients

The bar chart in Figure 177 shows the intracellular amount of each of the excipients per cell.
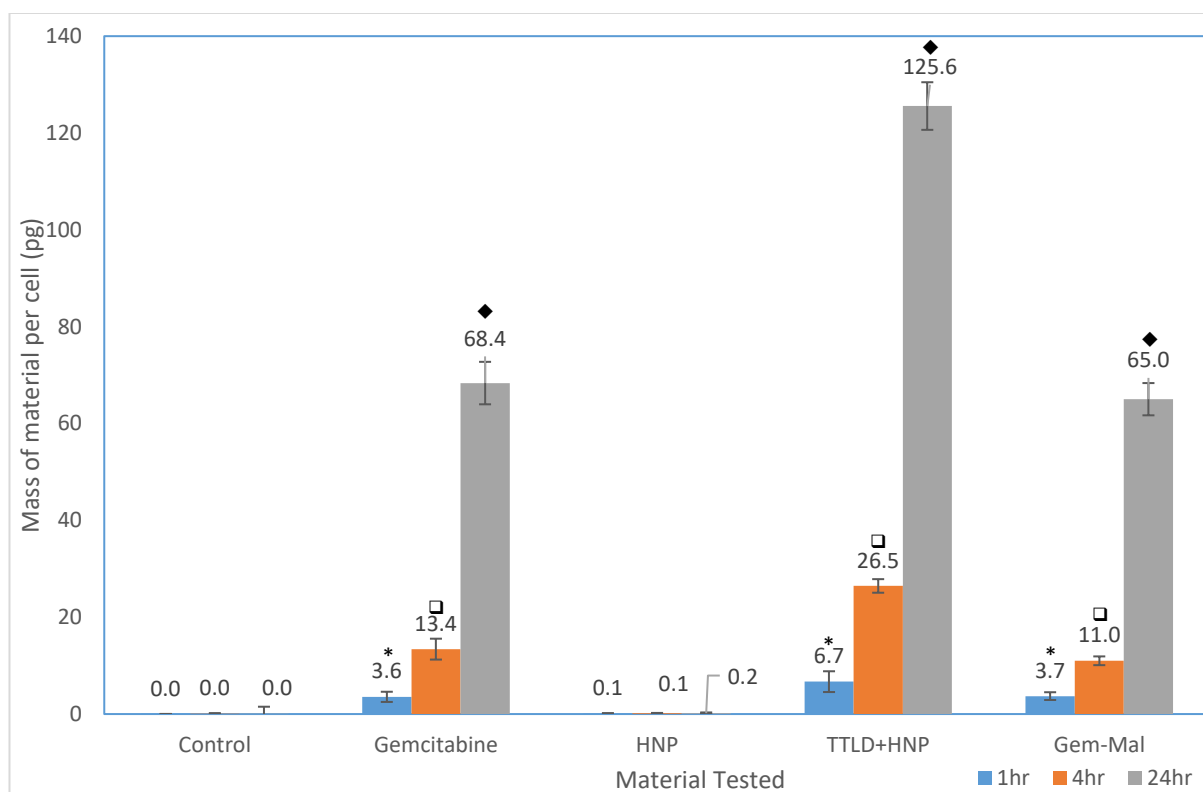
Figure 177: Bar chart displaying the average amount of gemcitabine inside the BxPC-3 cells after exposure to free drug (n=3) (± 4.27 %) compared to Gem-Mal (n=3), TTLD+HNPs (n=3) and HNPs (n=3) for 1 h, 4 h and 24 h exposure time. Data points labelled with *, ❑ and ◆ show statistically significant effects on % cell viability compared to the control for the 1 h, 4 h and 24 h time points respectively (P < 0.05).

Gemcitabine and Gem-Mal have very similar intracellular levels at all time points which suggests that Gem-Mal enters the cell via similar mechanisms. It is likely that both the free drug and prodrug enter via the tight junction in the cell membrane which can be a time consuming process, as well as being actively transported across the cell membrane with SLC28 and SLC29 nucleoside transporters (Mini *et al*. 2006; Rudin *et al*. 2011). The amounts

of detected drug after exposure to the TTLD+HNP formulation is significantly higher than at all time points when compared to gemcitabine and unbound Gem-Mal ($P < 0.05$). Hence this would indicate that the cellular trafficking mechanism of the formulation is different compared with the drug and prodrug. Numerous studies have indicated that nanoparticulate vehicles enter cells via endocytosis. This is often relatively rapid and results in much higher intracellular concentrations. As such, it is logical to postulate that endocytosis is the mechanism for the uptake of TTLC+HNP.

4.3.3. Effect of heat on cell viability

As previously discussed, the HNP-drug formulation requires heat activation before drug release is achieved. Our studies suggested that at 44 °C drug release is optimal. Hence we designed a study that allowed for this activation without adverse effects on the cells. After a 24 h incubation at 37 °C in a 5 % CO_2 atmosphere BxPC-3 cells which had been exposed to gemcitabine, Gem-Mal, TTLD+HNPs and the HNPs alone were placed in an incubator set to 44 °C for 0.5 h before returning back into the 37 °C 5 % CO_2 environment. The graphs in Figures 178, 179, 180 and 181 show the effects this 0.5 h of heating had on the percentage cell viability for gemcitabine, Gem-Mal, TTLD+HNP and HNPs respectively. The results garnered from the percentage cell viability of the BxPC-3 cells incubated in a 37 °C 5 % CO_2 environment and for 0.5 h at 44 °C have been named non-activated and heat activated respectively.
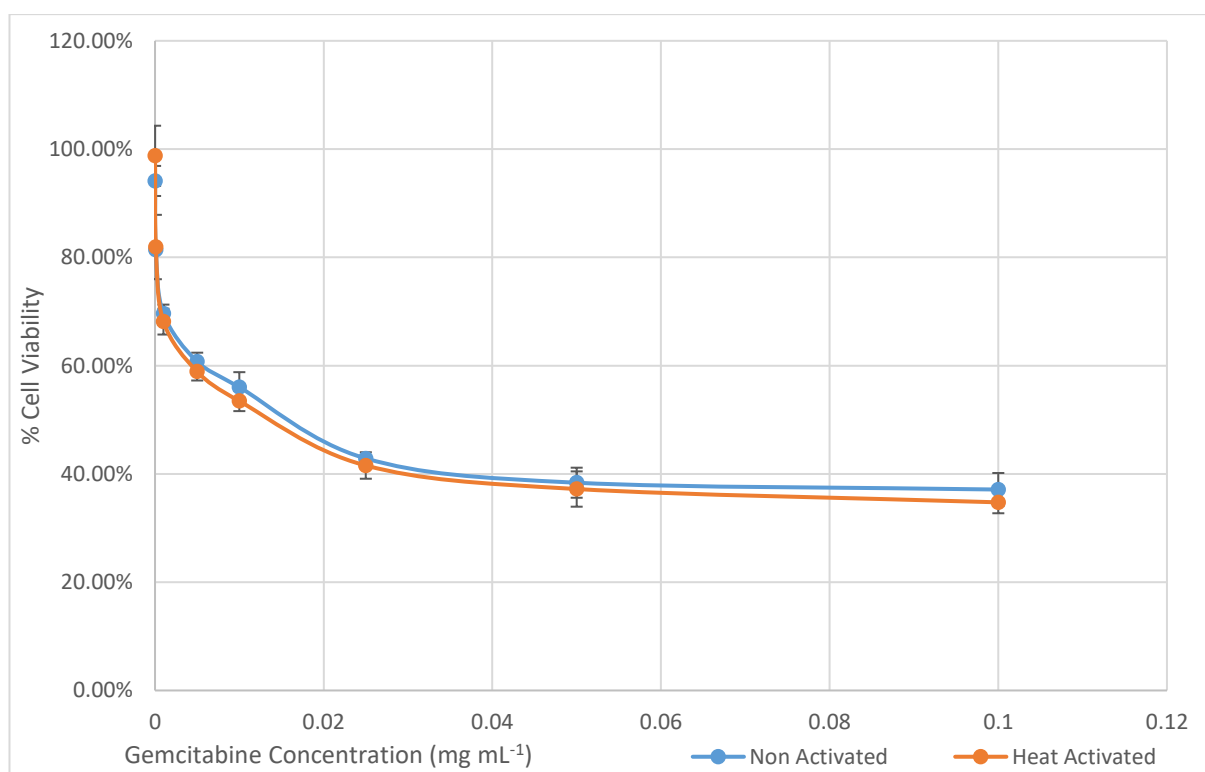
Figure 178: Graph of the change in percentage cell viability of gemcitabine dosed BxPC-3 cells with and without a 0.5 h incubation at 44 °C (n=3) (± 3.7 %). No statistical difference observed (P < 0.05).

The heat activated incubated cells that were dosed with gemcitabine, have a lower cell viability than the non-activated incubated cells, however the miniscule differences are of no statistical difference. The largest difference occurs at the lowest used concentration of

0.0001 mg mL^{-1}. This is surprising as it suggests that gemcitabine concentration is not the major factor in the differences in cell viability. This is confirmed with the error bars overlapping the differences between the cell viabilities suggesting that experimental errors are likely the cause of these differences.

There appears to be a slight difference between the heat activated and non-activated cell viabilities. In the cases of the Gem-Mal and the HNP only studies, there is no statistical difference between the two variables meaning that the slight differences are due to experimental errors ($P < 0.05$).
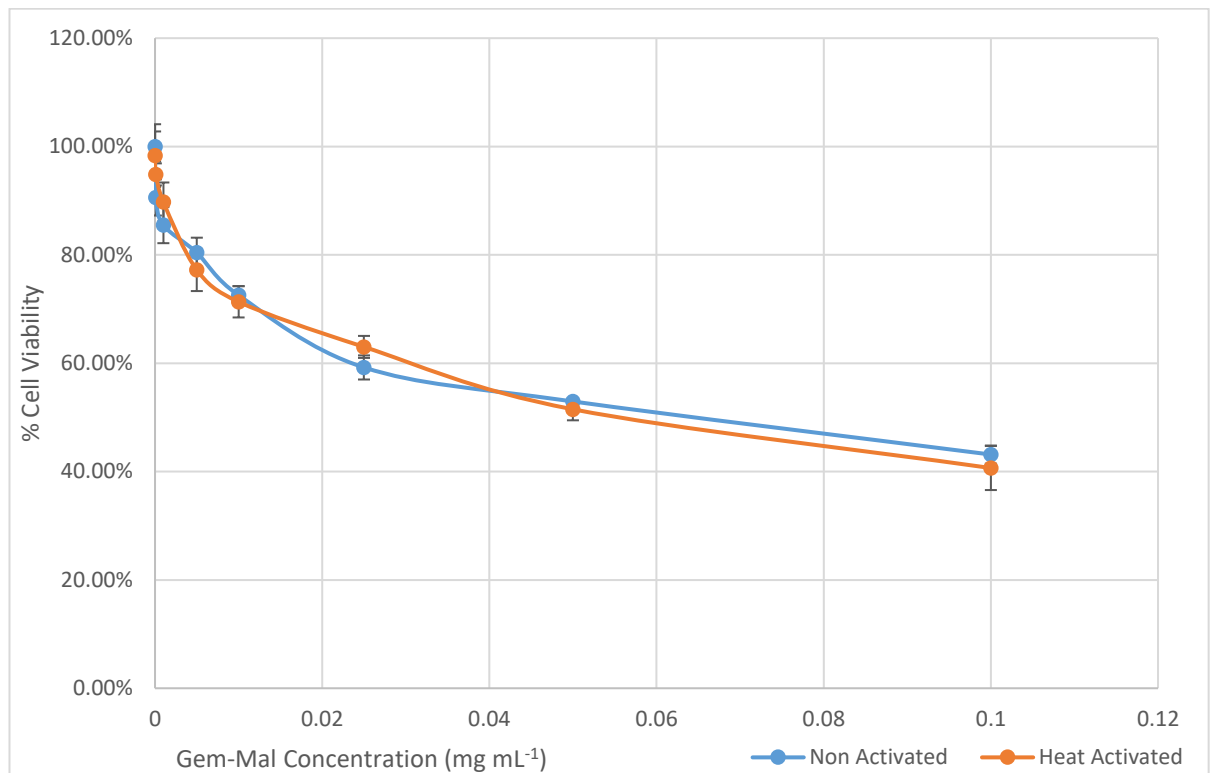
Figure 179: Graph of the change in percentage cell viability of Gem-Mal dosed BxPC-3 cells with and without a 0.5 h incubation at 44 °C (n=3) (± 3.6 %). No statistical difference observed ($P < 0.05$).
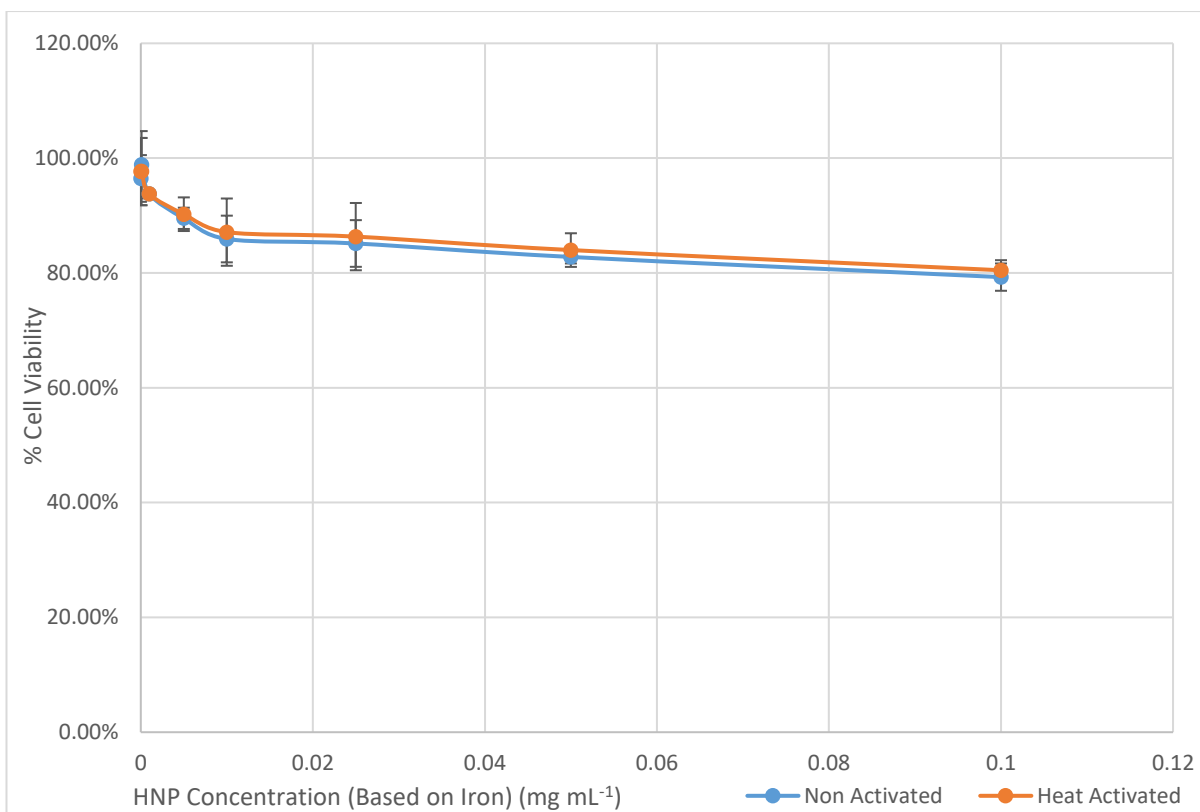
Figure 180: Graph of the change in percentage cell viability of HNP dosed BxPC-3 cells with and without a 0.5 h incubation at 44 °C (n=3) (± 5.9 %). No statistical difference observed ($P < 0.05$).

The only situation where there is a real difference between the heat activated and non-activated were the cells incubated is with the TTLD+HNP formulation shown in Figure 181. This was expected as the rate of retro Diels Alder was shown to increase at increased temperatures. The difference in cell viability between the heat activated and non-activated variables increases as the TTLD+HNP concentration increases.
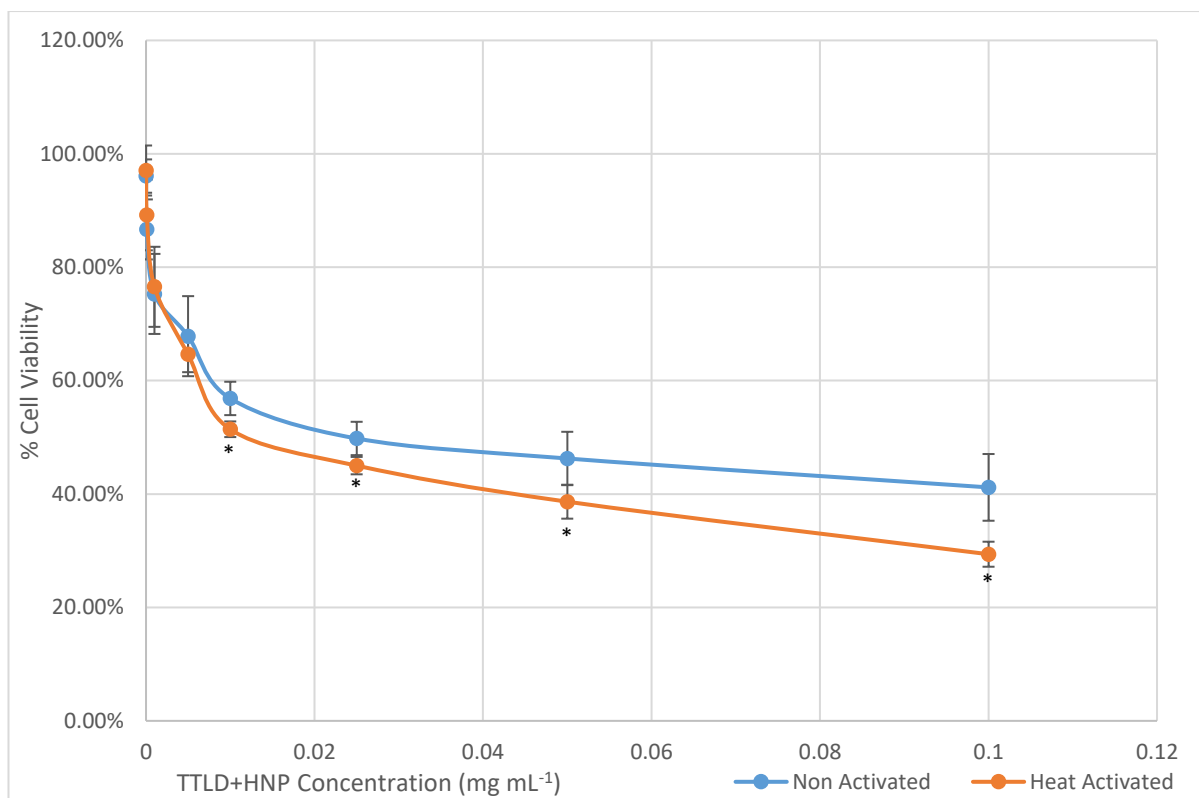
Figure 181: Graph of the change in percentage cell viability of TTLD+HNP dosed BxPC-3 cells with and without a 0.5 h incubation at 44 °C (n=3) (± 5.4 %). Data points labelled with * show statistically significant effects on % cell viability after heat activation compared to non-activated samples (P < 0.05).

The heat activated samples display a 2.4 fold decrease in cell viability compared to the non-activated samples based on their IC_{50} values of 0.0105 mg mL^{-1} and 0.025 mg mL^{-1} respectively. This indicates that an increase in temperature improves the activity of TTLD+HNP which is due to the intracellular release of Gem-Mal via the thermally triggered retro Diels Alder reaction.

4.4. Discussion

The IC_{50} of gemcitabine, Gem-Mal and the TTLD+HNP formulation differ in the trypan blue exclusion assay results when compared to the MTT assay results. Overall the IC_{50} values are lower when calculated via the MTT assay compared to the trypan blue exclusion assay. The main reason for this is that the MTT assay merely estimates the number of living cells based on their ability to metabolise MTT into formazan crystals and compares this activity to controls. The trypan blue exclusion assay provides the specific number of living cells in a sample allowing us to compare the population of living cells detected with controls. The MTT assay could indicate that gemcitabine, Gem-Mal and TTLD+HNP reduce percentage cell viability more than actual amounts, if those cells are in a state of reduced metabolism. These cells may still be alive but performing in suboptimal metabolism conditions due to the exposure of the introduced cytotoxic agents. The trypan blue exclusion assay will display a positive result for living cells, even if their metabolic processes have been reduced. Because of the advantage the trypan blue exclusion assay has over the MTT assay, the trypan blue exclusion assay derived IC_{50} results will be considered the true IC_{50} results for the rest of this study.

Overall the *in vitro* evaluation of Gem-Mal and the TTLD+HNP formulation has shown that Gem-Mal has a cytotoxic effect on BxPC-3 cells and that modification of the gemcitabine molecule to include the linker has not had a significant impact on its overall toxicity. The IC_{50} of Gem-Mal after 48 h is 0.07 mg mL^{-1} which 4.6 fold higher than gemcitabines IC_{50} of 0.0175 mg mL^{-1}. Due to Gem-Mals lower cytotoxicity, its potential to cause unwanted side effects is also lower as well until heat activation of the HNPs causes a significant release of the drug. It has already been shown in section 3.3.3.2 of this study that the TTLD+HNP formulation will release a much smaller portion of its Gem-Mal at 37 °C than at 44 °C. Because the uptake of the TTLD+HNP formulation is not instantaneous, part of this release at 37 °C will occur extracellularly. However due to the 11 fold uptake rate of the TTLD+HNP formulation, the majority of the formulation will be inside the cells releasing their drug cargo intracellularly. It is therefore advantageous that Gem-Mal (released from the TTLD+HNP formulation) has a lower cytotoxicity than gemcitabine until heat activation. This allows the TTLD+HNP formulation to function as a theranostic agent which are substances that are both diagnostic and therapeutic. The iron oxide cores provide visibility

of the TTLD+HNP formulation because they are excellent MRI contrast agents (Wang 2011). The HNPs themselves provide a therapeutic effect due to their ability to facilitate the release of their thermally labile attached drugs via the gold coatings surface plasmon resonance properties. The graph in Figure 182 displays the relationship of concentration of gemcitabine, Gem-Mal and the TTLD+HNP formulations in non-activated experimental conditions.
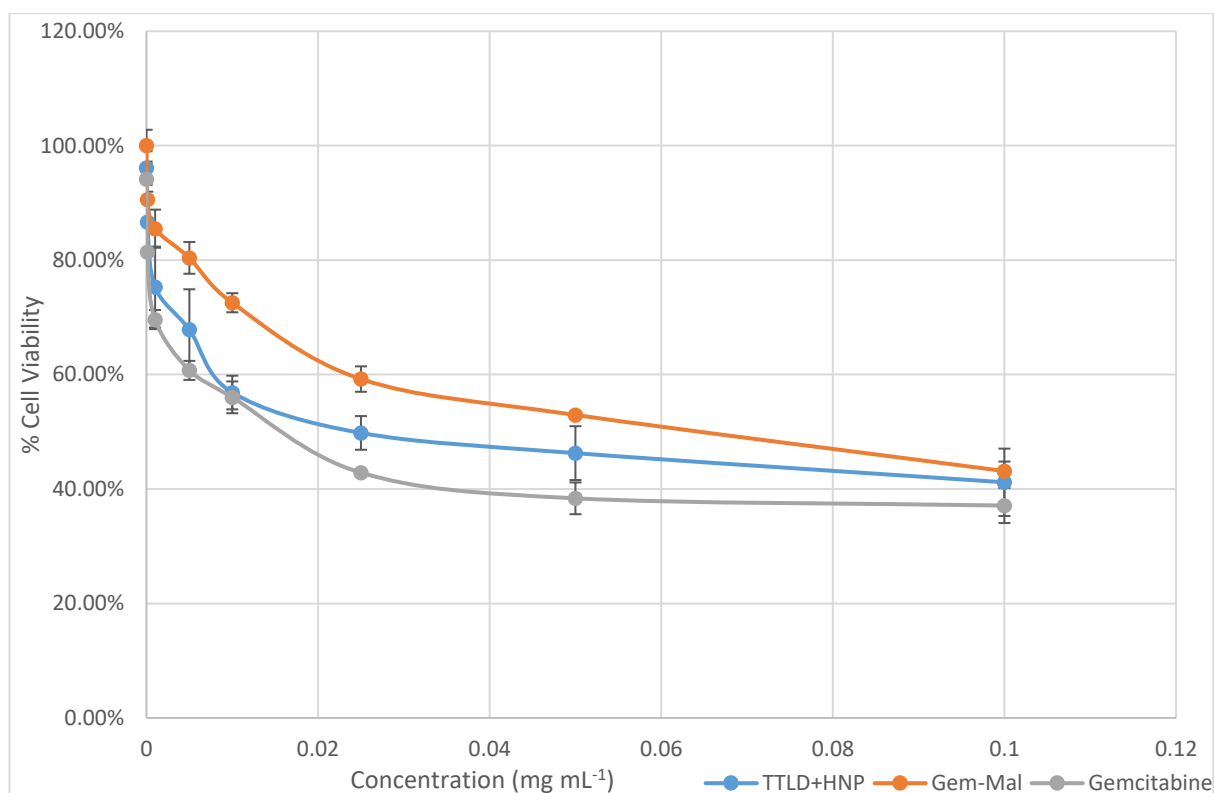
Figure 182: Comparative graph of the effect of gemcitabine, Gem-Mal and the TTLD+HNP formulation on percentage cell viability in non-activated experimental conditions (n=3, ±3.7 %, 3.6 % and 5.4 % respectively).

The graph above in Figure 182 is a graph of gemcitabine, Gem-Mal and the TTLD+HNP formulation effect on the 48 h cell viability with the non-activated conditions, in which their IC$_{50}$ values are 0.015 mg mL^{-1}, 0.07 mg mL^{-1} and 0.025 mg mL^{-1} respectively. Here we see that gemcitabines cytotoxicity is 1.6 fold higher than the TTLD+HNP formulation and 4.6 fold higher than Gem-Mal. At all concentrations gemcitabine exposure has the highest detrimental effect on percentage cell viability of BxPC-3 cells followed by the TTLD+HNP formulation and lastly the unbound Gem-Mal. The graph in Figure 183 below displays the effect of gemcitabine, Gem-Mal and the TTLD+HNP formulation on the 48 h cell viability after heat activation.
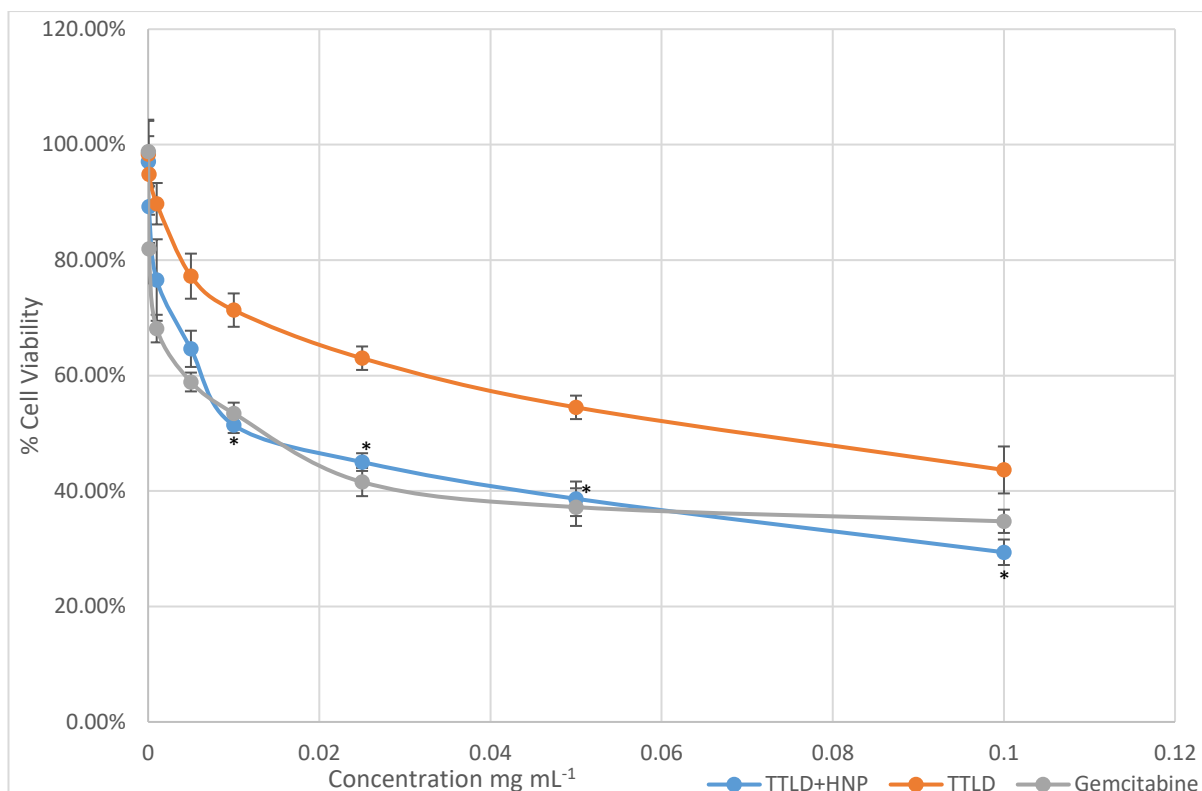
Figure 183: Comparative graph of the effect of gemcitabine, Gem-Mal and the TTLD+HNP formulation on percentage cell viability in heat activated experimental conditions (n=3, ±3.7 %, 3.6 % and 5.4 % respectively). Data points labelled with * show statistically significant effects on % cell viability after heat activation of TTLD+HNP compared to non-activated samples (P < 0.05).

The IC_{50} of gemcitabine has remained the same at 0.015 mg mL^{-1} after heat activation indicating that the 0.5 h, 7 °C temperature increase does not affect the cytotoxicity of gemcitabine. The TTLD+HNP formulation on the other hand has displayed a 56 % increase in cytotoxicity with its IC_{50} decreasing from 0.025 mg mL^{-1} in the non-activated experiment to 0.011 mg mL^{-1}, a 2.3 fold improvement. These results show us that the TTLD+HNP formulation after heat activation is 26 % more cytotoxic than gemcitabine alone, a 1.36 fold improvement in cytotoxicity. The IC_{50} of Gem-Mal has also decreased from 0.07 mg mL^{-1} in the non-activated experiments to 0.068 mg mL^{-1}. This is likely due to experimental errors causing such a small decrease. Regardless Gem-Mal remains significantly less cytotoxic than gemcitabine and TTLD+HNP with and without heat activation (P < 0.05). Table 12 provides a clearer comparison of each substances IC_{50} with and without heat activation.

Table 12: IC$_{50}$ values of Gemcitabine, Gem-Mal and the TTLD+HNP formulation with and without heat activation

	Gemcitabine	TTLD+HNP	Gem-Mal
Non Activated IC$_{50}$ (mg mL^{-1})	0.015	0.025	0.07
Heat Activated IC$_{50}$ (mg mL^{-1})	0.015	0.011	0.068
Activation Effect on cytotoxicity	Nil	+ 56 %	- 3 %

All of these profound revelations greatly enhances the TTLD+HNP formulation as a potential first line replacement of gemcitabine for the treatment of pancreatic cancer. Current use of gemcitabine for the treatment of pancreatic cancer poses many problems. Gemcitabine has a short half-life of 8-17 min after intravenous administration where the majority of the dose does not penetrate the intended pancreatic cancer cell target due to its hydrophilic nature (Griffith & Jarvis 1996; Immordino et al. 2004). This leads to a high dose requirement in order to achieve a therapeutic effect.

One of the main reasons why gemcitabine has the reported effectiveness of 23.8 % is due to the side effect caused by the nonspecific uptake of gemcitabine into healthy tissues. The majority of pancreatic cancer sufferers are elderly who cannot tolerate the side effects associated with gemcitabine use (Takeuchi *et al*. 2004). These side effects can include renal toxicity and hepatoxicity. The high dose requirement of gemcitabine prevents many sufferers of pancreatic cancer from receiving it as part of a life extension treatment or as a neoadjuvant chemotherapeutic treatment prior to the potentially lifesaving surgery to remove the rest of the tumours.

One thing to note, is that prior to the use of gemcitabine the first line drug for treating pancreatic cancer was 5-fluorouracil (5-Fu). Gemcitabine replaced 5-Fu because it displayed fewer and less serious side effects as well as a greater therapeutic effect (Burris *et al*. 1997). Based on the rapid uptake and lower cytotoxicity of the TTLD+HNP

formulation, its side effects should be reduced in *vivo*. Its improved in *vitro* cytotoxicity after heat activation surpasses that of gemcitabine. Together, these results demonstrate the potential of the TTLD+HNP formulation as a worthy replacement to gemcitabine as a first line treatment of pancreatic cancer.

The TTLD+HNP formulation has displayed a superior cytotoxicity to the currently used gemcitabine and a faster uptake which should prevent the systemic side effects present with gemcitabine. This would reduce the dose needed to achieve the same effectiveness as gemcitabine, thereby allowing more pancreatic cancer sufferers the opportunity to receive treatment improving the overall survival rates and reducing patient discomfort. Gem-Mal, the compound that is released from the TTLD+HNP formulation 4.6 times less cytotoxic that gemcitabine. This means that any release that might occur before its rapid cellular uptake will have a greatly reduced effect on the patients wellbeing. The TTLD+HNPs prior to activation are 1.6 times less cytotoxic than gemcitabine. This allows for higher doses of TTLD+HNP to be administered before a maximum therapeutic dose is reached, which further improves the cytotoxicity of the activated TTLD+HNP formulation at the tumour site.

The next logical step in the continuation of this research study would be to acquire microscopic images of the cells that have been exposed to and incubated with gemcitabine, Gem-Mal, TTLD+HNP and the HNPs alone and compare the cell morphology with those that have been heat activated at 44 °C. One method of carrying this out would be with the use of atomic force microscopy (AFM). This technique works on the basis that the AFM has a cantilever which has a probe in the form of a sharp tip. This tip scans the sample surface by being dragged which causes the cantilever to raise and dip depending on the topography of the surface. This would provide a 3D rendering of the cell shape indicating whether the cells are healthy, preparing for cellular apoptosis or are already dead (Pishkenari & Meghdari 2011). The drug uptake results have already concluded that the HNPs are taken up. This is evident with the 11 fold uptake rate of TTLD+HNP compared to gemcitabine alone. TEM imaging would further enhance this knowledge by providing images of nanoparticles in an intracellular environment. Lastly, fluorescence microscopy could also be employed on cells stained with a dye in order to observe the physical effects caused by exposure to gemcitabine, Gem-Mal, TTLD+HNP and the HNPs

alone with and without heat activation. A fluorescent molecule could also be attached to the HNP surface that would further confirm the uptake of the TTLD+HNP formulation as well.

4.5. Conclusion

The *in vitro* effects of Gem-Mal and the TTLD+HNP formulation has been evaluated successfully. The 11-fold increase in the uptake of Gem-Mal when attached to the HNPs surface is a very favourable discovery that further highlights the significant clinical potential this thermally sensitive formulation has for treating pancreatic cancer. The next steps should include the in *vivo* testing of the TTLD+HNP formulation in order to understand the clinical relevance of this novel treatment in whole living organisms especially with the possibility of reduced side effects with same dose regimens compared to gemcitabine. While the 4 week assessment of the TTLD+HNP displays medium term stability, the long stability of the TTLD+HNP formulation in various storage conditions also needs to be determined. If these experiments show promise then further successful testing with human trials could lead to this formulation replacing gemcitabine as the first line treatment for pancreatic cancer.

CHAPTER 5: GENERAL DISCUSSION

5.0. General Discussion

The objectives of this study included the successful synthesis of a thermally triggered drug delivery system via the use of a thiolated thermally labile linker. Another objective was that this novel formulation would display a significant and rapid release of its drug cargo at elevated temperatures. The data obtained from this study indicate that these characteristics are present in the thiolated thermally labile drug (TTLD) attached via a dative covalent bond to hybrid nanoparticles comprised of an iron oxide core and gold coat (HNPs) forming the new formulation abbreviated TTLD+HNP. This TTLD+HNP formulation would release a maleimide containing gemcitabine analogue called Gem-Mal. The synthesis of a thermally triggered drug formulation comprised of, a thermally labile linker functionalised with gemcitabine covalently attached to the gold surface of HNPs, has been successful. The linker and drug component dubbed TTLD displayed water solubility and the ability to break apart under elevated temperatures while retaining its stability at typical storage conditions. Within a closed system inside a round bottom flask, TTLD has a percentage release of 1 % when heated to 37 °C after 5 min. Within this environment, the opportunity for the released Gem-Mal to reattach back onto the HNP via the Diels Alder reaction was higher which slowed the net % release over time. Under *sink* conditions the % release of Gem-Mal across a dialysis membrane increased to 14 % after 5 min. This means that *sink* conditions improve the % release of Gem-Mal by 14-fold because the Diels Alder coupling reaction does not occur in any meaningful amount. This lack of the Diels Alder reaction in *sink* conditions leads to a higher net breakdown of the linker over time.

TTLD compounds were loaded onto HNPs at a concentration of 5 mg of TTLD per 1 mg HNP (based on iron mass) to form the formulation known as TTLD+HNP. Under aqueous *sink* conditions at pH 7 this TTLD+HNP formulation performed rapid and total drug release of Gem-Mal via the retro Diels Alder when exposed to a temperature of 44 °C within 1 h where 80 % was released within 1 min. This release also occurs at 37 °C to a much lower and overall incomplete manner where only 23 % was released after 1 h (13 % after 1 min). This is due to the reversible Diels Alder reaction establishing a temperature dependant equilibrium. This experiment was repeated at a pH of 7.4 and pH 5.6 within cell media producing very similar results to the experimental condition at pH 7 in water. This suggests that temperature serves as the majority, if not the sole trigger for drug release. No

detectable release occurred at 20 °C and 5 °C over 4 weeks, displaying the TTLD+HNP formulations medium term stability.

During the *in vitro* experiments, the attachment of TTLD to the HNPs improved the cytotoxicity of the formulation. Four substances (gemcitabine, Gem-Mal, TTLD+HNP and the HNPs alone) all displayed increasing cytotoxicity as the concentration rose. Out of the four investigated substances, only the HNPs alone lacked an IC_{50} after 24 h, 48 h and 72 h where the cell viability fell to just 90 %, 80 % and 77 % respectively at the highest experimental concentration of 0.1 mg mL^{-1}. This indicates that the Bx-PC3 cells tolerated the HNP presence well with little adverse effect. After 24 h the cell viability of Bx-PC3 cells exposed to 0.1 mg mL^{-1} of Gem-Mal and the TTLD+HNP formulation is 80 % and 70 % respectively.

The therapeutic activity of the heat activated TTLD+HNP formulation has already been observed and deemed advantageous over gemcitabine in terms of its lower IC_{50}, faster cellular uptake rate and controllable release. This is due to a combination of a faster cellular uptake of TTLD via attachment to HNPs and the large burst of released Gem-Mal that occurred during heating. As the uptake is time dependant, it's very likely that the concentration of the TTLD+HNP formulation required to illicit the same cytotoxic effect as gemcitabine would be lower at the 72 h mark. The IC_{50} of the TTLD+HNP formulation decreased by 56 % when activated, compared to the non-activated formulation improving its cytotoxicity to a level 36 % higher than gemcitabine. This is evident from the lower cell viability of 48 h 0.1 mg mL^{-1} TTLD+HNP dosed Bx-PC3 cells exposed to a temperature of 44 °C for 30 min compared with gemcitabine. Add to this the fact that the TTLD+HNP formulation has an 11-fold higher uptake and accumulation rate intracellularly compared to gemcitabine alone and it becomes clear. The TTLD+HNP formulation shows immense potential as the future first line treatment of pancreatic cancer and a worthy successor to gemcitabine.

The attachment of gemcitabine to the Diels Alder linker was achieved via an amide bond. It has been reported that the amide group attached to gemcitabine is enzymatically removed with hydrolysis by proteases and peptidases (Wickremsinhe *et al*. 2013). Therefore the cytotoxic activity of Gem-Mal may only occur after the maleimide linker component is enzymatically cleaved. Gemcitabine itself is a prodrug but Gem-Mal may be

functioning as a secondary prodrug after its initial release from the TTLD+HNP formulation. If Gem-Mal needs to be converted to gemcitabine first this might explain why the difference in cell viability from the 24 h to 48 h time point is greater for Gem-Mal than with gemcitabine but narrows over time. For example, the percentage cell viability at 24 h is 60 % for gemcitabine and 80 % for Gem-Mal, a difference of 20 %. At the 48 h mark the percentage cell viability is 37 % and 43 % for gemcitabine and Gem-Mal respectively which is a difference of 6 %. Gemcitabine and Gem-Mal have similar uptake times which means their intracellular concentration is nearly equal. This suggests that Gem-Mals activity is somehow gated by a time dependant process such as amide cleavage that doesn't apply to gemcitabine and/or Gem-Mal is simply less cytotoxic due to the presence of the amide coupled maleimide.

This study has progressed as far as the *in vitro* experiments detailed in Chapter 4. The next stages of this study will include *in vivo* testing of the novel TTLD+HNP in order to assess its clinical potential. *In vitro* assays give a good indication of the likely outcome *in vivo* however, they are not truly representative and therefore it is very important to carry out *in vivo* xenograft studies in order to obtain their ability in more realistic conditions. It is possible that the TTLD+HNP formulation has a longer half-life within the body leading to a higher rate of cellular uptake and subsequent cytotoxicity than observed in the *in vitro* experiments. The diagnostic properties of this formulation also needs to be evaluated, where the iron oxide cores of the HNPs are imaged with MRI to map their *in vivo* movement. This is important not just because of the diagnostic imaging opportunities, but also to map the extent that the Gem-Mal might be released systemically. Gem-Mal is released at 37 °C so side effects may occur if the TTLD+HNP formulation migrates as easily as gemcitabine does. Therefore the Gem-Mal released could cause side effects. Within a closed system this release is 6.7 % in 1 h and 17 % *in vitro* (based on *sink* conditions).

In vivo the formulation is not likely to be laser irradiated for 1 h. Therefore, further investigation taking into account drug release, efficacy and maximum tolerated dose needs to be carried out. It is possible that the slow release at 37 °C may allow for a higher dose of Gem-Mal compared to gemcitabine. The TTLD+HNP formulation would be administered intratumourally which would ultimately improve its half-life over gemcitabine which is administered intravenously. This is because the TTLD+HNP formulation would avoid the

rapid renal excretion after enzymatic conversion of its gemcitabine component (Eda *et al*. 1998). Therefore it may be possible to load a greater dose of Gem-Mal onto HNPs beyond the maximum tolerated dose of gemcitabine. This would lead to a higher concentration of the TTLD+HNP formulation which leads to a faster accumulation of this formulation within the tumour tissue. The possibility of whether a significant increase in the dose of TTLD+HNP would not cause severe side effects, can only be determined with in *vivo* experiments which further highlights their importance in future work (Pathania *et al*. 2014; Megha *et al*. 2015).

The excellent stability of the HNPs over a period of 6 months has been reported (C. M. Barnett et al. 2013). The TTLD+HNPs primary function is to act as a thermally triggered drug delivery system. Therefore this formulations goal is to facilitate drug release at elevated temperatures. The thermal stability of the TTLD+HNPs formulation over a 4-week period has shown us that no drug release occurs over time at 5 °C and 20 °C. Some drug formulations are freeze dried which is a process where the material is frozen and then the surrounding air pressure is reduce to allow the frozen water to evaporate via sublimation (Patel *et al*. 2014). The effects of freeze drying on the integrity of the TTLD+HNP formulation has not been determined. Conversely, drug formulations have shelf lives that range from several months to years. A 4-week stability study provides some estimation of the shelf life, but in order to fully determine the long term stability of the TTLD+HNP formulation, an extended shelf life experiment is required. The effects of storage at 5 °C and 20 °C as well as the long term freeze drying of the TTLD+HNP formulation needs to be determined in future work.

The TTLD+HNP drug delivery system could revolutionise the future of drug delivery far more than just improving the effectiveness of pancreatic cancer treatment. Other forms of cancers may garner advancements in survival and remission rates with the use of this formulation as well. The attached gemcitabine compound may be replaced with other drug substances tailored to treat other forms of cancer. Chemotherapy medicines are often given in combination as they sometimes prove more effective than standalone drug formulations. Gem-Mal does not play a part in its release from the TTLD+HNP formulation. That is solely dependent on the onset of the retro Diels Alder reaction. Therefore different thiolated thermally labile drug linkers could be synthesised and attached simultaneously to the HNP surface. The relevant concentrations of the attached drugs could be tuned

depending on the concentration of each linker with attached drug. This could lead to a form of "click chemistry" where perhaps hundreds of forms of the TTLD+HNP formulation arises from different compositions of attached drug linkers, tailored to the patients clinical needs and every attached drug linker would be released at the same rate intracellularly upon heat activation. Most drug candidates do not reach clinical use from the drug discovery and development stages due to various factors such as, poor bioavailability and reduced cell permeation. Previously benched drug candidates which showed great promise despite their setbacks, may see potential use again in a TTLD+HNP formulation, which could address the issues that prevented these drug candidates from being considered worthy of human trials and eventually clinical use. Overall it's not just that the TTLD+HNP formulation shows tremendous promise in improving pancreatic cancer treatment, but it's the capability of the TTLD+HNP formulation to change the very face of clinical pharmaceutics as a whole.

6.0. References

Affram, K. et al., 2015. In vitro and in vivo antitumor activity of gemcitabine loaded thermosensitive liposomal nanoparticles and mild hyperthermia in pancreatic cancer. *International journal of advanced research*, 3(10), pp.859–874.

Aird, K.M. & Zhang, R., 2015. Nucleotide metabolism, oncogene-induced senescence and cancer. *Cancer letters*, 356(2 Pt A), pp.204–10. 2016].

Alexander, C. et al., 2013. Enhanced uptake of nanoparticle drug carriers via a thermoresponsive shell enhances cytotoxicity in a cancer cell line. *Biomater. Sci*, 1.

Almoguera, C. et al., 1988. Most human carcinomas of the exocrine pancreas contain mutant c-K-ras genes. *Cell*, 53(4), pp.549–554.

Alsaab, H. et al., 2017. Folate Decorated Nanomicelles Loaded with a Potent Curcumin Analogue for Targeting Retinoblastoma. *Pharmaceutics*, 9(2), p.15.

Ameri, S.K., Singh, P.K. & Sonkusale, S.R., 2016. Three dimensional graphene transistor for ultra-sensitive pH sensing directly in biological media. *Analytica Chimica Acta*, 934, pp.212–217.

Anada, T. et al., 2009. Synthesis of calcium phosphate-binding liposome for drug delivery. *Bioorganic & Medicinal Chemistry Letters*, 19(15), pp.4148–4150.

Anand, P. et al., 2008. Cancer is a preventable disease that requires major lifestyle changes. *Pharmaceutical research*, 25(9), pp.2097–116.

Andersen, A.J. et al., 2016. Nanomechanical IR spectroscopy for fast analysis of liquid-dispersed engineered nanomaterials. *Sensors and Actuators B: Chemical*, 233, pp.667–673.

Ansari, P. & Häubl, G., 2016. Determination of cyclopiazonic acid in white mould cheese by liquid chromatography–tandem mass spectrometry (HPLC–MS/MS) using a novel internal standard. *Food Chemistry*, 211, pp.978–982.

Arora, V. et al., 2014. Synthesis and characterization of thiolated pectin stabilized gold coated magnetic nanoparticles. *Materials Chemistry and Physics*, 173, pp.161–167.

Atkins, P., 2006. *Inorganic Chemistry* 4th ed., Oxford University Press.

Ault, K.A., 2006. Clinical Study Epidemiology and Natural History of Human Papillomavirus Infections in the Female Genital Tract. *Infectious Diseases in Obstetrics and Gynecology*, 40470, pp.1–5.

Aulton, M., 2007. *The Design and Manufacture of Medicines* 3rd ed., Churchill Livingstone.

Bagherzade, G. & Etemad, O., 2016. Recto-sigmoid lipoma: a case report and review of the literature. *Journal of Coloproctology*, 37(1), pp.50–54.

Bandele, O.J. et al., 2012. In vitro toxicity screening of chemical mixtures using HepG2/C3A cells. *Food and Chemical Toxicology*, 50(5), pp.1653–1659.

Banerjee, J., Al-Wadei, H.A.N. & Schuller, H.M., 2013. Chronic nicotine inhibits the therapeutic effects of gemcitabine on pancreatic cancer in vitro and in mouse xenografts. *European Journal of Cancer*, 49(5), pp.1152–1158.

Baraniak, J. et al., 2014. N-Acyl-phosphoramidates as potential novel form of gemcitabine prodrugs. *Bioorganic & medicinal chemistry*, 22(7), pp.2133–40.

Barlow, S. & Schlatter, J., 2010. Risk assessment of carcinogens in food. *Toxicology and Applied Pharmacology*, 243(2), pp.180–190.

Barnett, C. et al., 2013. Poly(allylamine) Magnetomicelles for Image Guided Drug Delivery. *Pharmaceutical Nanotechnology*, 1(3), pp.224–238.

Barnett, C.M. et al., 2013. Physical stability, biocompatibility and potential use of hybrid iron oxide-gold nanoparticles as drug carriers. *Journal of Nanoparticle Research*, 15(6).

Batmani, Y. & Khaloozadeh, H., 2013. Optimal drug regimens in cancer chemotherapy: A multi-objective approach. *Computers in Biology and Medicine*, 43(12), pp.2089–2095.

Becker, S.M. et al., 2013. Chapter 10 – Targeted Drug Delivery: Multifunctional Nanoparticles and Direct Micro-Drug Delivery to Tumors. In *Transport in Biological Media*. pp. 391–416.

Bernas, T. & Dobrucki, J., 2002. Mitochondrial and nonmitochondrial reduction of MTT: interaction of MTT with TMRE, JC-1, and NAO mitochondrial fluorescent probes. *Cytometry*, 47(4), pp.236–42.

Bhattacharjee, S., 2016. DLS and zeta potential – What they are and what they are not? *Journal of Controlled Release*, 235, pp.337–351.

Bockhorn, M. et al., 2014. Borderline resectable pancreatic cancer: A consensus statement by the International Study Group of Pancreatic Surgery (ISGPS). *Surgery*, 155(6), pp.977–988.

Borgert, J. et al., 2012. Fundamentals and applications of magnetic particle imaging. *Journal of Cardiovascular Computed Tomography*, 6(3), pp.149–153.

Boutelle, R.C. & Northrop, B.H., 2011a. Substituent Effects on the Reversibility of Furan–Maleimide Cycloadditions. *The Journal of Organic Chemistry*, 76(19), pp.7994–8002.

Bouyssou, J.M.C. et al., 2014. Regulation of microRNAs in cancer metastasis. *Biochimica et Biophysica Acta (BBA) - Reviews on Cancer*, 1845(2), pp.255–265.

Brito, L.F.C. et al., 2016. Andrology laboratory review: Evaluation of sperm concentration. *Theriogenology*, 85(9), pp.1507–1527.

Brock, D. et al., 1993. Testicular cancer. *Seminars in Oncology Nursing*, 9(4), pp.224–236.

Brown, K. et al., 2014. The synthesis of gemcitabine. *Carbohydrate Research*, 387, pp.59–73.

Burris, H.A. et al., 1997. Improvements in survival and clinical benefit with gemcitabine as first-line therapy for patients with advanced pancreas cancer: a randomized trial. *Journal of clinical oncology : official journal of the American Society of Clinical Oncology*, 15(6), pp.2403–13.

Campos, P.M., Praça, F.S.G. & Bentley, M.V.L.B., 2016. Quantification of lipoic acid from skin samples by HPLC using ultraviolet, electrochemical and evaporative light scattering detectors. *Journal of Chromatography B*, 1019, pp.66–71.

Casadei, R. et al., 2015. Neoadjuvant Chemoradiotherapy and Surgery Versus Surgery Alone in Resectable Pancreatic Cancer: A Single-Center Prospective, Randomized, Controlled Trial Which Failed to Achieve Accrual Targets. *Journal of Gastrointestinal Surgery*, 19(10), pp.1802–1812.

Chakraborty, T., Chakraborty, I. & Ghosh, S., 2011. The methods of determination of critical micellar concentrations of the amphiphilic systems in aqueous medium. *Arabian Journal of Chemistry*, 4(3), pp.265–270.

Chambers, A.F., Groom, A.C. & MacDonald, I.C., 2002. Metastasis: Dissemination and growth of

cancer cells in metastatic sites. *Nature Reviews Cancer*, 2(8), pp.563–572.

Chen, E. et al., 2011. A novel shape-controlled synthesis of dispersed silver nanoparticles by combined bioaffinity adsorption and TiO2 photocatalysis. *Powder Technology*, 212(1), pp.166–172.

Chi, J. et al., 2017. Quantitation of levodopa and carbidopa in rat plasma by LC–MS/MS: The key role of ion-pairing reversed-phase chromatography. *Journal of Chromatography B*, 1054, pp.1–9.

Corocleanu, M., 2008. A possible "universal" cancer vaccine that might cause an immune response against emerging cancer cells that originate from any tissue. *Medical Hypotheses*, 70(2), pp.381–383.

Curtis, A. et al., 2015. Heat Dissipation of Hybrid Iron Oxide-Gold Nanoparticles in an Agar Phantom. *Journal of Nanomedicine & Nanotechnology*, 6(6).

Das, K. et al., 2014. Hyper-Rayleigh scattering from gold nanoparticles: Effect of size and shape. *Spectrochimica Acta Part A: Molecular and Biomolecular Spectroscopy*, 128, pp.398–402.

Dasari, S. & Bernard Tchounwou, P., 2014. Cisplatin in cancer therapy: Molecular mechanisms of action. *European Journal of Pharmacology*, 740, pp.364–378.

Dean, J.R. et al., 2002. *Practical Skills in Chemistry*, Pearson Education.

Diels, O. & Alder, K., 1929. Synthesen in der hydro-aromatischen Reihe, II. Mitteilung: Über Cantharidin. *Berichte der deutschen chemischen Gesellschaft (A and B Series)*, 62(3), pp.554–562.

Dong, J. et al., 2011. *Shape dependence of nonlinear optical behaviors of gold nanoparticles*,

Doshi, R.H. et al., 2015. The effect of immunization on measles incidence in the Democratic Republic of Congo: Results from a model of surveillance data. *Vaccine*, 33(48), pp.6786–6792.

Dost, K. & İdeli, C., 2012. Determination of polycyclic aromatic hydrocarbons in edible oils and barbecued food by HPLC/UV–Vis detection. *Food Chemistry*, 133(1), pp.193–199.

Eda, H. et al., 1998. The antiproliferative activity of DMDC is modulated by inhibition of cytidine deaminase. *Cancer research*, 58(6), pp.1165–9.

Eguchi, H. et al., 2015. A magnetic anti-cancer compound for magnet-guided delivery and magnetic resonance imaging. *Scientific Reports*, 5(1), p.9194.

Eldar-Boock, A. et al., 2013. Nano-sized polymers and liposomes designed to deliver combination therapy for cancer. *Current Opinion in Biotechnology*, 24(4), pp.682–689.

Engel, T. & Kickelbick, G., 2013. Thermoreversible Reactions on Inorganic Nanoparticle Surfaces: Diels–Alder Reactions on Sterically Crowded Surfaces. , 25(2), pp.149–157.

Eskandari, K. & Ghourchian, H., 2012. Structural changes of glucose oxidase upon interaction with gold-coated magnetic nano-particles. *International Journal of Biological Macromolecules*, 51(5), pp.998–1002.

Eyesan, S.U. et al., 2011. Surgical consideration for benign bone tumors. *Nigerian journal of clinical practice*, 14(2), pp.146–50.

Fang, Y. et al., 2015. Enhanced cellular uptake and intracellular drug controlled release of VESylated gemcitabine prodrug nanocapsules. *Colloids and Surfaces B: Biointerfaces*, 128,

pp.357–362.

Felt, S.A., Moerdyk-Schauwecker, M.J. & Grdzelishvili, V.Z., 2015. Induction of apoptosis in pancreatic cancer cells by vesicular stomatitis virus. *Virology*, 474, pp.163–173.

Ferreira, R. V et al., 2016. Thermosensitive gemcitabine-magnetoliposomes for combined hyperthermia and chemotherapy. *Nanotechnology*, 27(8), p.85105.

Fontein, D.B.Y. et al., 2013. Age and the effect of physical activity on breast cancer survival: A systematic review. *Cancer Treatment Reviews*, 39(8), pp.958–965.

Foster, S.O. et al., 2011. Smallpox eradication in Bangladesh, 1972–1976. *Vaccine*, 29, pp.D22–D29.

Fryer, R.A. et al., 2011. Mechanisms underlying gemcitabine resistance in pancreatic cancer and sensitisation by the iMiD^{TM} lenalidomide. *Anticancer research*, 31(11), pp.3747–56.

Galea, M., 2016. Benign breast disorders. *Surgery (Oxford)*, 34(1), pp.19–24.

Gandini, A., 2005. The application of the Diels-Alder reaction to polymer syntheses based on furan/maleimide reversible couplings. *Polímeros*, 15(2), pp.95–101.

Di Gangi, I.M. et al., 2014. Analytical metabolomics-based approaches to pancreatic cancer. *TrAC Trends in Analytical Chemistry*, 55, pp.94–116.

Gao, Q. et al., 2014. Comparison of several chemometric methods of libraries and classifiers for the analysis of expired drugs based on Raman spectra. *Journal of Pharmaceutical and Biomedical Analysis*, 94, pp.58–64.

Gao, Q. et al., 2014. Extensive intestinal first-pass metabolism of arctigenin: Evidenced by simultaneous monitoring of both parent drug and its major metabolites. *Journal of Pharmaceutical and Biomedical Analysis*, 91, pp.60–67.

Gao, Y. et al., 2014. Nanotechnology-based intelligent drug design for cancer metastasis treatment. *Biotechnology Advances*, 32(4), pp.761–777.

Garattini, S. & Grignaschi, G., 2016. Animal testing is still the best way to find new treatments for patients. *European Journal of Internal Medicine*, 39(1), pp.32–35.

Gasparotto, L.H.S. et al., 2012. Electrocatalytic performance of environmentally friendly synthesized gold nanoparticles towards the borohydride electro-oxidation reaction. *Journal of Power Sources*, 218, pp.73–78.

Gaudin, A. et al., 2016. PEGylated squalenoyl-gemcitabine nanoparticles for the treatment of glioblastoma. *Biomaterials*, 105, pp.136–144.

Gobbo, P. & Workentin, M.S., 2012. Improved Methodology for the Preparation of Water-Soluble Maleimide-Functionalized Small Gold Nanoparticles.

Goussé, C., Gandini, A. & Hodge, P., 1998. Application of the Diels–Alder Reaction to Polymers Bearing Furan Moieties. 2. Diels–Alder and Retro-Diels–Alder Reactions Involving Furan Rings in Some Styrene Copolymers. *Macromolecules*, 31(97), pp.314–321.

Gras, R., Luong, J. & Shellie, R.A., 2017. Gas chromatography with diode array detection in series with flame ionisation detection. *Journal of Chromatography A*, 1500, pp.153–159.

Griffith, D.A. & Jarvis, S.M., 1996. Nucleoside and nucleobase transport systems of mammalian cells. *Biochimica et Biophysica Acta*, 1286, pp.153–181.

Grishagin, I. V., 2015. Automatic cell counting with ImageJ. *Analytical Biochemistry*, 473, pp.63–65.

Guo, Y. et al., 2013. Photothermal ablation of pancreatic cancer cells with hybrid iron-oxide core gold-shell nanoparticles. *International Journal of Nanomedicine*, Volume 8(1), p.3437.

Guo, Z. & Gallo, J.M., 1999. Selective Protection of 2',2'-Difluorodeoxycytidine (Gemcitabine). *The Journal of Organic Chemistry*, 64(22), pp.8319–8322.

Gupta, S., Kesarla, R. & Omri, A., 2013. Formulation strategies to improve the bioavailability of poorly absorbed drugs with special emphasis on self-emulsifying systems. *ISRN pharmaceutics*, 2013, p.848043.

Gupta, V. et al., 2008. Delivery of molecules to cancer cells using liposomes from bacterial cultures. *Journal of nanoscience and nanotechnology*, 8(5), pp.2328–33.

Hagmann, W., Jesnowski, R. & Löhr, J.M., 2010. Interdependence of gemcitabine treatment, transporter expression, and resistance in human pancreatic carcinoma cells. *Neoplasia (New York, N.Y.)*, 12(9), pp.740–7.

Han, J. et al., 2013. Design, Synthesis, and Biological Activity of Novel Dicoumarol Glucagon-like Peptide 1 Conjugates. *Journal of Medicinal Chemistry*, 56(24), pp.9955–9968.

Han, J.W. et al., The application of support vector machine classification to detect cell nuclei for automated microscopy.

Hanahan, D. & Weinberg, R.A., 2011. Hallmarks of Cancer: The Next Generation. *Cell*, 144(5), pp.646–674.

Hanahan, D. & Weinberg, R.A., 2000. The Hallmarks of Cancer. *Cell*, 100(1), pp.57–70.

Hart, H., 2003. *Organic Chemistry - A Short Course* 11th ed., Houghton Mifflin (Academic).

Hayden, S.C. et al., 2013. Plasmonic enhancement of photodynamic cancer therapy. *Journal of Photochemistry and Photobiology A: Chemistry*, 269, pp.34–41.

Heinemann, V., 2001. Gemcitabine: progress in the treatment of pancreatic cancer. *Oncology*, 60(1), pp.8–18.

Hochster, H.S., 2003. Newer approaches to gemcitabine-based therapy of pancreatic cancer: Fixed-dose-rate infusion and novel agents. *International Journal of Radiation Oncology*Biology*Physics*, 56(4), pp.24–30.

Horibe, H., Kinoshita, Y. & Taniguchi, S., 2016. A case of pleomorphic adenoma in the sublingual gland. *Journal of Oral and Maxillofacial Surgery, Medicine, and Pathology*, 28(4), pp.315–318.

Hoskins, C., Min, Y., Gueorguieva, M., et al., 2012. Hybrid gold-iron oxide nanoparticles as a multifunctional platform for biomedical application. *Journal of Nanobiotechnology*, 10(1), p.27.

Hoskins, C., Min, Y., Gueorguieva, M., et al., 2012a. Hybrid gold-iron oxide nanoparticles as a multifunctional platform for biomedical application. *Journal of Nanobiotechnology*, 10(1), p.27.

Hoskins, C. et al., 2010. In Vitro and In Vivo Anticancer Activity of a Novel Nano-sized Formulation Based on Self-assembling Polymers Against Pancreatic Cancer. *Pharmaceutical Research*, 27(12), pp.2694–2703.

Hoskins, C., Lin, P.K.T., Tetley, L., et al., 2012b. The Use of Nano Polymeric Self-Assemblies Based on Novel Amphiphilic Polymers for Oral Hydrophobic Drug Delivery. *Pharmaceutical Research*, 29(3), pp.782–794.

Hoskins, C., Thoo-Lin, P.K. & Cheng, W.P., 2012a. A review on comb-shaped amphiphilic polymers for hydrophobic drug solubilization. *Therapeutic delivery*, 3(1), pp.59–79. Available at: http://www.ncbi.nlm.nih.gov/pubmed/23852673.

Hoskins, C., Thoo-Lin, P.K. & Cheng, W.P., 2012b. A review on comb-shaped amphiphilic polymers for hydrophobic drug solubilization. *Therapeutic delivery*, 3(1), pp.59–79.

Hruban, R.H. & Fukushima, N., 2008. Cystic lesions of the pancreas. *Diagnostic Histopathology*, 14(6), pp.260–265.

Huťan, M. et al., 2014. Superior mesenteric vein thrombosis – unusual management of unusual complication of Whipple procedure. *International Journal of Surgery Case Reports*, 5(10), pp.765–768.

Huyck, L., Ampe, C. & Van Troys, M., 2012. The XTT cell proliferation assay applied to cell layers embedded in three-dimensional matrix. *Assay and drug development technologies*, 10(4), pp.382–92.

Immordino, M.L. et al., 2004. Preparation, characterization, cytotoxicity and pharmacokinetics of liposomes containing lipophilic gemcitabine prodrugs. *Journal of Controlled Release*, 100(3), pp.331–346.

Islam, N. & Miyazaki, K., 2010. An empirical analysis of nanotechnology research domains. *Technovation*, 30(4), pp.229–237.

Jaidev, L.R., Krishnan, U.M. & Sethuraman, S., 2015. Gemcitabine loaded biodegradable PLGA nanospheres for in vitro pancreatic cancer therapy. *Materials Science and Engineering: C*, 47, pp.40–47.

Jayaram, R., Patel, D. & Santhanam, V., 2015. Benign pleomorphic adenoma of minor salivary gland showing perineural invasion: a rare entity. *British Journal of Oral and Maxillofacial Surgery*, 53(1), pp.81–82.

Jazayeri, M.H. et al., 2016. Various methods of gold nanoparticles (GNPs) conjugation to antibodies. *Sensing and Bio-Sensing Research*, 9, pp.17–22.

John, J. et al., 2015. Development and validation of a high-performance thin layer chromatography method for the determination of cholesterol concentration. *Journal of Food and Drug Analysis*, 23(2), pp.219–224.

Jones, C. & Mulloy, B., Introduction to Nuclear Magnetic Resonance. In *Spectroscopic Methods and Analyses*. New Jersey: Humana Press, pp. 1–14.

Jukes, A. et al., 2016. Growth hormone secreting pituitary adenoma with admixed gangliocytoma and ganglioglioma. *Journal of Clinical Neuroscience*, 31, pp.202–204.

Kagedan, D.J. et al., 2015. Enhanced recovery after pancreatic surgery: a systematic review of the evidence. *HPB*, 17(1), pp.11–16.

Kang, H. et al., 2015. Synergistic antiviral activity of gemcitabine and ribavirin against enteroviruses. *Antiviral Research*, 124, pp.1–10.

Kang, M.J., Jang, J.-Y. & Kim, S.-W., 2016. Surgical resection of pancreatic head cancer: What is the optimal extent of surgery? *Cancer Letters*, 382(2), pp.259–265.

Karim, H. et al., 2013. Differential role of thiopurine methyltransferase in the cytotoxic effects of 6-mercaptopurine and 6-thioguanine on human leukemia cells. *Biochemical and Biophysical Research Communications*, 437(2), pp.280–286.

Katarzyna, W. & Basiak, J., Recognition and repair of DNA-cisplatin adducts.

Kavitha, A.A. & Singha, N.K., " Click Chemistry " in Tailor-Made Polymethacrylates Bearing Reactive Furfuryl Functionality: A New Class of Self-Healing Polymeric Material.

Kesharwani, P. et al., 2015. Parenterally administrable nano-micelles of 3,4-difluorobenzylidene curcumin for treating pancreatic cancer. *Colloids and Surfaces B: Biointerfaces*, 132, pp.138–145.

Khandhar, A.P. et al., 2013. Monodisperse magnetite nanoparticle tracers for in vivo magnetic particle imaging. *Biomaterials*, 34(15), pp.3837–3845.

Khare, V. et al., 2016. Long-circulatory nanoparticles for gemcitabine delivery: Development and investigation of pharmacokinetics and in-vivo anticancer efficacy. *European Journal of Pharmaceutical Sciences*, 92, pp.183–193.

Kiew, L.-V. et al., 2010. Improved plasma stability and sustained release profile of gemcitabine via polypeptide conjugation. *International Journal of Pharmaceutics*, 391(1), pp.212–220.

Kim, M.P. & Gallick, G.E., 2008. Gemcitabine resistance in pancreatic cancer: picking the key players. *Clinical cancer research : an official journal of the American Association for Cancer Research*, 14(5), pp.1284–5.

Knall, A.-C., Hollauf, M. & Slugovc, C., 2014. Kinetic studies of inverse electron demand Diels–Alder reactions (iEDDA) of norbornenes and 3,6-dipyridin-2-yl-1,2,4,5-tetrazine. *Tetrahedron Letters*, 55(34), pp.4763–4766.

Kristensen, A. et al., 2016. Does chemotherapy improve health-related quality of life in advanced pancreatic cancer? A systematic review. *Critical Reviews in Oncology/Hematology*, 99, pp.286–298.

Kuramoto, N., Hayashi, K. & Nagai, K., 1994. Thermoreversible reaction of diels—alder polymer composed of difurufuryladipate with bismaleimidodiphenylmethane. *Journal of Polymer Science Part A: Polymer Chemistry*, 32(13), pp.2501–2504.

de la Escosura, A., Briones, C. & Ruiz-Mirazo, K., 2015. The systems perspective at the crossroads between chemistry and biology. *Journal of Theoretical Biology*, 381, pp.11–22.

Lachenal, G., 1995. Dispersive and Fourier transform near-infrared spectroscopy of polymeric materials. *Vibrational Spectroscopy*, 9(1), pp.93–100.

Laurent, S. et al., 2011. Magnetic fluid hyperthermia: Focus on superparamagnetic iron oxide nanoparticles. *Advances in Colloid and Interface Science*, 166(1), pp.8–23.

Lee, Y.-P. et al., 2013. Inhibition of human alcohol and aldehyde dehydrogenases by acetaminophen: Assessment of the effects on first-pass metabolism of ethanol. *Alcohol*, 47(7), pp.559–565.

Lee, Y.K. et al., 2003. On inductively coupled plasmas for next-generation processing. *Surface and Coatings Technology*, 169, pp.20–23.

Lemke, T., 2008. *Medicinal Chemistry* 6th ed.,

Lens, P.N.L. & Hemminga, M.A., 1998. Nuclear magnetic resonance in environmental engineering:

Principles and applications. *Biodegradation*, 9(6), pp.393–409.

Li, C., Huang, Z. & Wang, R.K., 2011. Elastic properties of soft tissue-mimicking phantoms assessed by combined use of laser ultrasonics and low coherence interferometry. *Optics express*, 19(11), pp.10153–63.

Li, Y. et al., 1998. Molecular analysis of the p53 gene in pancreatic adenocarcinoma. *Diagnostic molecular pathology : the American journal of surgical pathology, part B*, 7(1), pp.4–9.

Li, Y.-S., Church, J.S. & Woodhead, A.L., 2012. Infrared and Raman spectroscopic studies on iron oxide magnetic nano-particles and their surface modifications. *Journal of Magnetism and Magnetic Materials*, 324(8), pp.1543–1550.

Liang, A. et al., 2012. The surface-plasmon-resonance effect of nanogold/silver and its analytical applications. *TrAC Trends in Analytical Chemistry*, 37, pp.32–47.

Lima, K.M.G. et al., 2014. Environmentally compatible bioconjugated gold nanoparticles as efficient contrast agents for colorectal cancer cell imaging. *Sensors and Actuators B: Chemical*, 196, pp.306–313.

Ling, K.-S. et al., 2005. Mechanisms Involved in Chemoresistance in Ovarian Cancer. *Taiwanese Journal of Obstetrics and Gynecology*, 44(3), pp.209–217.

Ling, Q. et al., 2013. The diversity between pancreatic head and body/tail cancers: clinical parameters and in vitro models. *Hepatobiliary & Pancreatic Diseases International*, 12(5), pp.480–487.

Liu, Q.-H. et al., 2012a. Surviving cells after treatment with gemcitabine or 5-fluorouracil for the study of de novo resistance of pancreatic cancer. *Cancer Letters*, 314(1), pp.119–125.

Lü, L. et al., 2012. Exocytosis of MTT formazan could exacerbate cell injury. *Toxicology in Vitro*, 26(4), pp.636–644.

M. Barnett, C., 2013. Poly(allylamine) Magnetomicelles for Image Guided Drug Delivery. *Pharmaceutical Nanotechnology*, 1(3).

Ma'Radzi, A.H. et al., 2014. Synthesis of thermoresponsive block and graft copolymers via the combination of living cationic polymerization and RAFT polymerization using a vinyl ether-type RAFT agent. *Polymer*, 55(8), pp.1920–1930.

Mackie, R.M. et al., 1985. The number and distribution of benign pigmented moles (melanocytic naevi) in a healthy British population. *British Journal of Dermatology*, 113(2), pp.167–174.

Malvezzi, M. et al., 2013. European cancer mortality predictions for the year 2013. *Annals of oncology : official journal of the European Society for Medical Oncology / ESMO*, 24(3), pp.792–800.

Maraveyas, A. et al., 2012. Gemcitabine versus gemcitabine plus dalteparin thromboprophylaxis in pancreatic cancer. *European Journal of Cancer*, 48(9), pp.1283–1292.

Markman, J.L. et al., 2013. Nanomedicine therapeutic approaches to overcome cancer drug resistance. *Advanced Drug Delivery Reviews*, 65(13), pp.1866–1879.

Martin, N.K. et al., 2010. Leaky vessels as a potential source of stromal acidification in tumours. *Journal of Theoretical Biology*, 267(3), pp.454–460.

Matsuoka, F. et al., 2004. Hyperthermia using magnetite cationic liposomes for hamster osteosarcoma. *Biomagnetic research and technology*, 2(1), p.3.

May, J.P. et al., 2013. Thermosensitive Liposomes for the Delivery of Gemcitabine and Oxaliplatin to Tumors. *Molecular Pharmaceutics*, 10(12), pp.4499–4508.

Megha, K. et al., 2015. Low intensity microwave radiation induced oxidative stress, inflammatory response and DNA damage in rat brain. *NeuroToxicology*, 51, pp.158–165.

Meyer, J.N. et al., 2010. Intracellular uptake and associated toxicity of silver nanoparticles in Caenorhabditis elegans. *Aquatic Toxicology*, 100(2), pp.140–150.

Miao, X. et al., 2014. Highly sensitive carcinoembryonic antigen detection using Ag@Au core–shell nanoparticles and dynamic light scattering. *Sensors and Actuators B: Chemical*, 191, pp.396–400.

Mini, E. et al., 2006. Cellular pharmacology of gemcitabine. *Annals of Oncology*, 17(Supplement 5), pp.v7–v12.

Mohamed, E.T. & Safwat, G.M., 2016. Evaluation of cardioprotective activity of Lepidium sativum seed powder in albino rats treated with 5-fluorouracil. *Beni-Suef University Journal of Basic and Applied Sciences*, 5(2), pp.208–215.

Montes Ruiz-Cabello, F.J. et al., 2014. Electric double-layer potentials and surface regulation properties measured by colloidal-probe atomic force microscopy. *Physical Review E*, 90(1), p.12301.

de Montferrand, C. et al., 2013. Iron oxide nanoparticles with sizes, shapes and compositions resulting in different magnetization signatures as potential labels for multiparametric detection. *Acta Biomaterialia*, 9(4), pp.6150–6157.

Mukherjee, S.G. et al., 2012. Comparative in vitro cytotoxicity study of silver nanoparticle on two mammalian cell lines. *Toxicology in Vitro*, 26(2), pp.238–251.

Mwenge, W. et al., 2016. Polio Eradication Initiative: Contribution to improved communicable diseases surveillance in WHO African region. *Vaccine*, 34(43), pp.5170–5174.

N'Guyen, T.T.T. et al., 2013. Functional iron oxide magnetic nanoparticles with hyperthermia-induced drug release ability by using a combination of orthogonal click reactions. *Angewandte Chemie (International ed. in English)*, 52(52), pp.14152–6.

Nagy, J. et al., 2009. Why are tumour blood vessels abnormal and why is it important to know? *British Journal of Cancer*, 100, pp.865–869.

Nagy, R., Sweet, K. & Eng, C., 2004. Highly penetrant hereditary cancer syndromes. *Oncogene*, 23(38), pp.6445–70.

Namiki, Y. et al., 2016. Pancreatic lipoma with a solid nodule mimicking invasion from adjoining intraductal papillary mucinous neoplasm. *Radiology Case Reports*, 11(2), pp.50–53.

Nature, 2009. Beyond the diffraction limit. *Nature*, (3), p.361.

Nelson, K.M. et al., 2017. The Essential Medicinal Chemistry of Curcumin. *Journal of Medicinal Chemistry*, 60(5), pp.1620–1637.

Neue, U.D., 2007. Stationary phase characterization and method development. *Journal of Separation Science*, 30(11), pp.1611–1627.

Node, M. et al., 2001. Odorless substitutes for foul-smelling thiols: syntheses and applications. *Tetrahedron Letters*, 42(52), pp.9207–9210.

Okay, O., General Properties of Hydrogels. *Hydrogel Sensors and Actuators*, 6, pp.1-14.

Oluwasanmi, A. et al., 2016. Potential of hybrid iron oxide–gold nanoparticles as thermal triggers for pancreatic cancer therapy. *RSC Adv.*, 6(97), pp.95044–95054.

Onbulak, S. et al., 2012. Synthesis and Functionalization of Thiol-Reactive Biodegradable Polymers. *Macromolecules*, 45(3), pp.1715–1722.

Paiella, S. et al., 2016. The prognostic impact of para-aortic lymph node metastasis in pancreatic cancer: A systematic review and meta-analysis. *European Journal of Surgical Oncology (EJSO)*, 42(5), pp.616–624.

Parham, H., Pourreza, N. & Rahbar, N., 2009. Solid phase extraction of lead and cadmium using solid sulfur as a new metal extractor prior to determination by flame atomic absorption spectrometry. *Journal of hazardous materials*, 163(2–3), pp.588–92.

Parhi, P., Mohanty, C. & Sahoo, S.K., 2012. Nanotechnology-based combinational drug delivery: an emerging approach for cancer therapy. *Drug Discovery Today*, 17(17), pp.1044–1052.

Patel, M., Munjal, B. & Bansal, A.K., 2014. Differential effect of buffering agents on the crystallization of gemcitabine hydrochloride in frozen solutions. *International Journal of Pharmaceutics*, 471(1), pp.56–64.

Patel, N.R. et al., 2013. Nanopreparations to overcome multidrug resistance in cancer. *Advanced Drug Delivery Reviews*, 65(13), pp.1748–1762.

Patel, V.R. & Agrawal, Y.K., 2011. Nanosuspension: An approach to enhance solubility of drugs. *Journal of advanced pharmaceutical technology & research*, 2(2), pp.81–7.

Pathania, D. et al., 2014. Design and discovery of novel quinazolinedione-based redox modulators as therapies for pancreatic cancer. *Biochimica et Biophysica Acta (BBA) - General Subjects*, 1840(1), pp.332–343.

Peters, M.L.B., Tseng, J.F. & Miksad, R.A., 2016. Genetic Testing in Pancreatic Ductal Adenocarcinoma: Implications for Prevention and Treatment. *Clinical Therapeutics*, 38(7), pp.1622–1635.

Peterson, A.M., Jensen, R.E. & Palmese, G.R., 2011. Thermoreversible and remendable glassâ€"polymer interface for fiber-reinforced composites. *Composites Science and Technology*, 71, pp.586–592.

Pikul, P., Nowakowska, J. & Ciura, K., 2013. Chromatographic analysis of ivabradine on polar, nonpolar and chemically modified adsorbents by HPTLC. *Journal of Food and Drug Analysis*, 21(2), pp.165–168.

Pinho, A. V., Chantrill, L. & Rooman, I., 2014. Chronic pancreatitis: A path to pancreatic cancer. *Cancer Letters*, 345(2), pp.203–209.

Pishkenari, H.N. & Meghdari, A., 2011. Influence of the tip mass on the tip–sample interactions in TM-AFM. *Ultramicroscopy*, 111(8), pp.1423–1436.

Pliarchopoulou, K. & Pectasides, D., 2009. Pancreatic cancer: Current and future treatment strategies. *Cancer Treatment Reviews*, 35(5), pp.431–436.

Prasad, R. & Katiyar, S.K., 2013. Grape seed proanthocyanidins inhibit migration potential of pancreatic cancer cells by promoting mesenchymal-to-epithelial transition and targeting NF-κB. *Cancer Letters*, 334(1), pp.118–126.

Razzazan, A. et al., 2016. In vivo drug delivery of gemcitabine with PEGylated single-walled carbon nanotubes. *Materials Science and Engineering: C*, 62, pp.614–625.

Reckamp, K.L. et al., 2016. A Highly Sensitive and Quantitative Test Platform for Detection of NSCLC EGFR Mutations in Urine and Plasma. *Journal of Thoracic Oncology*, 11(10), pp.1690–1700.

Riss, T.L. et al., 2004. *Cell Viability Assays*, Eli Lilly & Company and the National Center for Advancing Translational Sciences.

Robinson, I. et al., 2010. Synthesis of core-shell gold coated magnetic nanoparticles and their interaction with thiolated DNA. *Nanoscale*, 2(12), pp.2624–2630.

Rosen, J.E. et al., 2012. Iron oxide nanoparticles for targeted cancer imaging and diagnostics. *Nanomedicine : nanotechnology, biology, and medicine*, 8(3), pp.275–90.

Rosenberg, B., It all started by accident over 40 years ago in the labora- tory of physicist-turned-biophysicist.

Roshani, R., McCarthy, F. & Hagemann, T., 2014. Inflammatory cytokines in human pancreatic cancer. *Cancer letters*, 345(2), pp.157–63.

Rudin, D. et al., 2011. Gemcitabine Cytotoxicity: Interaction of Efflux and Deamination. *Journal of drug metabolism & toxicology*, 2(107), pp.1–10.

Sa, B. et al., 2010. The role of surgery for pancreatic cancer: a 12-year review of patient outcome. *Ulster Med J*, 79(2), pp.70–75.

Sadava, D., 2008. *Life - The Science of Biology* 8th ed., Sinauer Publishing.

Sadjadi, S.-A. & Annamaraju, P., 2012. Gemcitabine induced hemolytic uremic syndrome. *The American journal of case reports*, 13, pp.89–91.

Sailor, M.J. et al., 2012. Hybrid Nanoparticles for Detection and Treatment of Cancer. *Advanced Materials*, 24(28), pp.3779–3802.

Salameh, S. et al., 2014. Contact behavior of size fractionated TiO2 nanoparticle agglomerates and aggregates. *Powder Technology*, 256, pp.345–351.

Salihov, S. V. et al., 2015. Recent advances in the synthesis of Fe3O4@AU core/shell nanoparticles. *Journal of Magnetism and Magnetic Materials*, 394, pp.173–178.

Santhosh, P.B. & Ulrih, N.P., 2013a. Multifunctional superparamagnetic iron oxide nanoparticles: Promising tools in cancer theranostics. *Cancer Letters*, 336(1), pp.8–17.

Saritas, E.U. et al., 2013. Magnetic Particle Imaging (MPI) for NMR and MRI researchers. *Journal of Magnetic Resonance*, 229, pp.116–126.

Sauer, J. & Sustmann, R., 1980. Mechanistic Aspects of Diels-Alder Reactions: A Critical Survey. *Angewandte Chemie International Edition in English*, 19(10), pp.779–807.

Savjani, K.T., Gajjar, A.K. & Savjani, J.K., 2012. Drug solubility: importance and enhancement techniques. *ISRN pharmaceutics*, 2012, p.195727.

Savka I. Stoeva et al., 2005. Three-Layer Composite Magnetic Nanoparticle Probes for DNA. *Journal of the American Chemical Society*, 127(44), pp.15362–15363.

Schanda, P. & Ernst, M., 2016. Studying dynamics by magic-angle spinning solid-state NMR spectroscopy: Principles and applications to biomolecules. *Progress in Nuclear Magnetic Resonance Spectroscopy*, 96, pp.1–46.

Scheltjens, G. et al., 2013. A self-healing polymer network based on reversible covalent bonding.

Reactive and Functional Polymers, 73(2), pp.413–420.

Schofield, J., 2009. Benign skin tumours. *Medicine*, 37(6), pp.309–311.

Shah, O.J. et al., 2013. Pancreaticoduodenectomy: a comparison of superior approach with classical Whipple's technique. *Hepatobiliary & Pancreatic Diseases International*, 12(2), pp.196–203.

Al Shemaili, J. et al., 2014. Frondoside A enhances the antiproliferative effects of gemcitabine in pancreatic cancer. *European Journal of Cancer*, 50(7), pp.1391–1398.

Shen, D.-W. et al., 2012. Cisplatin resistance: a cellular self-defense mechanism resulting from multiple epigenetic and genetic changes. *Pharmacological reviews*, 64(3), pp.706–21.

Shirley, L.A. et al., 2013. Therapeutic endoscopic ultrasonography: intratumoral injection for pancreatic adenocarcinoma. *Gastroenterology research and practice*, 2013, p.207129.

Shu, Y. et al., 2014. Stable RNA nanoparticles as potential new generation drugs for cancer therapy. *Advanced Drug Delivery Reviews*, 66, pp.74–89.

Sinha, A. et al., 2014. Nanoparticle targeting to diseased vasculature for imaging and therapy. *Nanomedicine: Nanotechnology, Biology and Medicine*, 10(5), pp.e1003–e1012.

Song, H. et al., 2014. A biodegradable polymer platform for co-delivery of clinically relevant oxaliplatin and gemcitabine. *Journal of Materials Chemistry B*, 2, pp.6560–6570.

Song, H.Y. et al., 2009a. Practical synthesis of maleimides and coumarin-linked probes for protein and antibody labelling via reduction of native disulfides. *Organic & Biomolecular Chemistry*, 7(17), p.3400.

Song, W. et al., 2014. Polypeptide-based combination of paclitaxel and cisplatin for enhanced chemotherapy efficacy and reduced side-effects. *Acta Biomaterialia*, 10(3), pp.1392–1402.

Song, Y., Baba, T. & Mukaida, N., 2016a. Gemcitabine induces cell senescence in human pancreatic cancer cell lines. *Biochemical and Biophysical Research Communications*, 477(3), pp.515–519.

Sonuç Karaboğa, M.N., Şimşek, Ç.S. & Sezgintürk, M.K., 2016. AuNPs modified, disposable, ITO based biosensor: Early diagnosis of heat shock protein 70. *Biosensors and Bioelectronics*, 84, pp.22–29.

Strober, W., 2001. Trypan Blue Exclusion Test of Cell Viability. In *Current Protocols in Immunology*. Hoboken, NJ, USA: John Wiley & Sons, Inc., p. Appendix 3B.

Su, Y. et al., 2014. Small molecule with big role: MicroRNAs in cancer metastatic microenvironments. *Cancer letters*, 344(2), pp.147–56.

Sugihara, S. et al., 2010. Synthesis of Thermoresponsive Shell Cross-Linked Micelles via Living Cationic Polymerization and UV Irradiation. *Polymer*, 55(8), pp.1920–1930.

Szalai, M.L. et al., 2007. Dendrimers Based on Thermally Reversible Furan - Maleimide Diels - Alder Adducts. *Macromolecules*, 40(1 mM), pp.818–823.

Takeuchi, N. et al., 2004. [Clinical problems in gemcitabine treatment for unresectable pancreatic cancer in the elderly--a multicentric retrospective study of 53 cases]. *Gan to kagaku ryoho. Cancer & chemotherapy*, 31(12), pp.1987–91.

Tarantola, D. & Foster, S.O., 2011. From smallpox eradication to contemporary global health initiatives: Enhancing human capacity towards a global public health goal. *Vaccine*, 29,

pp.D135–D140.

Teixeira, P.R. et al., 2016. Photochemically-assisted synthesis of non-toxic and biocompatible gold nanoparticles. *Colloids and Surfaces B: Biointerfaces*, 148, pp.317–323.

Temperini, A. et al., 2010. A simple acylation of thiols with anhydrides. *Tetrahedron Letters*, 51(41), pp.5368–5371.

Thakur, C. et al., 2014. Increased expression of mdig predicts poorer survival of the breast cancer patients. *Gene*, 535(2), pp.218–224.

Todolí, J.L. & Mermet, J.M., 2006. Sample introduction systems for the analysis of liquid microsamples by ICP-AES and ICP-MS. *Spectrochimica Acta Part B: Atomic Spectroscopy*, 61(3), pp.239–283.

Torres, A.M. & Price, W.S., 2016. Introduction to Nuclear Magnetic Resonance. *Analytical Biochemistry (Online)*, pp.1–6.

Tran, B. et al., 2013a. Association between ultraviolet radiation, skin sun sensitivity and risk of pancreatic cancer. *Cancer Epidemiology*, 37(6), pp.886–892.

Tran, B. et al., 2013b. Association between ultraviolet radiation, skin sun sensitivity and risk of pancreatic cancer. *Cancer Epidemiology*, 37(6), pp.886–892.

Tsume, Y. et al., 2014. The development of orally administrable gemcitabine prodrugs with d-enantiomer amino acids: Enhanced membrane permeability and enzymatic stability. *European Journal of Pharmaceutics and Biopharmaceutics*, 86(3), pp.514–523.

Turci, F. et al., 2016. Assessment of asbestos exposure during a simulated agricultural activity in the proximity of the former asbestos mine of Balangero, Italy. *Journal of Hazardous Materials*, 308, pp.321–327.

Tyson, M.D. & Castle, E.P., 2014. Racial Disparities in Survival for Patients With Clinically Localized Prostate Cancer Adjusted for Treatment Effects. *Mayo Clinic Proceedings*, 89(3), pp.300–307.

Uno, T. et al., 2012. NHC-catalyzed thioesterification of aldehydes by external redox activation. *Chemical Communications*, 48(13), p.1901.

Vandana, M. & Sahoo, S.K., 2010. Long circulation and cytotoxicity of PEGylated gemcitabine and its potential for the treatment of pancreatic cancer. *Biomaterials*, 31(35), pp.9340–9356.

Vashist, A. & Ahmad, H., 2013. Hydrogels: Smart materials for drug delivery. *Oriental Journal of Chemistry*, 29(3), pp.861–870.

Veeman, W.S., 1997. Nuclear magnetic resonance, a simple introduction to the principles and applications. *Geoderma*, 80(3–4), pp.225–242.

Verma, S. et al., 2012. Influence of process parameters on surface plasmon resonance characteristics of densely packed gold nanoparticle films grown by pulsed laser deposition. *Applied Surface Science*, 258(11), pp.4898–4905.

Vigderman, L. & Zubarev, E.R., 2013. Therapeutic platforms based on gold nanoparticles and their covalent conjugates with drug molecules. *Advanced Drug Delivery Reviews*, 65(5), pp.663–676.

Vinardell, M.P., 2015. The use of non-animal alternatives in the safety evaluations of cosmetics ingredients by the Scientific Committee on Consumer Safety (SCCS). *Regulatory Toxicology and Pharmacology*, 71(2), pp.198–204.

Vincent, A. et al., 2011. Pancreatic cancer. *The Lancet*, 378(9791), pp.607–620.

Vinken, M. & Blaauboer, B.J., 2016. In vitro testing of basal cytotoxicity: Establishment of an adverse outcome pathway from chemical insult to cell death. *Toxicology in vitro*, 39, pp.104–110.

Vukovic, I., Brinke, G. ten & Loos, K., 2013. Block copolymer template-directed synthesis of well-ordered metallic nanostructures. *Polymer*, 54(11), pp.2591–2605.

Wagstaff, A.J. et al., 2012. Cisplatin drug delivery using gold-coated iron oxide nanoparticles for enhanced tumour targeting with external magnetic fields. *Inorganica Chimica Acta*, 393, pp.328–333.

Wang, W. et al., 2013. Role of thiol-containing polyethylene glycol (thiol-PEG) in the modification process of gold nanoparticles (AuNPs): Stabilizer or coagulant? *Journal of Colloid and Interface Science*, 404, pp.223–229.

Wang, W.-B. et al., 2014. Recent studies of 5-fluorouracil resistance in pancreatic cancer. *World journal of gastroenterology*, 20(42), pp.15682–90.

Wang, Y.-X.J., 2015. Current status of superparamagnetic iron oxide contrast agents for liver magnetic resonance imaging. *World J Gastroenterol*, 21(47), pp.1–15.

Wang, Y.-X.J., 2011. Superparamagnetic iron oxide based MRI contrast agents: Current status of clinical application. *Quantitative imaging in medicine and surgery*, 1(1), pp.35–40.

Weyermann, J., Lochmann, D. & Zimmer, A., 2005. A practical note on the use of cytotoxicity assays. *International Journal of Pharmaceutics*, 288(2), pp.369–376.

Whatcott, C.J. et al., 2012. *Desmoplasia and chemoresistance in pancreatic cancer*, Transworld Research Network.

Wickremsinhe, E. et al., 2013. Preclinical absorption, distribution, metabolism, and excretion of an oral amide prodrug of gemcitabine designed to deliver prolonged systemic exposure. *Pharmaceutics*, 5(2), pp.261–76.

Wijdeven, R.H., Neefjes, J. & Ovaa, H., 2014. How chemistry supports cell biology: the chemical toolbox at your service. *Trends in Cell Biology*, 24(12), pp.751–760.

de Wilde, R.F. et al., 2012. Reporting precursors to invasive pancreatic cancer: pancreatic intraepithelial neoplasia, intraductal neoplasms and mucinous cystic neoplasm. *Diagnostic Histopathology*, 18(1), pp.17–30.

Williams, D. & Fleming, I., 2007. *Spectroscopic Methods in Organic Chemistry* 6th ed., McGraw-Hill Higher Education.

Wu, C.-H. et al., 2014. Multimodal Magneto-Plasmonic Nanoclusters for Biomedical Applications. *Advanced Functional Materials*, 24(43), pp.6862–6871.

Wu, Q. et al., 2014. Multi-drug resistance in cancer chemotherapeutics: Mechanisms and lab approaches. *Cancer Letters*, 347(2), pp.159–166.

Xiao, Z. et al., 2014. Molecular mechanism underlying lymphatic metastasis in pancreatic cancer. *BioMed research international*, 2014, p.925845.

Xie, J., Lee, S. & Chen, X., 2010. Nanoparticle-based theranostic agents. *Advanced drug delivery reviews*, 62(11), pp.1064–79.

Xiong, X.-B. et al., 2012. Amphiphilic block co-polymers: Preparation and application in nanodrug

and gene delivery. *Acta Biomaterialia*, 8(6), pp.2017–2033.

Yan, Y. et al., 2012. A poly(l-lysine)-based hydrophilic star block co-polymer as a protein nanocarrier with facile encapsulation and pH-responsive release. *Acta Biomaterialia*, 8(6), pp.2113–2120.

Yang, A., Cardona, D.L. & Barile, F.A., 2002. In VitroCytotoxicity Testing with Fluorescence-Based Assays in Cultured Human Lung and Dermal Cells. *Cell Biology and Toxicology*, 18(2), pp.97–108.

Yang, F. et al., 2011. Liposome based delivery systems in pancreatic cancer treatment: From bench to bedside. *Cancer Treatment Reviews*, 37(8), pp.633–642.

Yang, L. et al., 2016. Rare Primary Pleomorphic Adenoma in Posterior Fossa. *World Neurosurgery*, 93, p.484.

Yang, Y. et al., 2016. Analysis of silver and gold nanoparticles in environmental water using single particle-inductively coupled plasma-mass spectrometry. *Science of The Total Environment*, 563, pp.996–1007.

Yang, Y. et al., 2013. Biodegradable and amphiphilic block copolymer-doxorubicin conjugate as polymeric nanoscale drug delivery vehicle for breast cancer therapy. *Biomaterials*, 34(33), pp.8430–43.

Yu, W. et al., 2001. Synthesis of functional protein in liposome. *Journal of Bioscience and Bioengineering*, 92(6), pp.590–593.

Yun, S.-I. et al., 2009. Japanese encephalitis virus-based replicon RNAs/particles as an expression system for HIV-1 Pr55Gag that is capable of producing virus-like particles. *Virus Research*, 144(1–2), pp.298–305.

Z'graggen, K. et al., 2001. Biological implications of tumor cells in blood and bone marrow of pancreatic cancer patients. *Surgery*, 129(5), pp.537–546.

Zhang, G.-N. et al., 2011. Combination of salinomycin and gemcitabine eliminates pancreatic cancer cells. *Cancer Letters*, 313(2), pp.137–144.

Zhang, H. et al., 2013. Enhanced wavelength modulation SPR biosensor based on gold nanorods for immunoglobulin detection. *Talanta*, 115, pp.857–862.

Zhang, S. et al., 2007. Surface plasmon resonance characterization of thermally evaporated thin gold films. *Surface Science*, 601(23), pp.5445–5458.

Zhang, Y. et al., 2013a. Study human pancreatic cancer in mice: how close are they? *Biochimica et biophysica acta*, 1835(1), pp.110–8.

Zhang, Y., Kim, W.Y. & Huang, L., 2013. Systemic delivery of gemcitabine triphosphate via LCP nanoparticles for NSCLC and pancreatic cancer therapy. *Biomaterials*, 34(13), pp.3447–3458.

Zhi, X. et al., 2014. MUC4-induced nuclear translocation of β-catenin: a novel mechanism for growth, metastasis and angiogenesis in pancreatic cancer. *Cancer letters*, 346(1), pp.104–13.

Zhu, J., Kell, A.J. & Workentin, M.S., 2006. A retro-Diels-Alder reaction to uncover maleimide-modified surfaces on monolayer-protected nanoparticles for reversible covalent assembly. *Organic Letters*, 8(22), pp.4993–4996.

Zubrick, J., 1997. *The Organic Chem Lab Survival Manual* 4th ed., John Wiley & Sons.

7.0. Appendix